Doctoral theses at NTNU, 2020:252

Sethulakshmy Jayakumari

Formation and Characterization of β- and α-Silicon Carbide Produced During Silicon/Ferrosilicon Process

Doctoral thesis

Sethulakshmy Jayakumari

ISBN 978-82-326-4852-8 (printed ver.)
ISBN 978-82-326-4853-5 (electronic ver.)
ISSN 1503-8181

NTNU
Norwegian University of
Science and Technology

NTNU
Norwegian University of Science and Technology
Thesis for the Degree of
Philosophiae Doctor
Faculty of Natural Sciences
Department of Materials Science and Engineering

Doctoral theses at NTNU, 2020:252

NTNU
Norwegian University of
Science and Technology

Sethulakshmy Jayakumari

Formation and Characterization of β- and α-Silicon Carbide Produced During Silicon/Ferrosilicon Process

Thesis for the Degree of Philosophiae Doctor

Trondheim, September 2020

Norwegian University of Science and Technology
Faculty of Natural Sciences
Department of Materials Science and Engineering

NTNU
Norwegian University of
Science and Technology

NTNU
Norwegian University of Science and Technology

Thesis for the Degree of Philosophiae Doctor

Faculty of Natural Sciences
Department of Materials Science and Engineering

ISBN 978-82-326-4852-8 (printed ver.)
ISBN 978-82-326-4853-5 (electronic ver.)
ISSN 1503-8181

Doctoral theses at NTNU, 2020:252

Printed by NTNU Grafisk senter

"Perhaps time's definition of coal is diamond"

- *Khalil Gibran*

Dedicated to my soulmate and best friend, a passionate researcher
Rajeev, and to my two beautiful girls Gowri and Padma

Preface

This thesis is submitted to the Norwegian University of Science and Technology (NTNU), in partial fulfillment of the requirements for the degree of Philosophiae Doctor. The present work was conducted at the Department of Material Science and Engineering at NTNU, Trondheim, Norway, during the period from August 2015 to July 2020 under the supervision of Prof. Merete Tangstad.

Metal Production, an eight-year Research Centre under the SFI-scheme (Centres for Research-based Innovation, 237738), has funded this work. The author gratefully acknowledges the financial support from the Research Council of Norway and the partners at SFI Metal Production.

The main aim of the present research work was to investigate the formation and characterization of β- and α-Silicon Carbide produced during the Silicon/Ferrosilicon process. ELKEM Thamshavn provided the raw materials and the author performed all the experimental works.

Sethulakshmy Jayakumari

June 2020, Trondheim

Acknowledgement

Striving for this Ph.D. has been a profoundly life-changing and challenging experience for me. During these academic years, I have grown significantly as a scientist and as a person. For this, I have to thank my family, friends, scientific collaborators, and the nurturing influence of many that I have met. This thesis would not have materialized without the guidance and support that I received from many people. Now, its time to thank all of them, who made this thesis possible.

First, I owe my deepest gratitude to my supervisor Prof. Merete Tangstad for her excellent guidance throughout the research work. She gave me a chance, by opening the door to the field of metallurgy. I thoroughly appreciate her immense knowledge in the field of metallurgy, her teaching skills, and her motherly care and support towards her student's welfare. Without her constant guidance and persistent feedback, this thesis would not have eventuated. Merete, I learned a lot from you, and I am grateful for the wonderful opportunity that you provided me.

Next, I am extremely grateful to Prof. Antonius T. J. van Helvoort (NTNU) and Dr. Per Erik Vullum (SINTEF) for their exceptional guidance in the TEM/STEM analyses, as well as their supervision and valuable comments that helped in publishing our scientific findings (my first scientific article).

I would like to thank Dr. Eli Ringdalen (SINTEF), Dr. Michael Kizasek (SINTEF), Dr. Edin Henrik Myrhaug (ELKEM), Aasgeir Valderhaug (ELKEM), Birger Andersen (Wacker), and Prof. Halvard Tveit (NTNU) for the valuable and inspiring discussions, and their feedbacks to my queries in the field of silicon production.

I would like to thank the engineers in the Department of Material Science and Engineering at NTNU and SINTEF Materials and Chemistry, for the help and support they provided. I would like to thank Dmitry Slizovskiy, Jonas Einan Gjøvik, and Arman Hoseinpur Kermani for offering the technical support required for the experimental work.

I am thankful to Yingda Yu (NTNU) for the training with SEM, Morten Peder Raanes (NTNU) for taking the EPMA images, Trygve Lindahl Schanche (NTNU) for the microscopy sample preparations, Kristin Høydalsvik (NTNU) for running the XRD machine, and Julian Richard Tolchard (SINTEF) for teaching me the TOPAS software.

Thanks to Dr. Xiang Li for helping me conduct some of my experiments during my pregnancy period. I would also like to acknowledge Delphine Leroy (ELKEM) for arranging the raw materials for my experiments, Steinar Prytz (SINTEF) for providing the technical help for the induction furnace experiments, Irene Bragstad (SINTEF) taking the porosity measurements, Aksel Alstad (NTNU) for making the graphite sieves, Odd Corneliussen (NTNU) for crushing the raw materials, Kent Mogstad (past NTNU) for extending the technical support for Hot press furnace experiments, Birgitte Karlsen (SINTEF) for helping me with the last minute EPMA sample preparation, and Stein Rørvik (SINTEF) for providing the CT scans.

Now comes the time to thank the SFI project leaders and the NTNU administration at the Berg Bygg for their support. I am also grateful to all my friends and administrators in the

SIMANTI group since 2014. Special thanks to Andrea Broggi for all those inspiring academic discussions, and Vincent Canaguier for his tips and tricks while learning HSC and Inkscape software. And of course, a big thank you to my dearest friend Swapna for giving me the mental support as well as helping me enormously with the proof reading of my thesis.

I would like to express my eternal appreciation towards my parents and in-laws for their blessings and prayers. They gave us constant love, moral support, encouragement, and motivation to accomplish our goals.

The reason I am here in Norway is my husband Rajeev. His excellence in the field of research have always inspired me and helped me immensely in systematically planning my academics. The encouragement I received from him is beyond imagination. He is my best friend, the best mentor for me, and a best father to our kids. Words are not enough to say, "thanks a lot Rajeev, for our big achievement". Our beautiful daughters Gowri and Padma, they have always been very understanding, adjusting, and truly supportive of me accomplishing my PhD goals. Thanks to the Almighty for giving me strength, health, and peace to fulfill this achievement.

Abstract

Silicon carbide (SiC) is one of the main intermediate compounds generated during primary silicon (Si) production in submerged arc furnaces. Carbon materials, either biomass-based (charcoal and wood chips) or based on fossil sources (coal, coke, and petroleum coke) are the primary reduction materials for Si production. The interaction between carbon materials and silicon monoxide gas (SiO(g)) to form SiC is vital in this process. SiC exists as many forms of polytypes, and the most common forms of SiC prevailing at atmospheric pressure are the α-SiC and β-SiC. SiC is also observed during industrial excavations, accumulated in the form of crust in the high-temperature zones of the furnaces. Macroscopic and microscopic characterizations of these SiC samples have revealed that carbon materials added to the process initially transform to β-SiC at lower temperatures, and would further transform to α-SiC at temperatures ≥ 2000 °C. This thesis investigates the material structures and physical properties of SiC formed from industrial carbon materials (charcoal, coal, and petroleum coke), at temperatures ranging from 1674 to 2450 °C.

To study the production and properties of β-SiC formed from these carbon materials, a laboratory-scale experimental method was developed, simulating the industrial process. An induction furnace was used to produce β-SiC using charcoal, coal, and petroleum coke. Two different SiO(g) sources such as (SiO_2 + Si) and (SiO_2 + SiC), giving various SiO pressures, were also explored in this study. Experiments were performed at temperature ranges of 1674–1900 °C and the SiC samples produced at this temperature range were confirmed as β-SiC by the X-ray diffraction analyses. The formation of β-SiC is more efficient with charcoal, followed by coal and petroleum coke. This shows that besides the temperature, the physical properties of carbon materials such as porosity and cell wall thickness also determine the SiO(g) reactivity. Charcoal has a higher porosity and thinner cell walls compared with coal and petroleum coke. Also, more SiC was produced with the higher SiO pressure obtained by using (SiO_2 + Si) as the source for SiO(g).

Elemental silicon was produced in the SiC structures at higher SiO pressures and higher temperatures. Thermodynamic calculations show that Si production is possible only at a temperature above 1800 °C. In this work, the production of elemental Si in SiC particles was observed even at 1674 °C, at higher SiO pressures. This shows that the gas phase will not be in equilibrium with the condensation products. The formation of Si in SiC particles increased with an increase in temperature. The current findings indicate that it is possible to produce Si in SiC

particles quite high up in the furnace at lower temperatures (< 1800 °C), provided the partial pressure of SiO(g) is favorable.

Microscopic analyses revealed that SiC forms through two different mechanisms; (a) SiC surface crystals of varying sizes and shapes form on the pore wall surfaces, and (b) the carbon pore walls themselves transform to SiC. The SiC surface crystals form via the gas phase mechanism, where SiO(g) reacts with CO(g); whereas the pore walls transform to SiC as the diffused SiO(g) reacts with the solid carbon.

Morphological characterization of SiC particles formed from charcoal at a temperature around 1750 °C showed that SiC surface crystals in the shape of 'micro-bullets' grew on their surfaces either as solitary crystals or in clusters forming micro-bullet "flowers". Interestingly, such bullet-shaped SiC crystals were observed only on the charcoal substrates. This suggests that the carbon material properties as well as the local reaction conditions might control the morphology. The SiC lamella extracted from the bullet-shaped crystals had a high density of stacking faults in a non-periodic manner. However, it is noteworthy that despite the high stacking fault density, the sizes and morphologies of the micro-bullets are relatively homogeneous. The findings are relevant in the field of SiC ceramics from bio-carbon for the development of novel light-weight high-temperature-resistant materials. The SiC surface crystals formed on coal and petroleum coke were different from those formed on charcoal. SiC crystals in coal were long thick nanowires and whiskers, whereas, in petroleum coke, they were mostly whiskers.

The Shrinking Core Model (SCM) closely approximated the real particles in charcoal. The charcoal partly converted to SiC showed a sharp boundary between the SiC product layer and the unreacted carbon in the middle. However, coal and petroleum coke used in this study behaved differently, they did not follow the SCM mechanism. In coal particles, the SiC formed was more spatially distributed and in petroleum coke a sharp boundary was clearly visible between the pore walls that had transformed to SiC and the unreacted region.

β-SiC with elemental Si of varying amounts, produced by the original carbon materials were utilized for studying the transformation of β-SiC to α-SiC. A graphite tube furnace efficient for high-temperature experiments was utilized for the heat-treatment of β-SiC particles at temperatures ranging from 2100 to 2450 °C. Results showed that the transformation to α-SiC was greatly influenced by the original carbon source. Charcoal-converted β-SiC particles easily transformed to α-SiC at 2100 °C, compared with β-SiC from coal and petroleum coke.

Moreover, the amount of elemental Si in SiC particles enhanced the transformation to α-SiC at 2100 °C.

Based on this work, the following conceptual model for the industrial furnace could be discussed: β-SiC would form when carbon reacts with SiO(g), both through solid-gas reaction and gas phase. Once the β-SiC is formed, elemental Si would easily form in the SiC particles at temperatures lower than the theoretical Si production temperature. The β-SiC transforms to α-SiC at higher temperatures (≥ 2000 °C). Carbon material properties as well as the amount of elemental Si in β-SiC particles influence the transformation of β-SiC to α-SiC.

List of publications

1. **Sethulakshmy Jayakumari** and Merete Tangstad., "Silicon Carbide formation from coal or charcoal in the silicon/ferrosilicon process", *INFACON XV*, Cape Town, South Africa, February 2018.

2. **Sethulakshmy Jayakumari** and Merete Tangstad., "Formation of elemental silicon in β-SiC particles", *Silicon for the Chemical and Solar Industry XIV*, Svolvær, Norway, June 2018.

3. **Sethulakshmy Jayakumari**, Per Erik Vullum, Antonius T. J. van Helvoort and Merete Tangstad., "SiC crystalline micro bullets on bio-carbon based charcoal substrate", *Journal of crystal growth*, May 2020.

4. **Sethulakshmy Jayakumari** and Merete Tangstad., "Transformation of β-SiC from Charcoal, Coal, and Petroleum coke to α-SiC at higher temperatures", revised and re-submitted to *Metallurgical and materials transactions B,* July 2020.

Contents

List of Figures

List of tables

1 Introduction

Silicon carbide (SiC), commonly known as carborundum, is a unique compound of carbon (C) and silicon (Si). Compared with other materials, SiC generally exhibits higher hardness and mechanical strength at higher temperatures, and has an excellent thermal conductivity. It also has a lower coefficient of thermal expansion, high melting point, high resistance to corrosion and oxidation, and a wide bandgap [1, 2]. The excellent electronic properties of SiC make it a highly promising material in many industrial applications. SiC ceramics made from bio-carbon with anisotropic porosity is gaining more interest in the manufacturing of new lightweight, heat-resistant materials [3, 4]. Various methods are used for manufacturing SiC, such as the Acheson's process, physical vapor deposition (PVD), and chemical vapor deposition (CVD) [5]. SiC also forms during the industrial production of primary Si. In this process, SiC is produced when carbon added to the raw materials reacts with the silicon monoxide gas (SiO(g)) formed in the furnace. SiC has two main roles in the industrial production of Si [6];

(i) It acts as a requisite intermediate product for the final Si production.
(ii) It plays a vital role in distributing the energy inside the Si furnace.

Therefore, extensive knowledge of SiC formation is essential for understanding the Si production. Also, the demand for Si is rapidly increasing, particularly in the solar cell industry and photovoltaic applications [7], and to accomplish the increasing demands for Si, enhancing the quality of industrial Si production is a challenging requisite. Though the properties of commercial SiC are well documented, the formation processes as well as properties of the SiC formed during the industrial production of Si are not investigated to the same extent. This has been a major motive for the research presented in this thesis. In the present work, I have analyzed formation of different types of SiC from different carbon sources predominantly used in the Si production process. The following section gives a brief overview of Si production, more specifically the different SiC formations, and its importance in the Si process.

1.1 Silicon production

Si is produced industrially by reducing silicon dioxide (Quartz/SiO_2) with carbon, in a three-phase submerged arc furnace (SAF) [6]. The reaction, in an idealized form, can be written as:

$$SiO_2\,(s) + 2C\,(s) = Si\,(l) + 2CO\,(g) \qquad (1)$$

where, s, l, and g denote solid, liquid, and gaseous phases, respectively. However, the process is more complex than expressed by **reaction (1)**. A more detailed description of the different reactions in the Si process is given later in **section 2.4**.

The principal parts of a modern Si plant are illustrated in **Figure 1.1.1.** A typical modern Si plant consists mainly of a SAF, with a diameter of about 10 m and a depth of 4 m, the dimensions generally depending on the power supply [6, 8]. The heart of a Si plant is the electric SAF (**Figure 1.1.1**), where Si and high silicon ferroalloys (FeSi) are produced [6, 9]. In the FeSi production, iron oxide (Fe_2O_2) or scrap iron is also introduced into the charge materials, in addition to the SiO_2 and carbon materials. The furnace body consists of shallow crucibles made of steel shells and furnace linings made of thick carbon blocks that can withstand extremely high temperatures. The process requires a lot of electrical energy, which is delivered through the three consumable carbon electrodes located at the center of the furnace, as shown in **Figure 1.1.1** [6, 8, 9].

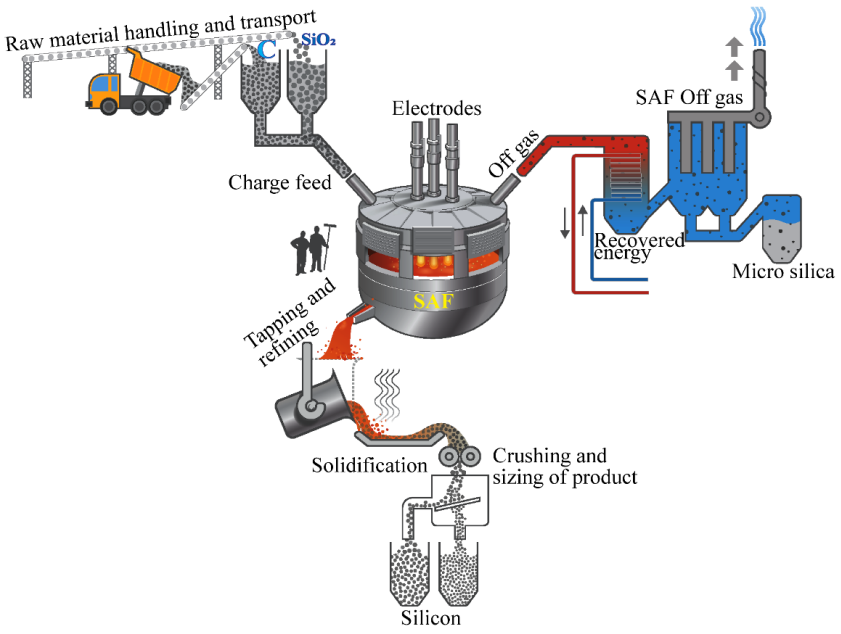

Figure 1.1.1. Principal parts of a modern Si plant, adapted from Schei et al. [6], redrawn by Ida Kero, SINTEF Industry.

The electrodes are positioned vertically, submerged deep into the charge mixture. They carry high currents that generate an electric arc between the electrode tips and the carbon-

containing crater walls or the liquid Si bath. These electrodes can resist the extreme temperatures generated by the electric arcs. The temperature could be several thousand degrees close to the arc region. Based on previous reports, the temperature at the core of the electric arc ranges between 20,000–30,000 K [8, 9]. The two main electrical conducting materials in the crater wall are carbon and SiC. In the crater wall area, the temperatures range from 1900 to 2200 °C. Secondary electric arcs might run towards the crater walls, thus capturing part of the energy from the main arc [8, 10]. There is a unit for handling the raw materials (SiO_2, carbon, and wood chips). The raw materials, which are mixed after weighing, are fed through the top of the furnace through the several charge feeding tubes (**Figure 1.1.1**).

A significant amount of the supplied energy is dissipated as heat from the electric arcs into the gas filled cavities around the electrode tips. Cavities arise as a result of the heat generated in the charge around the tip of the electrodes. The presence of such cavities was established by Zherdev et al. [11, 12, 13] who detected them by inserting electrical probes in the charge. Later, Otani et al. [14] also confirmed this in their study, where they inserted a visual probe into the cavity of the furnace to examine the inner structure of the furnace. These studies demonstrated that a gas filled cavity surrounds the electrodes. According to the pyrometer measurements, the temperature near the electrode and the crater wall ranges between 2000 to 2400 °C [14].

During the Si production process, the carbon sources (carbon from the raw materials) are converted to SiC as a result of its interaction with SiO(g) [6]. Some of the carbon monoxide (CO(g)) and SiO(g) would leave through the charge top. The CO(g) burns to form carbon dioxide (CO_2), whereas SiO(g) reacts with the oxygen (O_2) in the air to form SiO_2 fines called micro-silica. This by-product is collected from the off-gas handling system (**Figure 1.1.1**). Micro-silica is mostly used as an additive in concrete production, as it influences the mechanical properties of concrete.

Si is formed as liquid Si and is tapped into ladles through several tap holes on the side, close to the furnace bottom (**Figure 1.1.1**). Depending on the electrical efficiency of the furnace and Si recovery, a well operated furnace would use about 10.5 MWh per metric ton of the tapped Si [8]. The tapped Si consists of certain impurities (carbon, boron and phosphorus) coming from the raw materials. In the refining process, the liquid Si is passed through different stages to remove such impurities. Metallurgical grade Si is used as a raw material in the semiconductor and chemical industries. It is also used for alloying elements with other metals, for example in making aluminum (Al) alloys.

1.2 SiC deposits in Si production

The carbon content in the charge mix and properties of the selected carbon materials predominantly influence the Si yield in a Si/FeSi furnace [9]. For a maximum Si yield, the carbon added along with the raw materials should be optimal, which is challenging to establish accurately. If the carbon content in the charge is high, a large amount of carbon will react with the SiO(g) to form SiC. In addition, partly converted SiC with some unreacted carbon present in it also comes down to the inner zone of the furnace. This unreacted carbon further reacts with the SiO(g) in the inner zone forming additional SiC. In this scenario, the electrical conductivity of the materials in the high temperature zone increases due to the large quantities of SiC. Therefore, producing Si with low energy consumption and less emissions would be of a great advantage to the industry. To attain that, the energy distribution in the furnace must be controlled to obtain optimum reaction temperatures.

Accumulation of SiC was observed at the furnace hearth during excavations of industrial furnaces such as the 40 MW Si and 17 MW FeSi furnaces [15, 16, 17]. The structure of the SiC accumulated in the crust was different compared with the structure of the carbon-converted SiC. The initially formed carbon-converted SiC had the same structure as that of the original carbon material, which was of the cubic polytype β-SiC (3C, C here denotes cubic) [18, 19]. However, the SiC crust in the Si furnace was black in color, named as black-SiC, occupying a large volume, filling the inner parts of the entire furnace from the bottom to the top. It was assumed that the SiC crust might have formed from the transformed carbon particles. Analyses have shown that more than 90% of the SiC excavated from industrial Si furnace crusts were α-SiC that comprise hexagonal or rhombohedral polytypes [18, 19]. The structures and properties of different polytypes of SiC are described in detail in **section 2.3.2**.

Large gas channels were also noticed in the SiC crust and precipitates of SiC in the shape of dendrites were observed inside these gas channels. Tangstad et al. [15] proposed that the accumulated carbon or SiC exposed to temperatures higher than 2000 °C formed gaseous compounds containing carbon or Si. During cooling, at around 2000 °C, the gaseous products from carbon and Si bearing compounds are precipitated as α-SiC. Too much accumulation of SiC in the furnace compromises the furnace operation and contributes to a poor Si yield. Interestingly, the SiC crust observed after excavation by Tranell et al. [17] was smaller and similar to that obtained after a 150 kW pilot scale excavation done by Myrhaug [20]. Although the presence of SiC crusts have been known for quite some time, its properties and formation

mechanisms are not yet investigated thoroughly. Based on available literature, there are three main theories on the formation mechanisms of different types of SiC crusts in the furnace;

a) Carbon materials added to the process transform to β-SiC, which at higher temperatures would transform to α-SiC.

A part of the carbon sources converts to SiC in the outer reaction zone of the Si furnace as a result of its interaction with SiO(g). Myrhaug [20] described that the Si yield is strongly affected by the SiO(g) reactivity of the carbon materials, which is measured using the standard SiO(g) test [21, 22]. Laboratory experiments producing SiC from charcoal and coal (at temperatures from 1545 to 1900 °C) have confirmed that when carbon directly reacts with SiO(g), the resultant SiC is of the polytype β-SiC [18, 23]. Further heat-treatment experiments with β-SiC produced from coal at temperatures ranging from 2000 to 2500 °C have shown that the transformation of β-SiC to α-SiC takes place at 2350 °C [18]. This gives an indication that in the Si process, β-SiC formed in the outer zone travels to the inner zone and being exposed to higher temperatures (> 1800 °C to several thousands of degrees) it would gradually transform to α-SiC. Temperature is the main factor that influences this transformation of β-SiC to α-SiC [24, 25]. Lindstad [5] investigated the changes in the structures of commercially produced SiC and found that the transformation from β-SiC to α-SiC takes place at around 2200 °C.

b) The gaseous SiC compounds formed at higher temperatures later condense at lower temperatures on the crater wall as α-SiC.

The temperatures at the core of the electric arc are generally in the ranges of 20000–30000 K and form gases near the electrode. It is assumed that these gases cause the dendritic structures observed in the SiC crust [8, 9]. As the main constituents around the arc are Si and C, at around 3000 °C, quite large amounts of SiC_2(g), Si_2C(g), and Si(g) are produced. As these gases flow from the arc region to the regions of relatively lower temperatures, they condense and at around 2000 °C, most of them condense into solid SiC (α-SiC) and elemental Si.

c) β-SiC is precipitated from liquid Si.

When liquid Si cools, it forms SiC by reacting with any available carbon [6]. This can be represented as:

$$Si\ (l) + \underline{C}\ (s) = SiC\ (s) \qquad (2)$$

In addition, wettability of SiC formed from different carbon materials have been previously investigated on laboratory-scales by many researchers [26, 27, 28, 29]. The analysis of a SiC sample in one such study that investigated the wettability of Si in graphite crucibles identified it as β-SiC [29]. Even though the β-SiC at higher temperatures might again transform to α-SiC, this seems like the least plausible theory.

1.3 Objective and goals

The hypotheses mentioned above have led me to develop the main objective of this work, which is to study the formation mechanisms of SiC in the Si furnace and further evaluating the existing theories on SiC production. In the industrial Si production process, a temperature gradient exists in the furnace from its top to the bottom part ranging from 500 to 2000 °C and above. Several types of carbon materials are used to produce SiC in the Si process. A number of aspects are evaluated in choosing the type of carbon material to be used industrially, such as its strength and SiO-reactivity. The kinetics of the SiO(g) reaction with different types of carbon materials have been studied extensively and the rate of formation of SiC varies depending on the properties of the carbon materials used [20, 21]. Most of those studies were performed under controlled conditions at lower temperatures (< 1700 °C). However, Si production being a high temperature process (> 1800 °C), it is very relevant to investigate the SiC production at temperatures higher than 1700 °C, which is one of the main goals of this research. Also, how the SiO(g) affects both the formation of SiC from different types of carbon materials and formation of Si in SiC is another intriguing question that we have addressed in this research.

As a basis for future investigations of the various SiC producing mechanisms, I have investigated the structure of the SiC formed from different carbon materials at temperatures ranging from 1674 to 2450 °C and compared them with the industrial SiC samples. This study will document the extent of α-SiC formation from β-SiC, based on the original type of carbon materials. This work will also examine whether the presence of elemental Si in the β-SiC affects the extent of transformation to α-SiC.

1.4 Thesis outline

This thesis investigates the reactions between SiO(g) with selected carbon materials and analyzes the production of β-SiC at temperatures ranging from 1674 to 1900 °C. Charcoal, coal, and petroleum coke (pet-coke) were selected as carbon materials and a mixture of (SiO_2 + Si) and pellets made from (SiO_2 + SiC) were used as charge to generate SiO(g). The β-SiC produced from these carbon materials were used to explore the further transformation to α-SiC at temperatures ranging from 2100 to 2450 °C. The study evaluated the different SiC samples formed, with respect to the properties of the carbon materials used and estimated the extent of transformation of β-SiC to α-SiC, based on the original carbon sources. Finally, these laboratory-produced SiC samples were compared with and SiC samples obtained from the industry. The remaining part of the thesis is organized in the following manner.

Chapter 2 gives an overview of the different SiC structures observed in previous excavations, followed by the thermodynamics of different reactions that take place in the Si furnace. The details about carbon materials used in the Si/FeSi industry, such as its production and properties are reviewed afterwards. The structure of SiC, commonly occurring SiC polytypes, and factors affecting its stability, are also discussed. Afterwards the thermodynamics of Si-C system and SiC from gas are explained. Finally, the kinetics of the different reactions during Si process are also described, based on previous studies.

Chapter 3 describes the experimental set up, methodology, the different parameters used for each set of experiments, and the various analysis methods used for material characterization. The raw materials, including the structure and properties of charcoal, coal, and pet-coke, are also cataloged in this chapter.

Chapter 4 presents the results from the experiments in the order of charcoal, coal, and pet-coke, both from the β-SiC production and from its further conversion to α-SiC. In addition, analyses of the three industrial SiC samples are also included in this chapter.

Chapter 5 discusses the results, comparing them with theory and also with results from previous studies relevant to this work. C**hapter 6** concludes the main findings from this study. Finally, **chapter 7** details the novelty and industrial significance, and suggestions for future work are presented in **chapter 8**.

2 Theory and literature

This chapter elaborates the theoretical and literature framework that defines the key concepts of this study. The purpose of this chapter is to relate and discuss relevant theories and models, based on available literature. The first few sections give a detailed description of the various SiC structures procured during several Si/FeSi furnace excavations and the reactions that take place in the Si process. This is followed by a description of the carbon materials that are used as raw material in Si production and a brief overview about the structure and stability of SiC, theory of polytype formation, and the Si-C system. Finally, findings from previous studies on the kinetics of the different reactions occurring in the Si process are discussed in detail in the last section.

2.1 Inner structure of Si/FeSi furnaces: Zones and SiC structures

Diverse methods have been applied in the recent past and are still being developed to distinguish the different zones inside the industrial SAFs used for Si and FeSi production. It is difficult to observe the inner operation of a furnace. In the past, researchers have used, among other methods, electrical probes to investigate the inner structure of furnaces [6]. In addition, excavations executed in some of the industrial furnaces that were shut down owing to problems with operation or for furnace maintenance have ensued a detailed and better understanding of the chemical reactions and material flows inside the furnace. This section gives a brief summary of such observations, primarily focusing on the SiC formation.

The first comprehensive study of the inner structure of a furnace was done by Zherdev et al. [11, 12, 13]. They used electrical probes while the furnace was operating, which revealed that the electrodes were surrounded by a gas filled cavity. The cavity had formed above the pool of liquid Si and consisted of gases produced by reactions in the inner zone. The gases flowed through the charge material creating channels. They found that the size of the cavity depended on the content of Si in the FeSi, pressure of the gas, and rotation of the furnace.

Later Otani et al. [14] placed a visual probe in the cavity of a furnace to study its inner structure. This work also confirmed that a gas filled cavity surrounds the electrode. In addition, they found a reef-like bottom deposit consisting of SiC crystals with molten Si. This was located 5–15 cm below the tip of the electrode. **Figure 2.1.1** represents the status of a furnace after a run [14]. A viscous mass of a mixture of molten quartz and carbon materials was frequently falling down close to the electrode tip and vanished gradually. The materials in the cavity roof were confirmed to be condensates from the gas and these materials were gradually consumed,

moving the cavity roof upwards in the furnace. The temperatures near the electrode and the crater wall ranged 2000–2400 °C, according to their pyrometer measurements.

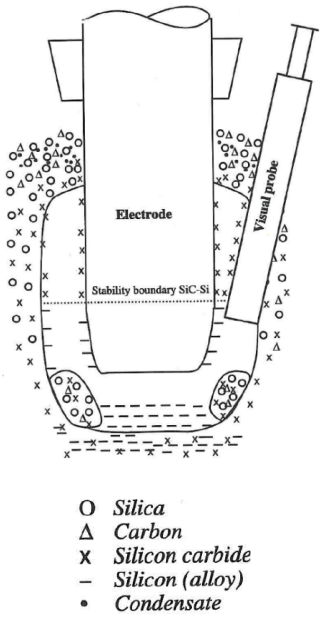

Figure 2.1.1. Inner structure of Si furnace according to Otani et al. [14].

Excavations of pilot scale furnaces have also been carried out after they were shut down to get more information regarding the state of the furnace. Schei and Sandberg [30] investigated a 40 kW single phase SAF to study the condensate reactions. Muller et al. [31] excavated a FeSi75 furnace after the furnace was shut down and observed accumulation of SiC in the furnace hearth, with the electrode deeply submerged in the cavity very close to the carbide-metal mixture. They assumed that the accumulated SiC crystals came from the vapor phase. They divided the main reaction zones into four as: (i) crater gas, 3000–2000 °C; (ii) crater wall, 2000–1800 °C; (iii) crater crust, 1800–1500 °C; and (iv) charge mix, < 1500 °C.

In the crater gas zone, if SiC is present, it will decompose to carbon-bearing gas species, mainly SiC_2 and Si_2C. These gas species will react with SiO(g) according to the reaction:

$$SiC\ (gas\ species) + SiO(g) \rightarrow 2Si\ (g) + CO(g) \qquad (3)$$

Muller et al. [31] states that this reaction takes place at a temperature of around 2500 °C. According to **reaction (3)** and depending on the amount of SiC gas species, two outcomes are possible. If the SiC gas species are scant and the SiO/CO gas ratio is above the equilibrium value, it could cause a higher Si yield. However, if the SiO/CO ratio drops below the equilibrium value, the SiC would not be consumed and would accumulate at the furnace hearth. The

accumulated SiC would eventually evaporate into the arc zone and affect the furnace operation [31].

Based on several small-scale excavations, Schei et al. [6] gave an overall schematic picture of the inner section of a working Si furnace, which is illustrated in **Figure 2.1.2.** The figure depicts the Si furnace, showing the conditions around one electrode and the different furnace zones, including the various reactions occuring in each of these zones [6]. As most of the energy supplied is dissipated from the electrode tips, temperature remains highest at the bottom part of the furnace, as shown in **Figure 2.1.2.** Based on the temperature distribution and chemical reactions that take place during the Si process, the interior of the furnace is divided into two; low and high temperature zones which could also be designated as the outer and inner reactions zones, respectively. The thermodynamics of the various reactions happening in the two zones will be explained in **section 2.4.**

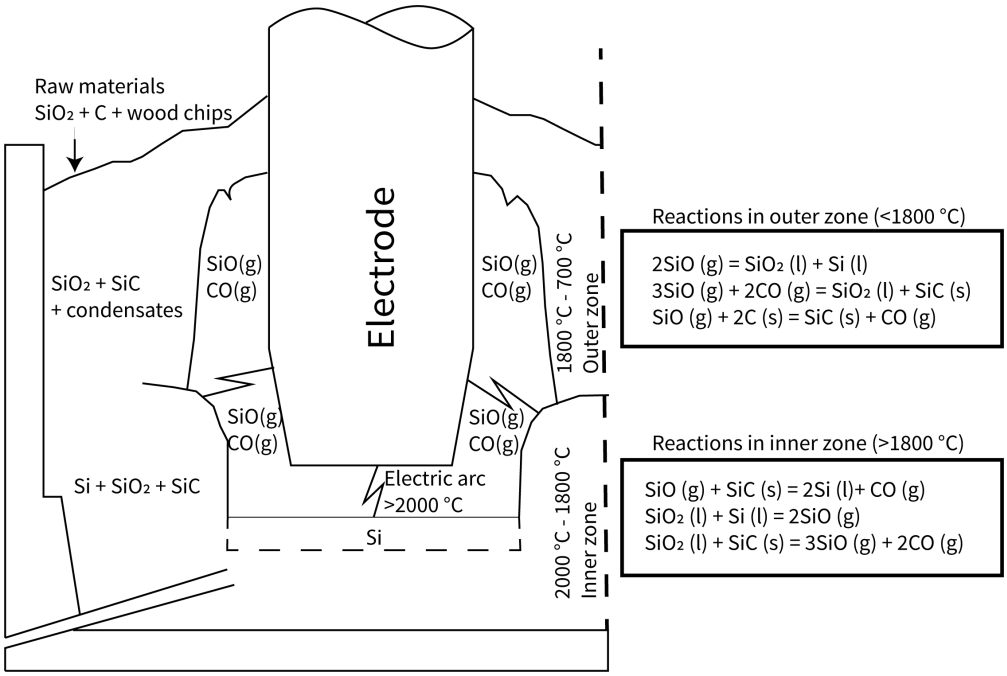

Figure 2.1.2. Schematic of inner section of a working Si furnace reprinted from Schei et al. [6].

The researchers later started to wonder whether the results and observations from small-scale furnace excavations would be comparable to those of the large-scale furnaces that had been operating for extended periods of time under variable conditions that were also more difficult to control. Recently, both pilot scale Si furnace experiments and large-scale industrial

Si/FeSi furnace excavations have revealed that the inner structure of a furnace varies between each cases [16, 17, 20, 32]. However, many of the features found in the pilot scale furnaces have also been observed in the industrial furnaces.

Tranell et al. [17] excavated a 17 MW FeSi75 furnace (Finnfjord) and Tangstad et al. [15, 16] excavated a 40 MW Si furnace (Elkem Thamshavn). The illustrations of both these furnaces with their conditions after shutdown, positions of the electrodes, the different reaction zones along with the region where SiC were deposited are shown in **Figure 2.1.3** and **Figure 2.1.4** [16, 17]. Accumulation of SiC in the form of crusts (marked by yellow circles) at the furnace hearth was observed during excavations of both the furnaces [15, 16, 17]. In the FeSi75 furnace, the crater wall around the electrode mainly had buildup of SiC with Si. However, the report did not elaborate on the phase analysis of the SiC samples [17].

In the Si furnace, the SiC crust (black-SiC) occupied almost half of the interior of the furnace, from its bottom to the top. The status of the Si furnace after opening the outer lining is shown in **Figure 2.1.5**. Large gas channels were observed in the SiC crust. Inside the gas channels, precipitates of SiC crystals in the form of dendrites were also noticed. A piece of the sample collected from the SiC crust deposit and the dendritic SiC crystal precipitates are shown in **Figure 2.1.6**. However, further analysis had shown that the structure of SiC crust that was observed after the excavations were entirely different from the SiC that had directly formed from the carbon materials reacting with SiO(g). **Figure 2.1.7** shows the images obtained from the electron probe micro-analyzer (EPMA) of both the SiC formed directly from the carbon materials and that of the deposited black-SiC crust.

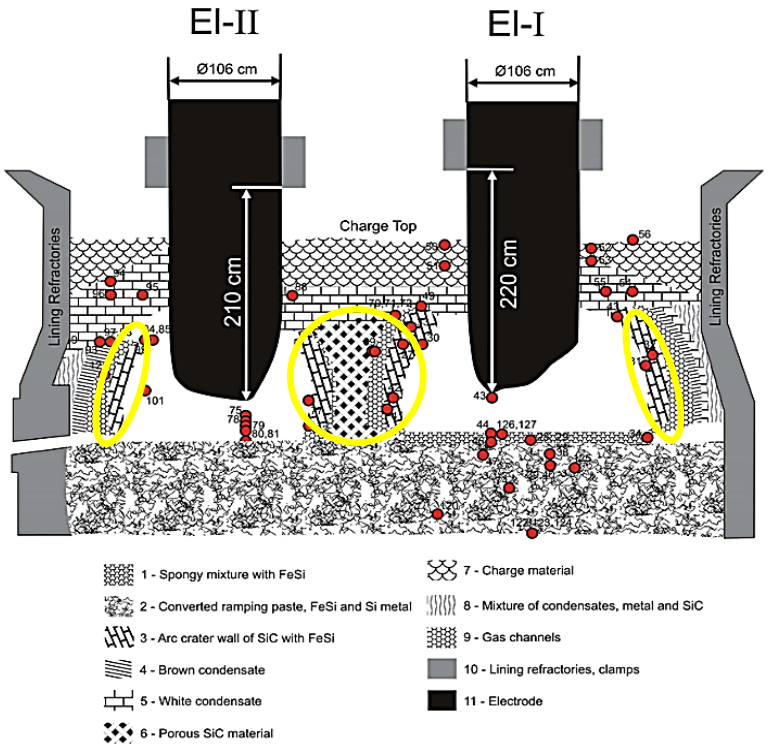

Figure 2.1.3. Schematic illustration of different zones in 17 MW FeSi furnace [17].

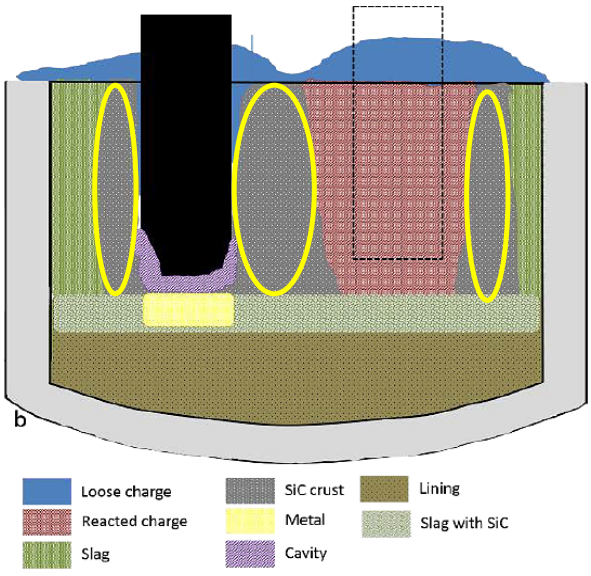

Figure 2.1.4. Schematic illustration showing different zones in 40 MW Si furnace [16].

Figure 2.1.5. Status of Si furnace after opening the outer lining [15].

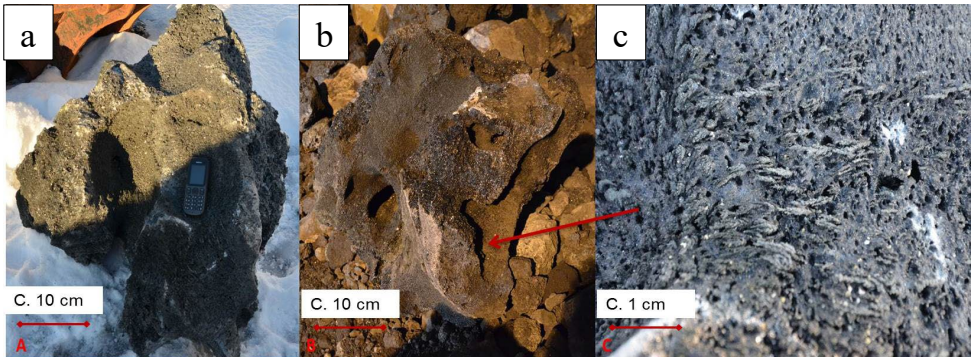

Figure 2.1.6. A piece of sample from (a) SiC crust deposit, (b) gas channels in SiC crust, and (c) dendritic SiC crystal precipitates on walls of gas channels [15].

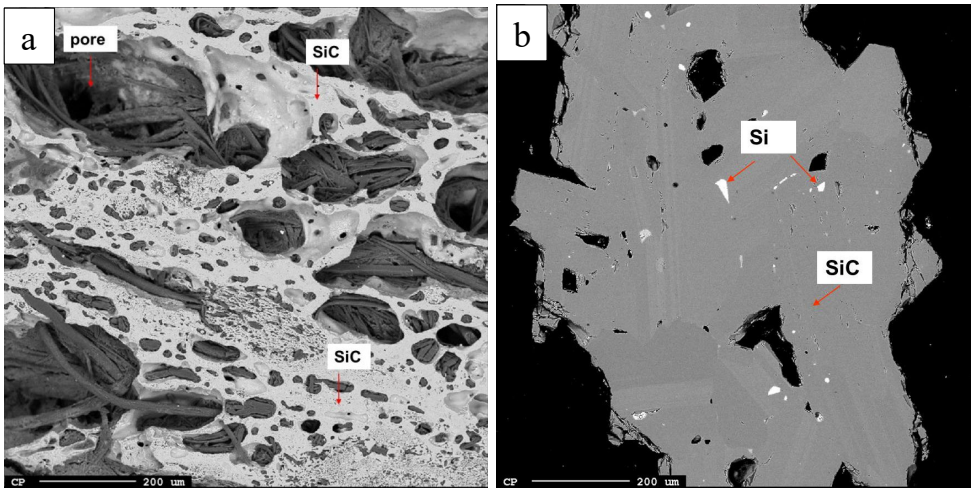

Figure 2.1.7. EPMA images of (a) SiC converted from carbon materials and (b) black-SiC crust [15].

The EPMA images showed the difference between the structures of original carbon material along with the SiC formed in it (**Figure 2.1.7a**) and the sample taken from the crust, which was very dense with some crystal grain boundaries in it (**Figure 2.1.7b**). The quantitative X-ray diffraction (XRD) analysis of the SiC revealed that more than 90% of the crust consisted of α-SiC. **Table 2-1** shows the results from the quantitative XRD analysis of the three black-SiC samples [15]. Analysis showed that hardly any cubic modification of β-SiC (3C) was present in the samples and that the most dominating α-SiC polytypes were 6H, 4H, and 15R, along with some additional amount of Si, where H and R stands for the hexagonal and rhombohedral symmetry, respectively.

Table 2-1. Quantitative XRD analysis of the three black-SiC samples [15].

SiC-polytypes	Sample no. 1	Sample no. 2	Sample no. 3
SiC 3C	0.3	1.1	0
SiC 6H	70	56.8	47.9
SiC 15R	24.4	11.7	9.4
SiC 4H	0.2	10.4	10.3
Si	1.6	4.3	19.1

Based on visual observation and classification of the collected samples from the excavations of two FeSi (FeSi75, **Figure 2.1.3** and FeSi50, **Figure 2.1.8a**) and three Si furnaces (**Figure 2.1.4**, **Figure 2.1.8b**, and **Figure 2.1.8c**), Ksiazek et al. [16] distinguished some main material zones. These different zones were:

1) Inactive zone: located at the walls of the furnace. This zone mostly consisted of the deposited slag and/or partly and fully melted raw materials.

2) Electrode track zone: this area followed the path of the electrode as the furnace outer shell was rotating.

3) Inner zone: located in the central part of the furnace towards and between the electrodes.

4) SiC zone: zone where most of the SiC deposits were located.

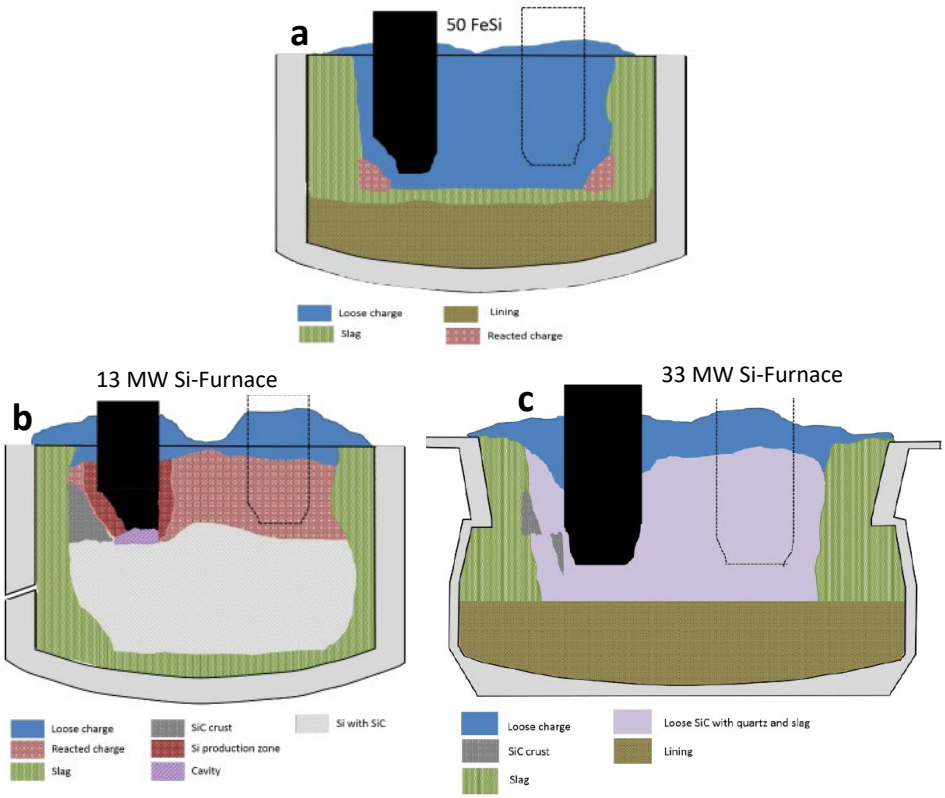

Figure 2.1.8. Different zones in (a) FeSi50 (Elkem Bjølvefossen) furnace [33], (b) 13 MW Si furnace (Wacker 1) and (c) 33 MW Si furnace (Wacker 2), described based on visual observation and classification of collected samples [16].

One of the main differences between the furnaces was the extent of SiC deposits. Hardly any SiC deposits/crusts and cavities were observed in the FeSi50 (Elkem Bjølvefossen), as shown in **Figure 2.1.8a** [33]. The furnace was mainly filled with partly and completely transformed SiC particles that were formed from coal. The EPMA of the SiC samples from the top portion revealed the original coal structure (**Figure 2.1.9a**) and was confirmed as SiC-3C (β-SiC) by XRD, whereas the SiC sample close to the electrode was very dense, consisting of large crystals with a structure

dissimilar to that of the original carbon (**Figure 2.1.9c**) and consisted of the α-SiC phase [33]. **Figure 2.1.8b** and **c** show the schematics of the 13 MW (Wacker 1) and 33 MW (Wacker 2) Si furnaces, and the position where SiC was observed in the form of crust. In addition to the SiC crust, SiC particles mixed with SiO_2 and slag were also observed. The SiC crust found in the 13 MW Si furnace was filled with very dense molten Si; its EPMA image is shown in **Figure 2.1.10** [34].

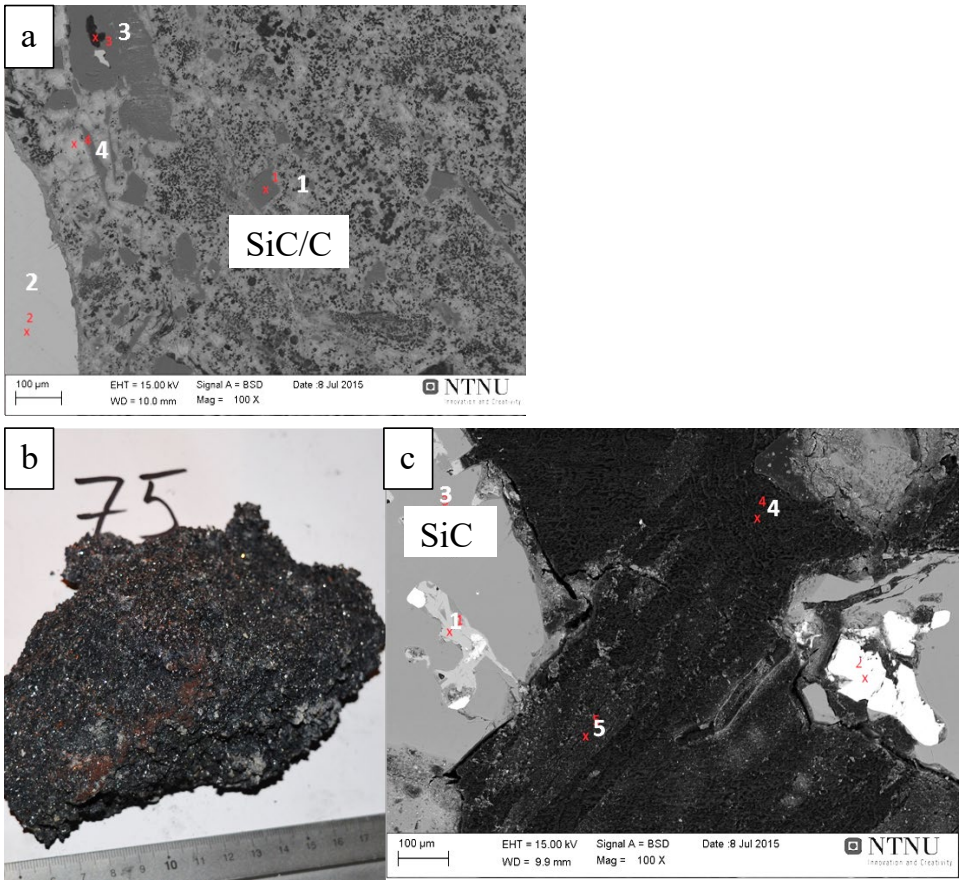

Figure 2.1.9. EPMA of SiC sample collected from (a) top portion of FeSi50 furnace, (b) macroscopic image, and (c) corresponding EPMA image of sample from near the electrode of FeSi50 furnace [33].

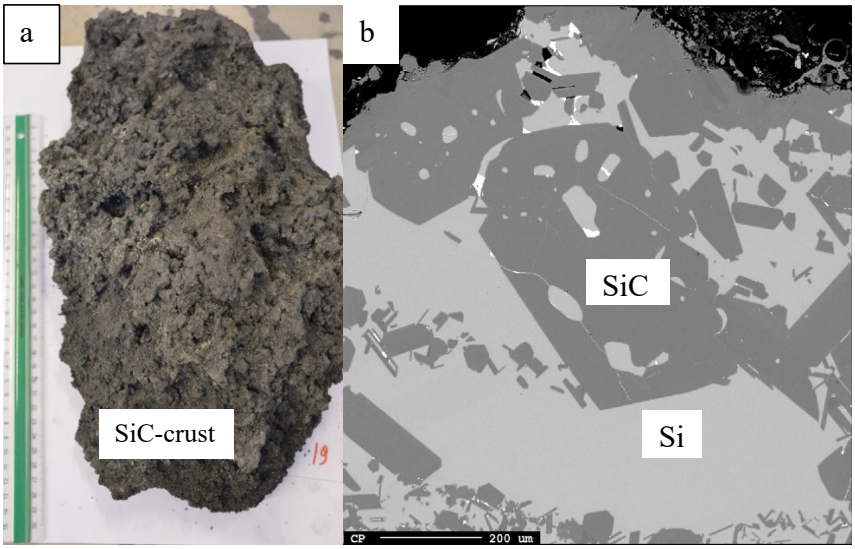

Figure 2.1.10. (a) SiC crust collected from the 13 MW Si furnace excavation and (b) its EPMA image [34].

Jusnes [35] excavated a FeSi75 (Finnfjord) furnace after it was shut down. The different materials and zones in the furnace are illustrated schematically in **Figure 2.1.11**. Layers of SiC were observed and the SiC samples collected from the top (position 1) and the bottom portion close to the electrode (position 2) were investigated under EPMA, which are shown in **Figure 2.1.12**. The sample from the top (position 1 in **Figure 2.1.11**) consisted of coal-converted SiC and is shown in **Figure 2.1.12a**, whereas the SiC sample from position 2 close to the electrode was very dense with a structure different from the original carbon, as shown in **Figure 2.1.12b** [35]. Hence, it was inferred that the SiC found in the bottom portion near to the electrode was α-SiC that had transformed from the carbon converted SiC particles.

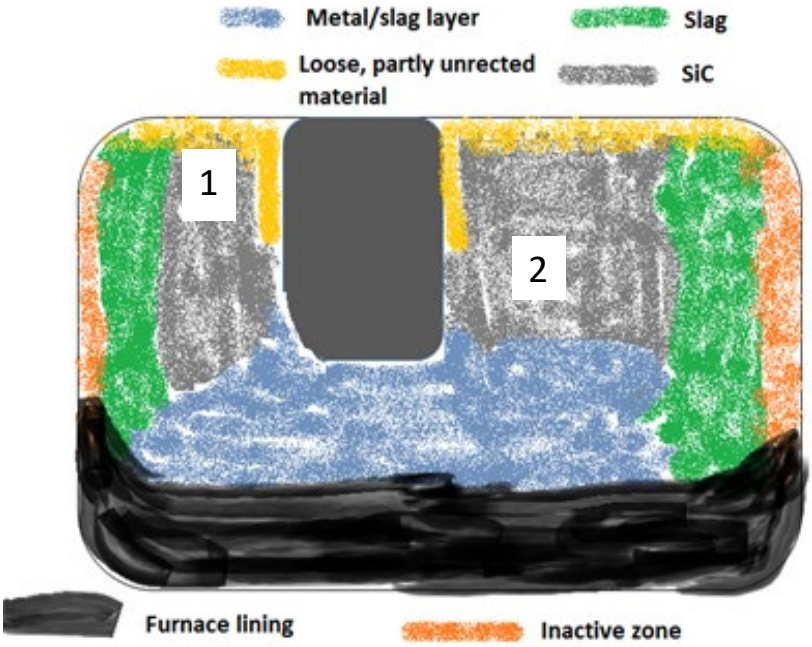

Figure 2.1.11. Schematic illustration of the materials and zones observed after excavation of FeSi75 furnace [35].

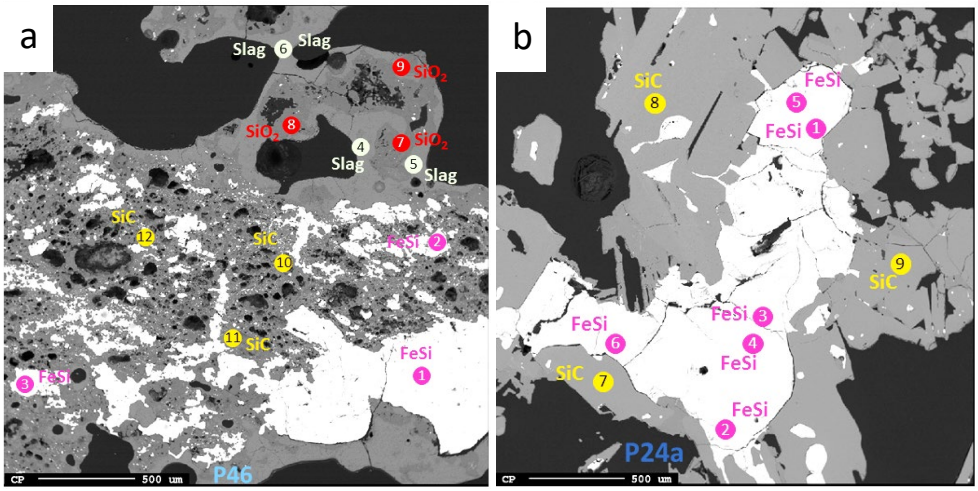

Figure 2.1.12. EPMA images of (a) SiC sample from top (position 1) and (b) SiC sample from position 2 close to the electrode [35].

Ksiazek [36] excavated the Si furnace 2 (Elkem Salten) and based on visual observation and microscopic characterization of the collected samples, identified the main material zones as illustrated in **Figure 2.1.13.** A reacted charge was observed behind the greenish condensate

layer close to the electrodes; it consisted mostly of a mixture of solid/smelted SiO_2 and the carbon material that was converted to SiC. The structure of the SiC particles in the reacted charge had the original carbon structure, which was coal, as shown in **Figure 2.1.14a** [36]. A heap of SiC with molten Si and slag was observed between the electrodes. The EPMA investigation revealed that the structure of this SiC was dense, filled with slag and molten Si (**Figure 2.1.14b**) [36].

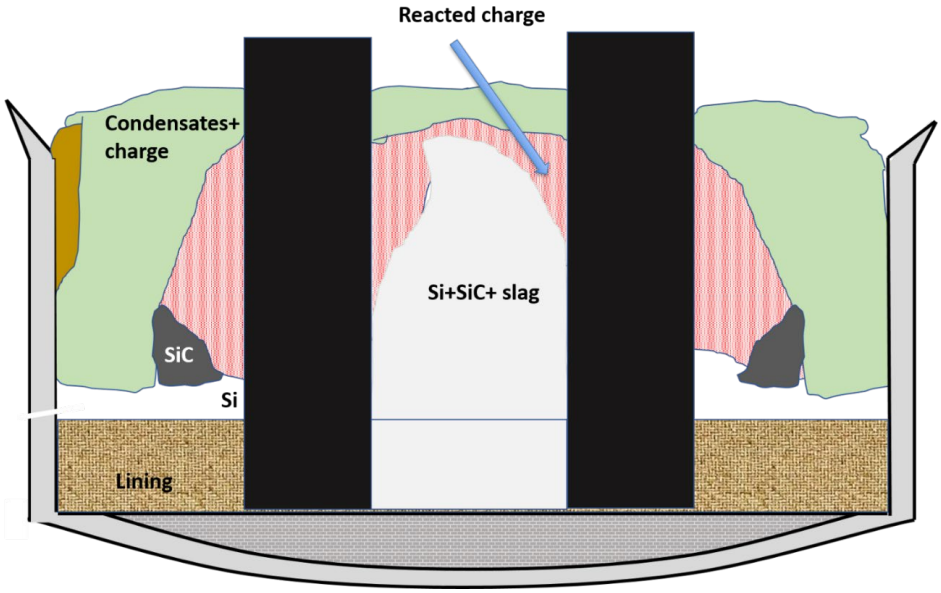

Figure 2.1.13. Main material zones found in Si furnace 2 (Elkem Salten) after excavation [36].

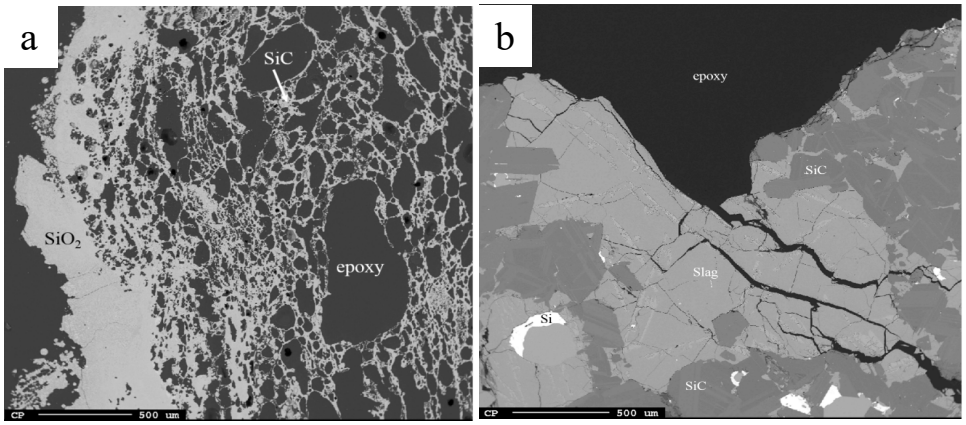

Figure 2.1.14. EPMA images of SiC samples (a) from the reacted charge and (b) between the electrodes [36].

Based on these large-scale Si/FeSi furnace excavations, the interior of a Si furnace describing the materials and zones is summarized by Folstad and Tangstad [37] and is shown schematically in **Figure 2.1.15.** The condensates of Si, SiO_2, and SiC glued together with the charge materials forms the crust and creates cavity below the charge as the raw materials are consumed. The cavities around each of the electrode tips are separated by charge materials in various states of conversion. The cavity is filled with main gas species such as SiO(g) and CO(g), in addition to some Si and carbon bearing hot gases. The size of the cavities varies between various furnaces and in some furnaces, only a few gas channels were noticed. The lower part of the cavity walls consisted of porous SiC partly filled with molten Si, which was observed in all the furnaces. These SiC crystals together with molten Si made the upper part of the deposits firm enough to create a wall. Heated materials capable of reacting were found above the SiC/Si cavity walls, whereas, materials closer to the furnace shell were rather inactive.

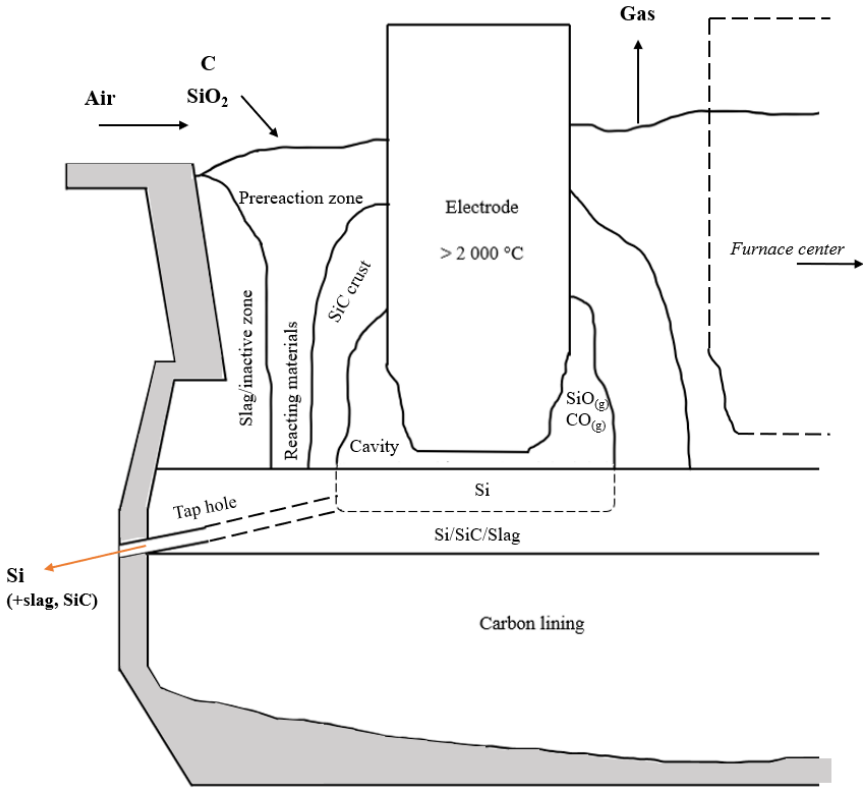

Figure 2.1.15. Schematic illustration of interior of Si/FeSi furnace describing materials and zones based on large-scale furnace excavations [37].

Myrhaug [20] excavated a 150 kW pilot scale Si furnace and analyzed the zones as well as the various samples collected from different positions of the furnace. The illustration of the furnace is shown in **Figure 2.1.16**. A small crater wall filled with SiC particles precipitated from the gas phase (zone 3, yellow region) was noticed and the upper zone (zone 5, green region) contained SiC produced directly form charcoal. The EPMA analysis of the SiC samples (collected from zone 5, green region) showed that the structure of SiC formed after the direct reaction between SiO(g) and the charcoal particles had the same structure as that of the original charcoal. Large dense SiC crystals filled with molten Si were observed in the SiC samples collected from the upper (**Figure 2.1.17a**) and lower regions of the crater wall (**Figure 2.1.17b** and **c**) [20]. The observations based on both the large-scale industrial Si/FeSi and the pilot scale Si excavations revealed that the SiC formed from the carbon sources changed its structure as it reached the bottom portion closer to the crater/electrode region.

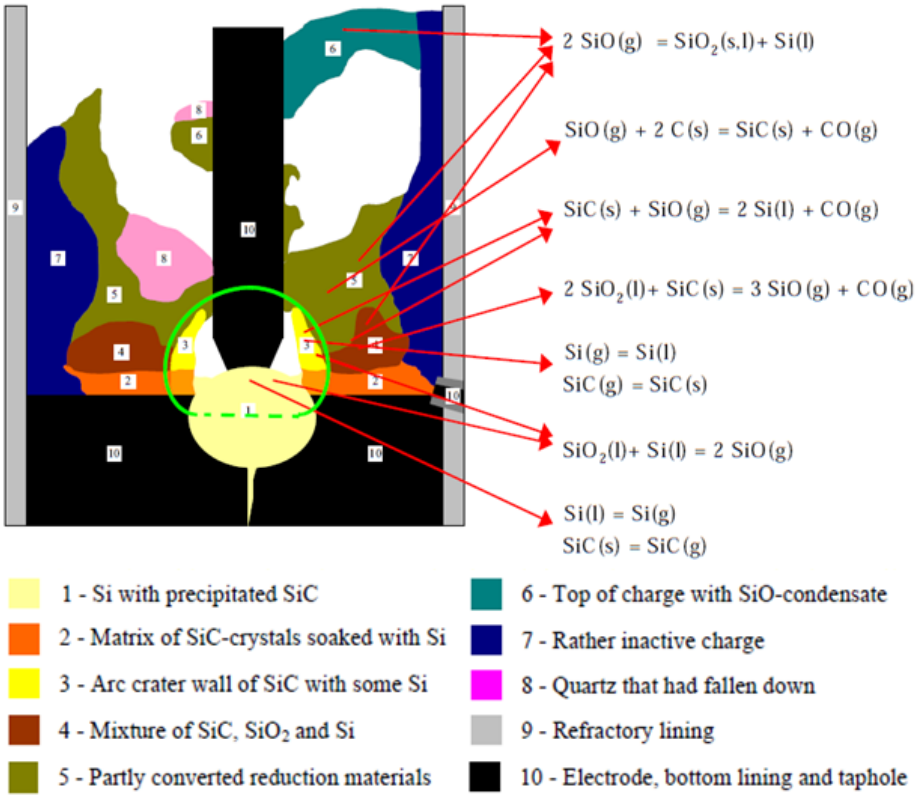

Figure 2.1.16. Different zones in 150 kW pilot scale Si furnace after a run [20].

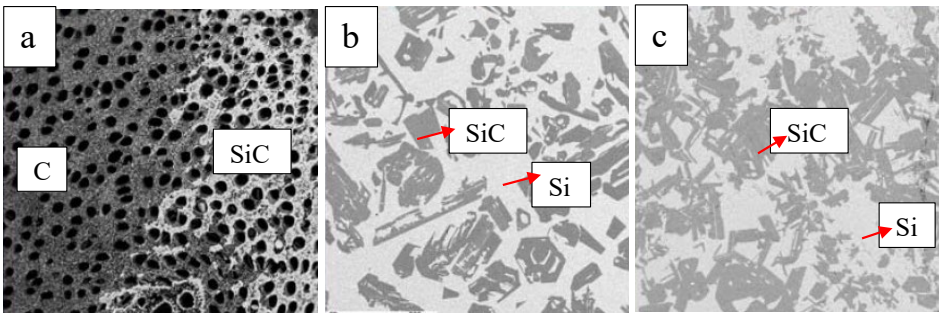

Figure 2.1.17. EPMA images of SiC samples (a) formed after direct reaction between SiO(g) and charcoal, from (b) upper and (c) lower regions of the crater wall [20].

Ringdalen [18] performed experiments producing β-SiC and α-SiC, to study the mechanism of formation of different types of SiC and evaluate the properties of SiC formed at different temperatures during the Si/FeSI process. Prior to the heat-treatment, SiC formed from coal at 1600 °C. The samples of this SiC were confirmed as the cubic modification, i.e., 100% β-SiC. These β-SiC particles were then heated from 2000 to 2500 °C in a mixture of inert Argon (Ar)/Helium (He) and CO atmosphere. Once the target temperature was achieved, the samples were held for an hour. The CO gas was used to simulate a gaseous atmosphere similar to that of an industrial Si furnace. **Figure 2.1.18a** to **c** show the macroscopic images of the β-SiC sample formed at 1600 °C, the sample after heat-treatment, and a sample of industrially produced α-SiC. The corresponding EPMA images are shown in **Figure 2.1.18d** to **f** [18].

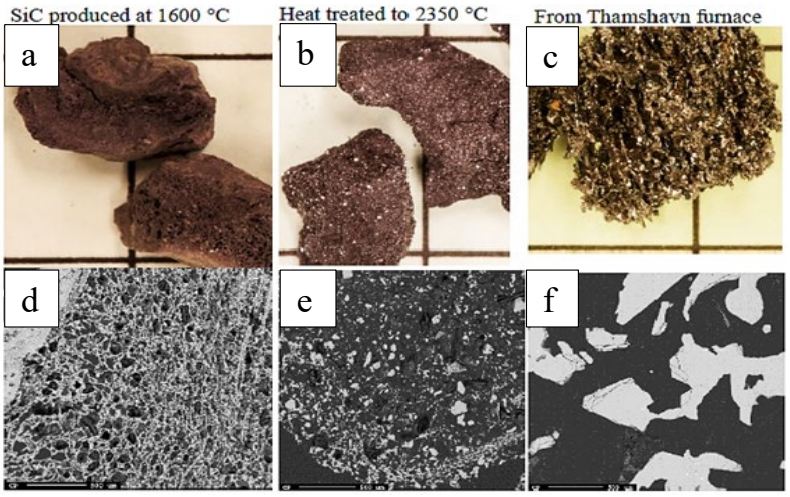

Figure 2.1.18. Macroscopic images and their corresponding EPMA images; β-SiC produced at 1600 °C (a and d), heat-treated β-SiC at 2350 °C (b and e), and industrial SiC sample (c and f) [18].

The SiC produced at 1600 °C had a smooth surface; it did not lose its original carbon structure and the SiC had formed homogeneously in the particle [18]. The heat-treated sample at 2350 °C and the industrial SiC sample showed a dense structure and the SiC had sintered together in the carbon pores. The macroscopic image shows that small crystals had formed on the SiC that was heat-treated in the laboratory, whereas large prominent crystals were noticed on the surface of the industrial SiC samples.

The XRD analysis of the heat-treated samples to quantitatively characterize the SiC polytypes showed that β-SiC was the only phase present until the temperature reached 2200 °C; however, at 2350 °C, 67% of it transformed to α-SiC containing the main phases 4H, 6H, and 15R, as shown in **Figure 2.1.19** [18]. Similar analysis was carried out for the industrial SiC samples (Si furnace at Elkem Thamshavn and Wacker 4) collected from the top and bottom parts of the furnaces (**Figure 2.1.20**) [18]. β-SiC was the only phase observed in the samples collected from the top, whereas the samples collected from the bottom region of the furnace were mostly α-SiC, consisting of the main polytype variations 6H, 4H, and 15R, along with some 2H and 8H polytypes. The samples heat-treated in the laboratory did not show any 2H and 8H polytypes in them. Also, interesting to note is that, even at 2500 °C, β-SiC was present in the samples heat-treated in the laboratory.

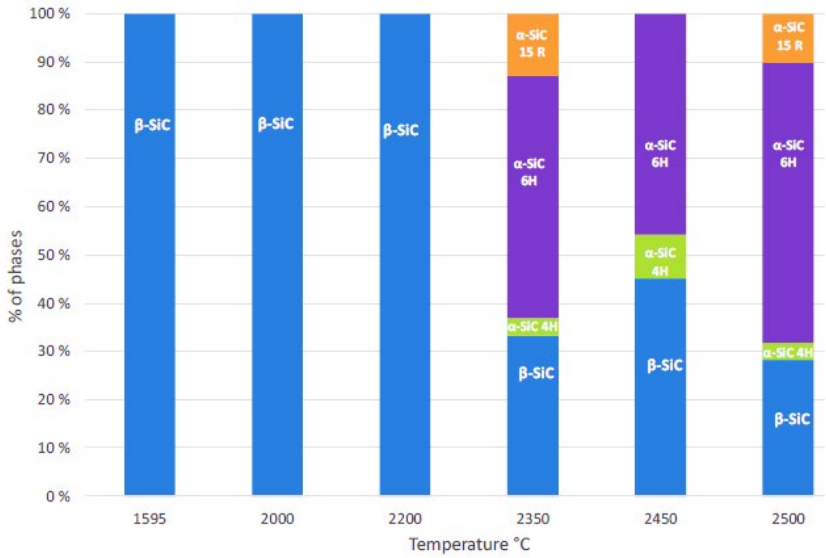

Figure 2.1.19. Quantitative XRD analysis of SiC polytypes in samples, before (at 1595 °C) and after heating at 2000, 2200, 2350, 2450, and 2500 °C [18].

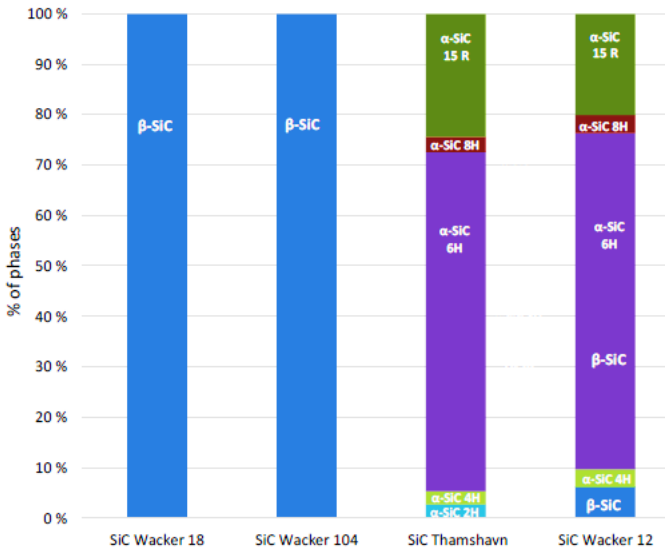

Figure 2.1.20. Quantitative XRD analysis of SiC polytypes in industrial SiC samples; two samples from the upper part (100% β-SiC) and two samples from the furnace bottom [18].

2.2 Carbon materials used for Si production

Several types of carbon materials are used in the Si production. They could be broadly classified into two groups based on their origins; fossil (coal, coke, and pet-coke) and biological (charcoal and wood chips) carbon materials. In choosing a carbon material, it is necessary to consider certain parameters such as its fixed carbon (fix-C) content, SiO-reactivity, electrical resistivity, ease of graphitization, porosity, mechanical and thermal strength, specific surface area, and impurity content [38]. Silicon (Si), aluminum (Al), calcium (Ca), titanium (Ti) and boron (B) are the most common impurities present in the carbon materials [39]. Wood chips are usually added to the raw materials for good permeability of gas flow in the furnace [40]. Composition of the reduction materials used in the furnaces differs depending on their availability and also on the experiences recorded by Si smelters around the world, as presented in **Figure 2.2.1** [40]. According to the composition recipes, wood chips is always used as one of the reduction materials.

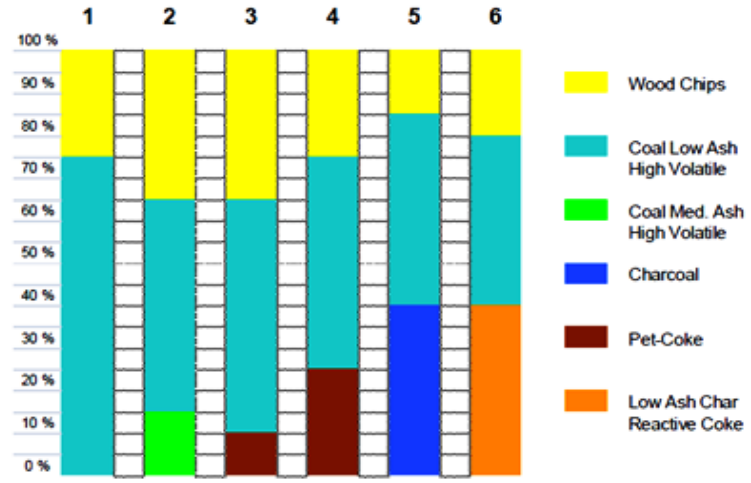

Figure 2.2.1. Composition recipes of reduction materials, obtained from Si smelters around the world [40].

2.2.1 Coal

Coal is a readily combustible sedimentary rock; more than 50% of its weight and 70% of its volume contains carbonaceous material [39–44]. Coal forms when organic plant materials are deposited in mires, the wetlands where peat accumulates. As additional organic material

accumulates on top of the mire, the peat becomes thicker. These organic materials over a course of millions of years convert to coal and it happens through two distinct processes named peatification and coalification. In peatification, bacterial activity takes place shortly after the deposition of the organic material in the mires to form peat and in coalification, the peat gets converted into coal over time through geochemical processes. During coalification, volatile products are driven off because of increasing temperature and pressure. Hence, over geological time scales, as the pressure and temperature increase, peat transforms progressively to lignite, sub-bituminous coal, bituminous coal, and anthracite. Some of the main contents of coal are explained below in detail.

Volatile matter comprises aliphatic carbon atoms (linked in open chains) or aromatic hydrocarbons (containing one or more of the six-carbon rings that are characteristic of benzene series) and mineral matter. These are often driven off at all temperatures when coal is heated, however it can be measured when the temperature reaches around 950 °C in the absence of air under specified conditions [42].

Moisture content decreases with increasing coal rank and can be divided into two; inherent and surface moisture. Inherent moisture is the water held mostly in the pores and surface moisture is the water held on the surface of coal. The moisture can be removed by heating coal at 105–110 °C under specified conditions until a constant weight is reached [42].

Fix-C is the carbon found in coal particles, which remains after the volatile matters and the moisture are driven off [42]. The fix-C content is determined by subtracting the percentages of moisture, volatiles, and ash content, as represented in the equation:

$$\text{Fix-C (\%)} = 100 - \text{Moisture (\%)} - \text{Volatile matter (\%)} - \text{Ash (\%)} \quad (4)$$

Ash consists of inorganic matter from the earth's crust, such as limestone, iron, aluminum, clay, silica, and some trace elements (zinc, copper, boron, lead, arsenic, cadmium, chromium, selenium, etc.). When coal is burned, these components transform to ash. The amount of incombustible material remaining in the coal is referred to as its ash content [42].

Coal can be characterized according to three basic properties; coal grade, type, and rank. The coal grade determines the measure of purity of the coal and composition of the mineral matter dispersed in the coal matrix. The coal type gives information about the plant material from which the coal was formed. The degree of coalification or the coal rank quantifies the extent of the coalification process. An increase in pressure, heat, and time increases rank of the coal as illustrated in **Figure 2.2.2** [43].

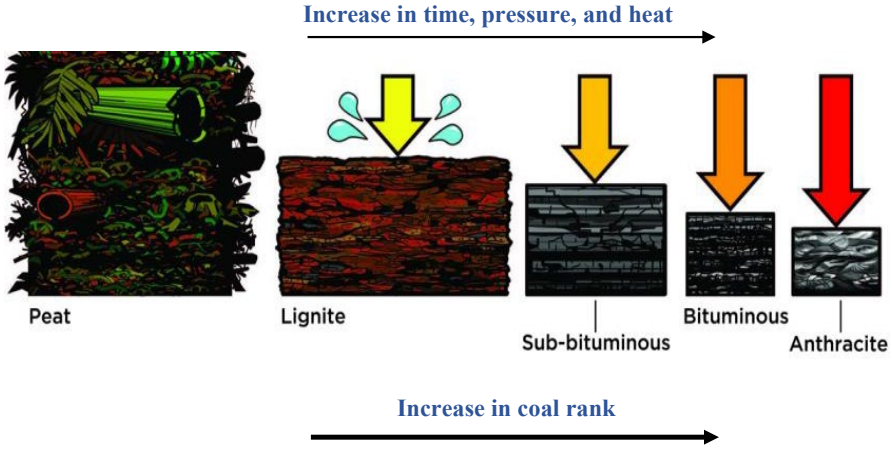

Figure 2.2.2. Schematic illustration of how increasing pressure, temperature, and time affects coal rank [43].

Proximate analysis, ultimate analysis, and the calorific/heating value are the conventional methods used for measuring the coal rank parameters. The proximate analysis gives information about the moisture content, ash, volatile matter, and the fix-C present in the coal. The ultimate or elemental analysis measures the amount of carbon, hydrogen, nitrogen, sulfur, and oxygen content. Coals with higher ranks such as bituminous and anthracite are classified with respect to the fix-C content on a dry basis and those with low ranks are classified according to the gross calorific value on a moist basis.

A petrographic analysis is carried out using the optical microscope, which measures the reflectance and gives information regarding the aromatic fraction (graphitic structure) of the coal [40]. This is expressed as the percentage of incident vertical light intensity that is reflected from a polished surface of coal. The macerals in the coal provide information about the coal type, i.e., the plant material from which that coal was formed. Macerals are of three groups; they are vitrinite, liptinite, and inertinite. Reflectance of vitrinite is the most acknowledged measure of rank and it increases with increasing rank. The micro texture in coal develops upon heating and is categorized into two; binder phase and filler phase carbons. The binder phase carbon has the reactive entities in coal (serves as a binder), which soften upon carbonization and the filler phase has the inert entities (serves as a filler) present in coal, which do not soften during carbonization [41]. The different analysis methods and tests used for characterizing coal are illustrated in **Figure 2.2.3** [44].

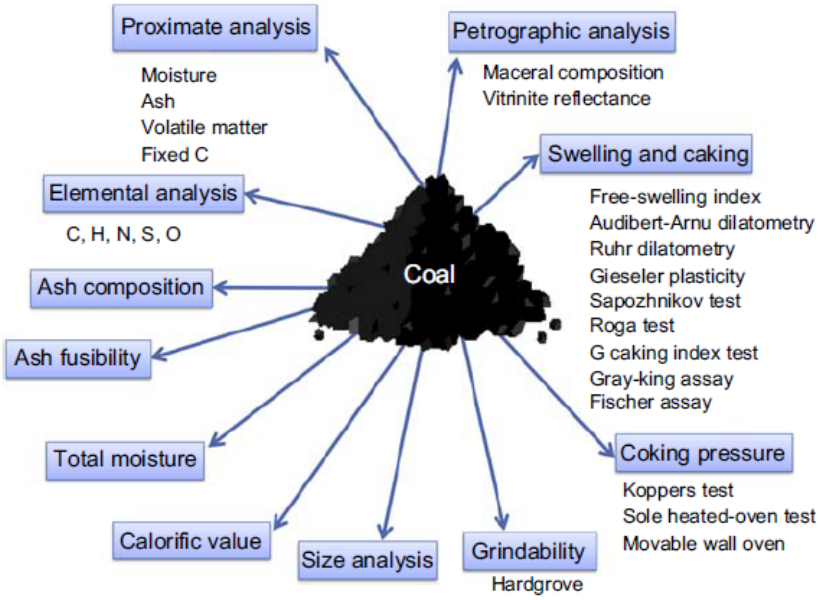

Figure 2.2.3. Analysis methods and tests for characterizing coal [44].

Heating value or the calorific value measures the amount of chemical energy stored in coal that is released as thermal energy during combustion. **Table 2-2** shows the typical compositions and heating values of different types of coal [42].

Table 2-2. Typical compositions and heating values of different types of coal [42].

Analysis	Anthracite	Bituminous	Sub-bituminous	Lignite
Fix-Carbon (wt.%)	85–98	45–85	35–45	25–35
Ash (wt.%)	10–20	3–12	≤ 10	10–50
Volatile matter (wt.%)	3–14	14–42	42–53	53–63
Moisture (wt.%)	< 15	2–15	10–45	30–60
Sulfur (wt.%)	0.6–0.8	0.7–4	< 2	0.4–1
Heating value (kJ/kg)	30238–34890	24423–33727	19306–30238	9304–19306

The term “rank” is the most important petrographic parameter used for determining the industrial application of coal. A higher rank of coal denotes higher fix-C, which is mostly found in bituminous and anthracite coals; however, it largely affects the porosity. During the coalification process, an increase in pressure causes some physical changes in the coal, such as loss of porosity. Fix-C and good porosity are the most significant parameters sought after in the metallurgical Si production process. Porosity of the carbon reductants and a maximum conversion to SiC are two of the most important parameters determining the final Si yield. Even though anthracite has a higher fix-C content than bituminous coal, in the coalification process, over time and under high pressure, it loses its porosity. Hence for metallurgical Si production, the industry mostly prefers the bituminous type of coal.

2.2.2 Charcoal

Charcoal is produced by slow pyrolysis, i.e., heating of wood in the absence of oxygen [45, 46]. During this process, complex carbonaceous substances break down into elemental carbon. Kilns of various types are used for converting wood to charcoal. The production of charcoal goes through the following stages:

1. 20–110 °C: As the wood is heated, it dries absorbing the heat. At this temperature range, water and highly volatile hydrocarbons are distilled off.
2. 110–270 °C: Water gets completely expelled and endothermic decomposition takes place, giving off certain gas species, e.g., CO, CO_2, etc.
3. 270–290 °C: At this temperature, an exothermic decomposition of wood begins, giving off mixed gases and vapors continuously, together with some tar.
4. 290–400 °C: The breakdown of the wood structure continues, giving off gases, condensable vapors, and tars. This process begins to predominate as the temperature increases.
5. 400–500 °C: Around 400 °C the transformation of wood to charcoal is practically complete along with forming some char; perhaps 30% by weight is trapped inside the structure.
6. 500–550 °C: Further heating to 500 °C drives off more tar, thereby increasing the fix-C content of the charcoal to about 75% and the carbonization process completes. About 75% of fix-C in charcoal is an appropriate measure for industrial purposes.

The quality of charcoal is determined by its various properties, such as moisture content, volatile matter, fix-C, and ash content [47]. Charcoal from the kiln has less than 1% moisture. It can however easily absorb moisture from the air, which could bring the moisture content to about

5–10% or even more. This lowers the calorific or heating value of charcoal. During the final carbonization stage at 550 °C the volatile matters reduce, and its content can vary from a higher value of 40% to a reduced value of 5% or less. At temperatures higher than 550 °C and up to 1000 °C the volatile content is close to zero and the yields fall near to 25%. However, most commercial charcoals are not produced at such high temperatures. A net volatile matter content of about 30% can be considered as good commercial charcoal. Fix-C in charcoal ranges from as high as around 95% to a lower value of about 50%; the fix-C value stays constant at temperatures up to 900 °C and it decreases gradually as the temperature increases above 900 °C. Depending on the wood species, the ash content varies from 0.5 to 5%. The charcoal yield and the properties present are significant during the primary and secondary heat-treatments [48].

According to Ramos [49], the anatomical characteristics of wood, such as shape, arrangement, and organization did not show any changes during slow pyrolysis and the charcoal surface was well-defined. In addition, upon carbonization, the fiber cell wall thinning in the wood structure disappeared and transformed into a glazed and amorphous appearance, as shown in **Figure 2.2.4**.

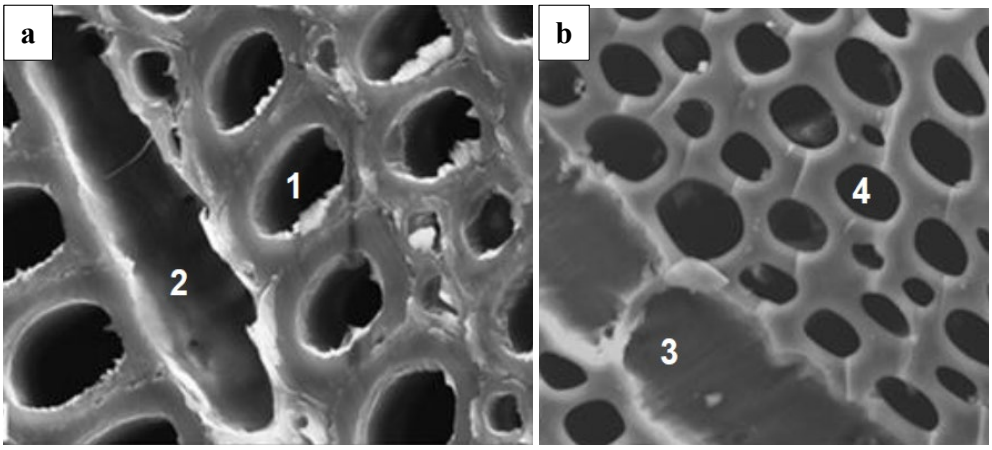

Figure 2.2.4. SEM images of wood (a) before pyrolysis; 1 and 2 show the fibers on wood cell walls, and (b) after pyrolysis; 3 and 4 show that the fibrous walls disappeared and formed a smooth surface on pore walls of charcoal [49].

2.2.3 Petroleum coke

Pet-coke is produced as a by-product of heating and distillation of crude oil [50, 51]. Compared with metallurgical coke, pet-coke has a higher heating value. The impurities in pet-coke consists of residual hydrocarbons left over from the processing, as well as elements such as nitrogen,

sulfur, nickel, vanadium, and other heavy metals. Due to the low volatile content and high heavy metal content, pet-coke is not an appropriate candidate for the Si industry [38]. The initial coking process produces "green coke", which then requires additional thermal processing to remove any residual hydrocarbons and also to increase the fix-C content [50].

Several grades of pet-coke can be produced depending on the coking operation temperatures, quality of the crude oil feedstock, and the length of the coking time. These different grades are the sponge, needle, shot, purge, and catalyst cokes. Sponge coke is the most common type of pet-coke, which is used as a solid fuel, while needle coke is premium grade coke made from special petroleum feed stock and it is used for manufacturing high-quality graphite electrodes for the steel industry. Shot coke, used as a fuel, is produced from the heavy petroleum feed stock and purge coke, used as a fuel in coke burning boilers, is produced by flexi-coking. The catalyst coke is used as fuel in the refining process. **Figure 2.2.5a** and **b** show the images of sponge coke and shot coke, respectively [50].

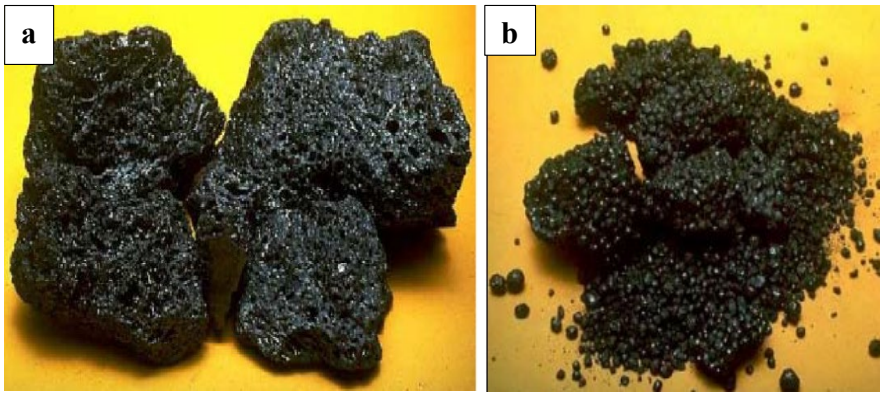

Figure 2.2.5. Images of (a) sponge coke and (b) shot coke [50].

2.2.4 Metallurgical coke

Metallurgical coke is produced by carbonizing coal or coal blends in coke ovens under controlled conditions [40]. Generally, bituminous coal is used for metallurgical coke production. For carbonizing coal, a coal blend of desired type is washed, crushed, and charged into the charging chamber. The coal blend is then heated from two sides by red hot silica brick walls. The various stages of carbonization process as a function of time and temperature are illustrated in **Figure 2.2.6**.

Volatiles and water usually evaporates during the preheating of coal. When the temperature reaches 350–380 °C, coal fuses and reaches a plastic phase. Organic tars and

aromatic hydrocarbons are driven off at this stage. At 450–500 °C, methane and the remaining volatile gases also disappear, followed by re-polymerization of the plastic matter into semi-coke. As the temperature increases to 1000 °C, the fluidity of the mass reaches its maximum and it begins to solidify and transforms into coke. Metallurgical coke is mostly used for the production of iron in blast furnaces because of its reactivity towards CO_2, and is not much used in the ferroalloy production. In Si production, factors such as SiO(g) reactivity, degree of conversion, amount, and type of impurities play important roles in the selection of a carbon reductant. Metallurgical coke does not fulfil these criteria to a satisfactory degree, therefore it is not considered for Si production. However, it could be used in the FeSi furnace. Coals of certain ranks do not go through the plastic phase called char upon heating; they are the anisotropic ones and are often preferred over metallurgical coke in Si production.

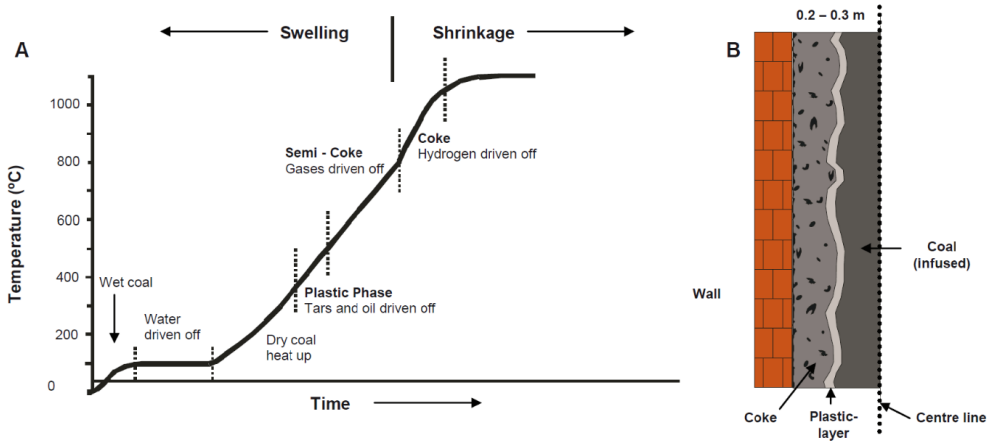

Figure 2.2.6. Coal carbonization process as a function of time and temperature [40].

2.2.5 Wood chips

Wood is a natural composite material with a hierarchical structure, mainly consisting of biopolymers such as cellulose, hemicellulose, and lignin forming a cellular microstructure of high porosity. **Figure 2.2.7** shows the macroscopic structure of wood with respect to the preferential cell orientation [4]. Wood chips are added directly in the Si production process [40]. In the region of charge materials, wood chips undergo certain stages such as pyrolysis and carbonization, and produce charcoal. The wood chips are added to improve the charge permeability, thereby allowing a better distribution of gas flow through the bulk raw materials.

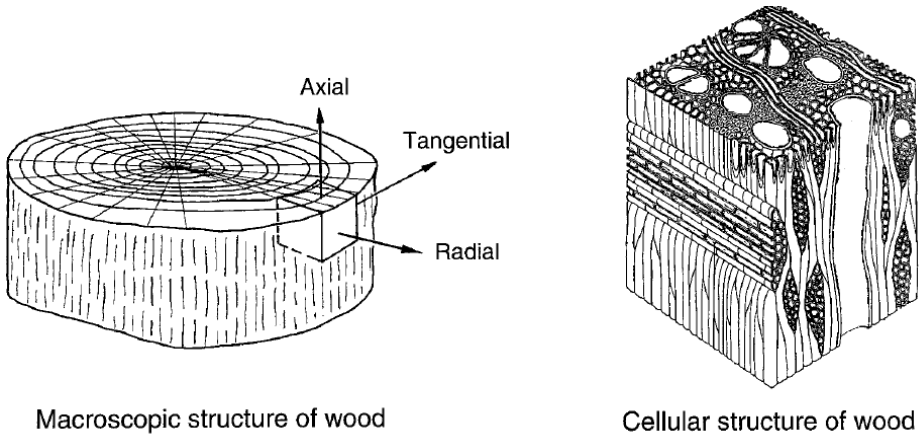

Figure 2.2.7. Macroscopic structure of wood with respect to the preferential cell orientation [4].

2.3 Silicon carbide

2.3.1 History and structure of SiC

SiC is a material long known to have a large variety of uses. It is a type of gem stone, used as an abrasive in the ceramic industry [1, 52, 53]. Edward Goodrich Acheson was the first man to produce SiC in the 1890's. SiC also occurs naturally as a mineral, called moissanite after Ferdinand Frédéric Henri Moissan, who identified the crystals of SiC in a meteorite from the Canyon Diablo crater in Arizona [52]. SiC is a non-oxide ceramic material with outstanding properties, which makes it an attractive material for many industrial applications [1]. SiC has been identified as an important structural ceramic material because of the unique combination of properties such as high thermal conductivity, wear resistance, good oxidation resistance, and strength retention at high temperatures. The combination of these properties is determined by the highly covalent chemical bonding between the Si and carbon atoms. The light weight SiC ceramics with low density, high strength, and corrosion resistance are used in manufacturing filters, catalyst carriers, and heat insulation structures [3, 4].

The only compound that can form when Si and carbon are combined is SiC. The Si and carbon atoms are always in a tetrahedral coordination in every SiC crystal, as expected for a three-dimensional covalently-bonded compound of group IV elements with sp^3 orbital hybridization [55]. Each carbon atom is located at the centroid of a tetrahedron and Si atoms are located at its vertices and vice versa. This geometry leads to a fourfold coordination, which is the signature of a covalently-bonded structure, such as that in Si_4C and C_4Si (**Figure 2.3.1**).

The strong covalence of the Si-C bond imparts extreme hardness to the crystals. The SiC crystals grow at high temperatures ranging from 1000 to 2800 °C. They grow both from vapor phase and solution, and appears as flat plates, needles, whiskers, and dendrites [56].

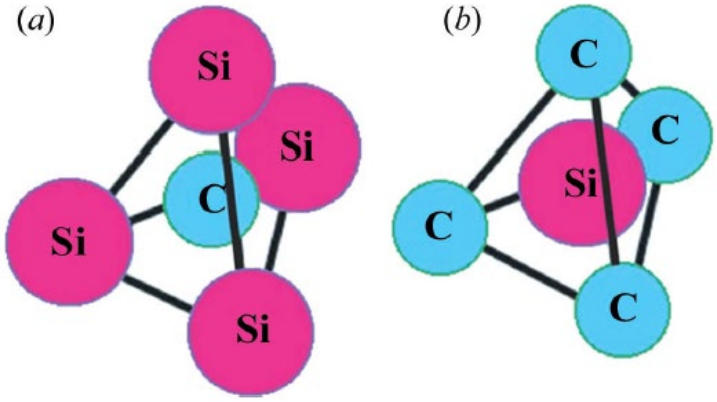

Figure 2.3.1. Simple tetrahedral coordination of Si and carbon atoms: (a) Si_4C tetrahedron (carbon atom located at the tetrahedron's centroid and Si atoms at its vertices) and (b) C_4Si tetrahedron (Si atom located at the tetrahedron's centroid and carbon atoms at its vertices) [55].

2.3.2 SiC and its polytypes

SiC could be distinguished from other compounds by its distinct polytypism [55, 57]. Polytypism is defined as the ability of a compound to exist in different crystallographic forms. In crystalline solids, the molecules or atoms are arranged on a regular periodic three-dimensional lattice. A crystal can grow from a pre-existing crystal (or crystallization of vapor/solution) by the addition of more molecules into the empty lattice sites. The crystal would grow continuously by the adsorption of atoms from the liquid or vapor phase, until it is incorporated to the crystal. The structural variation in crystals can happen only in one crystallographic direction and can be achieved by changing the stacking sequence of the atomic layer. This means that a crystal structure exhibits several one-dimensional stacking sequences without any changes in stoichiometry.

Around 250 different polytypes of SiC have been discovered so far and the repetitions of the stacking sequence vary from two layers to several hundreds of layers [54, 24, 58]. **Figure 2.3.2** represents the tetrahedral coordination of Si and C atoms, showing the two possibilities of orientation that satisfy the double tetrahedral coordination. **Figure 2.3.2a** shows two tetrahedron layers with the same relative orientation, which is termed as the untwined tetrahedral and **Figure 2.3.2b** shows two tetrahedron layers that are rotated 180° with respect

to each other, which is termed as the twinned tetrahedral. The different polymorphs of SiC that are closely related structurally are designated as polytypes. The crystal structures of these polytypes develop based on the tetrahedral co-ordination of Si and carbon atoms [59, 60]. Therefore, the various SiC polytypes could be considered as the modification of the piling up of layers of SiC_4 or CSi_4 tetrahedra. These tetrahedral atoms are arranged in such a way that all the atoms lie in parallel planes on the nodes of the regular hexagonal networks.

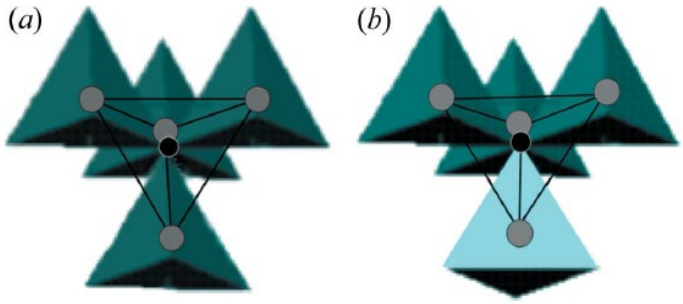

Figure 2.3.2. Double tetrahedral coordination of Si (in gray) and carbon (in black) atoms. Two tetrahedron layers are shown with (a) the same relative orientation and (b) a relative rotation of 180 ° [55].

Depending on this stacking order, different polytypes with different crystal modifications are formed. A cubic structure (e.g., zinc blende) (ABCA) is generated by stacking tetrahedron layers in the same relative orientation. This results in a SiC polytype with cubic symmetry (polytype 3C) called the β-SiC. The hexagonal (e.g., wurtzite) (ABA) and rhombohedral structures are formed when every second tetrahedral layer is antiparallel to the previous layer. The rest of the polytypes also belong to this category, which are collectively known as α-SiC.

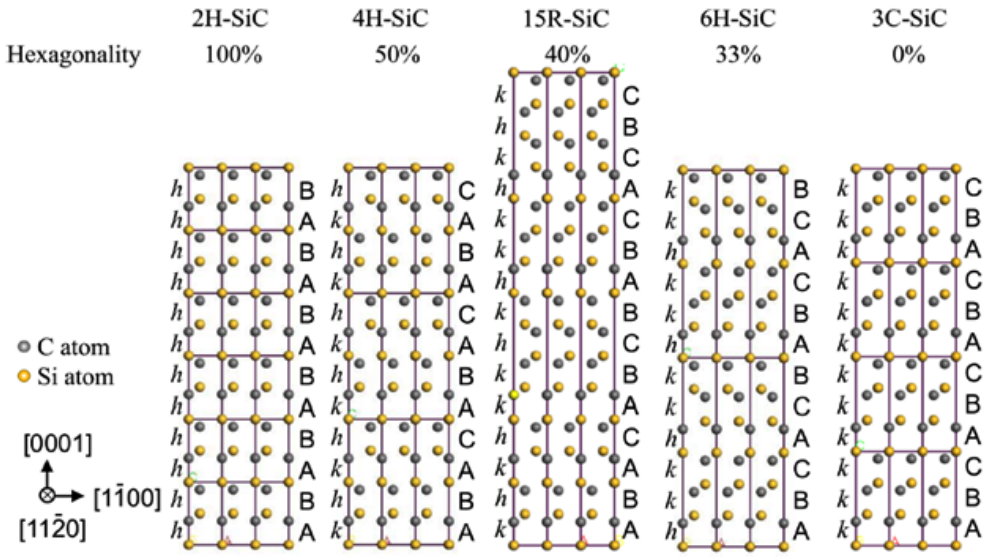

Figure 2.3.3. Stacking sequence in the most commonly occurring SiC polytypes 2H, 4H, 6H, 15R, and 3C with hexagonality. Letters h and k denote the symmetry in stacking sequence of tetrahedron layers corresponding to different SiC polytypes, based on Jagodzinski notation [61].

Figure 2.3.3 shows the stacking sequences of tetrahedron layers of the most common SiC polytypes 3C, 2H, 4H, 6H, and 15R [61]. The sequence ABC is the only one that can be generated by stacking tetrahedron layers in the same relative orientation, which results in the SiC polytype 3C with cubic symmetry (β-SiC). Other interesting sequences are the ABAB, ABAC, and ABCACB that form the SiC polytypes with hexagonal symmetry named 2H, 4H, and 6H respectively. Finally, it is also necessary to highlight the sequence ABACABCBABCACBC, which yields a typical SiC polytype named 15R. The crystal directions in the cubic and hexagonal polytypes are marked differently. In the cubic lattice, the ordinary Miller indices are based on the Cartesian co-ordinates x, y, and z, whereas the hexagonal lattice uses four-digit Miller-Bravais indices in the way [hkil]. The three hki signifies the components of crystallographic direction with respect to multiples of the vectors a_1, a_2, and a_3 that are arranged at angles of 120° with respect to the basal plane, which is illustrated in **Figure 2.3.4.** The value l with respect to the base vector c is parallel to the stacking direction of the crystal [62].

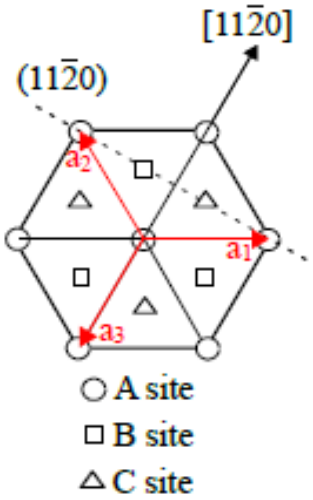

Figure 2.3.4. Crystal directions in hexagonal lattice that uses four-digit Miller-Bravais indices in [hkil] pattern [62].

In **Figure 2.3.3** the letters h and k denote the symmetry in the stacking sequence of the tetrahedron layers corresponding to the different SiC polytypes, based on the Jagodzinski notation [61]. Hexagonality is measured by the ratio of the hexagonal sites to the total number of sites, i.e., h/(h + k). In the 2H-SiC polytype, the local environment of each tetrahedron is purely hexagonal and is labeled h, and in 3C-SiC polytype, each tetrahedron is purely cubic and is labeled k [62]. Depending on the stacking sequence, the fraction of hexagonal lattice sites in the unit cell changes from 100% in 2H- to 0% in 3C-SiC. Where the rest of the polytypes are mixtures of zincblende and wurtzite structures, the lattice sites have both cubic and hexagonal environments [62]. The commonly occurring polytypes such as 4H, 6H, and 15R have the hexagonality of 50, 40, and 33%, respectively [62].

2.3.3 SiC polytypes and stability

Lundqvist [63] made the first attempt to explain the reason for SiC polytypism, suggesting that the polytype formation was controlled by impurities. Many evidences, based on experiments, support the idea that some impurities might stabilize some of the commonly occurring polytypes [63, 59, 64]. The existing theories of polytype formation can be divided into two categories; one based on the kinetic and growth considerations, and the other based on the thermodynamics. Almost all the crystal growth theories could be considered as variations of the theory of spiral growth around a screw dislocation [65]. According to the screw dislocation theory, thin platelets

of the basic structure form initially by surface nucleation, and later a layer-by-layer growth happens under conditions of high supersaturation [59, 24]. The crystal thus formed at this point might be perfect or contain defects such as twins or stacking faults due to the thermodynamic variations that transpire during the growth. When the supersaturation drops below the critical value, the crystal platelets thicken further by the addition of material leading to the formation of steps at the sites of screw dislocations. As the growth proceeds, these steps rotate around the center of the dislocation, creating a spiral hill. A crystal formed by the spiral growth mechanism occupies a structure corresponding to that step. **Figure 2.3.5** illustrates the step-by-step mechanism of the spiral growth process [24].

Based on this theory, for the repeating polytype, the whole stacking sequence is determined by the height of the spiral steps. Various growth patterns can be formed as a result of the interactions between the spirals originating from the emanation of more than one dislocation on the surface. **Figure 2.3.5** shows the successive stages of spiral growth generation in crystals [24]. As there were inconsistencies in the spiral growth theory, Jagodzinski [60] proposed a theory based on equilibrium thermodynamics, assuming that the cubic polytype was the most stable form and that the rest of the polytypes could have been formed as a result of the ordering of stacking sequence within the structure.

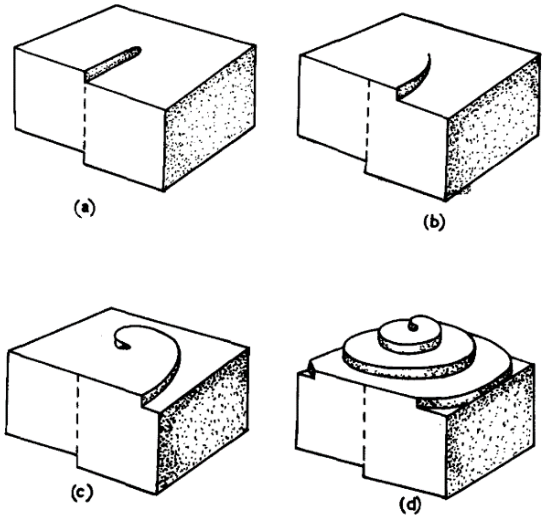

Figure 2.3.5. Different stages of spiral growth in crystals [24].

Many investigations have been performed in the past to understand the stability of the SiC polytypes both experimentally [25] and theoretically [61, 66, 67]. The roles of a wide variety of physical factors in determining the SiC polytype growth and stability have been investigated [25]. The most significant physical factors that influence the polytype formation are

temperature and impurities present in the raw materials. Several studies have reported the influence of temperature correlating the growth of different SiC polytypes. SiC crystals are grown at temperatures ranging from 1300 to 2800 °C [24]. Among the large number of SiC polytypes, only a very few are thermodynamically stable and found to occur more frequently. They are the five short-periodic polytypes 2H, 3C, 4H, 6H, and 15R. The 2H α-SiC modification has never been found to occur at higher temperatures. It has however been synthesized by special methods, for example by vapor-liquid-solid (VLS) process at temperatures around 1400 °C [24, 68].

Knippenberg [25] found that the transformation of β-SiC to α-SiC is irreversible. According to Knippenberg, two types of phase transformations are possible in the formation of SiC polytypes. One possibility is the transformation through a vapor phase in which the crystals will vaporize at high temperatures and then the vapor species recrystallizes forming the high temperature polytypes. The other mechanism is the solid state phase transformation, where, upon increasing the temperature, the atoms inside the crystals rearrange without changing the stoichiometry [25, 69]. One of the most accepted stability diagram of the SiC polytypes with respect to temperature is shown schematically in **Figure 2.3.6** [25]. The cubic modification 3C and the hexagonal modification 6H have the widest range of occurrence compared with the 2H, 4H, 8H, and 15R modifications.

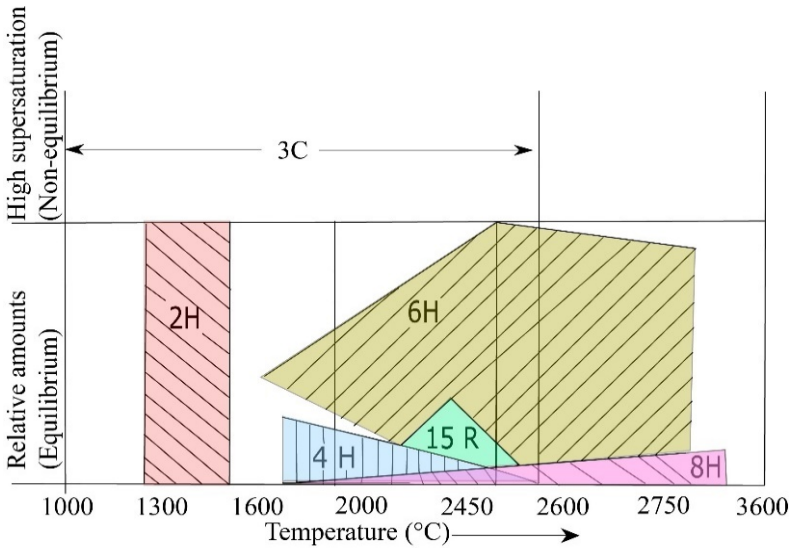

Figure 2.3.6. Stability diagram of SiC polytypes with respect to temperature; modified from Knippenberg [25].

Crystal growth experiment of SiC at temperatures ranging from 1000 to 2750 °C has shown that β-SiC (3C) formed initially might disappear through a process of transformation and later recrystallizes to α-SiC [60]. Baumann [70], found that β-SiC (3C) was stable up to 2100 °C during the formation of SiC at temperatures ranging from 1800 to 2400 °C. The transformation to α-SiC started as the temperature increased further and at 2400 °C the SiC particles completely transformed to α-SiC. An increase in temperature leads to the thermal diffusion of the atoms in the cubic β-SiC (3C) and a rearrangement of atoms within the SiC would thus lead to the formation of different α-SiC polytypes [69]. In studies based on crystal growth, β-SiC (3C) basically grew at temperatures lower than 2000 °C by CVD [71, 72], whereas, 4H or 6H configuration of α-SiC in most of the cases grew at higher temperatures [73, 74]. Kawanishi et al. [61] based on their analysis on the van der Waals interactions and entropy of different SiC polytypes, have reported that 3C is the most stable phase. Heine et al. [75] through their computational study of the origin of SiC polytypes, have found that 6H is the stable phase at higher temperatures, 4H is stable at lower temperatures, and 15R has a stable intermediate phase.

Bootsma et al. [76] investigated the different stages of phase transitions in SiC crystals of the polytypes 2H, 3C, 4H, and 15R. They proposed a mechanism by which the phase transition takes place at higher temperatures via 2H→3C, 3C→6H, and 3C→6H→4H→15R. They annealed SiC whiskers of 2H type in an Ar atmosphere of 1 atm pressure at 1500, 1600, and 1700 °C, for short periods of time. Results showed that the transformation of 2H to 6H SiC crystals took place via a 3C modification. The 2H whiskers transformed initially to cubic platelets, probably growing from the 3C-nuclei, which were already present in the whiskers. The number of 3C crystals increased with temperature and time. To study the transformation of 3C to 6H, the 3C crystals that were obtained after annealing the 2H-SiC was used. The 3C-SiC crystals were heated at a temperature ranging from 1600 to 2400 °C and the presence of α-SiC polytypes such as 6H, 4H, and 15R with 3C was observed. During heating, at temperatures from 1600 to 1700 °C, 100% of the crystals were 3C, which afterwards started reducing and formed the α-SiC polytypes, its quantity increasing with temperature and time. Among the 2H, 3C, 4H, and 15R structures in the SiC, 6H was the most stable phase at the temperature ranges of 1500–2830 °C.

Impurites present in the crystals also play an active role in the formation polytypes [60, 56, 64]. Nitrogen (N), aluminium (Al), phosphorus (P), oxygen (O) and boron (B) are the most common impurity elements that favors SiC polytype growth. N favors the growth of 3C, Al promotes the growth of 4H and 6H polytypes, and O enhances the 2H polytype growth. Doping

of SiC crystals with Al and B does not increase the polytypism in SiC crystals; it stabilizes the growth of short-period polytype structures 4H and 6H [56]. Electron donors such as N and P stabilize β-SiC, wheras electron acceptors such as Al and B stabilize α-SiC [60]. When SiC samples were heated at high pressures of N_2-gas ranging between 10 and 30 bar, transformation of α- to β-SiC (6H to 3C) was observed [60].

Studying the effect of B, N, and Al on the phase transformation of SiC, Coppi et al. [64] found that the presense of these impurities had a major role in the phase transformation and grain growth of SiC. In addition to the phase transition, the impurities also stabilized some polytypes at certain temperatures. Without adding these impurities, the transformation of β-SiC to α-SiC occurred at 2000 °C forming large hexagonal platelets. After heating for 1 h at 2150 °C in Ar atmosphere, the β-SiC transformed to 90% 6H and the remaining 10% was a combination of 4H and 15R. **Figure 2.3.7** shows the transformation of β-SiC to α-SiC at different annealing temperatures. Adding 2 wt.% B while annealing these samples at 2150 °C transformed the 6H to 4H, whereas switching to N_2-atmosphere slowed down the rate of transition. The rate of transformation was extremely dependent on the specific surface area of the starting material; they were proportional to each other [64]. **Figure 2.3.8** shows the morphology of the SiC sample under a scanning electron microscope (SEM), (a) before annealing (100% 3C), (b) after annealing at 2150 °C for 30 min in Ar (transformed to 52% 6H and 29% 3C), and (c) at 2000 °C for 60 min in Ar with the addition of 4 wt.% Al (transformed to 77% 4H and 23% 3C). After annealing, SiC crystals in the shape of hexagonal plate like structures were observed in the morphology [64].

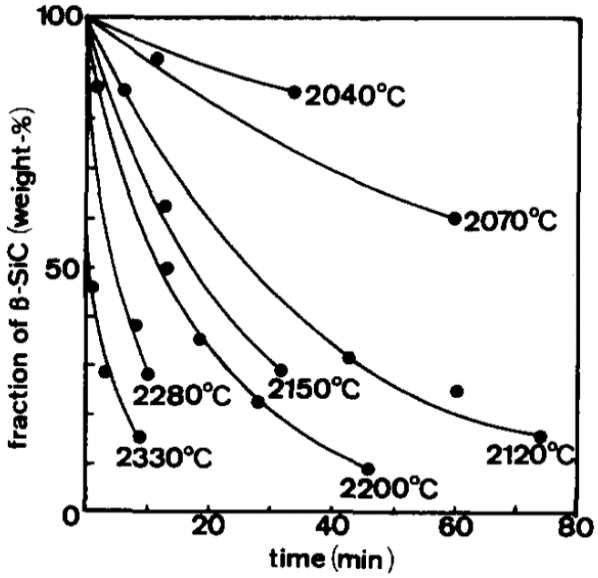

Figure 2.3.7. Transformation of β-SiC at different annealing temperatures in Ar atmosphere [64].

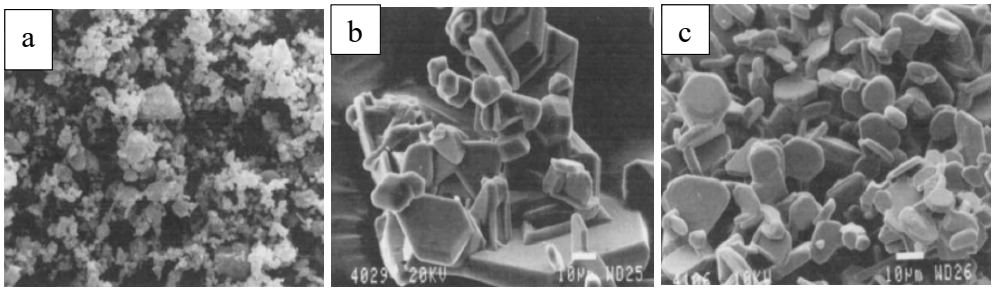

Figure 2.3.8. SEM morphology of SiC sample (a) before annealing (100% 3C), (b) after annealing at 2150 °C, 30 min, Ar (52% 6H and 29% 3C), and (c) at 2000 °C, 60 min, Ar with the addition of 4 wt.% Al (77% 4H and 23% 3C) [64].

2.3.4 The Si-C system

In the Si-C system, SiC is the only stable condensed compound in addition to carbon and Si. Various studies have previously shown that the peritectic temperature of SiC could vary [77, 78]. SiC decomposes peritectically at 2545 $\pm$ 40 °C and its eutectic temperature is 1404 $\pm$ 5 °C [79]. Both the systems consist of SiC as the intermediate compound with a composition of 50 at.% Si and 50 at.% carbon. The system could consist of solid or liquid Si; solid SiC if the at.% of carbon is below 50, and if it is above 50, then the system would be solid graphite and SiC. SiC does not melt at higher temperatures and pressures, but decomposes into Si rich vapor in

equilibrium with graphite, especially at temperatures from 2830 to 3160 °C [77, 80]. Hoel [81] assessed the work of both Scace and Slack [77] and Dolloff [78], and concluded that Scace and Slack provided the most reliable Si-C phase diagram, which is shown in **Figure 2.3.9**, depicting that the SiC decomposes peritectically at temperatures near 2800 °C.

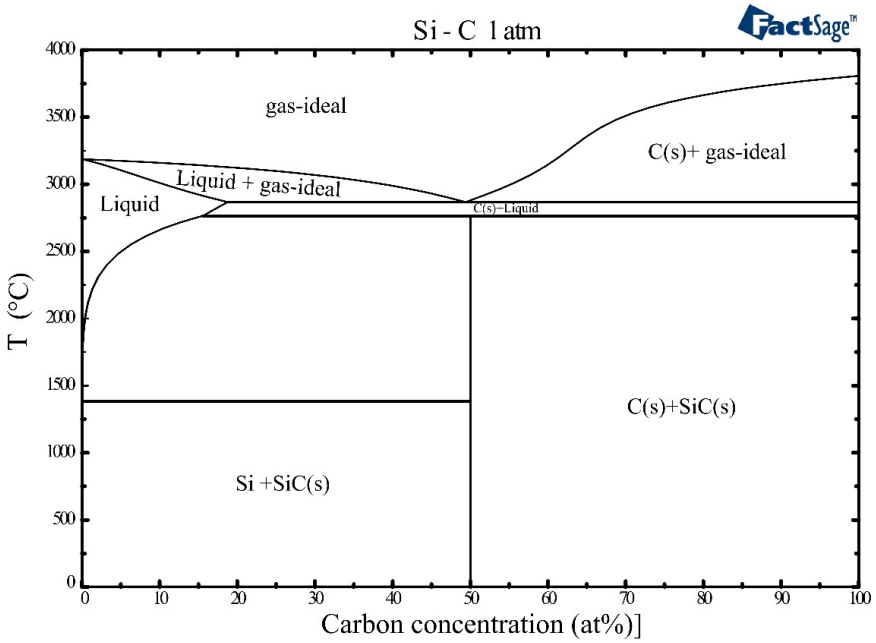

Figure 2.3.9. Si-C phase diagram showing SiC decomposing peritectically at temperatures near 2800 °C; created using the Factsage software by Jian Meng Jiao (NTNU).

The solubility of carbon in liquid Si in equilibrium with SiC can be expressed by **reaction (2)**. Measuring the amount of dissolved carbon in the Si phase at different temperatures could provide the relation between temperature and carbon solubility in liquid Si coexisting with solid SiC. Several researchers have tried to measure the solubility of carbon in liquid Si to establish the solubility curve [77, 78, 82, 83, 84]. However, setting up the experiment at such high temperatures is a challenging task. The differences between each experimental set up and analysis method could also lead to considerable variations in the measured carbon level.

Scace and Slack [77] carried out experiments to find the solubility of carbon in Si over a temperature range from 1560 to 2900 °C, well above the melting point of Si, using a 50 kW graphite resistance furnace in an Ar atmosphere of 35 atm. They found that the solubility of carbon in liquid Si was about $1/5^{th}$ of that reported by Hall in Scace and Slack [77]. Also, the solubility of carbon in Si at 2100 °C was less than 1 at.%, whereas it reached 19 at.% of carbon at 2830 °C, the peritectic temperature of SiC [77]. Durand and Duby [85] evaluated the

solubility values based on the works performed by Hall [82], Scace and Slack [77], and Oden and McCune [83]. Extrapolating the data from the three experimental works, Durand and Duby [85] obtained a carbon solubility value of 110 ppm mass. This value was much higher than the value obtained by extrapolating the data measured by Hall [82]. They also found that the solubility values obtained by Scace and Slack [77] and Oden and McCune [83] were lower compared with that of Hall [82].

Adding certain elements enhances the solubility of carbon in liquid Si [82]. According to Hall [82], addition of Al to Si increases the carbon solubility and the SiC crystals obtained were identified as having the cubic modification, which is β-SiC, at a temperature near 1600 °C. Dalaker and Tangstad [86] investigated the solubility of carbon in liquid Si in the temperature range of 1414–1559 °C in Ar atmosphere with various B additions. A solubility limit of 65 ppm mass at the melting point of Si was observed, which was nearly the average of previously reported values. The study showed that adding B to Si increased the solubility of carbon when compared with the carbon solubility in pure Si. The solubility of carbon in liquid Si reported by various studies are summarized in Ciftja [28] and is represented in **Figure 2.3.10**. To summarize, based on the above discussions it is suggested that the solubility of carbon at the melting point of Si ranges around 40–60 ppm by mass. From **Figure 2.3.10**, it could be deduced that the solubility values attained by Ottem [87] (from Hall [82]), Hall [82], Yanaba et al. [88], and Dalaker and Tangstad [86], are in reasonable agreement within this range.

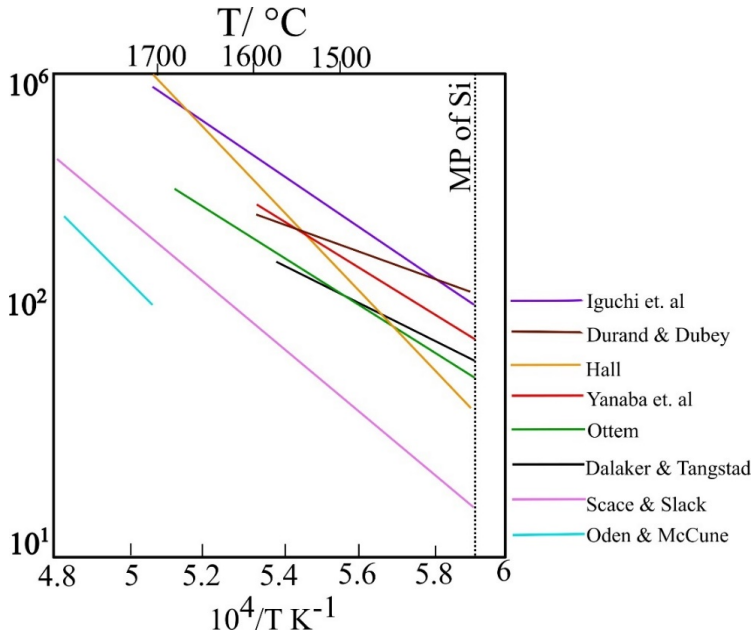

Figure 2.3.10. Solubility of carbon in liquid Si from various studies, reprinted from [86].

2.3.5 SiC produced from gas species

In the Si furnace, the arc near the electrode has temperatures above 2000 °C and it might be at this temperature region that the gas species are produced, which might later condense on cooling. Based on observations made during Si furnace excavations, one existing hypothesis is that a very small amount of SiO_2 goes into the crater zone and a reasonable amount of SiO_2 reacts before it enters the high temperature zone of the furnace [6]. This means that only some of the SiO_2 would be found at the bottom of the furnace. Hence, inside the crater, the main constituents around the arc would be Si and carbon. **Figure 2.3.11** shows the equilibrium ratio of gas species for a mixture of SiC:Si = 1:1, which equals to a Si:C ratio of 2:1. The software HSC Chemistry 9 was used to create all figures in this section. At around 3000 °C, large amounts of $SiC_2(g)$ as well as Si(g) are produced. As this gas is removed from the arc area, it will condense and at around 2000 °C, and most of the carbon would condense into solid SiC phase, in addition to producing some solid carbon. As the arc is originating from the carbon electrodes, one could assume a lower ratio of Si:C = 2:3, as shown in **Figure 2.3.12**.

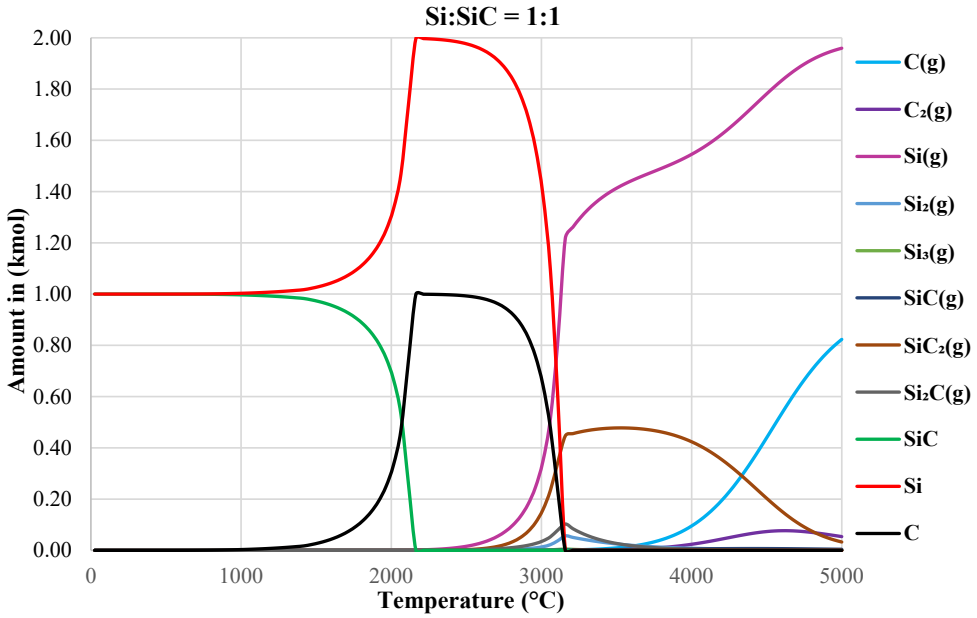

Figure 2.3.11. Equilibrium of gas species, using a mixture of Si:SiC = 1:1

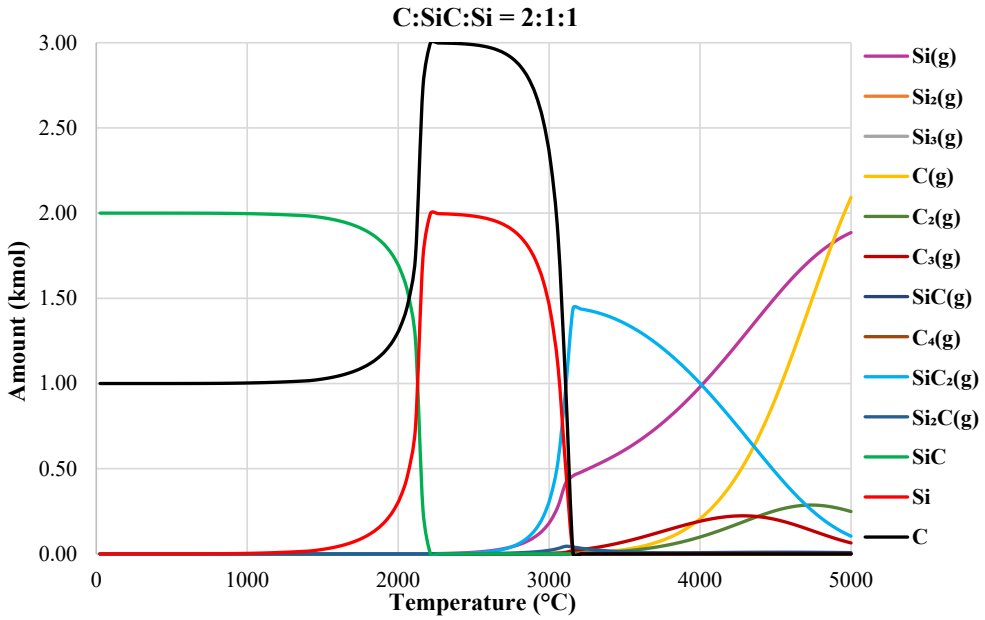

Figure 2.3.12. Equilibrium of gas species, using a mixture of C:SiC:Si = 2:1:1.

The second hypothesis is that a large quantity of SiO_2 would be present in the high temperature area, close to the arc. According to the general theory, some amount of unreduced SiO_2 along with some SiC would be present at the bottom of the crater zone [6]. If there are some amounts of unreduced SiO_2, Si, and SiC present close to the arc, the equilibrium of the gas species can be modeled as shown in **Figure 2.3.13** and **Figure 2.3.14**, using a mixture of SiO_2:Si:SiC in the ratios 1:2:2 and 1:1:1, respectively. When SiO_2 is present at higher temperatures around the arc, the dominating gas species are Si(g), SiO(g), and CO(g), which is in accordance with the general theory. Here also, while cooling, the gas species would precipitate to solid SiC.

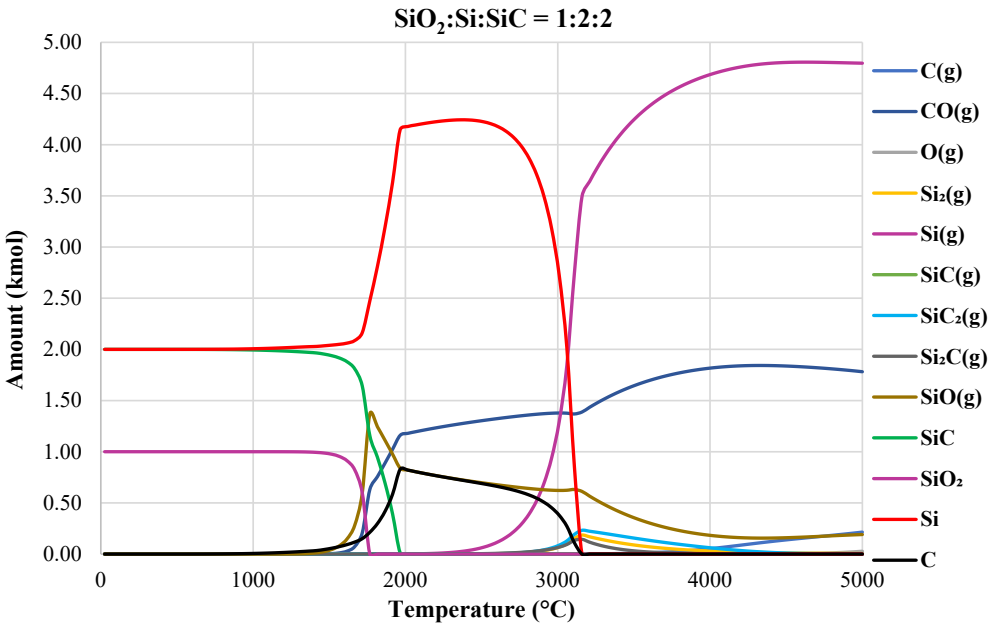

Figure 2.3.13. Equilibrium of gas species, using a mixture of SiO_2:Si:SiC = 1:2:2.

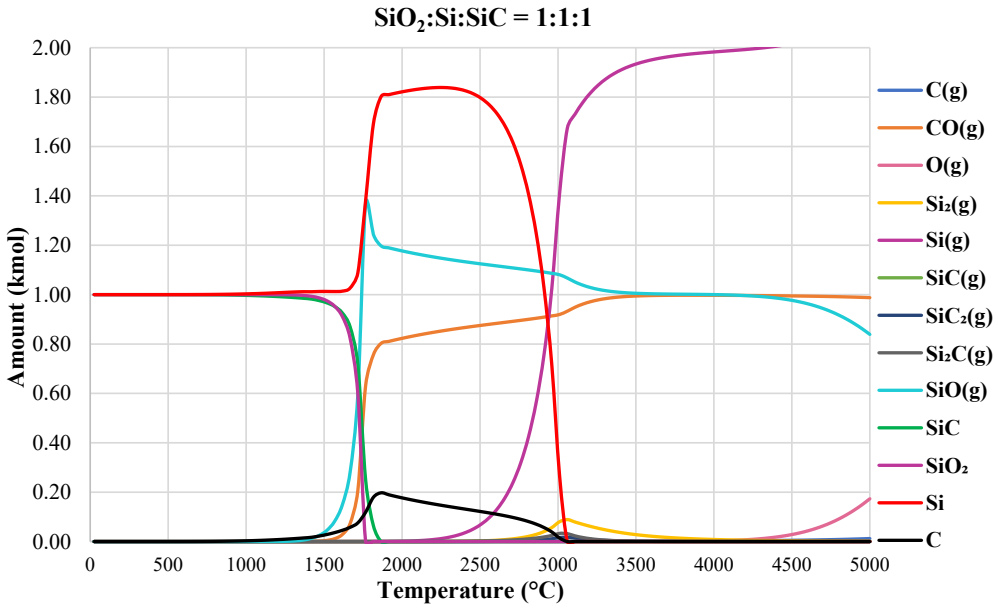

Figure 2.3.14. Equilibrium of gas species, using a mixture of SiO_2:Si:SiC = 1:1:1.

Kong et al. [89] performed a detailed study of the possible reactions responsible for the formation of SiC from the gas species. According to the study, the carbon bearing gaseous

reactive intermediates are Si(g), C(s), SiC_2(g), and Si_2C(g). There are six plausible reactions for the formation of SiC via gas phase:

$$Si\ (g) + C\ (s) = SiC\ (s) \quad (5)$$

$$Si_2C\ (g) = SiC\ (s) + Si\ (g) \quad (6)$$

$$SiC_2\ (g) = SiC\ (s) + C\ (s) \quad (7)$$

$$Si_2C\ (g) + SiC_2\ (g) = 3SiC\ (s) \quad (8)$$

$$Si_2C\ (g) + C\ (s) = 2SiC\ (s) \quad (9)$$

$$SiC_2\ (g) + Si\ (g) = 2SiC\ (s) \quad (10)$$

Kong et al. [89] discussed the probability of these reactions in a Si-C system based on the equilibrium of gas species concentrations using thermodynamic data. The equilibrium concentration of Si_2C(g) is low, therefore the reactions involving Si_2C(g) are less significant, which are the **reactions (6)**, **(8)**, and **(9)**. **Reaction (5)** is also insignificant, as it is a gas-solid reaction, the reaction kinetics of which is low. Moreover C(s) has to be generated by **reaction (7)** because both Si(g) and Si_2C(g) are competing for the C(s) to form carbide. The free energy for **reaction (9)** is more negative than for **reaction (5)**, hence **reaction (9)** is more favorable than **reaction (5)**. In comparison, the **reactions (7)** and **(10)** are more important than the other reactions. Both are gas phase reactions, their reaction kinetics are fast, and they both have large negative free energies. Between the free energies of these two reactions, **reaction (10)** has the largest negative free energy, making it more stable than **reaction (7)**. **Figure 2.3.15** shows the equilibrium compositions of different gas species up to 4727 °C from Kong et al. [89]. At temperatures above 2500 °C, carbon bearing gas species such as Si(g), C(s), SiC_2(g) and Si_2C(g) are similar to the equilibrium gas species calculated using the HSC software for different combinations of Si and SiC (**Figure 2.3.11** and **Figure 2.3.12**). This confirms that at lower temperatures (~2000 °C) SiC can form and precipitate from the gas species. **Figure 2.3.16** shows the variations in the free energies of the reactions from **(5)** to **(10)** with temperature, calculated using the HSC chemistry 9, and they are in good agreement with the calculations presented in Kong et al. [89].

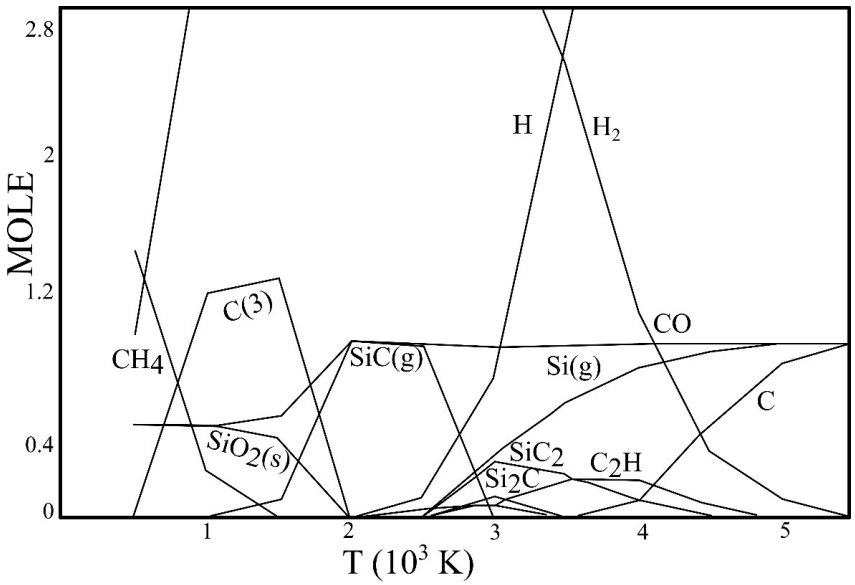

Figure 2.3.15. Equilibrium compositions of different SiC gas species up to 4727 °C [89].

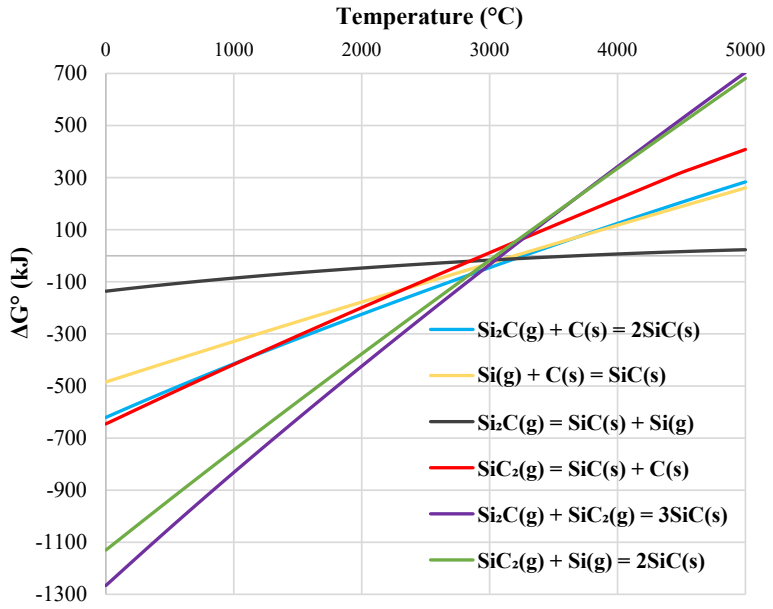

Figure 2.3.16. Distribution of free energy values of reactions (5)–(10) at temperatures up to 5000 °C.

Avrov et al. [90] investigated the mass transfer of β-SiC to α-SiC transformation in a system where conditions were suitable for SiC growth from the gaseous phase. The growth temperature ranged from 1800 to 2300 °C. One of the main stages of SiC monocrystals sublimation growth was the mass transfer through gaseous phase. The study modeled the growth

of SiC crystals both under vacuum and in different gaseous atmospheric conditions (N_2, Ar, or a mixture of both), and compared them with the experimental results. The growth rate ($\boldsymbol{V}$) of SiC crystals in vacuum was determined using the following equation:

$$\boldsymbol{V} = \frac{\boldsymbol{M_{SiC}}}{\boldsymbol{\rho_{SiC}}} * \boldsymbol{j_{SiC}} \qquad (11)$$

where $\boldsymbol{M_{SiC}}$, $\boldsymbol{\rho_{SiC}}$, and $\boldsymbol{j_{SiC}}$ are the molar mass, density, and mass transfer rate, respectively. The growth rate of SiC in vacuum increased with an increase in temperature, which was in good agreement with the theoretical calculated data. It was also higher than the growth rates in different gaseous atmospheres (N_2, Ar, or a mixture of both). The quantitative XRD analysis showed that the polytype transformation from β-SiC to α-SiC took place at 2027 °C. After being held for 60 min at 2327 °C, 100% of the initial source material of β-SiC had transformed to α-SiC. Upon completing the transformation to α-SiC, the vapor pressure over the source material decreased, thereby gradually reducing the mass transfer to the growing SiC mono crystal and the corresponding growth rate decreased. In another study by Lindstad [5], during the recrystallization of SiC in an Acheson furnace, the SiC samples collected at a temperature range of 2020–2500 °C showed an increase in the weight fraction of the α-SiC and SiC crystal grain sizes. Therefore, an assumption was made that the grains nucleated from the gas phase reaction later grew as α-SiC.

2.4 Thermodynamics of chemical reactions in furnace

It is important to explore the thermodynamics of the Si-O-C system to understand and improve the process of Si [6]. The Gibbs phase rule gives the relationship between the number of phases and components for a given system under equilibrium conditions [6], which can be expressed as:

$$Ph + F = C + 2 - R \qquad (12)$$

where Ph is the number of phases, F is the number of degrees of freedom, C is the number of components in a system, and R is the number of restrictions. In the Si process the different phases are determined by temperature and gas pressure. The three main elements in the Si process are Si, O, and C, which together form the Si-O-C system. In the Si-O-C system, Ph + F = 5, five phases are present, which are SiO_2, SiC, Si, C, and the gaseous phase. The sum of all gases in the process is close to 1 atm. **Figure 2.4.1** shows the equilibrium partial pressure of SiO(g)

(pSiO(g)) as a function of temperature for the **reactions (13), (16), (17),** and **(18),** calculated using the HSE Chemistry 9 software. **Figure 2.4.1** shows that the invariant point SiO_2-SiC-Si co-exists with pSiO(g) of 0.71 bar at 1800 °C, whereas according to Schei et al. [6] the SiO_2-SiC-Si co-exists at temperature 1811 °C with pSiO(g) of 0.67 bar. However, it gives an interpretation that Si can be produced at a temperature range of 1800–1811 °C.

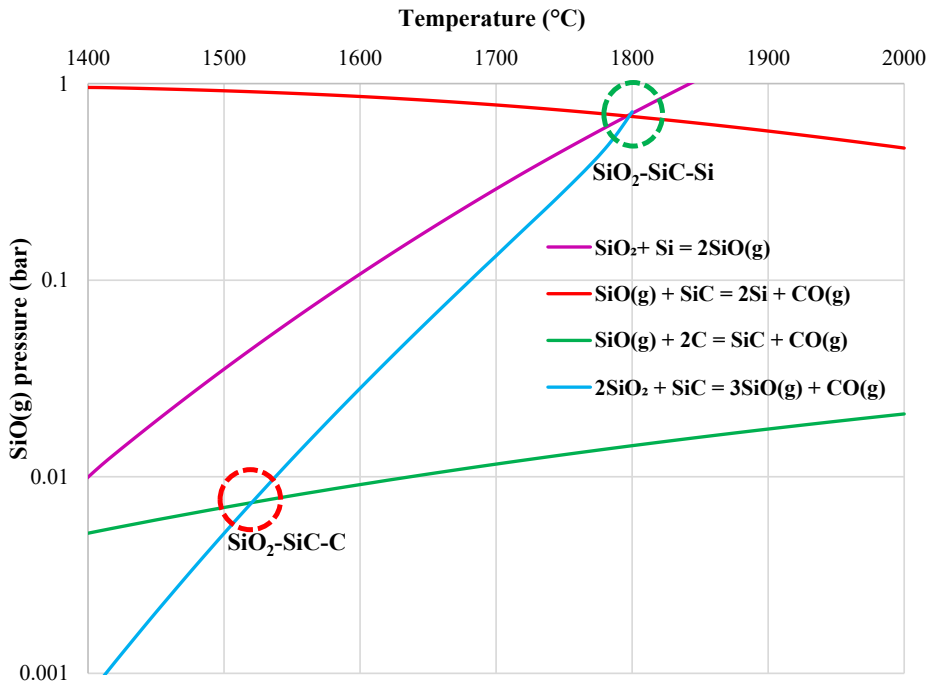

Figure 2.4.1. Equilibrium partial pressures of SiO(g) for various reactions in SiO_2-SiC-C-SiO-Si system at the temperature range 1400–2200 °C. Red and green circles show the two invariant points SiO_2-SiC-C and SiO_2-SiC-Si, respectively.

At equilibrium with 1 atm of total pressure, selecting the temperature as a free variable, there are two possible combinations that could occur together with a gaseous phase. These two invariant points in the Si-O-C system are SiO_2-SiC-C and SiO_2-SiC-Si, represented respectively by the red and green circles in **Figure 2.4.1**. The SiO_2-SiC-C co-exists with pSiO(g) = 0.004 bar, at 1512 °C, as shown in **Figure 2.4.2.**

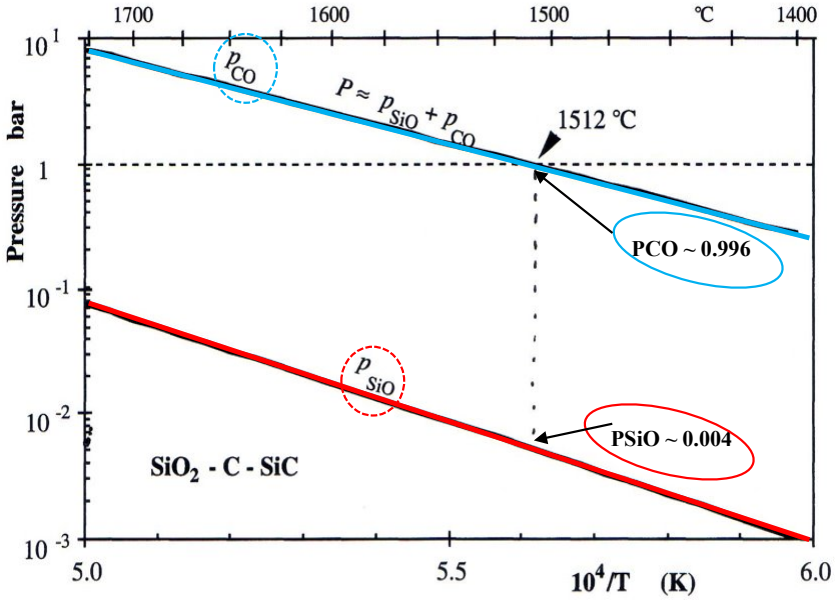

Figure 2.4.2. Equilibrium partial pressure versus temperature in SiO_2-SiC-C invariant system [6].

The following are the reactions occurring in the outer zone of the furnace [6]:

$$SiO\ (g) + 2C\ (s) = SiC\ (s) + CO\ (g) \qquad \Delta H_{1500\ ^\circ C} = -74\ kJ \qquad (13)$$

$$2SiO\ (g) = SiO_2\ (s, l) + Si\ (l) \qquad \Delta H_{1500\ ^\circ C} = -616\ kJ \qquad (14)$$

$$3SiO\ (g) + CO\ (g) = 2SiO_2\ (s, l) + SiC\ (s) \qquad \Delta H_{1500\ ^\circ C} = -1389\ kJ \qquad (15)$$

SiC is produced in the outer zone, also called the low temperature zone (< 1800 °C), when SiO(g) reacts with the carbon materials that are added into the furnace [6]. **Reaction (13)** is crucial for producing SiC, one of the main intermediate compounds to produce Si in the inner reaction zone of the furnace. Before the temperature reaches 1600 °C, pSiO(g) produced according to **reactions (16)** and **(17)** is high enough to produce SiC according to **reaction (13)**. If the entire carbon reacts according to **reaction (13)** in the outer zone, most of the SiO(g) is captured before it leaves the furnace. Hence the SiO reactivity of the carbon materials is an important factor and plays a major role in determining the Si yield. The SiO reactivity of carbon materials and its kinetics are explained in **section 2.5.1**. The reaction enthalpies were calculated using the HSC chemistry 9 software.

If the SiO gas is not completely captured by the carbon materials, the rest will rise upwards and condenses at the low temperature region according to **reactions (14)** and **(15)**,

which prevent some of the surplus SiO(g) escaping from the furnace and it could be the second main recovery mechanism. This condensation reaction is strongly an exothermic reaction, releasing a lot of heat, which heats up the colder region and the charge.

The inner reaction zone is also called the high temperature zone (> 1800 °C). The SiC from the outer reaction zone will react with the SiO_2 in the inner reaction zone. The invariant point SiO_2-SiC-Si co-exists with pSiO(g) of 0.67 bar at 1811 °C, as shown in **Figure 2.4.3**. The following are the reactions occurring in the inner zone of the furnace [6]:

$$SiO_2\ (s, l) + Si\ (l) = 2SiO\ (g) \qquad \Delta H_{1800\,^\circ C} = 598\ kJ \quad (16)$$

$$2SiO_2\ (s, l) + SiC\ (s) = 3SiO\ (g) + CO\ (g) \qquad \Delta H_{1800\,^\circ C} = 1367\ kJ \quad (17)$$

$$SiO\ (g) + SiC\ (s) = 2Si\ (l) + CO\ (g) \qquad \Delta H_{1800\,^\circ C} = 171\ kJ \quad (18)$$

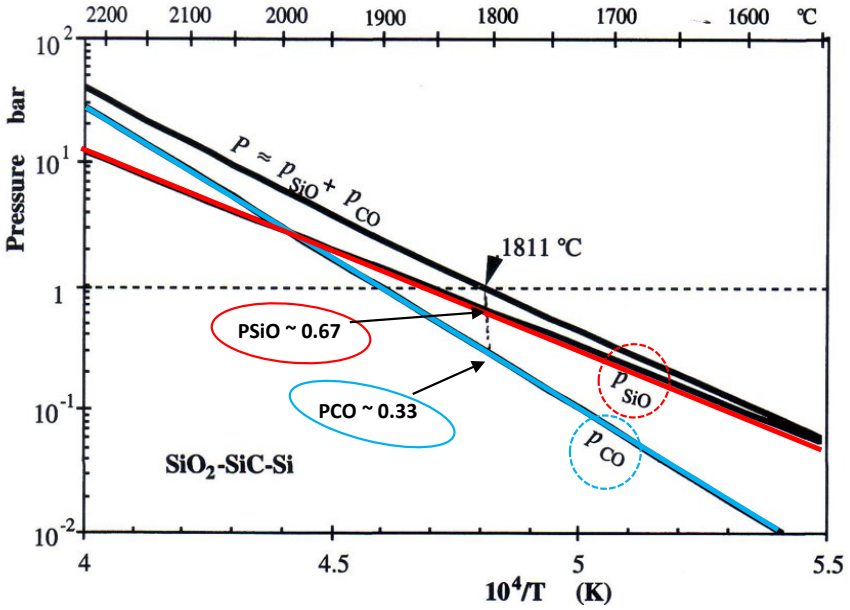

Figure 2.4.3. Equilibrium partial pressure versus temperature in SiO2-SiC-Si invariant system [1].

Reactions (16) and **(17)** are strongly endothermic, consuming most of the heat added from the arc. These two reactions produce SiO(g) required for the SiC reaction in the outer zone of the furnace and for the Si producing reaction in the inner zone of the furnace. **Reaction (18)** is the Si producing reaction and as mentioned in the previous section, production of SiC in the outer reaction zone is the most important factor required to produce Si in the inner zone. When compared with **reactions (16)** and **(17)**, **reaction (18)** is less endothermic, however, it is indeed dependent on the high SiO(g) pressure and high temperature in the gaseous mixture in the inner

zone of the furnace to produce Si. According to **Figure 2.4.3**, the **reaction (18)** takes place at 1811 °C with pSiO(g) of 0.67 bar and as the temperature decreases, pSiO(g) also decreases gradually. Hence, below 1811 °C, back reactions occur, such as inverse of **reactions (16)** and **(17)** (which are **reactions (14)** and **(15)**). The described reaction mechanisms indicate that Si cannot be produced by **reaction (18)** at temperatures below 1811 °C.

2.5 Kinetics of different reactions during Si production: Previous studies

2.5.1 Reaction between SiO(g) and carbon materials

SiO reactivity of carbon and the formation of SiC is a gas-solid reaction. One suitable model for studying the non-catalytic reaction of carbon particles with the surrounding SiO gas is the shrinking core model (SCM) [91]. The progress of gas-solid reaction of a non-porous solid to ash or a resultant product is explained below and is depicted in **Figure 2.5.1**[92].

1. The gaseous reactant diffuses through the gas/fluid film surrounding the particle to its surface.
2. Chemical reaction on the surface creates a thin layer of the resultant product on the particle surface.
3. The gaseous reactant further penetrates and diffuses through the resultant product layer to the surface of the unreacted core.
4. The reactant gas reacts chemically forming a layer of the resultant product.
5. The gaseous products created by the reaction diffuse through the product layer to the exterior surface of the solid.
6. The gaseous products diffuse through the gas/fluid film back to the surroundings.

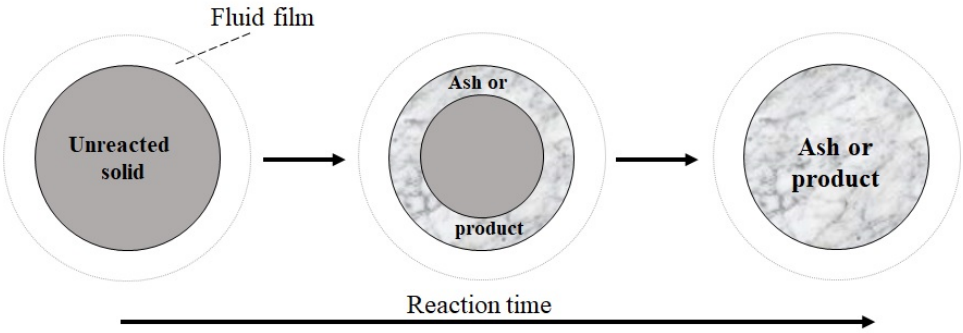

Figure 2.5.1. Gas-solid reaction of a solid particle to ash or a final product, adapted from Szekely [92].

As the reaction proceeds, the unreacted core diminishes in size. However, the overall size of the solid might or might not change, depending on the relative densities of the solid reactant and the resultant product. The chemical reaction might occur at the sharp interface or within a narrow region between the unreacted core and the product layer, which could be porous or non-porous. In both cases, the gaseous reactant must be able to penetrate through the product layer in order to proceed and complete the reaction. Therefore, the overall process consists of a chemical reaction that initially occurs at the interface. The gaseous reactants and products then diffuse through the solid product layer and through the boundary layer at the external surface of the solid. Hence, the overall rate of complete conversion of a particle could be controlled by either the rate of the chemical reaction or the rate of diffusion.

Szekely and Evans [93] developed a grain model for porous solids, picturing it as an aggregate of small nonporous particles of uniform size or pellets made up of fine concentrate particles. Sohn [94] reviewed a grain model that gives an appropriate solution, in which the porous solid particle was assumed to be composed of solid grains. It was assumed that the diffusion of the reactant gas through the product layer around the individual grain offered little resistance to the overall rate. This assumption is valid for small grains, in which case, the chemical reactions are assumed to take place in an infinitely thin layer on the unreacted core of small non-porous grains of uniform size within the particle. This layer consists purely of the solid reactant, while the gases are transported from bulk gas to the surface of the particles by diffusion and from the surface to the grains through pore diffusion. This is illustrated in **Figure 2.5.2.**

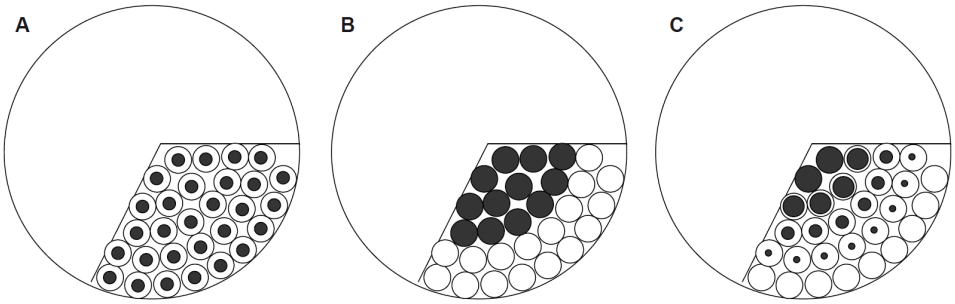

Figure 2.5.2. Schematic illustration of different stages of gas-solid reaction based on grain model by Sohn [94].

To compare the models with real situations, samples are sliced and the cross-sections of the partly reacted solid particles are examined. In several situations, the SCM closely approximates the real particles. During the conversion of carbon to SiC from SiO(g), the reaction

starts on the surface of the particle, initially forming a peripheric layer of SiC. The thickness of the SiC layer increases as the reaction proceeds. According to Schei and Halvorsen [95], the reaction rate slows down as the thickness of the SiC layer increases, as the SiO(g) has to diffuse through the already formed SiC layer to reach the unreacted carbon to convert it completely.

"Reactivity" is a term frequently used by metallurgists for suitable reduction materials [96] and "SiO-reactivity" refers to the ability of carbon materials to react with SiO(g) according to **reaction (13)**. In the Si production process, maximum conversion of carbon to SiC in the outer zone improves the Si yield. Selecting carbon materials with high SiO-reactivity is hence crucial. The SiO-reactivity is dependent on the structure (porosity and cell wall thickness), properties (mainly fix-C, volatiles, and ash content), and the type of the carbon materials, and have been studied extensively [20, 21, 22, 40].

The SINTEF SiO-reactivity test is the most acknowledged test for evaluating the reactivity of carbonaceous reduction materials towards SiO(g). The principle of SINTEF test is based on a gas analysis technique. A gas with known concentration of SiO(g) is passed through a packed bed of the reduction material to be tested, at a temperature of 1650 °C. The carbon material would then react with the SiO(g) according to **reaction (13)**. As the composition of the outgoing gas is continuously monitored, the amount of SiO(g) that passes through the carbon bed without reacting can be calculated and used as the measure of reactivity [40]. **Figure 2.5.3** shows the reactivity scale of carbon reductants according to the SINTEF SiO-reactivity test [41].

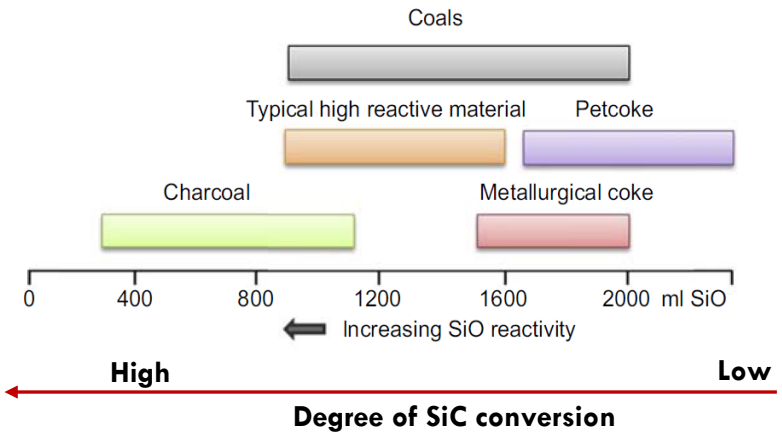

Figure 2.5.3. Reactivity scale of carbon reductants according to SINTEF SiO-reactivity test [41].

The kinetics between carbonaceous materials (coal, charcoal, and coke of diameter 8–25 mm) and SiO(g) were studied by Myrhaug [20]. Pellets of (SiO_2 + SiC) were used (**reaction (17)**) to generate SiO(g). The spherical shaped carbon particles were connected to a thermo-balance by a tungsten wire and the weight was monitored as they reacted with the SiO(g)

according to **reaction (13)**. This test was similar to the SINTEF SiO-reactivity test for carbon materials and the reaction temperature was set to 1650 °C. As the conversion happened according to **reaction (13)**, the particle weight increased, and the degree of conversion $\boldsymbol{X}$ was calculated from the recorded weight with the following equation:

$$\boldsymbol{X} = \frac{\boldsymbol{m_p - m_{p0}}}{\boldsymbol{w_{FC0} m_{p0}\left(\frac{Mm_{SiC} - 2Mm_c}{2Mm_c}\right)}} \qquad (19)$$

where $\boldsymbol{m_p}$ and $\boldsymbol{m_{p0}}$ are the actual and initial weights of the sphere, respectively, $\boldsymbol{w_{FC0}}$ is the mass fraction of the fix-C in the particle just before conversion starts, and $\boldsymbol{Mm_{SiC}}$ and $\boldsymbol{Mm_c}$ are the molar masses of SiC and carbon, respectively. To estimate the kinetic parameters, a mathematical model describing the degree of conversion versus time was used. Among the selected set of kinetic models, the SCM gave the best result of the reaction kinetics for the partially converted carbon spheres. **Figure 2.5.4** shows the EPMA images of the partly converted spheres of charcoal, coal, and coke with their shrinking unreacted cores. The charcoal-derived partially converted SiC particles had a sharp boundary between the unreacted core and the porous layer. The progress of conversion was more spatially distributed in the cases of both coal and coke. The study showed that smaller particles converted faster than the lager particles of the same type and the charcoal particles converted faster compared with coal and coke of same radius [20].

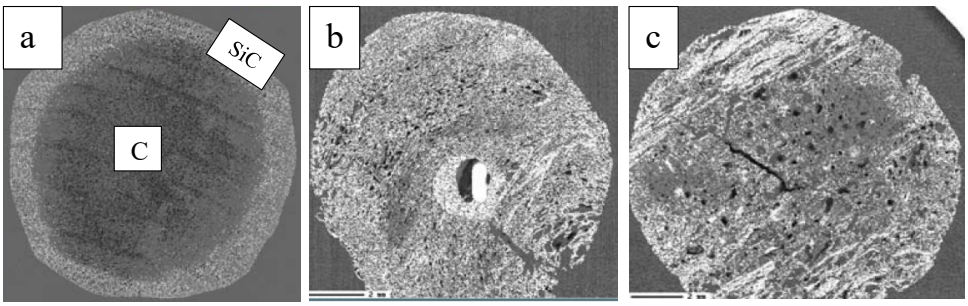

Figure 2.5.4. EPMA images of partly converted spheres of (a) charcoal, (b) coal, and (c) coke, showing their shrinking unreacted cores [20].

Bituminous coals are classified into three types according to their volatile matter content [40]; low, medium, and high volatile bituminous coal, with the content of volatile matter between 14–22%, 22–31% and > 31%, respectively. Increasing coal rank decreases the volatile content and moisture, but it increases its reflectance, calorific value, and the carbon and hydrogen contents. Increased rank, or maturity of the coals, tends to give a lower reactivity towards SiO(g) [40]. Raanes and Gray [21] tested the SiO(g)-reactivity of nine different bituminous coals with respect to their original rank. The bituminous coals of lower ranks and lower vitrinite reflections

showed higher SiO-reactivities. **Figure 2.5.5** shows the SiO-reactivity of the nine different bituminous coals compared with the original rank of the materials. The y-axis shows the reactivity number, which expresses the amount of SiO(g) passing through the carbon samples without reacting; highly reactive materials show lower reactivity numbers.

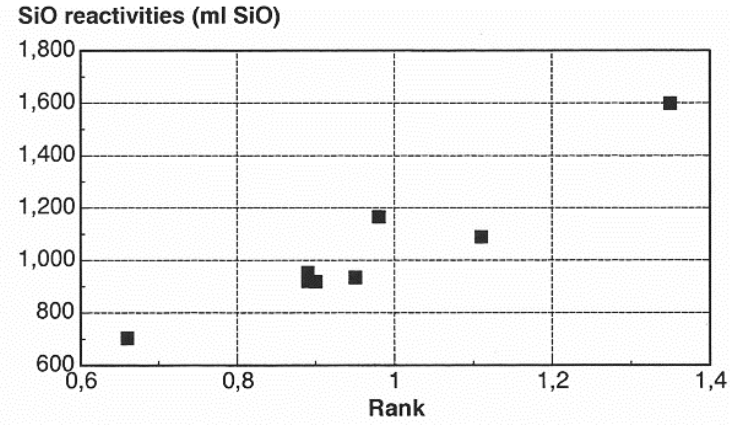

Figure 2.5.5. SiO-reactivity of nine different bituminous coals versus original rank of materials [21].

The SiO-reactivity of carbonaceous reducing agents such as charcoal, Iscor coke, Lurgi char, and pet-coke in the FeSi process was studied by Paull and See [97]. Among the tested carbonaceous materials, Lurgi char showed higher reactivity and higher strength when converted to SiC. The role of structure and properties of carbon materials from pet-coke and coal in the carbothermal reduction of SiO_2 to produce SiC were investigated by Narciso-Romero et al. [98]. Four different types of pet-coke and three types of metallurgical cokes from bituminous coal of various ranks were chosen for the study. All the carbon materials exhibited different behaviors while reacting with SiO_2 to form SiC. The factors including intrinsic material properties such as the degree of structural order, presence of impurities that are catalytically active, and the physical characteristics such as particle size, specific surface area, and porosity were the controlling factors determining the rate of these reactions.

Buø [99] studied the reaction rates of reduction materials in the Si and FeSi process. She performed a thermo-gravimetric analysis (TGA) to measure the reaction rates of different types of cokes. The different coke samples had a wide distribution of binder and filler phase components in their texture. Particles of reduction materials together with the SiO(g) generating source (pellets made from (SiO_2 + SiC)) were placed in an alumina crucible and heated at 1690 °C for 89 min. The weight losses during the experiments were measured continuously, which could be expressed as the reaction rates of conversion to SiC. The amounts of SiC formed were

different for the various coke samples. She observed that the measured reaction rate decreased with increasing amounts of the coke sample. However, the measured reaction rate increased with decreasing particle size. Here the **reaction (17)** was extremely heat consuming, and hence for larger quantities of coke materials, more SiO(g) was required and this was achieved by introducing more heat into the system.

The petrographic analysis of coal (vitrinite of reflection) in Raanes and Gray [21] has revealed that the reactivity decreased with increasing rank of coal. Buø et al. [100] showed the importance of petrographic analysis in the selection of coals and cokes for Si and FeSi production. The properties of coke are related to properties of coal. The porosity of the coke increases with the increasing reactive content of macerals in coal, especially that of vitrinite in coal, and also with the increasing content of binder phase in coke. Higher content of the binder phase in coke leads to a lower volume weight with a higher porosity and a higher SiO-reactivity. A highly porous coke with thin cell walls increases the reactivity towards SiO gas during the production of Si and FeSi. These studies thus showed that the reactivity of carbon towards SiO(g) mainly depended on the coal rank and the distribution of binder and filler phases in the coke [21, 100].

Myrvågnes and Lindstad [101], and Myrvågnes [40] also studied the importance of properties of coal and coke in the production of Si alloys. Both studies used three types of coal samples, two of them with same rank but different maceral compositions. They observed that the large number of inert particles in the calcined coal that had a higher amount of filler phase showed lower reactivity towards the SiO(g). Coal with a higher rank consists of clastic SiO_2 grains in the coal matrix, which increases the reactivity. This is because the carbon reacts with the SiO_2 grains as well as the SiO gas and thus increases the reactivity. Petrographic analysis of calcined coal showed a lot of depositional carbon in the pores of coal. It is believed that the depositional carbon sealed the pore walls and blocked the reaction towards the SiO(g), resulting in a reduced reactivity.

Ramos [49] investigated the SiO-reactivity of eucalyptus-derived charcoal, produced under different carbonization parameters. Metallurgical coke was also used for the purpose of comparison. All charcoals tested had significantly higher SiO-reactivity than coke due to the high porosity in charcoal compared to coke. There was a strong correlation among the wood variables and the properties of charcoal that formed from the wood clones. The reactivity of charcoal was mainly influenced by its apparent density and the functional chemical groups. The temperature during the carbonization of charcoal also had a strong influence on the degree of conversion and hence, also on the SiO-reactivity. A summary of the various studies on SiO(g)-reactivity of carbon materials is given in **Table 2-3.**

Table 2-3. Summary of various studies on SiO(g)-reactivity of carbon materials.

Selected works	Carbon materials and charge materials used for producing SiO(g)	Materials that showed high SiO-reactivity and the influencing parameters
Myrhaug [20]	Charcoal, coal, and coke at 1650 °C (SiO_2 + SiC)	Charcoal Small particle size
Myrvågnes and Lindstad [101] Myrvågnes [40]	Three different coals varying in rank at 1650 °C 1. Blue gem - homogeneous and low mineral content 2. Staszic - Same rank as blue gem but inhomogeneous with different macerals and mineral 3. Peak down - SiO_2 inclusions, Ash content was high, 11% (SiO_2 + SiC)	Peak down, SiO_2 inclusions in coal Small particle size
Narciso-Romero et al. [98]	Four pet-cokes Three metallurgical cokes at 1500 °C (SiO_2 + SiC)	Optical texture, porosity, and catalytic inclusions enhanced the SiC formation in both the coke types
Paull and See [97]	Charcoal, Iscor coke, Lurgi-char, and pet-coke at 1650 °C for FeSi (SiO_2 + SiC)	Lurgi-char SiC with high strength
Buø [99]	Seven different cokes at 1690 °C (SiO_2 + SiC)	Rate of SiC formation was same for all cokes and it increased with decreasing particle size
Raanes and Gray [21]	Eight coals of different ranks at 1650 °C (SiO_2 + SiC)	Reactivity increased with decreasing coal rank and vitrinite reflectance
Buø et al. [100]	Cokes from coal and petrographic analysis at 1690 °C (SiO_2 + SiC)	Coal with higher binder phase, lower filler phase, and porosity with thin cell walls
Ramos [49]	Charcoal from different wood clones and coke at 1650 °C (SiO_2 + SiC)	Charcoal Properties of wood clone and the charcoal carbonization temperature

2.5.2 Kinetics study of SiO(g) producing reactions in Si process

Studying the kinetics of the reactions between (SiO_2 + SiC) and (SiO_2 + Si) to produce SiO(g) (**reactions (17)** and **(16)**) give a better understanding about the high temperature zones in the Si furnace [102] - [106]. These two reactions are strongly endothermic reactions. Andersen [102] performed TGA and wettability test to understand the kinetics of the SiO(g) producing reactions at higher temperatures. When heating the (SiO_2 + SiC) pellets, an exponential increase in the reaction rate at 1450–1700 °C and a constant or reduced reaction rate from 1730 to 1750 °C were observed. The rate increased rapidly at temperatures above 1750 °C. The calculated activation energy for this reaction was 398 kJ/moles for temperatures up to 1786 °C. When heating with a mixture of (SiO_2 + Si), an exponential increase in the reaction rate was observed at temperatures from 1450 to 1750 °C, followed by a slight decrease in the rate till the temperature reached 1860 °C. The rate showed an exponential increase later up to a temperature of 1910 °C. The calculated activation energy was 438 kJ/mole for the reaction with (SiO_2 + Si), which was higher compared with the calculated activation energy for (SiO_2 + SiC). The findings concluded that the reaction between the solid-liquid (SiO_2 + SiC) was faster compared with the liquid-liquid (SiO_2 + Si) reactions at temperatures around 1850–1900 °C. Similar results were also observed with the wettability tests.

Bao et al. [104] studied kinetics of the same SiO(g) producing reactions in TGA under Ar atmosphere in the temperature range of 1550–1820 °C. At temperatures lower than 1550 °C, both reactions were very slow and then increased exponentially to 1730–1820 °C, until the charge materials were almost consumed. At temperatures 1550–1730 °C, the (SiO_2 + Si) mixture reacted a maximum of 1.5 times faster compared with the reaction using mixture of (SiO_2 + SiC). For (SiO_2 + Si), liquid Si enhanced the rate of its melting temperature. However, the reaction with a mixture of (SiO_2 + SiC) dominated at around 1800 °C. It was also established that SiO_2 goes through various phase transformations or polymorphs upon heating.

Tangstad et al. [105] studied the reaction rate of (SiO_2 + SiC) with various polymorphs of SiO_2 at temperatures from 1650 to 2000 °C. When the quantity of SiC exceeded the stoichiometric amount, the reaction rate per gram of SiO_2 increased and no noticeable difference was reported between the different polymorphs of SiO_2. In addition, the reaction area also influenced the reaction rate. The activation energy was 460 kJ/mole at temperatures above 1700 °C, the melting point of SiO_2.

Hertl and Pultz [106] investigated the kinetics and mechanisms of the reaction between SiO_2 and SiC at temperatures from 1270 to 1490 °C. They found that during the reaction

between SiO_2 and SiC, CO(g) would form and at some point, the CO(g) must be chemisorbed at the surface. It would block the reaction sites between the SiO_2 and SiC and suppresses the reaction rate. Hence, the chemisorption by CO(g) is the rate determining step. The activation energy for this reaction at 1270–1490 °C was 131–97 kcal/mole (547– 406 kJ/mole).

Sindland [103] studied the reactivity of a SiO_2 and Si mixture as a function of time (30–180 min) and temperature (1650–1950 °C) in Ar atmosphere and showed that the reactivity of the Si and SiO_2 mixture increased with time and temperature. She further carried out a comparison between the two SiO(g) producing reactions in a Si furnace; the reaction between SiO_2 and SiC (as reported previously [105]) and the reaction between SiO_2 and Si. The two reactions had reaction rates in the same ranges with the same available reaction areas. The activation energies for both reactions were also in a similar range and they both contributed to the formation of SiO(g), when the reaction areas were approximately the same. If the available area for reactions was different it would have determined which reaction contributes most to the formation of SiO(g) in an industrial Si furnace.

2.5.3 The Si producing reaction

As mentioned, according to theory, Si is produced at a temperature of 1811 °C and a pSiO(g) of 0.67 bar, following **reaction (18)**. Below is a description of previous studies on Si production in SiC particles, which were conducted at lower temperatures (< 1800 °C).

Tangstad et al. [107] simulated the Si furnace experiments to study the SiO(g) condensation reaction and the cavity formation at low temperatures. A graphite crucible capable of holding industrial sized particles was utilized and was filled with a layer of (SiO_2 + Si) mixture followed by a mixture of (SiO_2 + SiC) layered on top of it. Experiments were performed in an induction furnace at 1900 °C. The advantage of using the induction furnace is that it creates a temperature gradient from the bottom to the top, similar to that of an industrial Si furnace, and therefore is a good choice for Si related experiments. The temperature measured at the bottom was 1900 °C and at the top it was about 1400 °C. After the experiments, samples from different layers were taken out for analysis. For samples collected from the top portion, the temperature recorded was around 1450 °C and the samples had remained unreacted without the presence of any condensates. Samples taken from a position where the temperature was around 1500–1600 °C showed formation of brown and white condensates. Brown condensates typically form on the SiC surface and they are mostly a mixture of Si and O, whereas white condensates are typically a mixture of SiO_2 and Si droplets.

They also analyzed two SiC samples, each collected from regions where the measured temperatures were 1500 °C and 1760 °C, respectively. The formation of Si inside these two SiC samples is shown in **Figure 2.5.6.** The Si in SiC might have been produced as per **reaction (18)**. However, around 1500 °C, pSiO(g) was more than 0.9 bar, which is too high for the **reaction (18)** to happen. Even though this was not observed in all the particles, it indicated that Si could form at lower temperatures further up in the furnace. These findings were in good agreement with the results from Myrhaug [20] where Si had formed in charcoal-converted particles collected from the low temperature zone (**Figure 2.5.7**; sample collected from zone 7, blue region in **Figure 2.1.16** of a 150 kW pilot furnace).

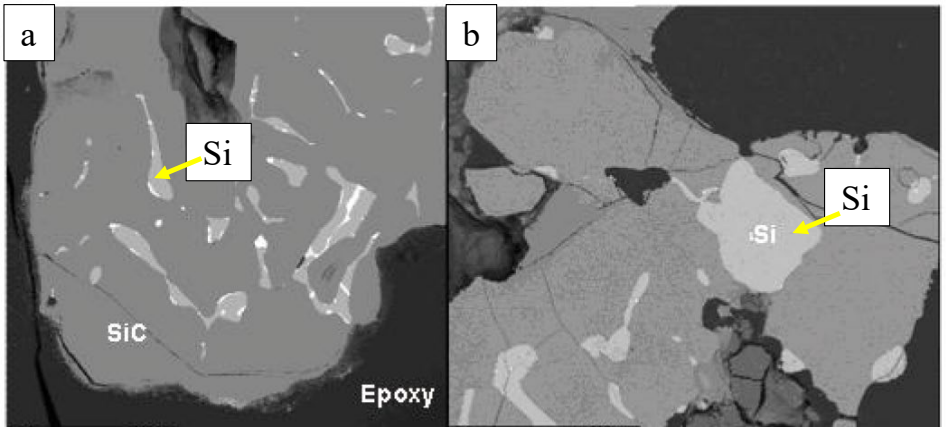

Figure 2.5.6. Formation of Si inside SiC samples collected from regions of (a) 1500 °C and (b) 1760 °C from Si furnace [107].

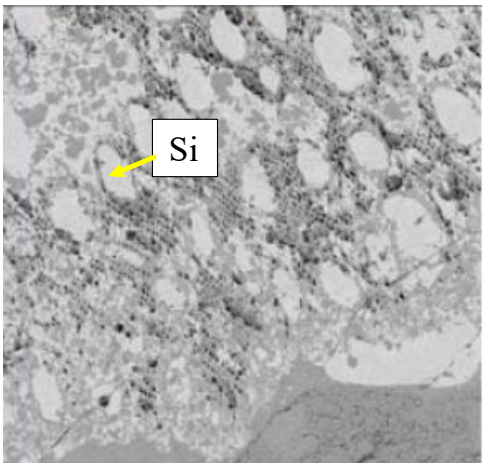

Figure 2.5.7. EPMA image showing Si formation in charcoal-converted SiC particles, collected from low temperature zone (zone 7, Figure 2.1.16) of 150 kW pilot scale Si furnace [20].

Vangskåsen [32] excavated a 150 kW pilot scale Si furnace and observed the same phenomenon in SEM investigation of the samples, i.e., presence of Si in the SiC particles collected from high up in the furnace (low temperature region). **Figure 2.5.8a** shows the cross-section of the crucible from this pilot scale Si furnace and Si was detected in the SiC particles collected from zone 5. The SEM image displaying the presence of Si in the SiC sample is shown in **Figure 2.5.8b**. After conducting laboratory-scale Si/FeSi experiments in a graphite crucible, Saadieh et al. [108] also reported formation Si in the SiC particles taken from above the cavity wall in the low temperature region, formed according to **reaction (18)**. Although the formation of Si was not observed in all the SiC particles collected from low temperature regions, these results suggest that Si could form at lower temperatures too and this could impact the industrial Si production.

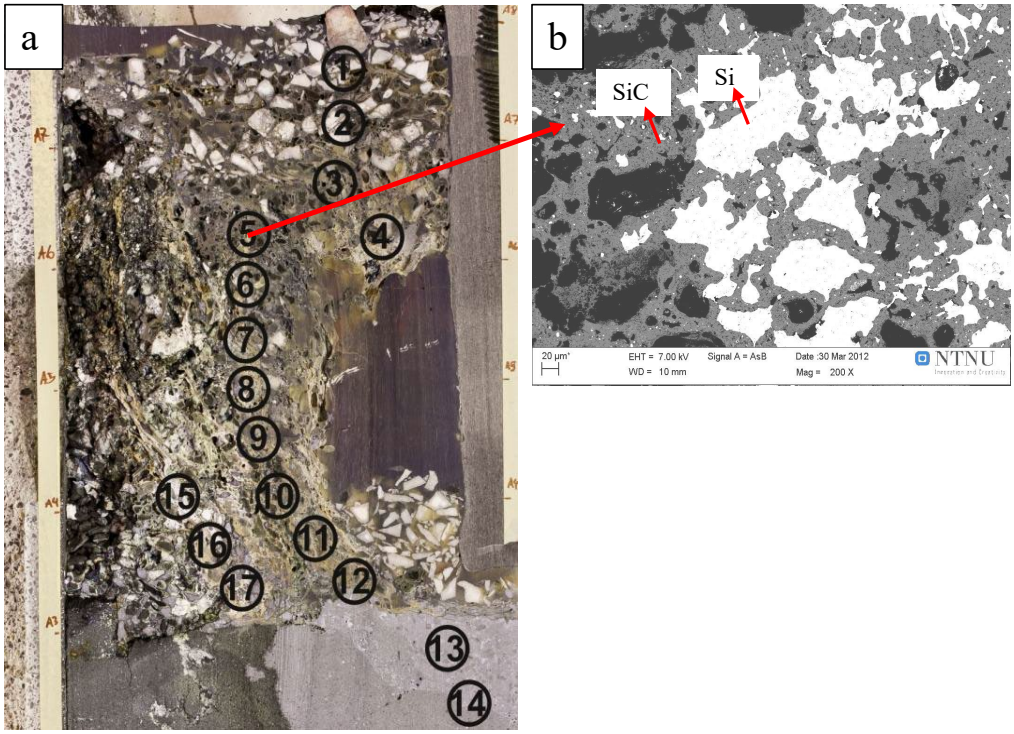

Figure 2.5.8. (a) Cross-section of crucible from pilot scale Si furnace [32]; presence of Si was detected in SiC particles from zone 5. (b) SEM image of SiC sample with Si, collected from zone 5.

3 Experimental apparatus, raw materials, and procedures

This chapter includes details of the experimental techniques as well as the equipment used in this study. The research aims at investigating the two different forms of SiC, β-SiC and α-SiC, formed from charcoal, coal, and pet-coke, at temperatures ranging from 1700 to 2450 °C. It will also be explored how different carbon sources as well as the charge types used for SiO(g) generation affect the production of SiC and Si.

3.1 Overview of experiments

The experimental work comprises two studies; the formation of β-SiC and elemental Si in the SiC structure (**Study A**), and the transformation from β-SiC to α-SiC (**Study B**). Carbon material heated between 1700–1900 °C in an atmosphere containing SiO(g) forms SiC. The goal of this work is to study the extent of SiC formation in the various types of carbon materials used for the process. Eventually, Si would be generated in the β-SiC particles at this temperature range. It will also be investigated if the amount of Si thus produced in the β-SiC particles depends on the type of the carbon material used. This is referred to as **Study A**.

The β-SiC and β-SiC + Si particles will be transformed to α-SiC at the temperature ranges of 2100–2450 °C. During the industrial Si process, β-SiC particles are produced at lower temperatures in the Si furnace. Later, the β-SiC particles will descend to a region of higher temperature where Si production takes place. The crater region has temperatures ranging from 1800 °C to > 2000 °C. When the β-SiC particles enter the region of such high temperatures, they might transform to α-SiC, depending on the temperature. The transformation of β-SiC to α-SiC is referred to as **Study B**. The four different furnaces used for the various sets of experiments and their corresponding purposes are as follows:

(a) **Study A**: An induction furnace was used to produce β-SiC and the features of Si formation in the β-SiC particles that were formed from different carbon materials were evaluated [**section 3.3.1**]. Two types of experiments were conducted in this process;
    (i) Constant volume experiments
    (ii) Constant weight experiments

(b) **Study A**: To validate the induction furnace experiments, i.e., the production of SiC and Si using the selected carbon sources, small-scale experiments were performed in a graphite tube furnace in a more controlled environment [**section 3.3.2**].

(c) **Study B**: A graphite tube furnace was used to subsequently convert β-SiC to α-SiC [**section 3.4**].

(d) **Study B**: A hot-press furnace was used in the final stages to check whether the pressure applied on β-SiC has any effects on the process of conversion to α-SiC [**section 3.5**].

An overview of the furnaces, experiments, and the analyses performed is represented schematically in **Figure 3.1.1**.

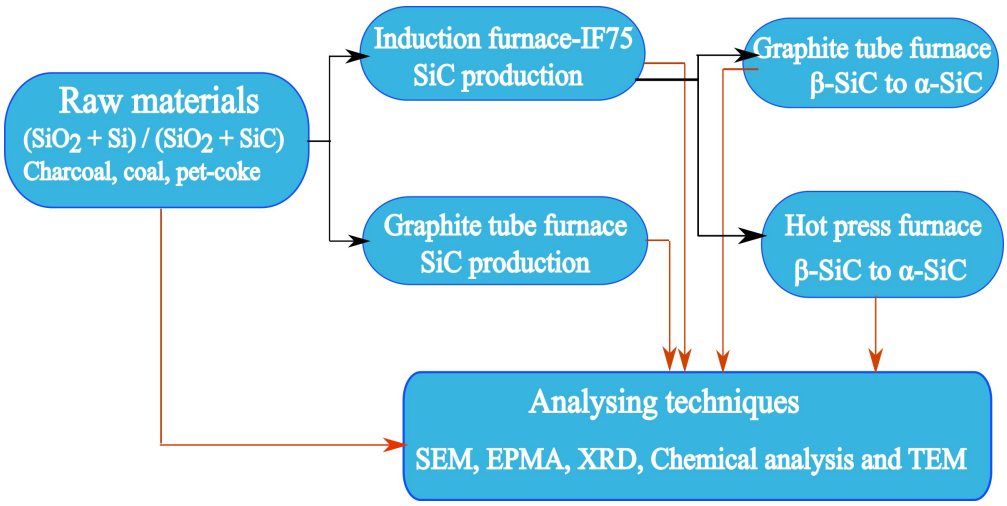

Figure 3.1.1. Overview of furnaces, experiments, and analysis methods.

3.2 Raw materials

To generate SiO(g) in the SiC production experiments, a mixture of (SiO_2 + Si) and pellets made from (SiO_2 + SiC) were used. Charcoal, coal, and pet-coke were used as the raw carbon materials.

3.2.1 SiO_2 and Si

As shown in **Figure 3.2.1**, a mixture of SiO_2 and Si of sizing 5–10 mm was used as raw materials for generating SiO(g). The Si (Si 4010) used in this study was 99% pure Si. The compositional

analysis of SiO_2 and Si obtained from the supplier is given in **Table 3-1** and **Table 3-2,** respectively.

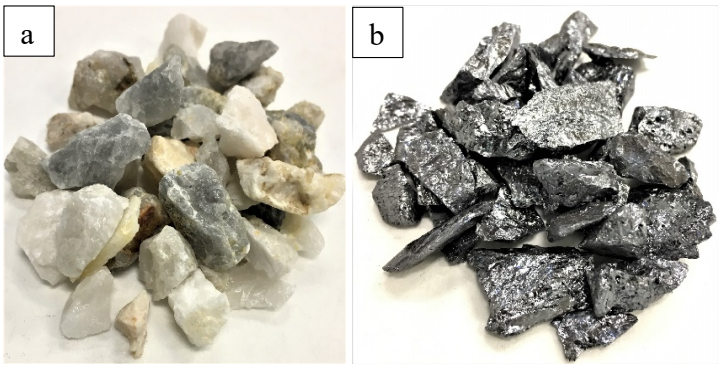

Figure 3.2.1. (a) SiO_2 and (b) Si used to generate SiO(g).

Table 3-1. Compositional analysis of SiO_2 provided by the supplier.

Contents	SiO_2	Fe_2O_3	Al_2O_3	CaO	TiO_2	MgO	Na_2O	K_2O	P_2O_5
Wt.%	99.82	0.0352	0.1157	0.0058	0.0031	0.0028	0.004	0.0205	0.0014

Table 3-2. Compositional analysis of Si provided by the supplier.

Product	Si (wt.%)	Fe (wt.%)	Ca (wt.%)	Ti (ppmw)	P (ppmw)
Si 4010	Min 99.0	Max 0.40	Max 0.10	200–300	20–40

3.2.2 Pellets made from SiO_2 and SiC

Another source of raw material used to generate SiO(g) was pellets made from (SiO_2 + SiC). Pellets of grain sizes 4–6.35 mm and 1–2 mm were used for the induction furnace experiments and graphite tube furnace experiments, respectively. These pellets were made from a mixture of ground SiO_2 and fines made from α-SiC [20] in the molar ratio of SiO_2:SiC = 2:1. It was pelletized at room temperature using water as binder. The pellets were dried for 6 h at 110 °C and were then calcined for 20 min at 1200 °C. **Figure 3.2.2** shows the (SiO_2 + SiC) pellets of various grain sizes used for the experiments.

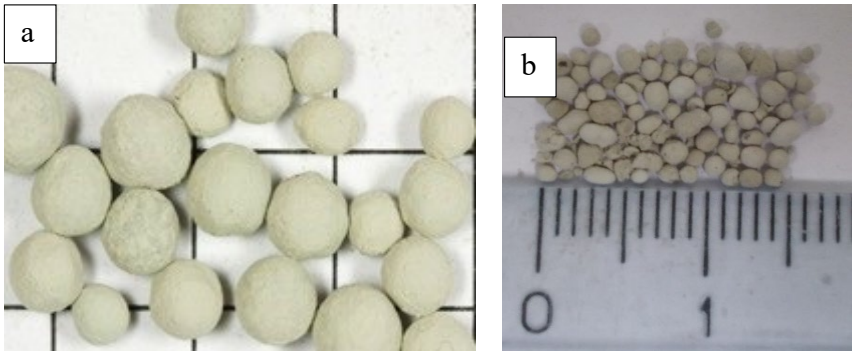

Figure 3.2.2. (SiO_2 + SiC) pellets of grain sizes (a) 4–6.35 mm and (b) 1–2 mm used to generate SiO(g).

3.2.3 Carbon materials

Charcoal, coal (heat-treated/calcined), and pet-coke with sizes of 5–10 mm were used to produce SiC (**Figure 3.2.3**). These were carbon materials provided by an industrial Si producer; their compositional analysis is given in **Table 3-3.** The ash composition mainly consisted of Al_2O_3, Fe_2O_3, CaO, TiO_2, SiO_2, MgO, K_2O, Na_2O, and P_2O_5 [39]. **Table 3-4** shows the ash composition in charcoal, calcined-coal, and pet-coke used in this study.

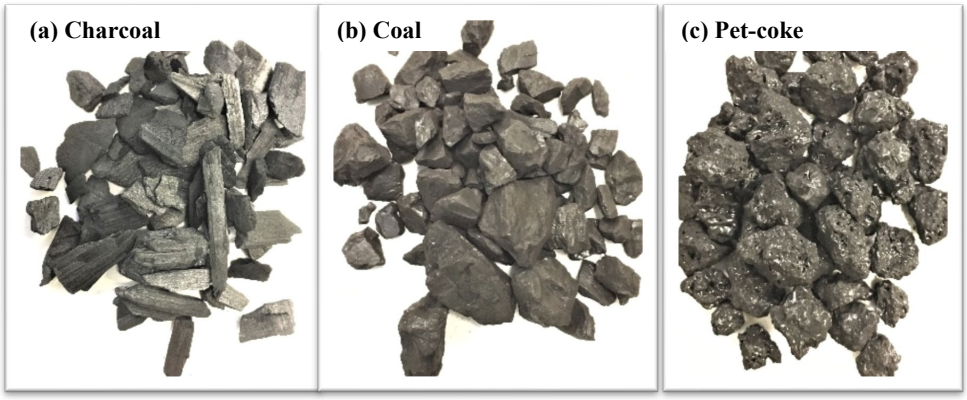

Figure 3.2.3. (a) Charcoal, (b) coal, and (c) pet-coke used for β-SiC production.

Table 3-3. Compositional analysis of coal, charcoal, and pet-coke on a dry basis.

Contents (DB-Dry Basis)	Coal (wt.%)	Charcoal (wt.%)	Pet-coke (wt.%)
Fix-C	58.36	90.32	89.8
Ash	1.06	1.62	0.2
Volatiles	40.58	8.06	10
Fix-C (after calcination)	91.9		

Table 3-4. Ash composition in calcined coal, charcoal, and pet-coke

Ash composition	Calcined coal (wt.%)	Charcoal (wt.%)	Pet-coke (wt.%)
TiO_2	0.84	0.02	0.24
Al_2O_3	25.9	0.4	7.0
Fe_2O_3	11.4	0.5	13.1
CaO	2.7	47.0	17.1
MgO	1.8	6.0	1.3
MnO	0.09	3.20	0.75
Na_2O	2.30	0.20	4.40
K_2O	0.38	13.20	0.14
P_2O_5	0.27	5.50	0.52

3.2.3.1 Thermal treatment (calcination) of coal

The amount of fix-C content in carbon materials is a significant factor in the Si production using carbothermic reduction. As **Table 3-3** shows, coal consisted of ~40% volatiles and fix-C was up to 58.36% of the total composition. This is lower compared with charcoal and pet-coke because of the high number of volatiles present in coal. The calcination was done to: (i) Remove the volatiles and increase the amount of fix-C closer to those in charcoal and pet-coke. (ii) Preserve consistency of particle size (5–10 mm) during the experiments because coal swells and increases in size during heating.

The calcination of coal was carried out in the induction furnace according to the description by Myrvågnes [40]. A representative sample of approximately 1 kg was used. Coal was heated in the graphite crucible (40 cm high and 15 cm outer diameter) at 1200 °C for 20 min in the induction furnace, after which it was removed, and a new batch of coal was added. The temperature profile for the calcination of six batches of coal is shown in **Figure 3.2.4.** The

heat-treated coal was then crushed and sieved. The final particle size distribution ranged between 5–10 mm. After calcination, the coal samples were analyzed at the D-laboratory Sweden AB (D-Lab) and the amount of fix-C present in the heat-treated coal had increased to 91.9%. **Figure 3.2.5** show the coal particles before and after calcination, before crushing them to the desired particle size for the experiments.

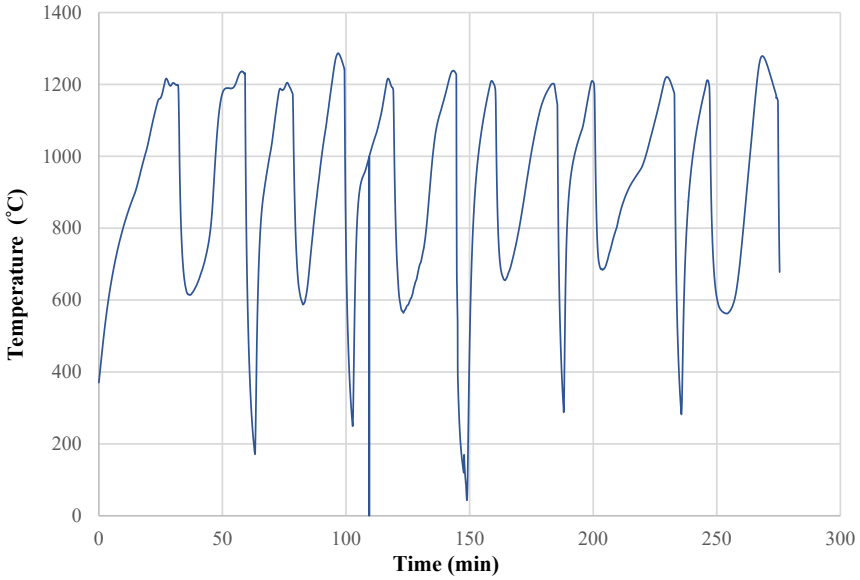

Figure 3.2.4. Temperature profile of the calcination process of six batches of coal.

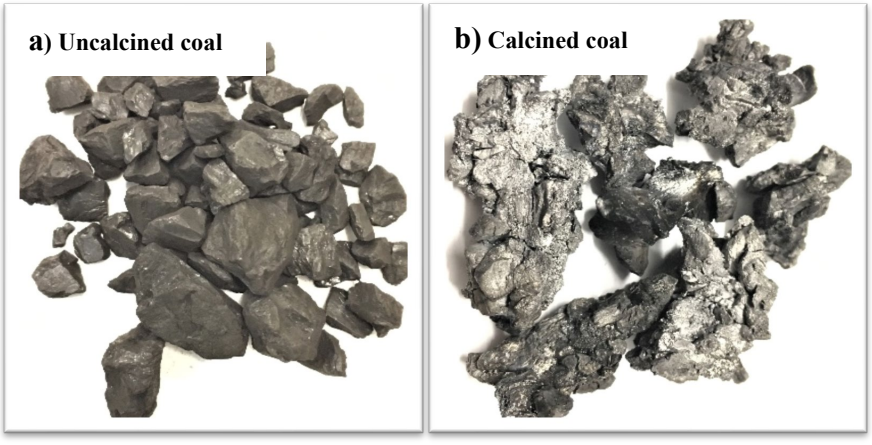

Figure 3.2.5. (a) Coal before calcination and (b) Coal after calcination.

3.2.4 Characterization of charcoal, coal, and petroleum coke

Various characterization methods were used to understand the properties and structures of the selected carbon materials. SEM and computed tomography (CT) scan of charcoal, coal, and pet-coke were performed to examine the structural variations such as pore size, shape, and cell wall thickness. In addition, the porosity and surface area of the selected carbon sources were also measured.

Porosity of the carbon material is an essential factor to produce SiC, and thereby, for the formation of Si. Higher the porosity, faster the diffusion of SiO(g) gas will be, which in turn expedites the transformation to SiC. **Figure 3.2.6** shows SEM images of a charcoal particle in the longitudinal and transverse directions, and **Figure 3.2.7** shows CT images of the different charcoal particles. These images clearly show the high porosity of charcoal. The charcoal particles selected for the analysis had similar morphologies. The pores in the charcoal particles were homogeneous, evenly distributed, and plenty. The cell walls, or the pore walls, between the pores in charcoal were thin.

Figure 3.2.8 and **Figure 3.2.9** shows SEM and CT images of the structure of a coal particle before and after the heat-treatment at 1200° C, respectively. After the heat-treatment, the coal particles were quite porous; however, the pores were no longer homogeneous. Both thick and thin cell walls were noticed in the same coal particle. SEM and CT images from two different parts of a pet-coke particle (**Figure 3.2.10** and **Figure 3.2.11**) show that it had a fewer number of pores with thicker cell walls, compared with charcoal and coal.

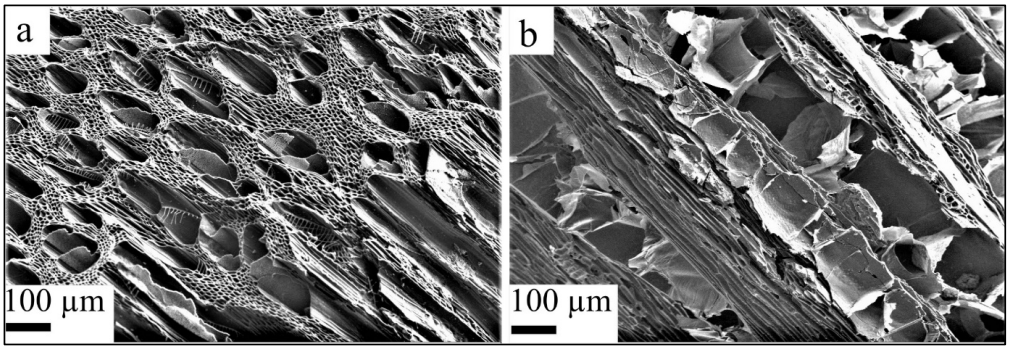

Figure 3.2.6. SEM morphology of charcoal in (a) longitudinal and (b) transverse directions.

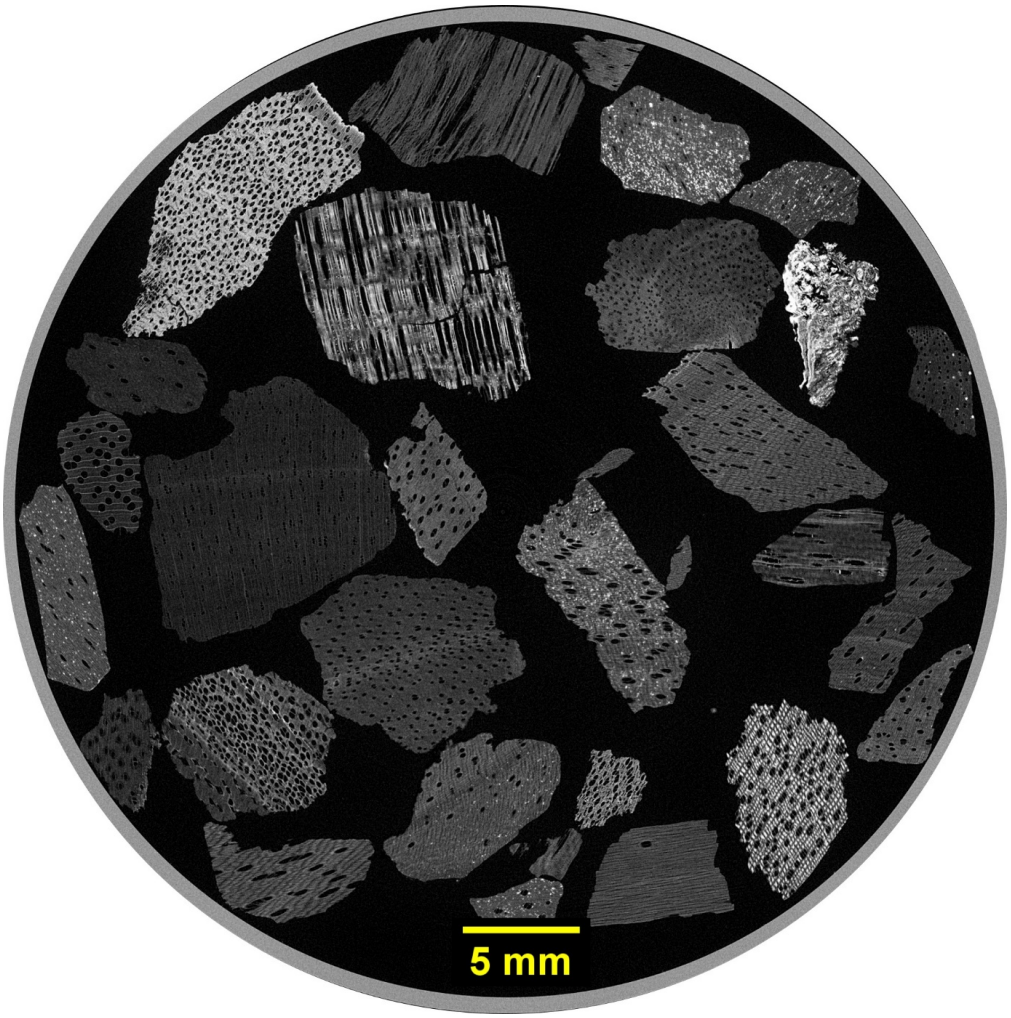

Figure 3.2.7. CT image of different charcoal particles.

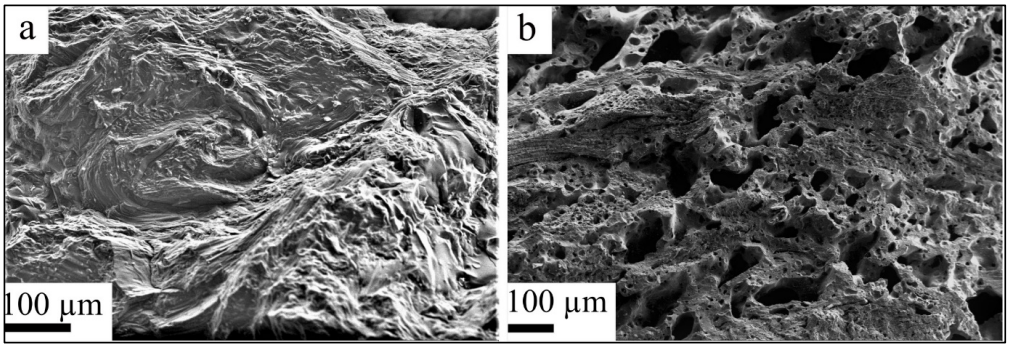

Figure 3.2.8. SEM morphology of coal (a) before and (b) after heat-treatment at 1200 °C.

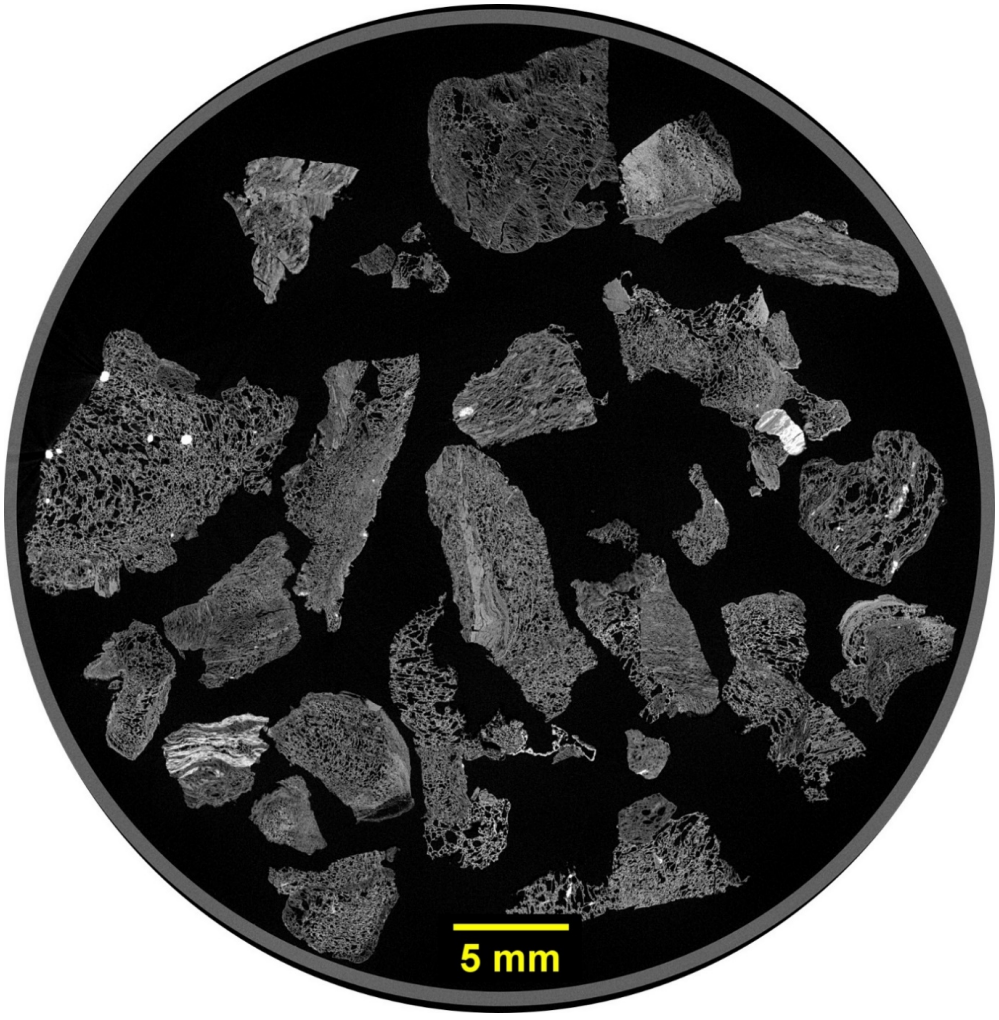

Figure 3.2.9. CT image of several heat-treated coal particles.

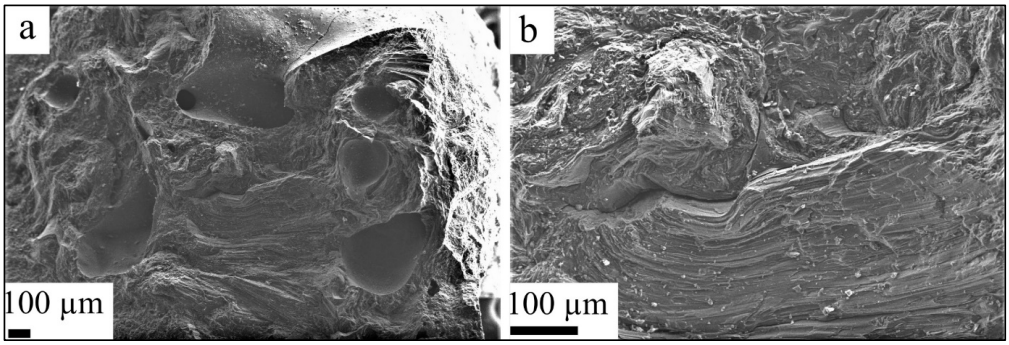

Figure 3.2.10. SEM images of two different surfaces of pet-coke.

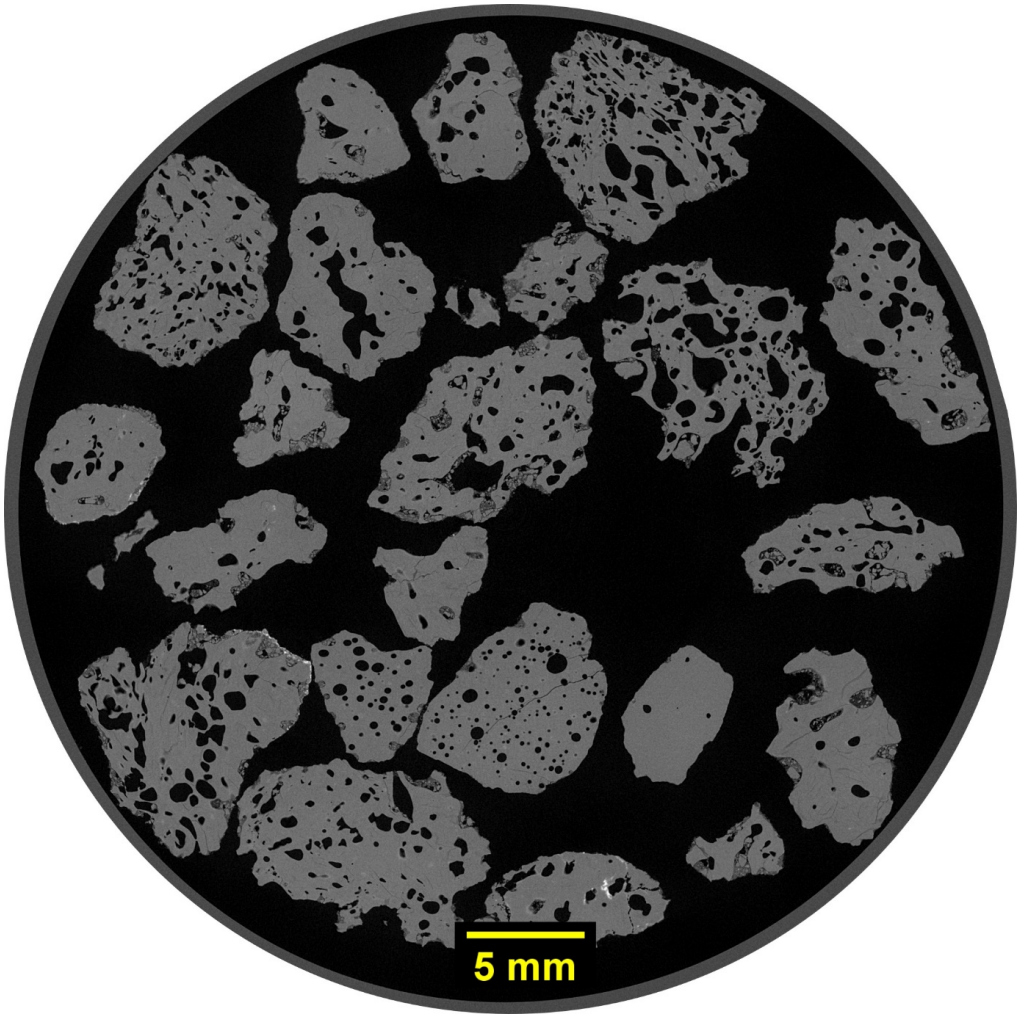

Figure 3.2.11. CT image of several pet-coke particles.

Table 3-5 gives the porosities and the surface areas of the carbon materials, which confirm that charcoal possesses good porosity and surface area, followed by coal and pet-coke. The porosity values match the micro-structural images (**Figure 3.2.6–Figure 3.2.11**) of the carbon materials. **Figure 3.2.12** shows the porosity values determined using the Brunauer–Emmett–Teller (BET) method, in comparison with the average cell wall thicknesses of charcoal, calcined (heat-treated) coal, and pet-coke. The cell wall thickness was measured from the EPMA images of the carbon materials using the ImageJ software. The cell wall thickness at different regions of the carbon particle was measured and the average cell wall thickness was calculated, which is plotted in **Figure 3.2.12**. Charcoal exhibits higher porosity and has thinner cell walls compared with calcined coal and pet-coke.

Table 3-5. Porosities and surface areas of charcoal, coal, and pet-coke.

Carbon material	Porosities (%)	Surface area (m^2/g)
Charcoal	75	98.41
Coal (calcined)	56	1.25
Pet-coke	20	0.30

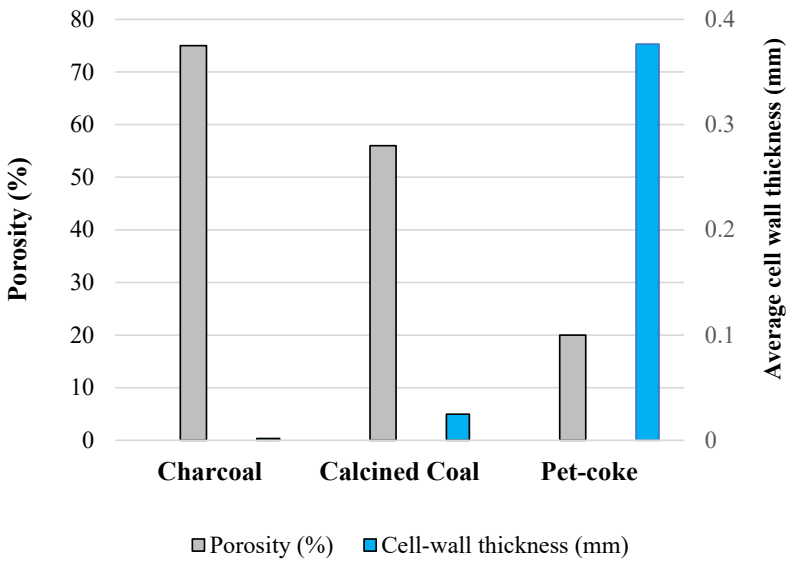

Figure 3.2.12. Porosities and cell wall thicknesses of charcoal, calcined coal, and pet-coke.

3.3 Study A: Production of β-SiC and Si in β-SiC particles

Study A comprises producing β-SiC in an induction furnace and in a graphite tube furnace. The main experiments were carried out in the induction furnace, and the small-scale, controlled experiments were performed in the graphite tube furnace to validate the induction furnace experiments. The experiments produced β-SiC from three types of carbon materials, charcoal, coal, and pet-coke, at different set temperatures.

3.3.1 Induction furnace experiments

An induction furnace was used to produce β-SiC and study the features of Si formation in the β-SiC particles formed from charcoal, coal, and pet-coke. The induction furnace works on the principle of electromagnetic induction. The furnace uses electrical energy to generate heat by inducing eddy currents within an area/material of interest. Heat is generated by the interaction between the electromagnetic field induced by the induction coil and a conductive work piece, i.e., a graphite crucible placed in the furnace. The current passing through the inductor induces a magnetic field, which oscillates with the frequency of the applied alternating current (AC). The changing magnetic field then induces eddy currents within the conductive material, following Lenz's law, counteracting the original source of the force field, eventually leading to Joule heating.

Figure 3.3.1 shows the IF75 induction furnace along with the power supply, used for the study. The induction furnace uses a high frequency current (~3000 kHz) to heat the crucible. A high purity carbon crucible (graphite) is used as a susceptor, which absorbs the electromagnetic energy and convert it into heat. The induced heat from the carbon crucible will conduct the thermal energy (reaching temperatures up to 2000 °C) to the material inside the crucible through radiation and conduction.

This furnace has a maximum power supply of 75 kW and an induction coil of total height up to 310 mm from the furnace bottom. A refractory lining provided inside the furnace reduces the risk of shorting the induction coil. A well-equipped water-cooling set is also included, which removes the excess heat generated during the furnace operation, and an exhaust system sucks out the gases that are formed during the experiments. While heating, a temperature gradient develops from the bottom to the top of the furnace because of heat loss. This temperature gradient simulates the interior conditions of an industrial Si furnace. In the industrial Si

manufacturing processes, the highest temperature is detected at the bottom region of the furnace and it decreases towards the upper part of the furnace.

Figure 3.3.1. IF75 induction furnace used for experiments, along with power supply.

A 40 cm tall graphite crucible with an inner diameter of 11.5 cm was used for holding the raw materials in the experimental set up. The advantage of using a crucible of this size is that it can hold particles whose sizes are close to those of the particles used in the industry, which is usually > 5 mm. First, either a mixture of (SiO_2 + Si) of 5–10 mm in size or pellets of (SiO_2 + SiC) were added. Carbon particles of 5–10 mm in size were then added on the top of this charge mix. On heating, SiO(g) reacts with the carbon materials. It forms SiC and elemental Si, according to **reactions (13)** and **(18).** The sketch of the induction furnace used for this study, with the graphite crucible containing raw materials placed inside, is given in **Figure 3.3.2**.

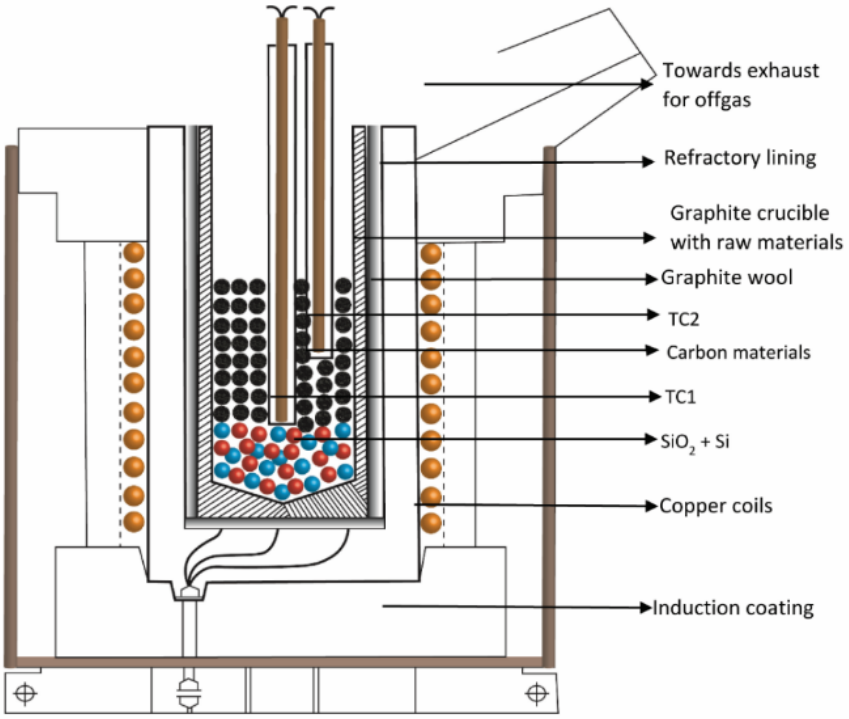

Figure 3.3.2. Sketch of induction furnace and graphite crucible containing raw materials.

3.3.1.1 Graphite crucible

A graphite crucible of grade EG-92 (**Figure 3.3.3**) was used for this study and the properties of the graphite crucible are given in **Table 3-6**. The inner diameter, height, and thickness of the crucible wall are 11.5, 40, and 2.3 cm, respectively. This graphite crucible can hold industrial sized particles of sizes up to 10–20 mm.

Figure 3.3.3. Graphite crucible used for β-SiC production in induction furnace.

Table 3-6. Quality details of the EG-92 grade graphite crucible as provided by the supplier.

Grade EG-92	
Bulk density (g/cm^3)	1.74
Hardness	70
Electrical resistivity (μΩm)	7
Porosity (%)	16
Ash content (%)	0.1
Tensile strength	15
Young's modulus	13
Coefficient of thermal expansion	1.6
Thermal conductivity	200

3.3.1.2 Thermocouple (Type C)

The type C thermocouple that can record temperatures high up to 2300 °C was used to measure the temperature at the bottom of the carbon layer. This thermocouple was made of high melting point alloys such as tungsten with 5% rhenium for the positive leg and tungsten with 26% rhenium for the negative leg. These two wires of different compositions, a sheath, and insulation materials make the complete thermocouple. When the two legs are joined together to form a thermocouple circuit, it forms a temperature difference between the two ends. This temperature difference creates a voltage and a current is formed within the circuit. This voltage is used to measure the temperature and the junction where the temperature is measured is called the hot junction. The opposite end is called the cold junction, which is connected to a voltmeter for recording the temperature during the experiments. An alumina tube and a graphite tube are used to protect the thermocouple from extreme heat, mechanical stresses, and to prevent reacting with materials inside the crucible. The thermocouple, alumina tube, and graphite tube used are shown in **Figure 3.3.4**.

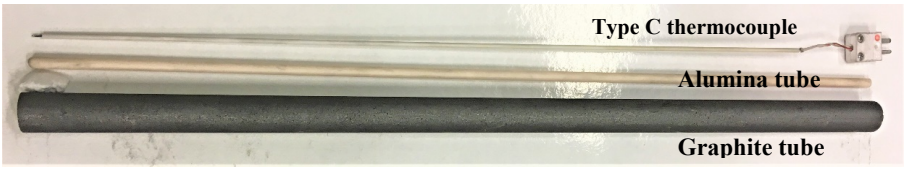

Figure 3.3.4. Thermocouple, alumina tube, and graphite tube used for the induction furnace experiments.

3.3.1.3 Thermal conditions inside induction furnace during production of β-SiC

A temperature gradient forms from the bottom to the top of the crucible in the induction furnace, which helps simulating a condition similar to that of the industrial Si furnace, where temperature at the bottom is always higher and gradually decreases towards the upper part of the furnace. To get a better understanding of the temperature distribution in the graphite crucible during the SiC production, temperatures were measured at every 1 cm from the bottom of the crucible up to the topmost part of the carbon layer. In all experiments, one thermocouple (TC1) was placed on the top of the (SiO_2 + Si) mixture and a second thermocouple (TC2) was placed in the middle portion of the carbon layer (**Figure 3.3.2**). To measure the temperature gradient inside the furnace, a third thermocouple was placed on the top of the (SiO_2 + Si) mixture and a second thermocouple was placed at the very bottom of the crucible. Once the temperature measured by TC1 reached the target temperature, the thermocouple that was positioned at the very bottom was pulled up, while recording the temperatures at every 1 cm.

Figure 3.3.5 shows the vertical temperature gradient formed inside the crucible from the top to the bottom during the SiC production from charcoal, coal, and pet-coke at 1750 °C (constant weight experiments). In this case, a mixture of (SiO_2 + Si) was filled up to a height of 5–6 cm in the crucible; the temperature measured at that region was around 1799–1783 °C. Carbon material of desired amount was placed on top of this mixture. The temperature measured at this region ranged from 1760 to 1776 °C.

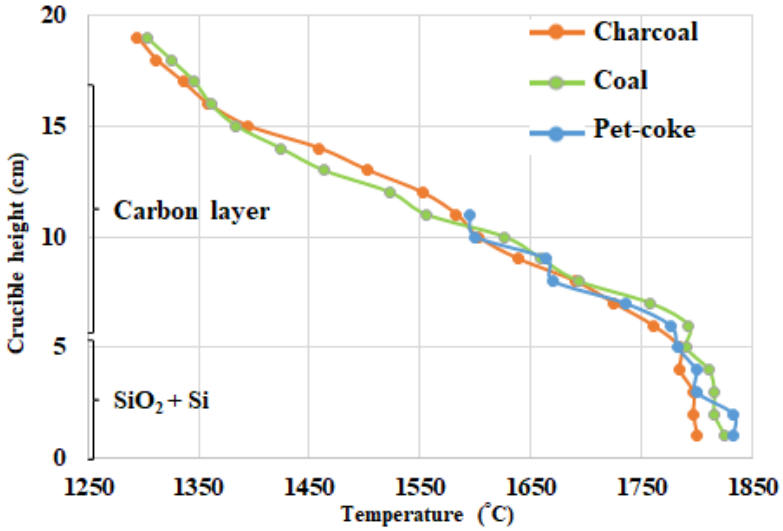

Figure 3.3.5. Vertical temperature gradients inside the crucible from top to bottom during constant weight experiments using charcoal, coal, and pet-coke.

Figure 3.3.6 shows the vertical temperature gradient formed inside the crucible from the top to the base, from the experiments with pet-coke at 1750 °C and 1800 °C (F1-IF75 and F2-IF75 **Table 3-12**). For the experiment conducted at 1750 °C (F1-IF75), the temperature measured 5–6 cm away from the crucible base, i.e., the position where the carbon layer starts, was around 1776 °C. Whereas, for the experiment conducted at 1800 °C (F2-IF75), the temperature measured at the same location was around 1802 °C. In a similar experimental setup, Jusnes [109] have measured the vertical temperature gradient inside the crucible; the temperature gradient data obtained in the present study is similar to the one recorded in their study.

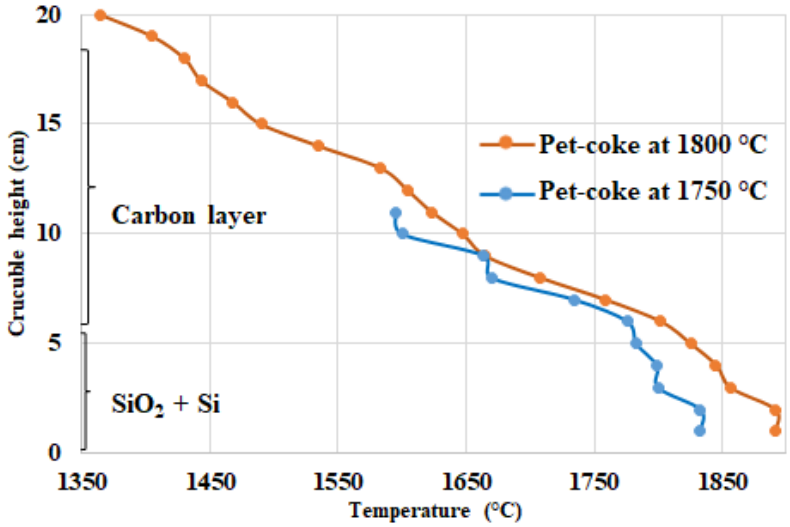

Figure 3.3.6. Vertical temperature gradients inside the crucible from top to base during the constant weight experiments using pet-coke at 1750 °C and 1800 °C.

Once the temperatures measured by TC1 attained a set target temperature, the experiment was held at this constant temperature for 1 h for all the experiments. **Figure 3.3.7** shows examples of temperature profiles of SiC production experiments using charcoal, coal, and pet-coke at 1750 and 1800 °C. The red line represents the temperature measured by TC1 at the top portion of the (SiO_2 + Si) mix, which was the experiment target temperature, and the blue line shows the temperature measured by TC2 at the middle portion of the carbon layer. The temperature profiles show that the temperature at a position 4–5 cm above the charge mix (in between the carbon layer) was always 150 °C lower than the temperature at the top of the charge mix and that a vertical temperature gradient existed inside the induction furnace for all of the experiments, simulating conditions similar to an industrial Si furnace.

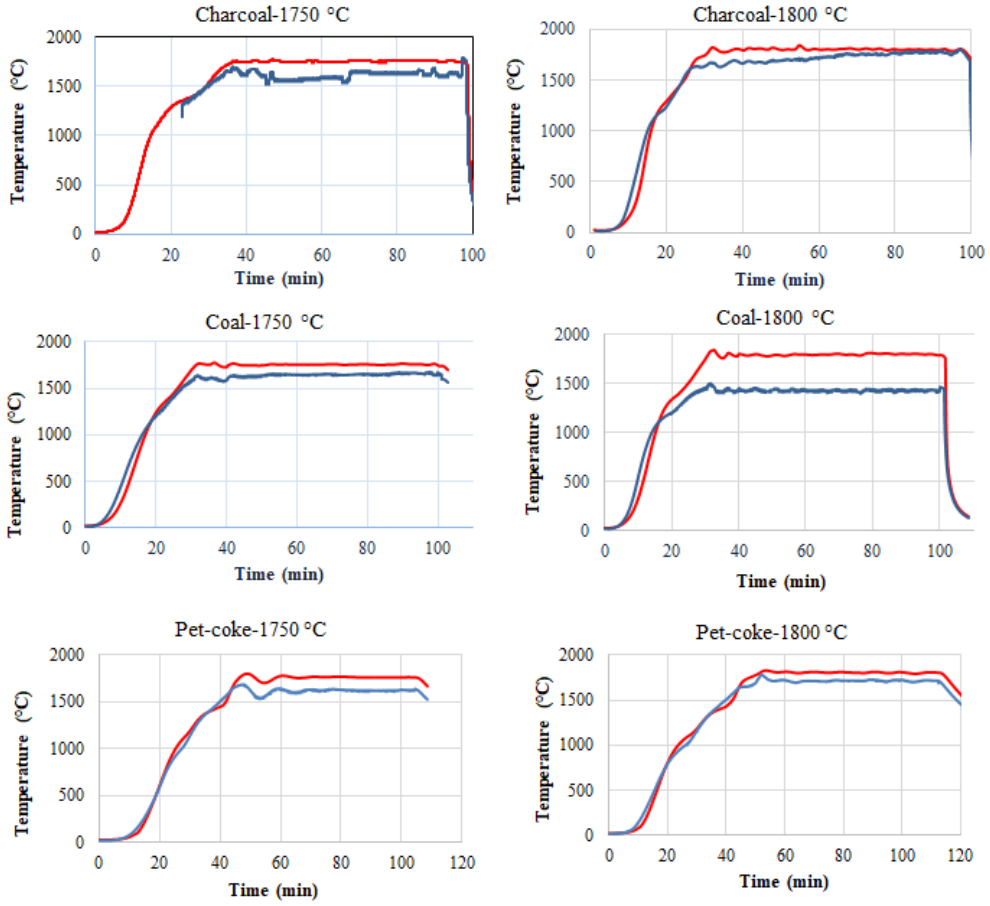

Figure 3.3.7. Temperature profiles of SiC production experiments with charcoal, coal, and pet-coke at 1750 and 1800 °C. Red and blue lines represents temperatures measured by TC1 (at top of the charge mix) and TC2 (at middle portion of the carbon layer), respectively.

Two types of experiments were performed in the induction furnace; constant volume and constant weight experiments, which are described below. For the constant volume method, a 10 cm thick carbon layer was used for all the experiments, and for the constant weight experiments, weight of the raw materials were kept constant, according to the stoichiometry. The main purpose of conducting two sets of experiments was to compare variations in the amount of SiC thus produced. A complete overview of the experiments performed in the induction furnace is presented in **Figure 3.3.8**.

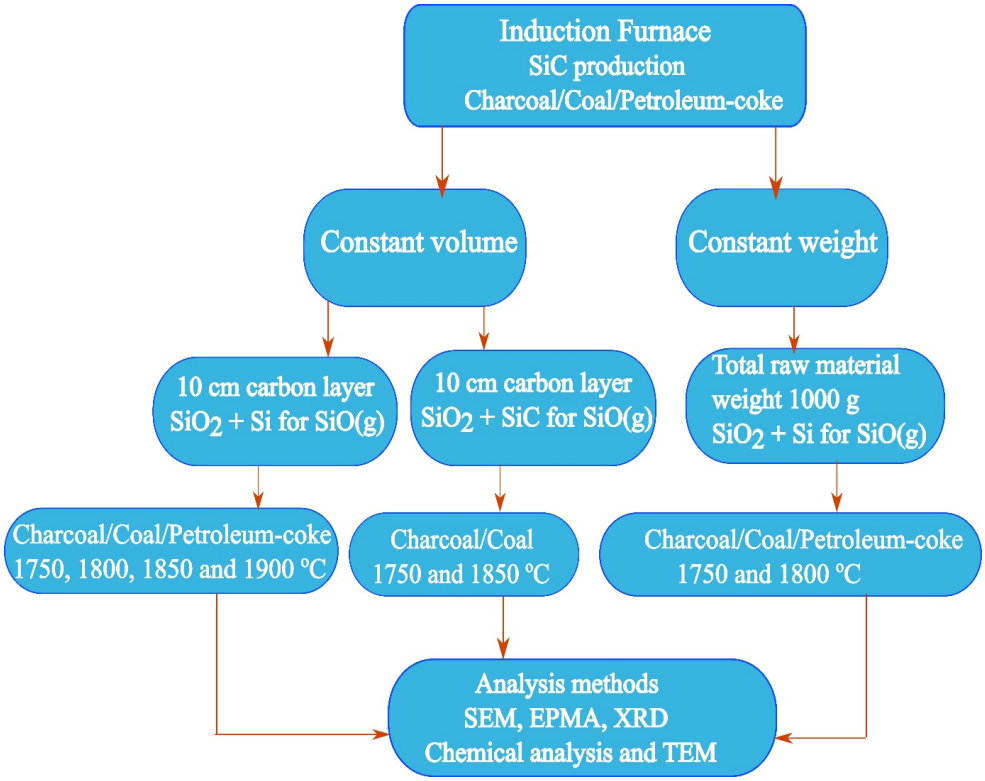

Figure 3.3.8. Overview of experiments performed in induction furnace.

3.3.1.4 Constant volume experiments

First a mixture of (SiO_2 + Si) of 5–10 mm in size were added in the crucible as raw materials for generating SiO(g) according to **reaction (16)**. A 10 cm thick layer of carbon particles of 5–10 mm in size was added on top of the (SiO_2 + Si) mixture, to facilitate the conversion to β-SiC. These experiments are termed as the constant volume experiments.

The carbon materials differ in their densities, and the amount of (SiO_2 + Si) mixture needed to form a 10 cm thick layer of each of the three different carbon materials varied according to the stoichiometry, which is summarized in **Table 3-7**. Therefore, the heights of the (SiO_2 + Si) mix in the crucible also differed between the experiments conducted with each of these carbon materials. However, the position of the thermocouple TC1 was always on top of the charge mix layer, which is where the SiO(g) is generated.

The same experimental setup was used to generate SiO(g) using the other raw material, (SiO_2 + SiC) pellets. Here also a constant volume of carbon materials was used, i.e., a 10 cm

thick layer of carbon materials was added on top of the (SiO_2 + SiC) pellets. TC1 was placed on the top of the (SiO_2 + Si) mixture/(SiO_2 + SiC) pellets to measure the temperature at the top of the charge mix. TC2 was placed in the middle portion of the carbon layer (4–5 cm above the charge mix layer) to assess the temperature distribution in the carbon layer. The schematic representation of the complete experimental set up used for β-SiC production in the graphite crucible, along with distribution of the raw materials and position of the thermocouples is shown in **Figure 3.3.9**.

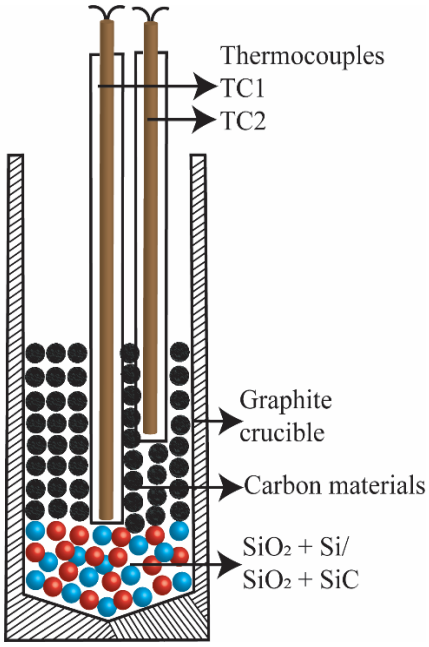

Figure 3.3.9. Schematic representation of complete experimental set up in graphite crucible for β-SiC production.

3.3.1.4.1 Experimental conditions set for the constant volume experiments

The quantities of carbon materials utilized to form a 10 cm thick layer and the corresponding quantities of SiO(g) generating charge mixes (SiO_2 + Si) of 5–10 mm in size) are presented in **Table 3-7**. Each of the experiments was labeled using a combination of alphabets and numbers based on the carbon materials and target temperatures used; A, B, and C denote charcoal, coal, and pet-coke, respectively, and the numbers 1–4 denote the different target temperatures. The target temperatures were set differently for the various experiments. The graphite crucible filled with the charge mix and carbon materials was placed in the induction furnace and was heated at a rate of 25 °C/min. Once the target temperature was attained it was held constant for 1 h.

The conditions set for each of these experiments are described in **Table 3-7.** The experiment performed at 1900 °C with charcoal (A4-IF75,**Table 3-8**) was stopped after holding it at the target temperature for 15 min, as the thermocouples malfunctioned during the experiment. The molar ratios of the raw materials SiO_2:Si:C and SiO_2:SiC:C were calculated based on stoichiometry (see Appendix A).

Table 3-7. Quantities of carbon materials and (SiO_2 + Si) used for constant volume experiments.

Experiment codes	Carbon materials	Quantity used to fill 10 cm in crucible (g)	SiO_2 + Si (g)
A	Charcoal	247	(309 + 144) = 453
B	Coal	397	(496 + 232) = 728
C	Pet-coke	705	(882 + 412) = 1294

Table 3-8. Experimental conditions set for constant volume experiments using (SiO_2 + Si).

Carbon material and experiment number	Molar ratio of the charge mixture (SiO_2:Si:C) of size 5–10 mm	Target temperature (°C)	Holding time (min)
Charcoal, A1-IF75	1:1:4	1750	60
Charcoal, A2-IF75	1:1:4	1800	60
Charcoal, A3-IF75	1:1:4	1850	60
Charcoal, A4-IF75	1:1:4	1900	15
Coal, B1-IF75	1:1:4	1750	60
Coal, B2-IF75	1:1:4	1800	60
Coal, B3-IF75	1:1:4	1850	60
Coal, B4-IF75	1:1:4	1900	60
Pet-coke, C1-IF75	1:1:4	1750	60
Pet-coke, C2-IF75	1:1:4	1800	60
Pet-coke, C3-IF75	1:1:4	1850	60
Pet-coke, C4-IF75	1:1:4	1900	60

Similar experiments were conducted using pellets of (SiO_2 + SiC) as charge mix to generate SiO(g). For these experiments only two of the carbon materials were utilized, charcoal and coal. These experiments were also labeled using alphabets and numbers. G and H denote charcoal and coal, respectively, and the numbers 1–2 denote the two different temperatures at

which the experiments were conducted. The quantities of both charcoal and coal used to form a 10 cm thick layer and the corresponding quantities of the charge mix (pellets of (SiO_2 + SiC)) are presented in **Table 3-9**. The conditions set for the constant volume experiments using (SiO_2 + SiC) are given in **Table 3-10**.

Table 3-9. Quantities of carbon materials and (SiO_2 + SiC) pellets used for constant volume experiments.

Experiment codes	Carbon materials	Quantity used to fill 10 cm in crucible (g)	SiO_2 + SiC pellets (g)
G	Charcoal	260	550
H	Coal	409	550

Table 3-10. Experimental conditions set for constant volume experiments using pellets of (SiO_2 + SiC).

Carbon material and experiment number	Molar ratio of the charge mixture (SiO_2:SiC:C) of size 5–10 mm	Target temperature (°C)	Holding time (min)
Charcoal, G1-IF75	2:1:6	1750	60
Charcoal, G2-IF75	2:1:6	1850	60
Coal, H1-IF75	2:1:6	1750	60
Coal, H2-IF75	2:1:6	1850	60

3.3.1.5 Constant weight experiments

A second set of experiments was performed, keeping the sum of the weights of the raw material (SiO_2 + Si) and carbon material equal to 1000 g. The ratio of the raw materials used was calculated according to the stoichiometry. These experiments were termed as the constant weight experiments.

3.3.1.5.1 Experimental conditions set for constant weight experiments

A mixture of (SiO_2 + Si) of desired quantity was used for generating SiO(g) in this set of experiments. The experiment codes D, E, and F denote the carbon materials used, which are charcoal, coal, and pet-coke, respectively. **Table 3-11** shows the quantities of raw materials utilized in the experiments to attain a constant weight. The experiments were conducted at two

temperatures, 1750 and 1800 °C. The temperature conditions set for these experiments along with their holding times are given in **Table 3-12.**

Table 3-11. Quantities of carbon materials and (SiO_2 + Si) used for constant weight experiments.

Experiment codes	Carbon materials	Weight (g)	Height of the layer of materials in the crucible (cm)	SiO_2 + Si (g)
D	Charcoal	400	16	(441+ 206) = 640
E	Coal	400	11.5	(441+ 206) = 640
F	Pet-coke	400	6.5	(441+ 206) = 640

Table 3-12: Experimental conditions set for constant weight experiments using (SiO_2 + Si).

Carbon material and experiment number	Molar ratio of the charge mixture (SiO_2:Si:C) of size 5–10 mm	Target temperature (°C)	Holding time (min)
Charcoal, D1-IF75	1:1:4	1750	60
Charcoal, D2-IF75	1:1:4	1800	60
Coal, E1-IF75	1:1:4	1750	60
Coal, E2-IF75	1:1:4	1800	60
Pet-coke, F1-IF75	1:1:4	1750	60
Pet-coke, F2-IF75	1:1:4	1800	60

3.3.2 Graphite tube furnace experiments: small-scale set up to produce β-SiC

A vertical graphite tube furnace as shown in **Figure 3.3.10** (Thermal Technology Model 1000-3560-FP20) was used to validate the induction furnace experiments and also to study the features of Si produced in β-SiC in a more controlled environment. This furnace can operate up to 2600 °C in an inert atmosphere of Ar or He. The furnace is equipped with a thermocouple of type C that can measure temperatures up to 1500 °C and a pyrometer that measures the temperatures above 1500 °C. A gas analyzer (ABB 2020) is connected to the off-gas lance to detect the concentrations of certain types of gases that form during the experiments. The furnace chamber is a graphite cylinder that is 265 mm tall with a diameter of 150 mm and surrounded by graphite heating elements. A water-cooling system made of copper tubes that circulates water is mounted on the top of the graphite chamber to remove the heat generated during the experiments.

Figure 3.3.10. Graphite tube furnace (Thermal Technology Model 1000-3560-FP20).

The graphite tube and the graphite crucible used for the experiments are shown in **Figure 3.3.11**, along with an illustration of the experimental set up inside. A 250 mm tall graphite tube with an outer diameter of 95 mm that could be placed inside the furnace was used for the experimental set up. The graphite tube consists of two parts, a reaction chamber at the bottom and a condensation chamber on top of it. A small graphite crucible (dimensions: height - 65 mm, outer diameter - 40 mm) is placed inside the reaction chamber to hold the raw materials. First, the graphite crucible is filled with the desired quantity of a mixture of (SiO_2 + Si) or pellets of (SiO_2 + SiC). A graphite sieve with 2 mm holes (**Figure 3.3.11**, inset) is placed on top of the charge mix to separate the carbon particles from the SiO(g) source.

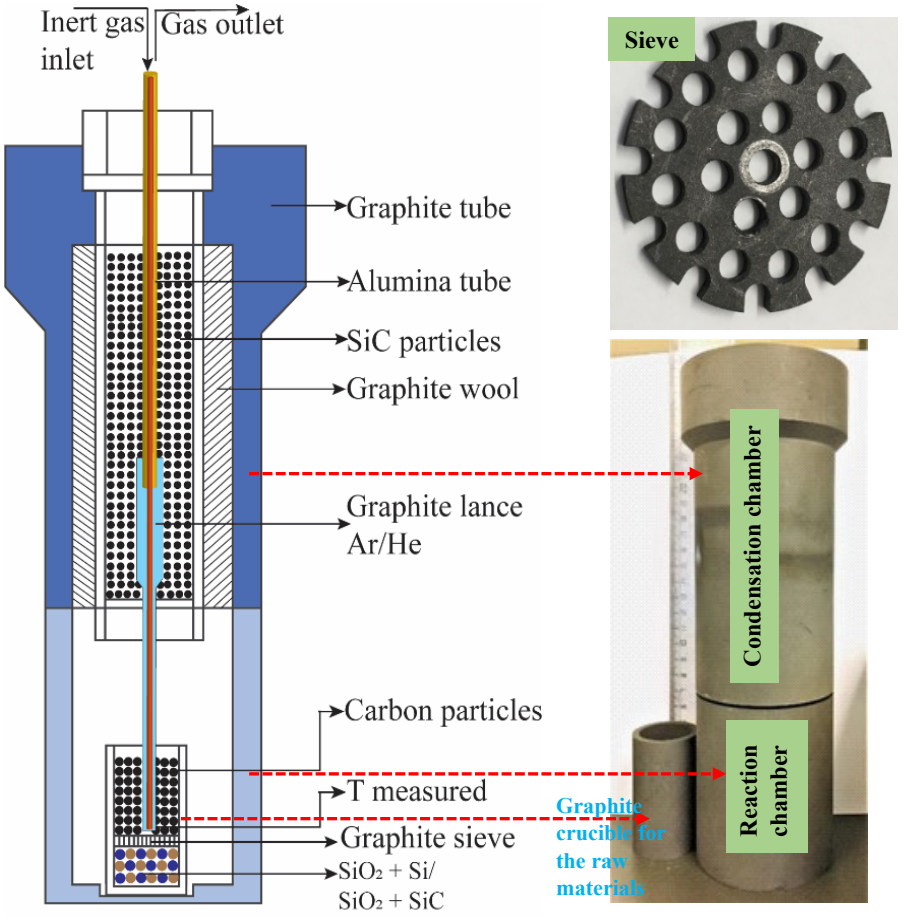

Figure 3.3.11. Schematic illustration of experimental set up inside the graphite tube furnace. Inset shows the graphite sieve with 2 mm holes. Graphite tube (reaction and condensation chambers) and the small graphite crucible placed inside it are also shown.

An alumina tube attached with a graphite lance was inserted through the condensation chamber into the reaction chamber, and was mounted on top of the charge mix, to flush inert gas into the system. A type C thermocouple was also inserted through the alumina tube through the gas lance and placed on top of the sieve. This was to measure the temperature at the top of the charge mix, where SiO(g) is generated. The desired quantity of carbon materials was then added on top of the sieve to be converted to β-SiC and Si. The graphite crucible containing the raw materials was carefully inserted into the graphite chamber for heating. The condensation chamber was then filled with SiC particles of 5 mm in size. This was done to fix the graphite lance in place and to capture the condensation products. Once the target temperature was attained, it was held for 1 h and then let to cool till it reached 25 °C. The temperature close to

the bottom of the graphite chamber was measured and there was a temperature difference of around 15 °C at every 1 cm from the bottom to the top of the graphite chamber [103]. Therefore, to get a desired temperature at the top of the charge mix, a slightly higher furnace set point temperature was used. **Figure 3.3.12** shows an example of the temperature profile inside the graphite tube furnace. The profile shows temperature pattern of the experiment with charcoal and the (SiO_2 + Si) mixture, conducted at a target temperature of 1755 °C. The temperature inside the furnace reached the target value of 1755 °C at the furnace set point temperature of 1790 °C.

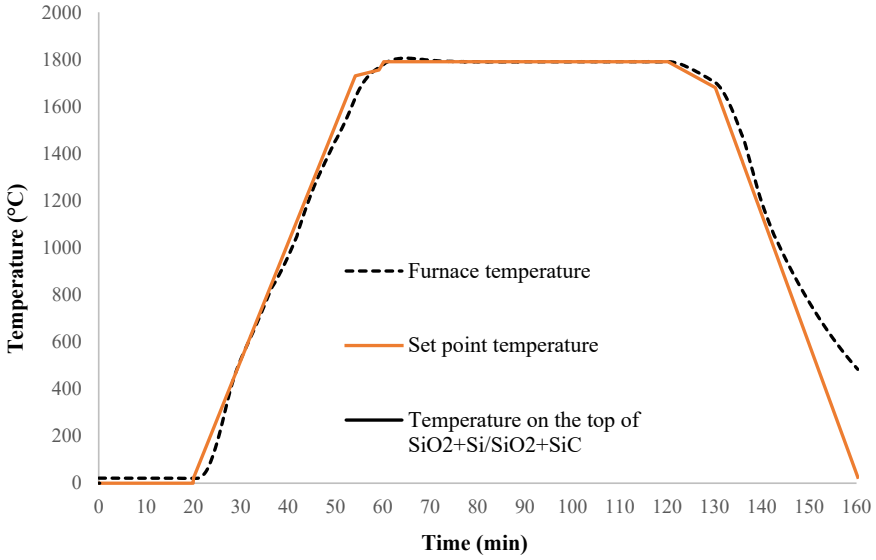

Figure 3.3.12. Temperature profile of experiment with charcoal and (SiO_2 + Si) mixture.

Figure 3.3.13 shows magnified image of the temperature profile from **Figure 3.3.12**, showing the temperature variations at 1740–1810 °C. When heated, the furnace temperature (dotted line) rises as expected and reaches the target set point temperature (1790 °C, orange line) in about 57 min. It continues to rise for the next 4–5 min reaching up to 1805 °C, after which point, it comes down to the set point temperature taking about 10 min and stays at this temperature until the experiment is finished. Meanwhile, the temperature at the top of the (SiO_2 + Si)/(SiO_2 +SiC) mixture that is measured by the type C thermocouple (black solid line) also increases up to 1771 °C and after 10–13 min, it drops down to ~1750 °C, i.e., the desired target temperature at the position of the graphite sieve. Similar temperature patterns were observed in all experiments, the only difference between them being the various set point temperatures assigned for each experiment. **Table 3-13** gives the furnace set point temperatures

and the temperatures measured at the top of the graphite sieve, for all experiments conducted to produce β-SiC.

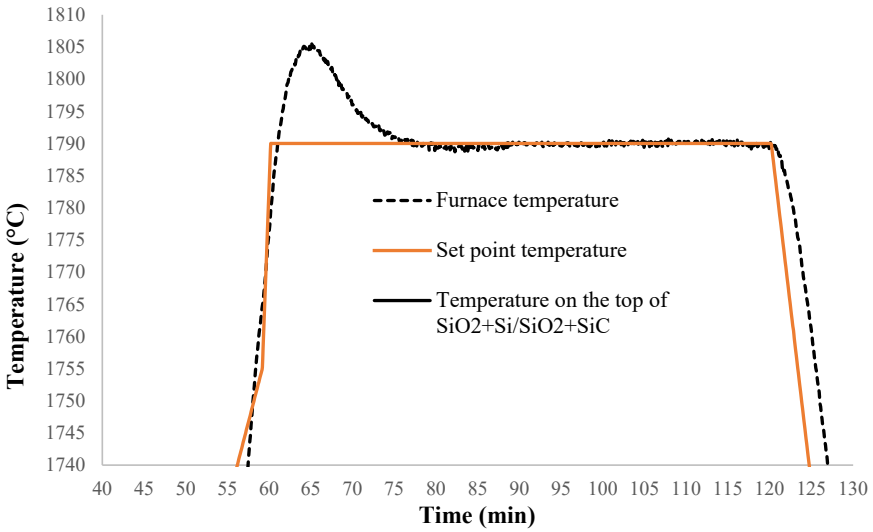

Figure 3.3.13. Variations in temperatures inside the furnace (measured by pyrometer) and at top of the charge mix (measured by thermocouple). The experiment was conducted at the set point temperature of 1790 °C.

Table 3-13. Experimental conditions for β-SiC production in graphite tube furnace.

Expt. name	Carbon material	Quantity of carbon (g)	Charge for SiO(g) generation	Quantity of charge (g)	Set point temperature (°C)	Temperature at top of the charge mix (°C)
A5	Charcoal	7	SiO_2 + Si	10 + 5	1840	1822
A6	Charcoal	7	SiO_2 + Si	10 + 5	1790	1755
A7	Charcoal	7	SiO_2 + Si	10 + 5	1725	1674
B5	Coal	7	SiO_2 + Si	10 + 5	1790	1765
B6	Coal	7	SiO_2 + Si	10 + 5	1725	1686
C5	Pet-coke	12	SiO_2 + Si	10 + 5	1775	1748
C6	Pet-coke	12	SiO_2 + Si	10 + 5	1725	1694
C7	Pet-coke	12	SiO_2 + Si	10 + 5	1875	1832
C8	Pet-coke	12	SiO_2 + Si	10 + 5	1875	1836
G3	Charcoal	10	SiO_2 + SiC	10	1775	1756
H3	Coal	10	SiO_2 + SiC	10	1775	1750
I1	Pet-coke	12	SiO_2 + SiC	10	1775	1752

3.4 Study B: Transformation of β-SiC to α-SiC

In Study B, experiments were conducted to evaluate the transformation of β-SiC (derived from charcoal, coal, and pet-coke) to α-SiC. The same vertical graphite tube furnace used in Study A (Thermal Technology Model 1000-3560-FP20) was used for this set of experiments. The graphite tube and the graphite crucible used in the production of β-SiC were used again to form α-SiC.

The heat-treatment of β-SiC particles in the graphite tube is represented schematically in **Figure 3.4.1**. The β-SiC particles are heated inside the reaction chamber to convert them to α-SiC. The particles chosen for the experiment were sized 5–10 mm in diameter and loaded into the small graphite crucible. The heating was done in a controlled atmosphere using a mixture of an inert gas and CO. The purpose of using CO gas was to simulate an atmosphere similar to the industrial Si production. There is however no literature that suggests that gas atmospheres are vital for the conversion of β-SiC to α-SiC. The gas lance inserted through the condensation chamber into the reaction chamber was used to pump gas during heat-treatment.

The condensation chamber was filled with coal particles of 2–4 mm in size to capture the volatile matter, especially the SiO gas formed during heating, and they also kept the gas lance fixed. Volatiles and condensed SiO gas formed inside the chamber can clog the off-gas system and damage the filters, besides compromising the gas collection system. Therefore, the compounds developed in this chamber were collected for safety purposes alone and not considered in this study.

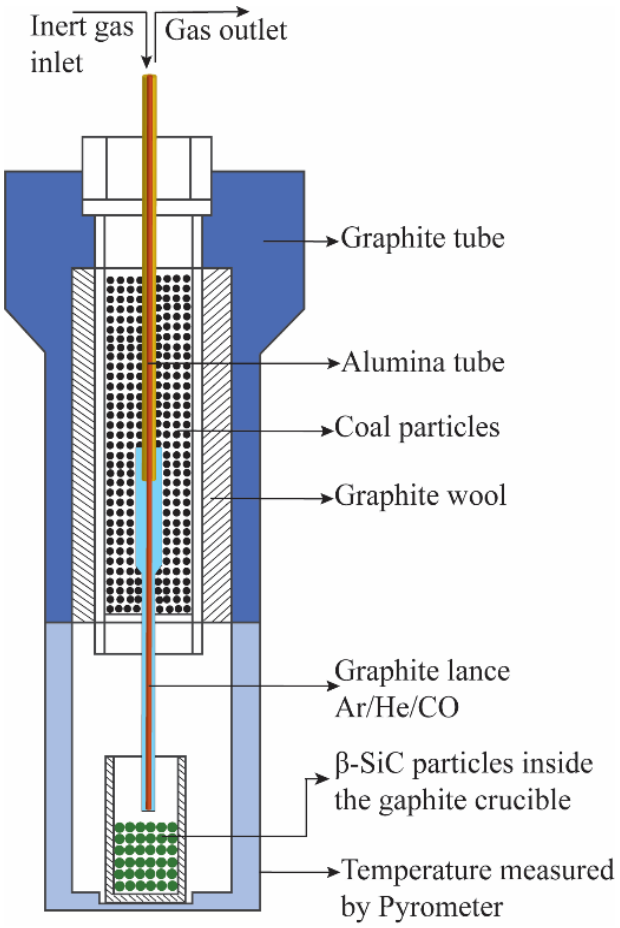

Figure 3.4.1. Schematic cross-section of experimental set up in graphite tube to form α-SiC.

Prior to heating, the furnace chamber was purged with Ar gas flowing at rate of 0.5 L/min for 20 min, followed by evacuation to a residual pressure around 0.240 mbar. The graphite cylinder was then filled with Ar at 1 atm pressure to remove the moisture and air components adsorbed by the graphite parts of the furnace. As soon as the heating procedure began, a mixture of 0.5 L/min CO and 0.3 L/min Ar was injected simultaneously into the reaction chamber where the small graphite crucible containing β-SiC particles was placed. The furnace was heated to reach the target temperature at the rate of 10 °C/min. Once the temperature reached the target value, it was held for 1 h.

Figure 3.4.2 shows an example of temperature profile of the experiment. It shows the temperature evolution during the experiment with charcoal-derived β-SiC, performed at 2450 °C. While heating the β-SiC particles, the inert gas was switched from Ar to He for temperatures

higher than 1800 °C, to prevent ionization of Ar at higher temperatures and for safe operation of the furnace. As the heating experiments were conducted at extreme temperatures (2100–2450 °C), they were measured using a pyrometer kept outside the reaction chamber. Based on earlier records, a difference of ~15 °C exists between the temperatures measured by the pyrometer kept outside the reaction chamber and the one that is located inside the reaction chamber, which measures the temperature at the bottom of the graphite crucible [103].

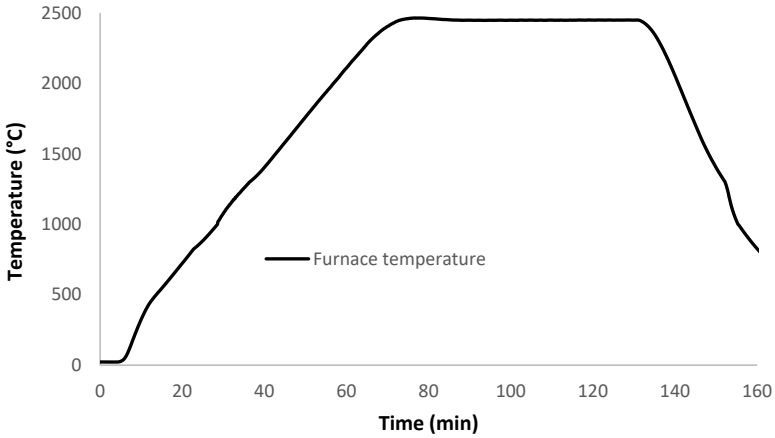

Figure 3.4.2. Evolution of temperature inside graphite tube furnace during conversion of β-SiC to α-SiC.

3.4.1 Experimental conditions set for transformation to α-SiC

The β-SiC particles obtained from the induction furnace experiments conducted at 1900 °C using (SiO_2 + Si) were further used to study the conversion of β-SiC to α-SiC. Two types of β-SiC samples were collected after the induction furnace experiments with charcoal, coal, and pet-coke. The first type was collected from the middle layer (M) of the crucible, which contained partly and completely converted β-SiC. The samples had some unreacted carbon as well as a small portion of Si in them. The other type of sample was collected from the lower layer (L), which had β-SiC with elemental Si present in it. These two types of β-SiC samples derived from charcoal, coal, and pet-coke were used for analyzing the process of transformation of β-SiC to α-SiC. Another set of experiments was performed with β-SiC collected from experiments conducted at 1750 °C using pellets of (SiO_2 + SiC). These particles did not have elemental Si in them. These experiments were performed to substantiate the influence of Si in forming α-SiC. The conditions set for each of these experiments are given in **Table 3-14** to **Table 3-17**.

In the case of pet-coke, β-SiC particles obtained after the induction furnace experiments conducted at 1900 °C alone were not enough to perform the heat-treating experiments. Therefore, samples produced by the experiments conducted both at 1850 and 1900 °C were used for the heat-treatment of β-SiC converted from pet-coke (**Table 3-16**). The β-SiC samples from both the experiments were combined for each layer and the total percentage of Si in the middle and lower layers were estimated by chemical analysis.

Table 3-14. Experimental conditions set for charcoal-derived β-SiC particles.

Expt. code	Raw materials collected at 1900 °C (SiO_2 + Si) for SiO(g))	Quantity of Si in β-SiC (wt.%)	Target temperature (°C)
A1-Re-M	β-SiC from M	9	2100
A2-Re-L	β-SiC from L	39	2100
A3-Re-M	β-SiC from M	9	2300
A4-Re-L	β-SiC from L	39	2300
A5-Re-M	β-SiC from M	9	2450
A6-Re-L	β-SiC from L	39	2450

Table 3-15. Experimental conditions set for coal-derived β-SiC particles.

Expt. code	Raw materials collected at 1900 °C (SiO_2 + Si) for SiO(g))	Quantity of Si in β-SiC (wt.%)	Target temperature (°C)
B1-Re-M	β-SiC from M	9	2100
B2-Re-L	β-SiC from L	24	2100
B3-Re-M	β-SiC from M	9	2300
B4-Re-L	β-SiC from L	24	2300
B5-Re-M	β-SiC from M	9	2450
B6-Re-L	β-SiC from L	24	2450

Table 3-16. Experimental conditions set for pet-coke-derived β-SiC particles.

Expt. code	Raw materials collected at 1850 and 1900 °C (SiO_2 + Si) for SiO(g))	Quantity of Si in β-SiC (wt.%)	Target temperature (°C)
C1-Re-M	β-SiC from M	8.7	2100
C2-Re-L	β-SiC from L	18.8	2100
C3-Re-M	β-SiC from M	8.7	2300
C4-Re-L	β-SiC from L	18.8	2300
C5-Re-M	β-SiC from M	8.7	2450
C6-Re-L	β-SiC from L	18.8	2450

Table 3-17. Experimental conditions set for charcoal-derived β-SiC particles with no Si present in them.

Expt. code	Raw materials collected at 1750 °C (SiO_2 + SiC) for SiO(g))	Quantity of Si in β-SiC (wt.%)	Target temperature (°C)
G1-Re	β-SiC	0	2100
G2-Re	β-SiC	0	2180
G3-Re	β-SiC	0	2300
G4-Re	β-SiC	0	2450

A few selected experiments were performed to check the reproducibility of β-SiC to α-SiC transformation. For these experiments only He was used in place of the mixture of inert gas and CO. As previously mentioned, the purpose of using CO gas was to simulate the controlled atmosphere in industrial Si production. Here He alone was used to check whether the gas atmosphere makes any difference during the transformation of β-SiC to α-SiC. The heating rate used was 50 °C/min, which was slightly different than the previous experiments. The experimental set up used was same as that shown in **Figure 3.4.1**. The details of the experimental set up are given in **Table 3-18**.

Table 3-18. Conditions set for replicated experiments to convert β-SiC to α-SiC.

Expt. Code	Raw materials	Quantity of Si in β-SiC (wt.%)	Target temperature (°C)
H1-Re	β-SiC-Charcoal using (SiO_2 + SiC)	0	2100
H2-Re	β-SiC-Charcoal using (SiO_2 + SiC)	0	2200
H3-Re	β-SiC-Charcoal using (SiO_2 + Si)	10	2100
H4-Re	β-SiC-Charcoal using (SiO_2 + Si)	10	2200
H5-Re	β-SiC-Coal using (SiO_2 + Si)	24	2100
H6-Re	β-SiC-Coal using (SiO_2 + Si)	24	2200
H7-Re	β-SiC-Pet-coke using (SiO_2 + Si)	11.29	2300
H8-Re	β-SiC-Pet-coke using (SiO_2 + Si)	11.89	2300

3.5 Transformation of β-SiC to α-SiC in hot-press furnace.

A set of experiments was carried out in a hot-press furnace to evaluate whether pressure and time duration have any effect on the transformation of β-SiC to α-SiC. Charcoal-derived β-SiC particles with 9 wt.% Si, produced at 1900 °C in the induction furnace, was used for the experiments. Inside the hot-press furnace, there is a graphite cylinder of diameter 25 mm that has graphite punches on each end. A dense graphite insulator surrounds the graphite cylinder. The schematic representation of the hot-press furnace is given in **Figure 3.5.1**, and the cross-section of the graphite dies with position of its punches before and after the experiments is shown in **Figure 3.5.2**, reprinted from Juven [110]. β-SiC particles of around 2–3 g were crushed to fine powder and then poured into the graphite cylinder. The mold containing the β-SiC powder was then inserted into the hot-press. The furnace was at first evacuated and then filled with Ar. This process was repeated for three times, until it reached the ambient pressure. An outlet was then opened to allow a slow flow of Ar through the furnace. The pressing ram was then used to apply a uniaxial pressure on the graphite mold to hot press the β-SiC sample.

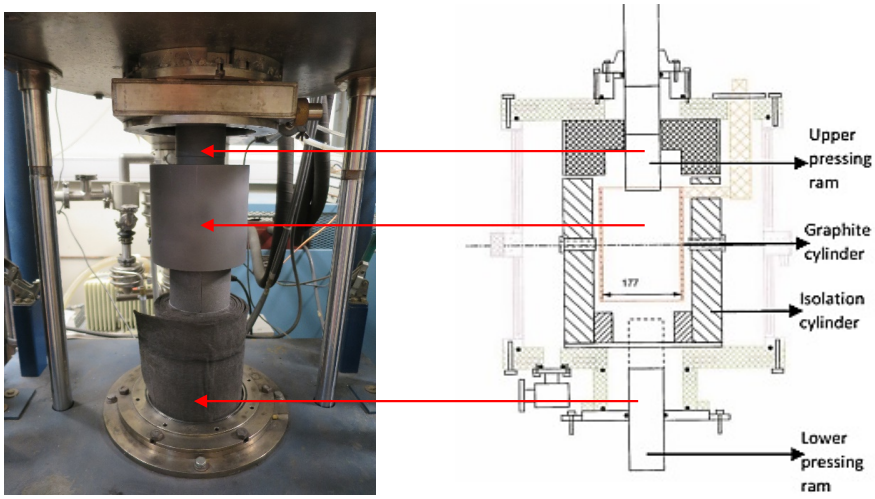

Figure 3.5.1. Hot-press furnace with parts and its schematic representation (NTNU Data file).

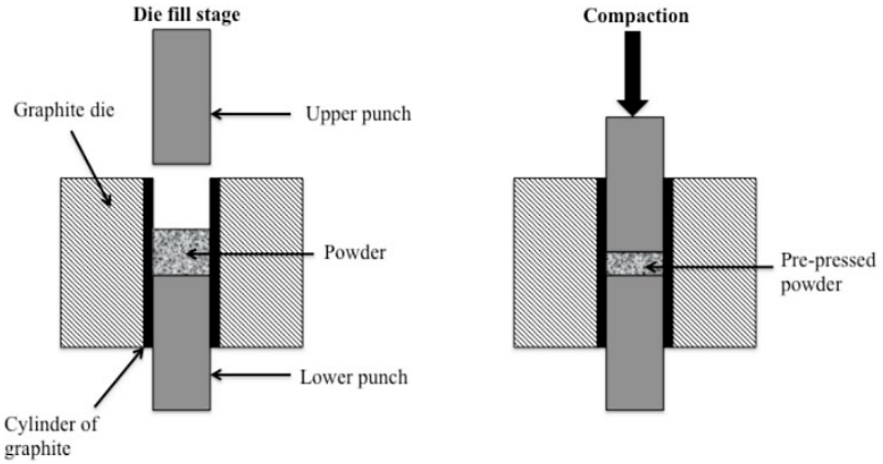

Figure 3.5.2. Cross-section of graphite dies with punches before and after experiments [110].

During hot pressing, the temperature increased at a rate of 10 °C/min to reach the target temperature. Once the target temperature was attained, pressure was applied and held for some time. Temperature profiles of the three hot press experiments are shown in **Figure 3.5.3** and experimental details are given in **Table 3-19**. At the end of the dwell time, the pressure was released, and the apparatus cooled at a rate of 10 °C/min. The gas flow and water-cooling were turned off once the temperature reached 90 °C. The graphite crucible containing the sample was then removed and the sample was analyzed by XRD to inspect whether the β-

SiC over time and pressure had converted to α-SiC. The maximum temperature that can be used in this furnace is 2100 °C.

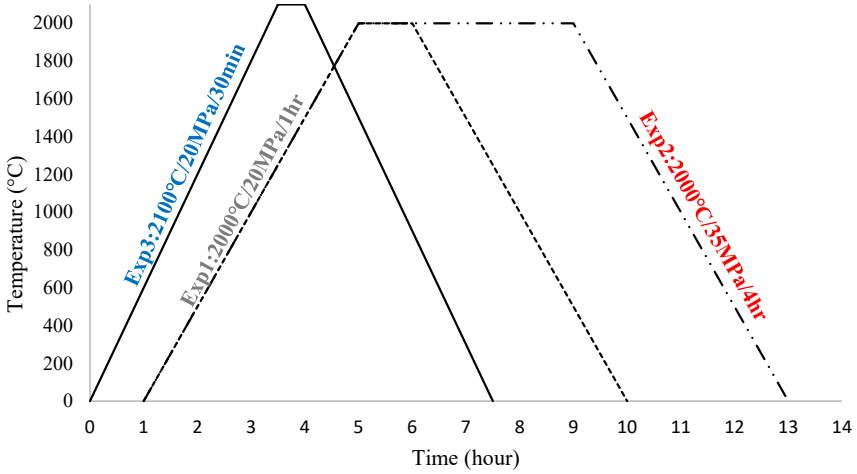

Figure 3.5.3. Temperature profiles of experiments conducted in hot-press furnace.

Table 3-19. Temperature, pressure, and time durations used for hot-press furnace experiments.

Experiment no.	Temperature (°C)	Pressure (MPa)	Holding time
1	2000	20	1 h
2	2000	35	4 h
3	2100	20	30 min

3.6 Analytical techniques

Various instruments, techniques, and software packages were used for analyzing samples collected from the experiments conducted in this research. Brief descriptions of those techniques and analysis methods are presented in this section.

3.6.1 HSC Chemistry 9

The software package HSC chemistry 9, developed by the Outotec research center in Finland, offers powerful calculation methods to study the effects of different variables on a chemical system at equilibrium. Many calculation modules are available in HSC, e.g., the Rea module was used to analyze chemical reaction equilibria and energy requirements.

In this work, the equilibrium compositions of the different Si and carbon bearing species were calculated using the GEM module in HSC. The amount of the raw materials, temperatures, and the various gas species of the system selected from the HSC database were specified to perform the calculations and the resultant equilibrium compositions were obtained.

3.6.2 Scanning electron microscopy

The SEM (LVFESEM, Zeiss Supra, 55 VP, 1-15 kV) was used to characterize the surface morphologies of SiC particles. The energy dispersive X-ray spectroscopy (EDX, Oxford Instruments 80 mm^2 SDD) was utilized for quantitative analysis of the condensates, and for the elemental mapping of the lamella extracted from a SiC micro-bullet crystal.

3.6.3 Computed tomography

The CT scan of the selected carbon particles were performed by Stein Rørvik at SINTEF Industry.

3.6.4 Electron probe micro-analyzer

EPMA back-scattered electron imaging (EPMA-BSE) of the SiC samples was performed in the JEOL JXA-8500, located at the NTNU to identify different phases present in the selected SiC samples. The samples were mounted in an iodoform containing epoxy mixture. This gives a good

contrast between the carbon particle and the epoxy-resin matrix during imaging [111]. Morten Peder Raanes at the Department of Material Science, NTNU, operated the EPMA for the selected samples.

3.6.4.1 Sample preparation in iodoform-epoxy

A 10 wt.% iodoform was added into the epoxy-resin and stirred thoroughly until the iodoform was completely mixed. A hardener of $3/25^{th}$ of the mass of resin was then added to the iodoform-resin mixture and mixed well. This solution was poured into a mold containing the sample and kept in an ice bath until the solution solidified completely. The surface of the sample was later polished for the characterization analysis. **Figure 3.6.1** shows the sample in an iodoform-epoxy mixture before and after solidification as well as the comparison between samples in an iodoform-epoxy and a normal epoxy.

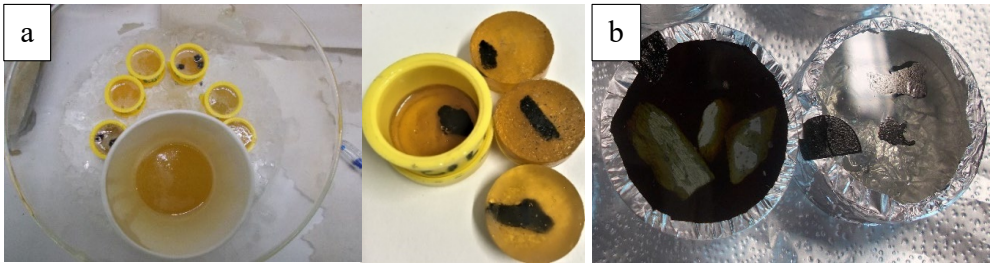

Figure 3.6.1. (a) Sample in iodoform-epoxy mixture kept for solidifying in ice bath and sample after solidification. (b) Sample in an iodoform-epoxy (left) and a normal epoxy (right).

3.6.5 X-ray diffraction

The XRD technique was used to quantitatively determine distribution of SiC polytypes in the β-SiC and α-SiC samples. The samples to be examined were first pulverized on a Tungsten carbide (WC) disc in the RETSCH Vibratory Disc Mill RS 200, at 700 rpm for 40 s. Each particle in the powder is a randomly oriented small crystal. Hence, to produce smooth, continuous diffraction lines or peaks during the XRD analysis, it is essential that the samples be crushed as fine as possible. The back-loading technique was used for preparing the samples to identify the SiC polytypes present in them and to avoid orientation at the surface of the sample. The powder was then placed under a beam of monochromatic X-rays. The X-ray diffractograms of β-SiC/α-

SiC samples were obtained using a powder X-ray diffractometer (Bruker D8 Focus) in Bragg-Brentano geometry using Cu-Kα radiation.

3.6.5.1 Quantitative analysis of SiC polytypes

TOPAS (Total pattern analysis solution; Bruker AXS, Version 5) is a software package used for analyzing the profile and structure of complex mixtures with many phases. Accurate determination of phase compositions in SiC based materials that consists of large number of polytypes with overlapping Bragg reflection is an arduous task. Therefore, the Rietveld refinement of TOPAS V5 software, built around a general non-linear least squares system, was chosen for the quantitative phase analysis of SiC polytypes.

The initial step was importing the XRD data files of the SiC samples individually. All other parameters, such as the emission profile, background, and instrument settings were then loaded, followed by importing the structure entries for the different phases. For the quantitative analysis of the SiC polytypes, structures of the most common polytypes such as 3C, 4H, 6H, and 15R were used. During the analysis, it was assumed that the sample has no preferential orientation. The amorphous phase, which indicates that unreacted carbon exists in the SiC samples before and after heating, was excluded during the quantitative analysis. Finally, refinement was performed to obtain both calculated pattern and its difference from measured XRD data of the selected SiC sample. **Figure 3.6.2** shows the fitted diffractogram of charcoal-derived β-SiC sample heated at 2200 °C. The deviation from observed data is represented by the gray curve with the corresponding d-spacing values. The phase quantification results are given in wt.%.

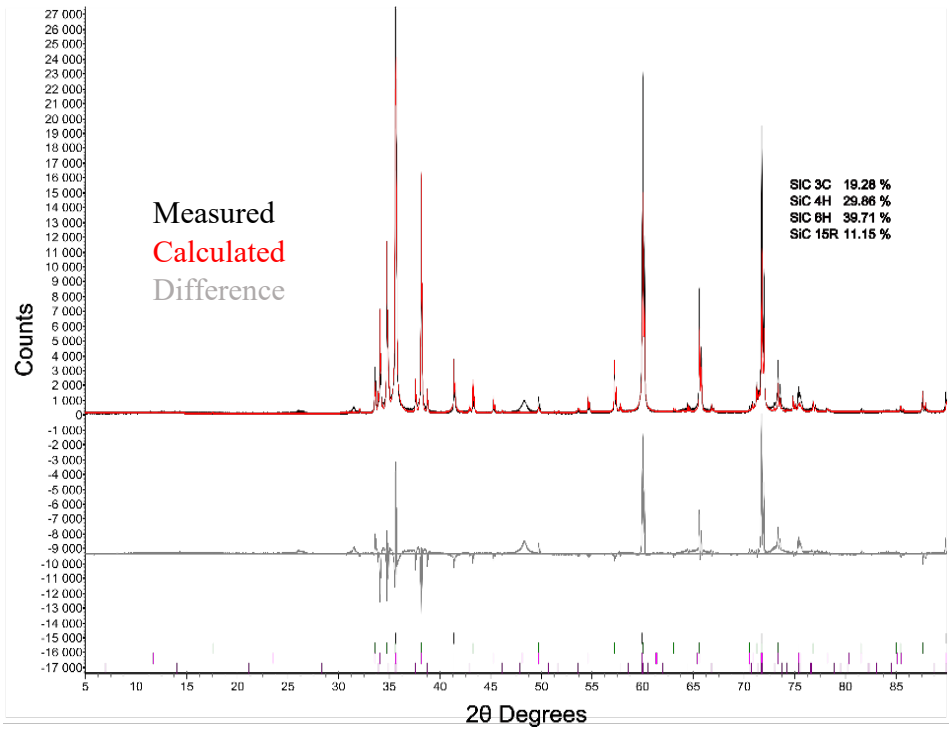

Figure 3.6.2. Fitted diffractogram of charcoal-derived β-SiC sample heated at 2200 °C.

3.6.6 Chemical analysis

Chemical analysis of the samples was carried out at the D-lab in Sweden. The analysis method described below is based on the information obtained from the D-lab. The analysis was performed to estimate the amount of SiC, Si, and free carbon present in the SiC samples produced from charcoal, coal, and pet-coke. The free carbon analysis was carried out in a multiphase carbon analyzer LECO RC-612, a ramped instrument, at 100–1000 °C in an oxygen atmosphere, whereas the carbon analyzer LECO CS-444, a combustion instrument, was used for analysis of total carbon in an oxygen atmosphere. Both the instruments performed the analysis by burning the sample in oxygen and detecting the CO_2 using an infrared (IR) cell. The total Si was determined with an X-ray fluorescence (XRF) instrument. The following calculations were used to find the total SiC, Si in SiC, and elemental Si in each sample. C_{total}, C_{free}, and Si_{total} denote total carbon, free carbon, and total Si, respectively.

$$\%SiC = \left(\%C_{total} - \%C_{free}\right) \times \frac{Molar\ mass\ of\ SiC}{Molar\ mass\ of\ carbon} = \left(\%C_{total} - \%C_{free}\right) \times 3.3385 \quad (20)$$

$$Si\ in\ SiC = \%\ SiC \times \frac{Molar\ mass\ of\ Si}{Molar\ mass\ of\ SiC} \quad (21)$$

$$Elemental\ Si = Total\ Si - Si\ in\ SiC \quad (22)$$

In the cases of charcoal- and coal-converted SiC, $\%C_{free}$ was less than 10% and total carbon was less than 50%. Therefore, the $\%SiC$ was calculated based on both total and free carbon according to equation (20). In some of the SiC samples derived from pet-coke, $\%C_{free}$ was more than 50%, especially in the samples collected at 1750 and 1800 °C. As a higher amount of free carbon in the samples increases an uncertainty in the measurements, the percentage of elemental Si in the SiC particles could not be calculated for the samples collected from these two experiments. Therefore, the $\%SiC$ formed in them was calculated based on the total carbon content according to equation (23), as it does not require the value of free carbon.

$$\%SiC = (100\% - \%C_{total}) \times \frac{Molar\ mass\ of\ SiC}{Molar\ mass\ of\ Si} = (100\% - \%C_{total}) \times 1.428 \quad (23)$$

The $\%SiC$ and the elemental Si in SiC samples were calculated according to equations (20) and (22) for the SiC samples produced at 1850 and 1900 °C.

A minimum of 4 g of SiC from each layer was required to perform the chemical analysis. The SiC particles left in each layer after the validation experiments in graphite tube furnace were not enough to conduct the analysis and the samples from each layer had higher amounts of unreacted carbon in them. Here also the $\%SiC$ formed in the different layers was calculated based on the total carbon content according to equation (23). The derivations of equations (20) and (23) is given in Appendix A.

3.6.7 Transmission electron microscopy

The transmission electron microscopy (TEM) technique was utilized to get a detailed set of crystallographic information of selected SiC samples. TEM gives the crystal structure, size, and shape; however, only a few thin particles could be analyzed in the TEM. Two common TEM techniques, the bright field (BF) TEM imaging and selected area diffraction (SAD), were performed to obtain detailed description of the polytypes present in the selected SiC samples. For this study, the aim was to characterize the morphology and crystalline structure of the selected SiC samples that were heated up to 1750 and 2450 °C, and to ensure the polytype distribution present in each of these samples. Prof. Antonius T. J. van Helvoort and Dr. Ragnhild

Sæterli at the Department of Physics, NTNU, operated the instrument (JEOL JEM-2100) located at the TEM Gemini Centre.

3.6.7.1 Sample preparation for TEM characterization

The selected SiC samples were finely crushed manually using a mortar and pestle; after that the fines were mixed in isopropanol. A droplet of the sample containing isopropanol was transferred to a holey carbon film (ca. 20 nm thick) on a 300-mesh copper grid. The C-foil was used as the electron transparent support for viewing the SiC particles while performing TEM.

3.6.8 Scanning transmission electron microscopy

The scanning transmission electron microscopy (STEM) characterization was done with a double Cs corrected cold FEG JEOL ARM200F, operated at 200 kV. A high-angle annular dark field STEM (HAADF-STEM) analysis was performed to investigate the contrast variations in a SiC micro-bullet lamella. A TEM lamella was extracted from the center of a micro-bullet with a Helios G4 UX Dual Beam focused ion beam (FIB). Carbon protection layers were first deposited on either side of the SiC micro-bullet by e-beam assisted deposition to avoid damage induced by Ga^+ beam and implantation of the micro-bullet prior to milling out the lamella. The lamella was extracted using the standard lift-out technique and was welded into a cutout trench in the central post of a Cu FIB half grid. Coarse thinning was performed at an accelerating voltage of 30 kV for the Ga^+ ions. Final thinning and polishing were performed at 5 and 2 kV on either side of the lamella to minimize eventual surface damage. TEM lamella was extracted by FIB as shown in **Figure 3.6.3a** from an average sized micro-bullet. **Figure 3.6.3b** shows the lamella preparation from the micro-bullet before welding to the TEM grid. Per Erik Vullum at SINTEF operated both the FIB and STEM/TEM for the selected SiC sample.

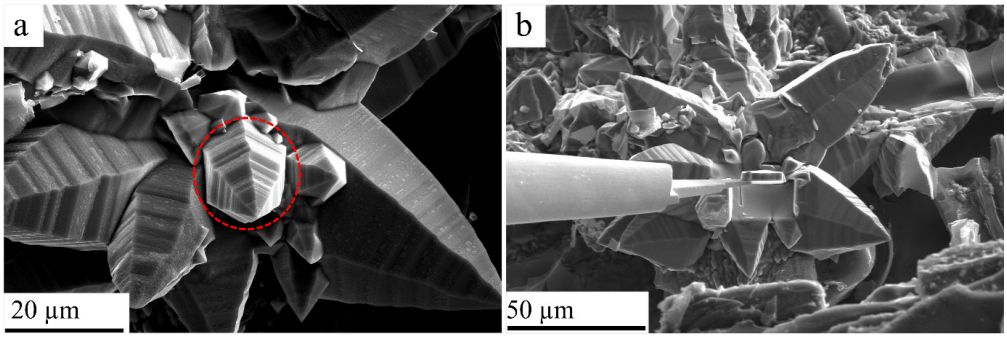

Figure 3.6.3. (a) Micro-bullet marked by red circle was chosen for TEM. FIB stage was rotated and tilted to have the growth direction of bullet parallel to the ion beam while cutting out the lamella. (b) Secondary image showing orientation of the bullet during lift-out and transferring to the TEM grid.

3.6.9 ImageJ

ImageJ is an open source image-processing program designed for scientific image analysis. This software was used to measure the cell wall thickness of carbon materials used in this study.

4 Results

The present study aimed at evaluating β-SiC formation in charcoal, coal, and pet-coke, and its transformation to α-SiC at higher temperatures. Results from the β-SiC production experiments, and the subsequent experiments performed for heat-treatment of β-SiC to form α-SiC, are described in this chapter. They are organized in the order of the three carbon materials used in this study, charcoal, coal, and pet-coke, and are presented based on the experiments, followed by the characterization and quantitative analyses of the SiC samples obtained from those experiments.

An induction furnace and a graphite tube furnace were used to produce β-SiC from charcoal, coal, and pet-coke. The graphite tube furnace experiments were performed to validate the results from the large-scale induction furnace experiments. These experiments are referred to as Study A, comprising the first part of the research. The type of materials produced in the crucible after the experiments are schematically illustrated in **Figure 4.0.1**.

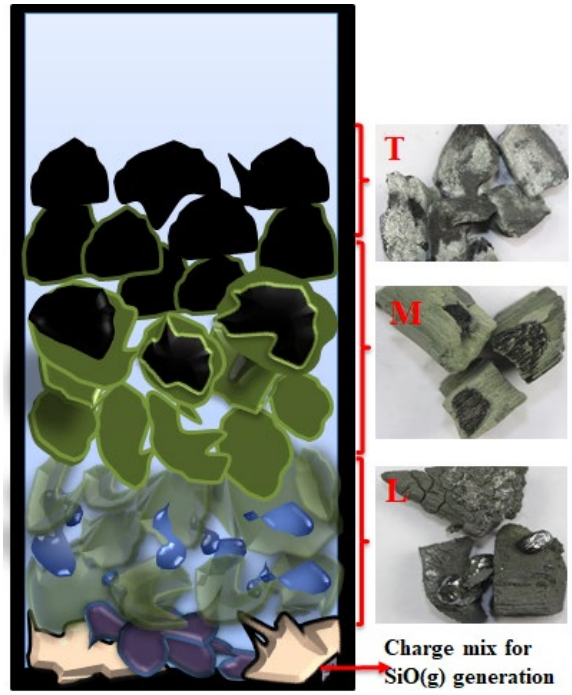

Figure 4.0.1. Schematic representation of cross-section of crucible, after SiC production experiments. Samples collected from top (T), middle (M), and lower (L) layers of initial carbon layer are shown.

The product samples were collected from the lower, middle, and top layers of the crucible after completing the experiments, and are denoted by L, M, and T, respectively, as shown in **Figure 4.0.1**. The samples retrieved from the lower region of the initial carbon layer contained SiC with some Si in them (represented by L in graphs and figures). The middle region had carbon partly and completely transformed to SiC (represented by M in graphs and figures). The top region of the carbon layer contained only unreacted carbon particles and was mostly covered by a thin layer of condensates/volatiles. The SEM morphology, EPMA-BSE, XRD, chemical, and TEM analyses of these samples were performed to evaluate their structures and characteristics.

Study B comprised experiments to transform β-SiC particles obtained from the induction furnace experiments to α-SiC at higher temperatures, in a graphite tube furnace. The samples collected from these experiments were also analyzed using SEM, EPMA-BSE, XRD, and TEM. The charcoal-converted β-SiC particles were further heat-treated at various pressures and temperatures, for different time durations in a hot-press furnace, to evaluate the transformation to α-SiC.

Findings from all these experiments and analyses are described in the following sections, arranged based on the three carbon materials that were used to produce SiC, viz., charcoal, coal, and pet-coke. Three samples of industrially produced SiC were also analyzed to validate the research. Results from those analyses are included in the final section of this chapter.

4.1 Charcoal

This section presents results from the experiments performed using charcoal as raw material to produce SiC and Si. Two sets of experiments were performed in the induction furnace, constant volume and constant weight experiments. Two distinct sources to generate SiO(g) were used, a mixture of (SiO_2 + Si) and pellets made from (SiO_2 + SiC). The quantities of raw materials used and the target temperatures set for these experiments are detailed in **Table 3-7** to **Table 3-12.** To validate the results, similar experiments were performed in a more controlled environment in the graphite tube furnace.

Figure 4.1.1 shows the visual appearance of samples collected from the top, middle, and lower layers of the initial charcoal layer from the induction furnace, and **Figure 4.1.2** presents similar samples collected from the graphite tube furnace experiments. In both the cases, samples from the three different layers looked alike. The unreacted particles from the top layer resembled the original charcoal. The particles from the middle layer consisted of both completely and partly transformed SiC particles. The particles in the lower layer had completely transformed to SiC, with some additional Si droplets on them. SiC particles from the middle layer

were soft, flaky, and green in color, whereas particles from the lower part were hard, dark bluish in color, and most of them had droplets of Si on them.

The visual appearances of the SiC particles within the various layers were quite similar in all the experiments. Nevertheless, the quantities of unreacted charcoal and SiC particles from the middle and lower layers were different, depending on the temperatures at which they were produced. The charcoal-converted SiC particles from the induction furnace experiments were light and flaky, and a considerable amount of SiC was lost as fines while retrieving the samples by hand. It was relatively easier to collect samples from the graphite tube furnace, and the temperature measurements in the graphite tube furnace were more accurate compared with those in the induction furnace.

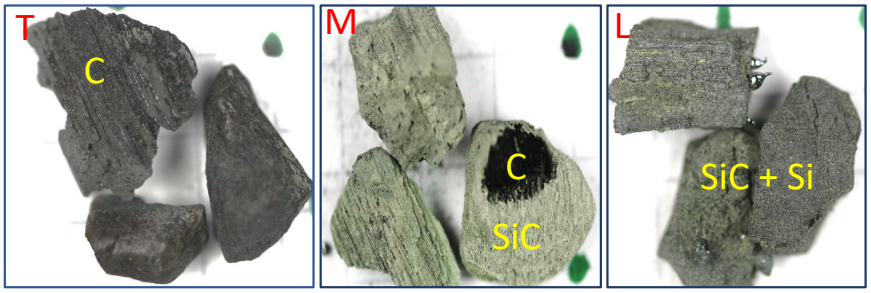

Figure 4.1.1. Samples collected after induction furnace experiments from top (T), middle (M), and lower (L) layers of initial charcoal layer. Unreacted charcoal, charcoal converted to SiC, and Si are also marked.

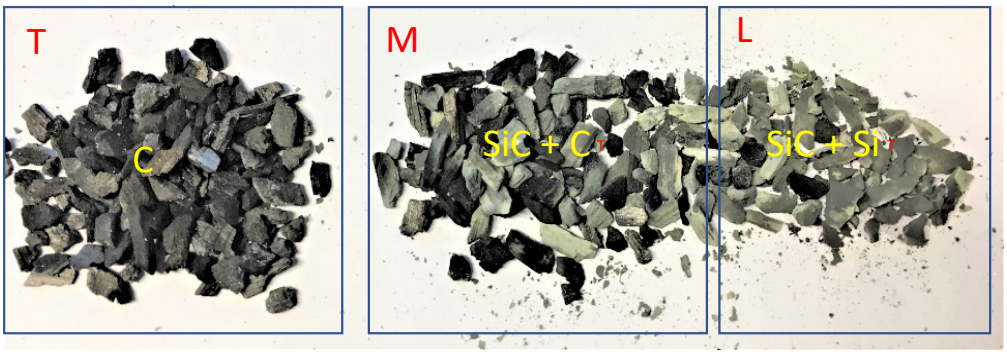

Figure 4.1.2. Samples collected from top (T), middle (M) and lower (L) layers of initial charcoal layer after graphite tube furnace experiments.

4.1.1 β-SiC production: Induction furnace experiments

Figure 4.1.3 and **Figure 4.1.4** represent the quantities of initial charcoal and final products collected respectively from the constant volume and constant weight experiments, which were performed at 1750 and 1800 °C in the induction furnace. A mixture of (SiO_2 + Si) was used in these experiments to generate SiO(g). Some of the SiC was lost as fines while handling the samples. The approximate quantities weighed (**Figure 4.1.3** and **Figure 4.1.4**) show that more SiC was produced in the lower layer, where temperature was the maximum. The quantities of SiC obtained after the constant volume and constant weight experiments were comparatively similar. In the constant volume experiments, ~13.75 and ~29.75% of the total charcoal had transformed to SiC at 1750 and 1800 °C, respectively. At these two temperatures, respectively ~14.56 and ~30% of the total charcoal transformed to SiC in the constant weight experiments. There were no sizeable differences between the quantities of SiC particles produced by these two methods.

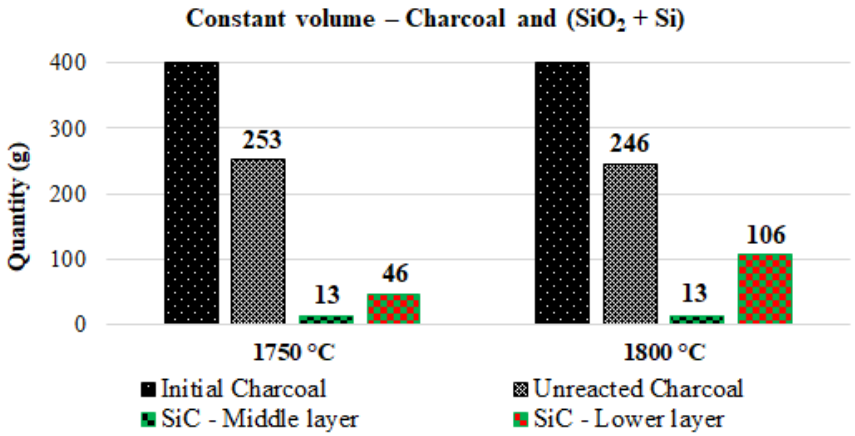

Figure 4.1.3. Quantities of initial product (charcoal) and final products collected from three different layers in the crucible, from the constant volume experiments. They were conducted at 1750 and 1800 °C in the induction furnace, using (SiO_2 + Si).

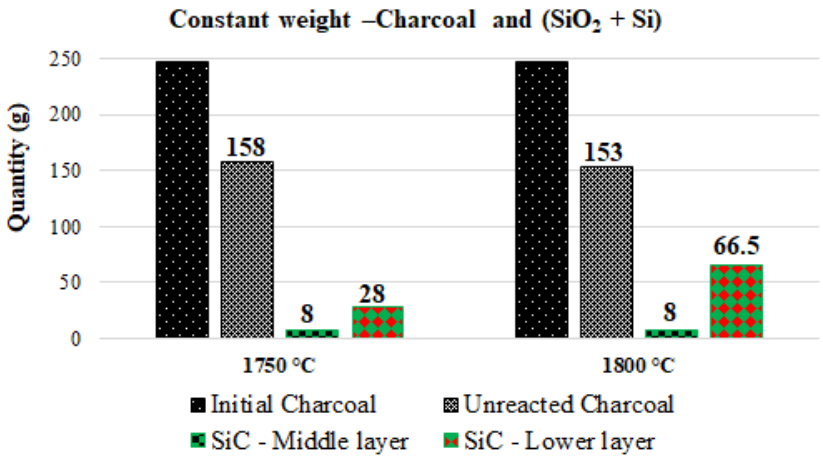

Figure 4.1.4. Quantities of initial product (charcoal) and final products collected from three different layers in the crucible, from the constant weight experiments. They were conducted at 1750 and 1800 °C in the induction furnace, using (SiO_2 + Si).

In the induction furnace experiments, while using pellets of (SiO_2 + SiC) to generate SiO(g), upon heating, they started foaming towards the carbon materials and had to be pushed down to the bottom with the help of a rod. Therefore, the experiments conducted using (SiO_2 + SiC) were not completely successful, and their quantities could not be measured. However, samples could be collected from these experiments for further analysis. **Figure 4.1.5** shows the cross-sections of the crucibles displaying their interior conditions after conducting experiments with (SiO_2 + SiC) at 1750 and 1850 °C. Only the constant volume experiments were conducted with the (SiO_2 + SiC) pellets. Samples collected from all these experiments were analyzed further using the various techniques described in the following sections.

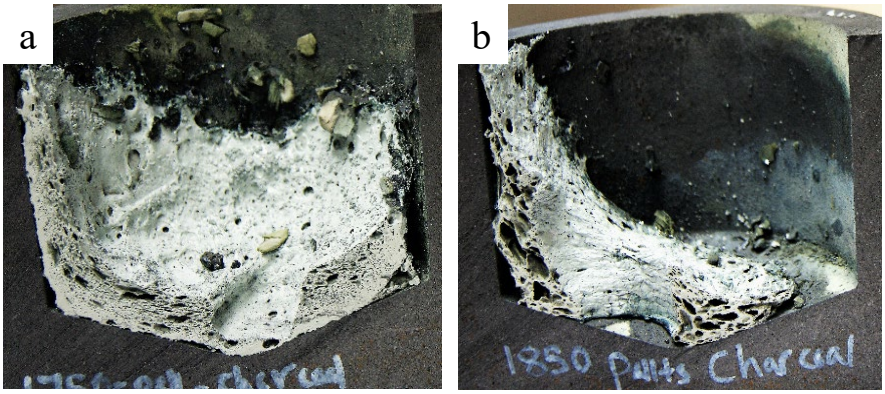

Figure 4.1.5. Cross-sections of crucibles displaying conditions inside them, after conducting experiments with pellets of (SiO_2 + SiC), at (a) 1750 and (b) 1850 °C.

4.1.1.1 SEM morphology

Surface morphologies of SiC particles from the lower and middle layers of randomly selected experiments (constant volume and constant weight) were examined under the SEM. The analysis provides information on formation of SiC crystals (size and shape) in the carbon materials, and reveals the structural variations evolving in them as Si starts forming in SiC. The SiC particles from the lower and middle layers of the crucible, where temperatures ranged ~1700–1900 °C, were selected for the morphological characterization. **Figure 4.1.6** to **Figure 4.1.15** show the SiC crystals developed in the charcoal particles during the induction furnace experiments. SiC crystals of varying sizes have formed in the charcoal pores. The SiC crystals are in the form of small pyramid-shaped clusters. More crystals form on the surfaces with an increase in temperature, and the particle structure becomes denser. The SiC particles from the lower layer, where the temperature was higher, become further denser as Si starts forming in the SiC particle, and its original carbon structure disappears (**Figure 4.1.12** to **Figure 4.1.15**).

Figure 4.1.6 shows charcoal partly converted to SiC, taken from the upper portion of the middle layer, where the temperature was < 1700 °C. A topochemical reaction is taking place, and most of the SiC crystals initially form at the pore entrance. **Figure 4.1.7** and **Figure 4.1.8** display the images of a partly converted charcoal particle from the middle layer; the seed crystals initially formed in the charcoal pores enlarge as the reaction progresses. The original wood structure is clearly visible in most of these images.

Figure 4.1.9 to **Figure 4.1.10** show images of SiC crystals exposed to a temperature ≥ 1750 °C. The carbon particles in this layer were exposed to larger quantities of SiO(g), and upon heating, more SiC crystals form as the reaction time prolongs. They become denser, filling the inner pores, and the original structure of charcoal gradually disappears. The samples obtained from the regions of higher temperatures (~1800 °C) show that the initial SiC structure disappears completely as Si starts forming in SiC (**Figure 4.1.12** to **Figure 4.1.15**).

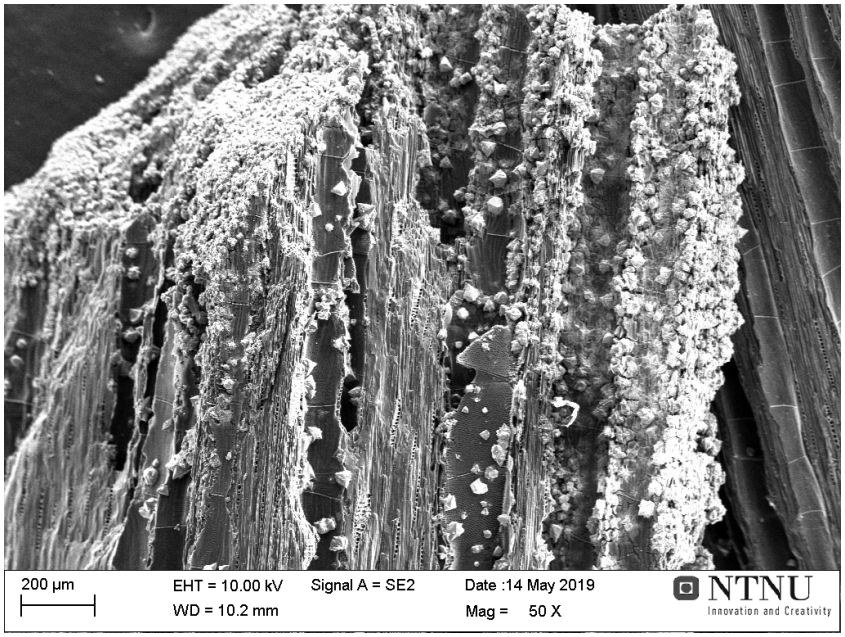

Figure 4.1.6. Charcoal partly converted to SiC, taken from upper portion of middle layer, where temperature was < 1700 °C. A topochemical reaction could be observed, as most of the SiC crystals initially form at the pore entrance, and the original wood structure is clearly visible.

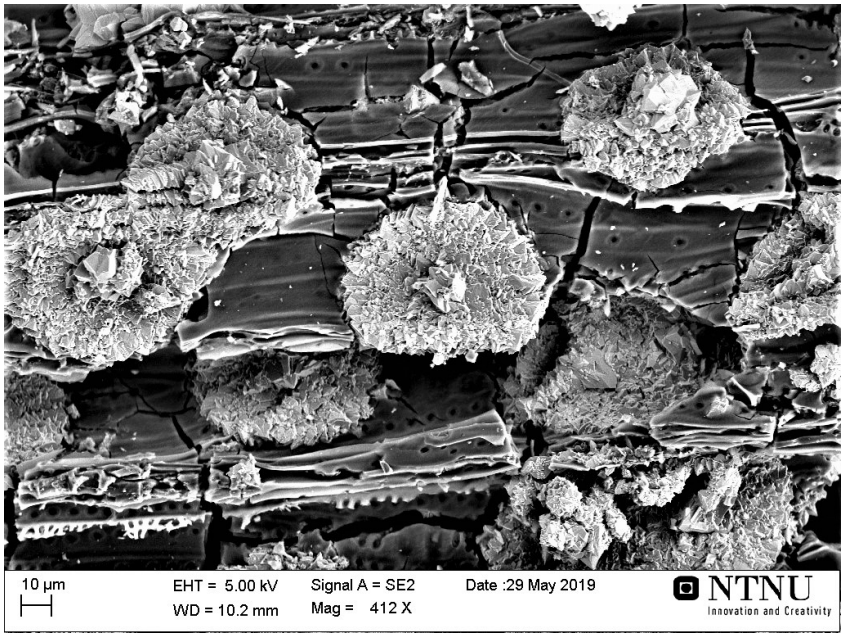

Figure 4.1.7. Sample collected from middle layer. Charcoal particle is less exposed to SiO(g) at temperatures < 1700 °C, and seed crystals initially formed in the charcoal pores get bigger as the reaction progresses. The original wood structure is still visible.

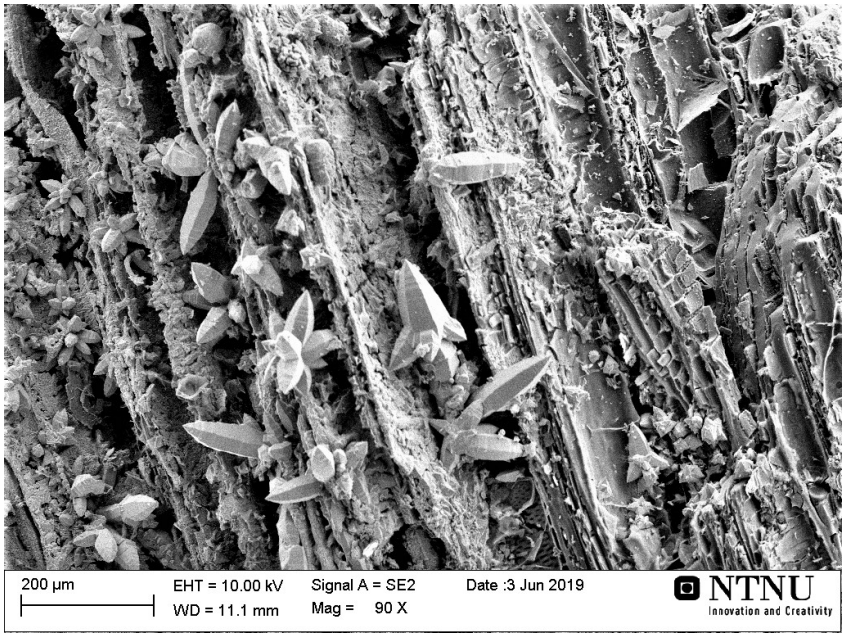

Figure 4.1.8. Charcoal-converted SiC particle taken from middle layer that was exposed to temperature ranges of 1700–1750 °C. SiC crystals of varying sizes grow on the pores of charcoal without compromising the orginal structure.

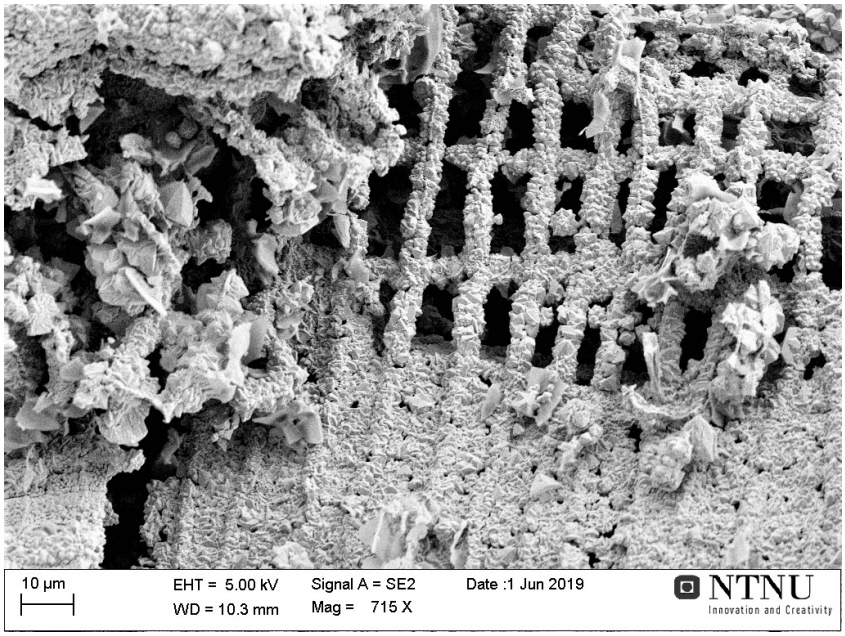

Figure 4.1.9. Charcoal-converted SiC particle from middle layer where temperature was ~1750 °C. In some regions, the pores are filled with dense SiC crystals and smaller SiC crystals formed on the cell walls are clearly visible.

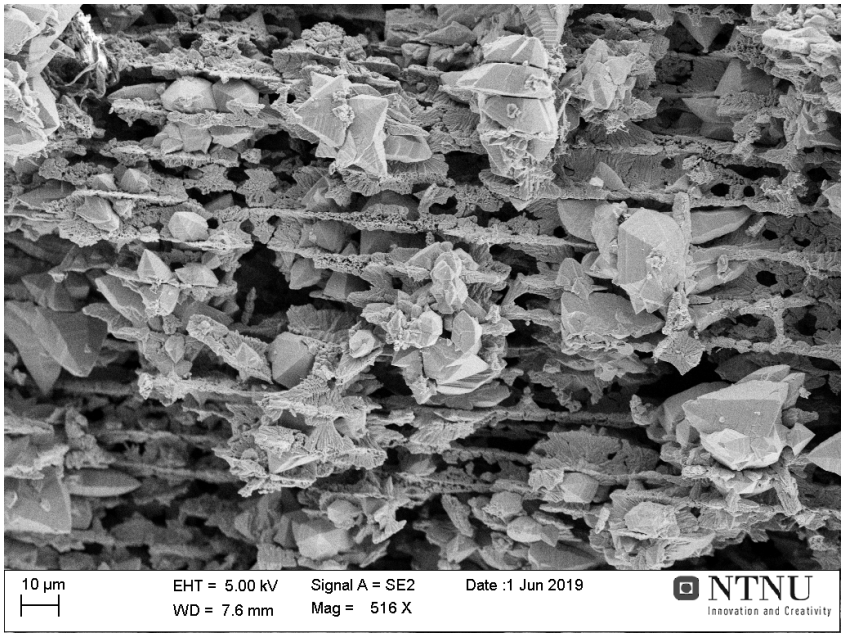

Figure 4.1.10. Charcoal-converted SiC particle from middle layer at ~1750 °C. Pores are filled with SiC crystals of varying sizes, still retaining some of the orginal structure.

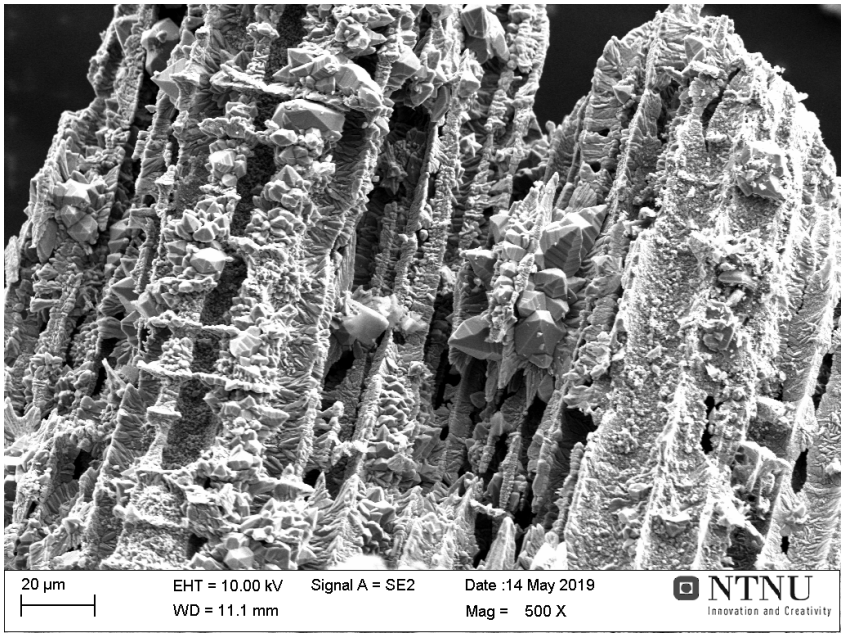

Figure 4.1.11. Charcoal-converted SiC particle from lower layer where temperature was ~1800 °C. Pores are getting densely filled with SiC crystals of different sizes; the orginal carbon structure has started disappearing.

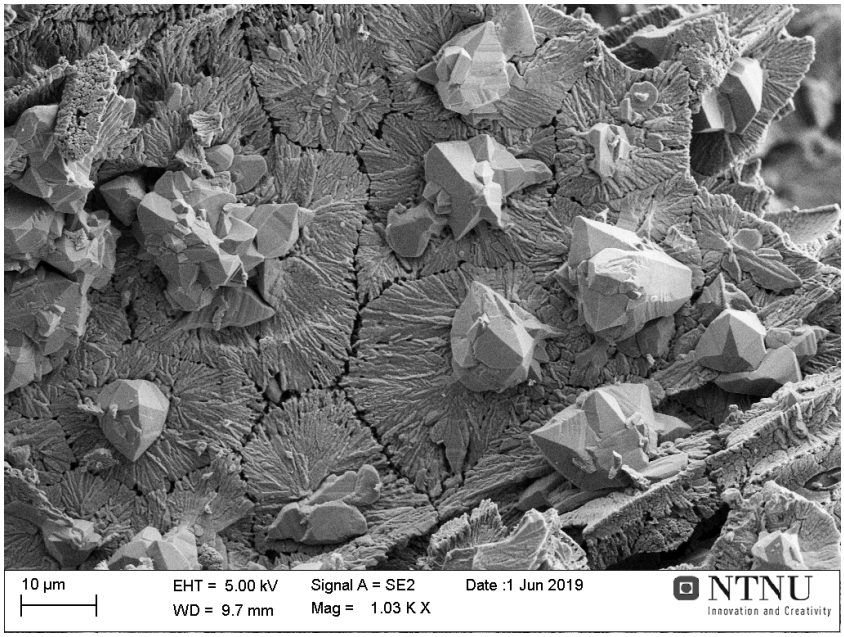

Figure 4.1.12. Charcoal-converted SiC particle from lower layer where temperature was ~1800 °C. Pores are completely filled with SiC and the original charcoal structure has almost disappeared.

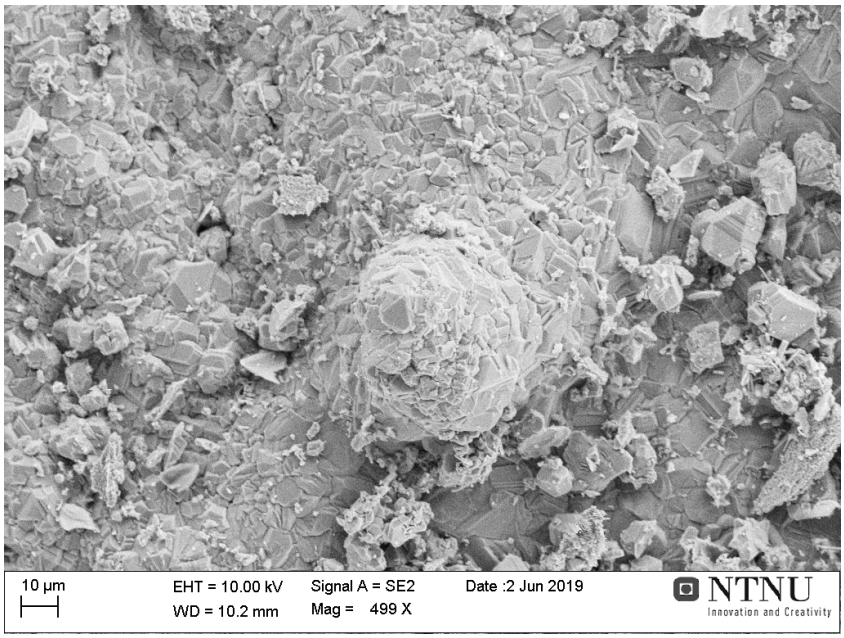

Figure 4.1.13. Charcoal-converted SiC particle from lower layer where temperature was ≥1800 °C. A smooth surface is visible with formation of Si in the SiC particle, and the structure of original charcoal has disappeared completely.

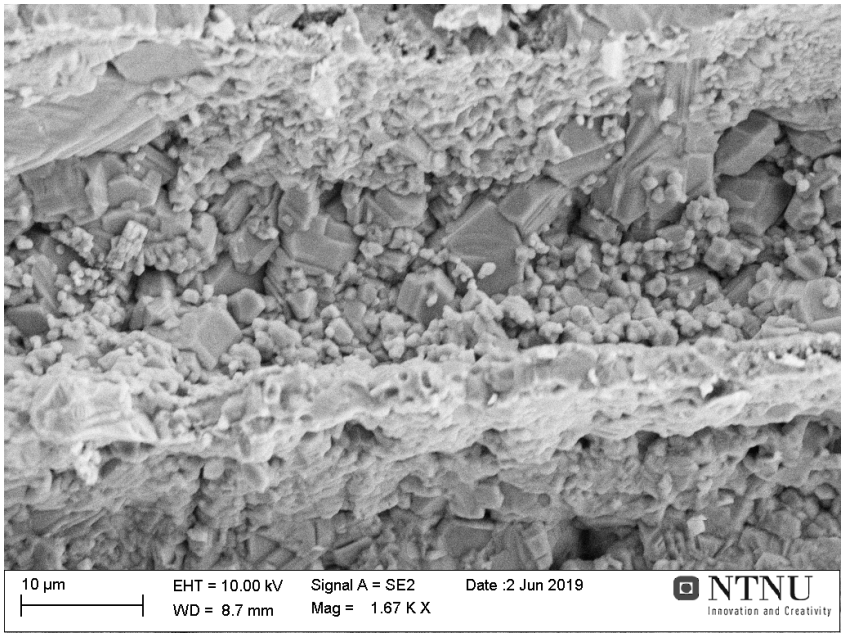

Figure 4.1.14. Charcoal-converted SiC particle from lower layer where temperature was ≥1800 °C. SiC particle has Si in it with almost no trace of the original charcoal.

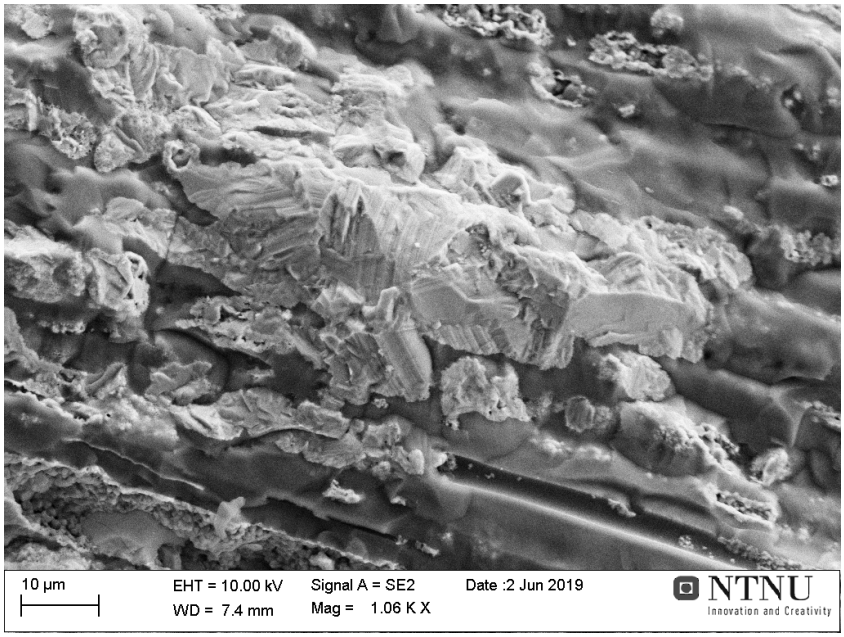

Figure 4.1.15. Charcoal-converted SiC particle from lower layer where temperature was ~1900 °C. Si has formed in the SiC particle with no traces of the original charcoal.

4.1.1.2 EPMA-BSE imaging

The EPMA-BSE analysis of the SiC particles produced at different temperatures was carried out to determine the phases, composition, and the elemental distribution in them. **Figure 4.1.16** shows EPMA images of SiC particles produced from charcoal, collected from the lower and middle regions of the crucible, after the constant volume induction furnace experiments conducted at 1750, 1800, 1850, and 1900 °C. The dark gray regions in the images are SiC formed when SiO(g) reacts with carbon. The light gray or nearly-white regions are the elemental Si in SiC formed by SiO(g) reacting with SiC, and is mostly visible in the particles collected from the lower layer. Pure carbon and epoxy are almost black in color.

Figure 4.1.16 shows that as the temperature increases, more Si is produced in the SiC particles in the lower layer (images on the left side, a, c, e, and g). Simultaneously, these particles become denser, and the original structure of charcoal disappears. In the middle layer, the carbon particles were exposed to slightly lower temperatures and lower quantities of SiO(g) than the lower layer. The Si phase is not present in these samples (images on the right side, b, d, f, and h), and the original charcoal structure is still visible even after being exposed to SiO(g). The SiC structures observed in the EPMA images are in good agreement with those observed in the SEM morphology images.

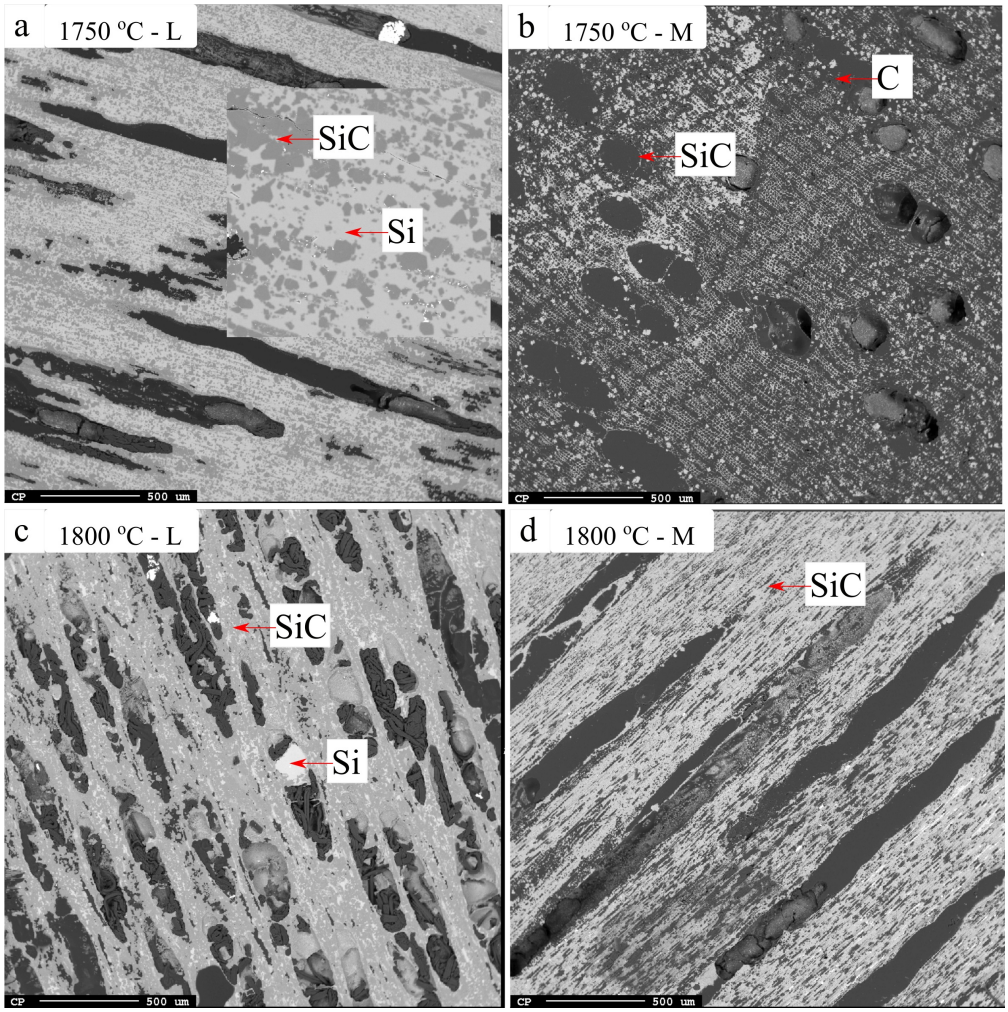
a
1750 °C - L
SiC
Si
CP
500 um
b
1750 °C - M
C
SiC
CP
500 um
c
1800 °C - L
SiC
Si
CP
500 um
d
1800 °C - M
SiC
CP
500 um

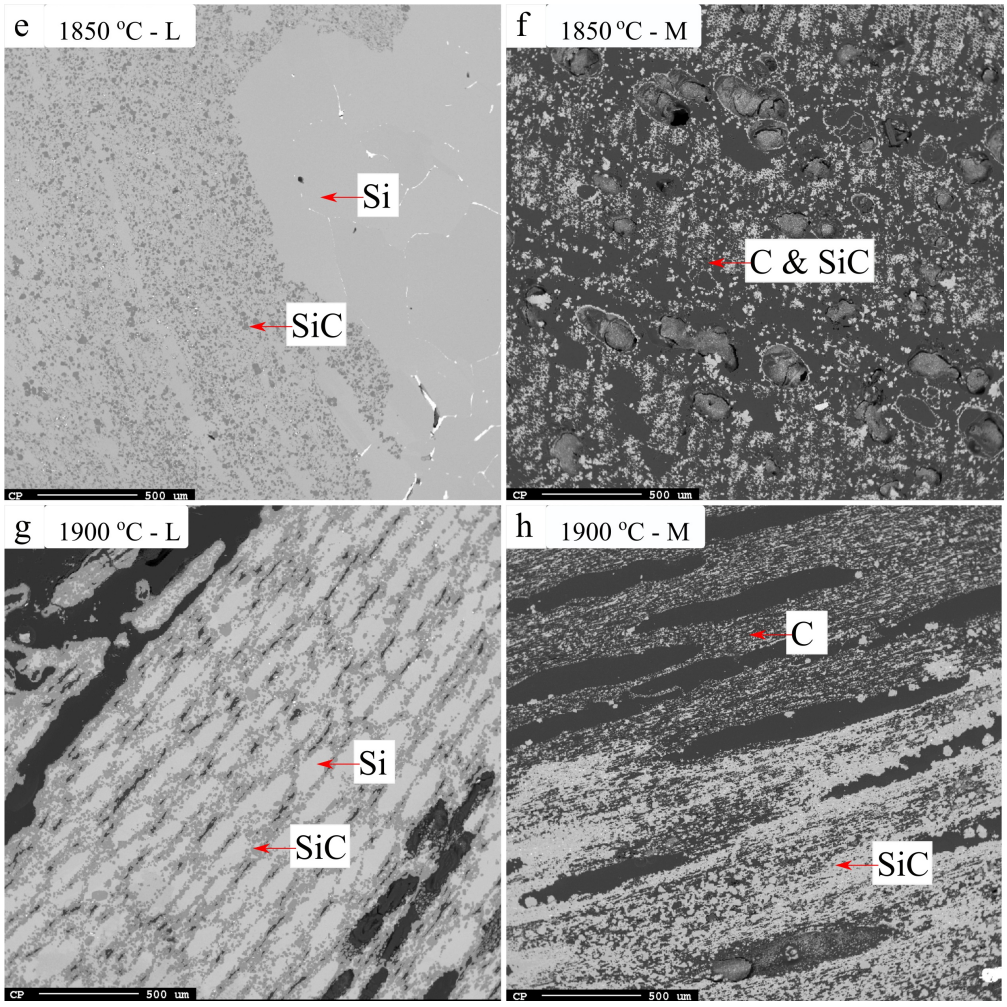

Figure 4.1.16. EPMA-BSE images of charcoal-converted SiC particles collected from (a, c, e, g) lower (L) and (b, d, f, h) middle (M) layers. Samples are from constant volume induction furnace experiments, conducted at 1750, 1800, 1850, and 1900 °C. Dark gray region is SiC, and light gray or nearly-white region is elemental Si in SiC. Pure carbon and epoxy are mostly black in color.

Elemental mapping technique was also applied to determine the phases between carbon, Si, and SiC. **Figure 4.1.17** shows the elemental distribution of Si, carbon, and SiC in a selected area of the SiC particle, collected from the experiment conducted at 1900 °C. The formation of Si in SiC progresses as the temperature increases while the charcoal pores disappear. **Figure 4.1.18** shows the EPMA elemental mapping of a portion of the SiC particle, with Si flowing out from the particle in the form of a droplet. The droplet that could be visually observed on the SiC particle is thus confirmed as elemental Si.

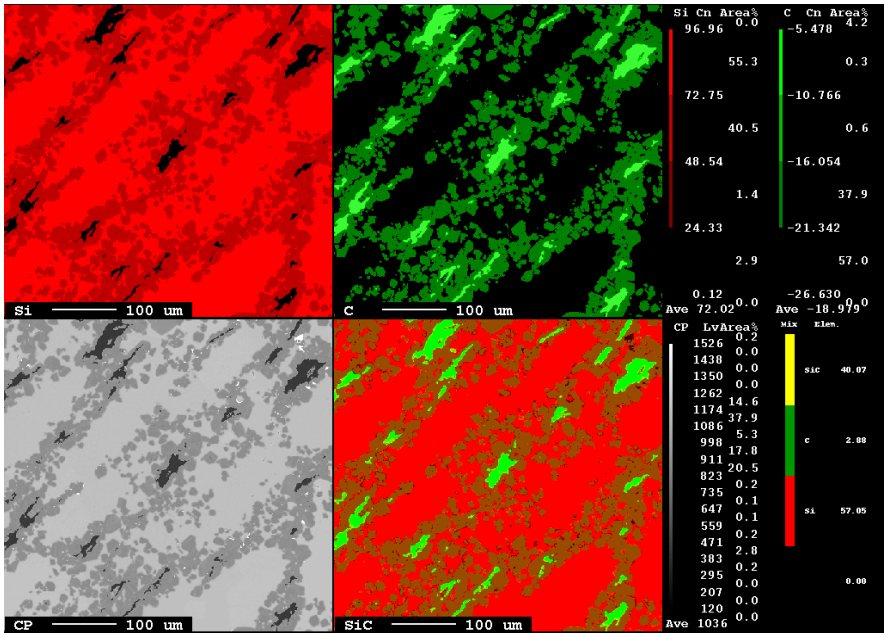

Figure 4.1.17. Elemental distributions of Si, carbon, and SiC in selected area of a SiC particle (EPMA image), collected from the experiment conducted at 1900 °C. Si continues to form in SiC as temperature increases, while the charcoal pores vanish.

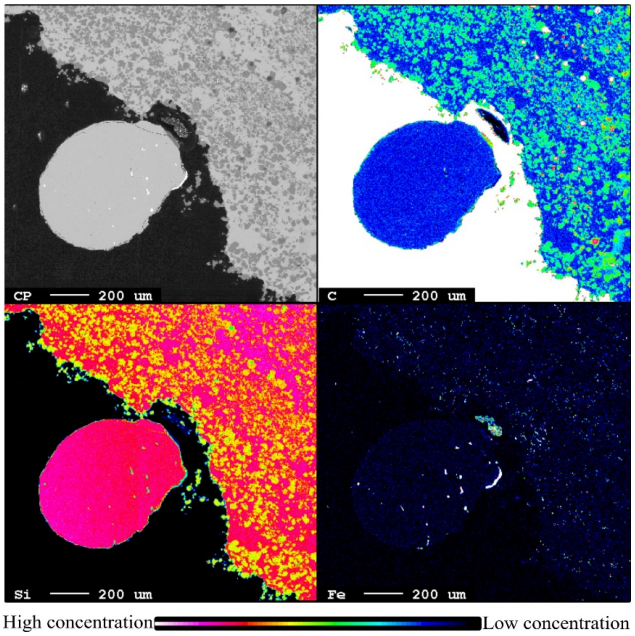

Figure 4.1.18. EPMA of a portion of SiC particle, and elemental mapping of carbon, Si, and Fe in the particle. Si is flowing out from the particle in the form of a droplet.

Figure 4.1.19 gives the overview of a partly converted SiC particle. The topochemical reaction explained by the SCM of a gas-solid reaction [**section 2.5.1**] could be observed here. The concentration of SiC is higher at the outer layer and it decreases towards the center of the particle. There is a sharp boundary between the SiC layer and the unreacted carbon. Also, the initial wood structure with thin cell walls is clearly visible, which shows that the original structure is retained at some portions of the charcoal particle even after it was exposed to SiO(g).

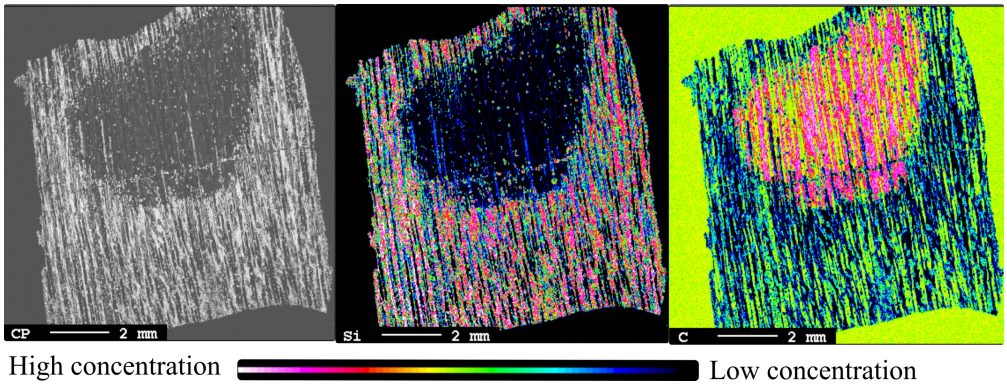

Figure 4.1.19. EPMA of partly converted SiC particle, and elemental distributions of Si and carbon in it. Topochemical reaction according to SCM of a gas-solid reaction could be observed.

Figure 4.1.20 shows the elemental distribution of Si and SiC in a completely converted SiC particle that has elemental Si in it. It shows that once the particle is completely transformed to SiC, Si starts forming in it, which is distributed homogenously throughout the particle. Pores in charcoal are large, and are distributed homogeneously. Therefore, the SiO(g) can easily diffuse into the charcoal pores, easily converting the whole particle to SiC, and Si also forms rapidly throughout the SiC particle. The pores are clearly visible in **Figure 4.1.19**, whereas in **Figure 4.1.20** they vanish as molten Si starts filling them.

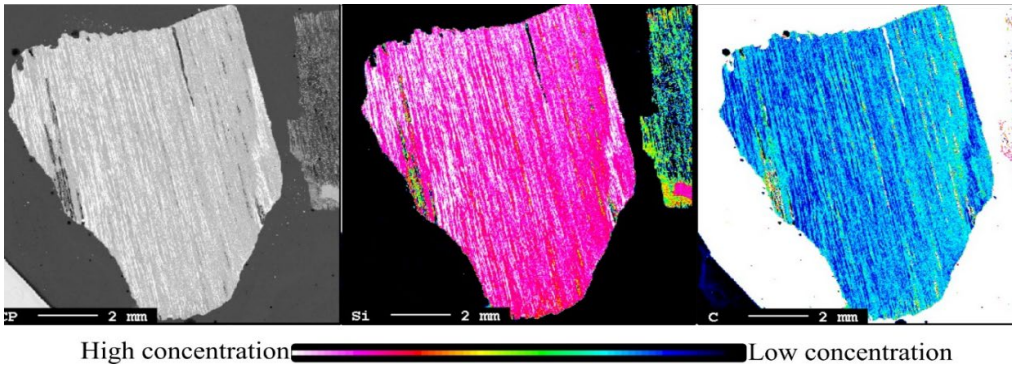

Figure 4.1.20. EPMA of completely converted SiC particle, and elemental distributions of Si and carbon in it. Si has started forming in the SiC particle, and pores in the charcoal vanish as they get filled with molten Si.

Figure 4.1.21 shows the EPMA-BSE images of SiC particles from the middle (images on the left) and lower (images on the right) regions, collected after the constant weight induction furnace experiments conducted at 1750 and 1800 °C. The structures of the SiC particles and the different phases present in them are similar to those in the SiC particles collected from the constant volume experiments at similar temperatures (refer **Figure 4.1.16**).

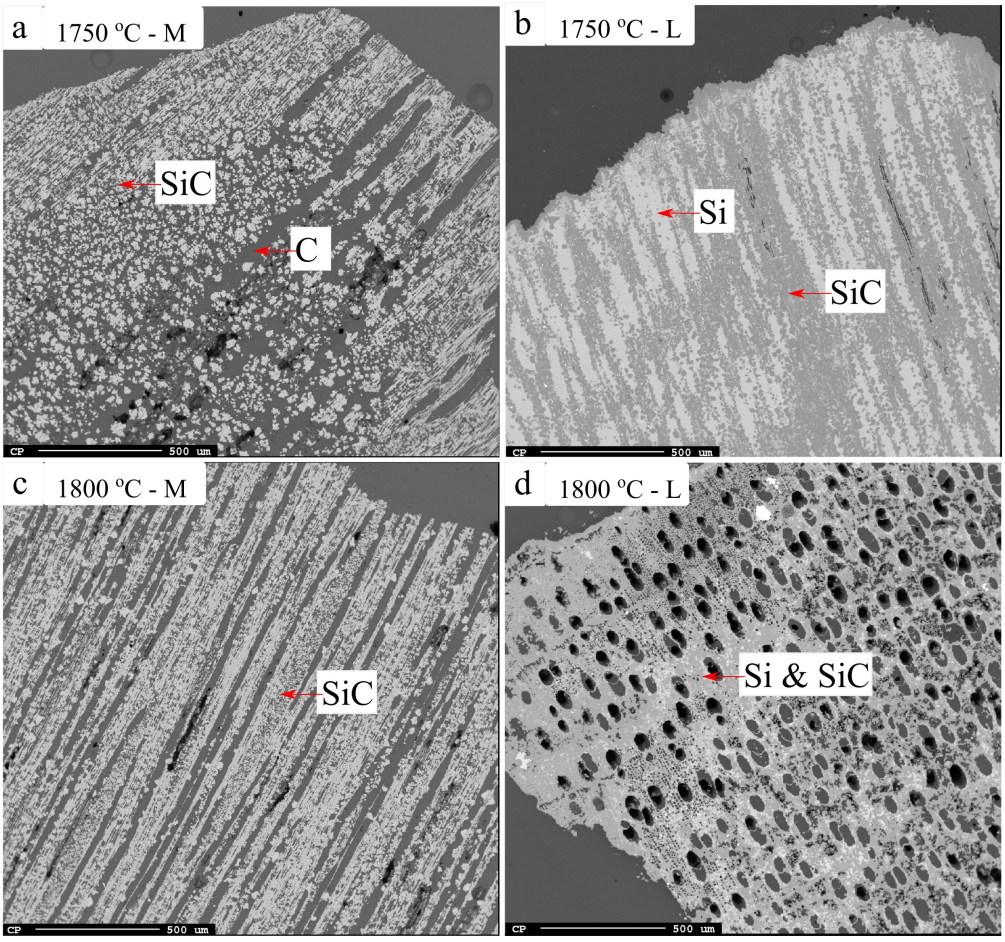

Figure 4.1.21. EPMA-BSE images of charcoal-converted SiC particles collected from (a, c) middle (M) and (b, d) lower (L) regions, after conducting the constant weight induction furnace experiments at 1750 and 1800 °C.

Figure 4.1.22 shows the EPMA-BSE image of a SiC particle from the constant volume induction furnace experiment conducted at 1750 °C using (SiO_2 + SiC) pellets. In these particles SiC has formed homogeneously through the charcoal pores, and hardly any elemental Si phase is present in them.

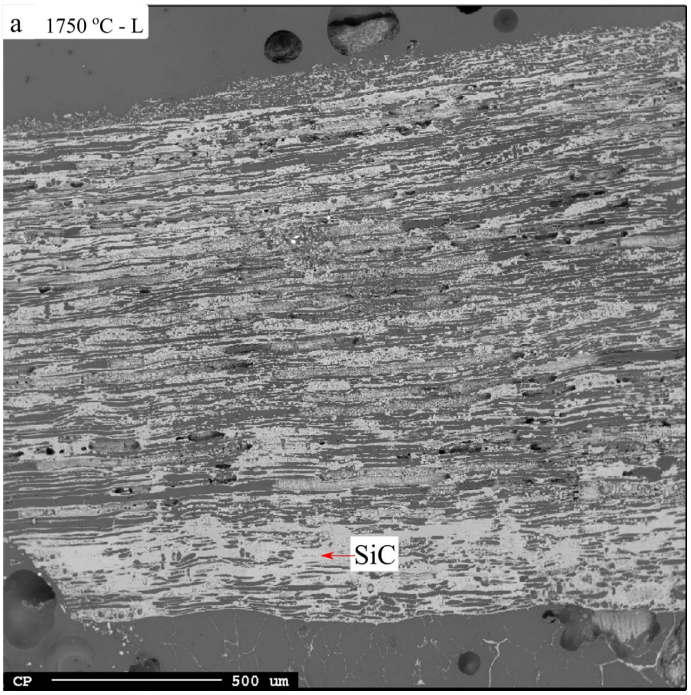

Figure 4.1.22. EPMA-BSE image of charcoal-converted SiC particle from constant volume induction furnace experiment conducted at 1750 °C, using pellets of (SiO_2 + SiC). SiC has formed homogeneously through the charcoal pores, and hardly any elemental Si phase is observed in the particle.

4.1.1.3 XRD analysis

XRD analyses of SiC particles collected from the middle and lower layers were carried out to identify the distinct crystal phases of SiC. The X-ray diffractograms were collected using a Bruker D8 Focus XRD, running in Bragg Brentano collection mode using Cu-Kα radiation, and the data were analyzed using the Bruker Topas v5 software. **Figure 4.1.23** shows the X-ray diffractograms of SiC samples from the lower and middle layers, collected after the constant volume experiments conducted at 1750, 1800, 1850, and 1900 °C. These experiments used a mixture of (SiO_2 + Si) at a higher SiO pressure. The quantitative XRD analysis shows that the SiC particles obtained from charcoal has the cubic form, which is the β-SiC (3C-SiC polytype) phase. Elemental Si peaks are also identified in SiC particles from both the lower and middle layers. However, the highest Si peak is present in the SiC sample that was taken from the lower part. Intensities of the Si peaks increase with increasing temperature, which indicate that Si production increases with an increase in temperature.

EPMA investigation had shown that no elemental Si phase is present in the SiC particles collected from the middle layer. A few grams of SiC particles were crushed to fine powder while

preparing the XRD samples. Among the SiC particles some might have had Si in them. This could be the reason for the presence of elemental Si in the XRD of samples from the middle layer. The chemical analysis also detected Si in the middle layer, which is presented in the next section.

There is hardly any carbon peak (broad peak at around 2θ = 26°) present in the SiC particles. This shows that the original carbon particles have completely transformed to SiC. Overall, presence of Si is observed in all samples produced at temperatures ≥ 1750 °C. β-SiC exhibits twins and stacking faults that lie parallel to the [111]-growth direction. As a result, peak broadening, irregular fluctuations in the background intensities, and extra peaks both at 2θ = 33.7° and 38.3° (shown as red dotted lines in **Figure 4.1.23** to **Figure 4.1.25**) could be observed in the diffractograms.

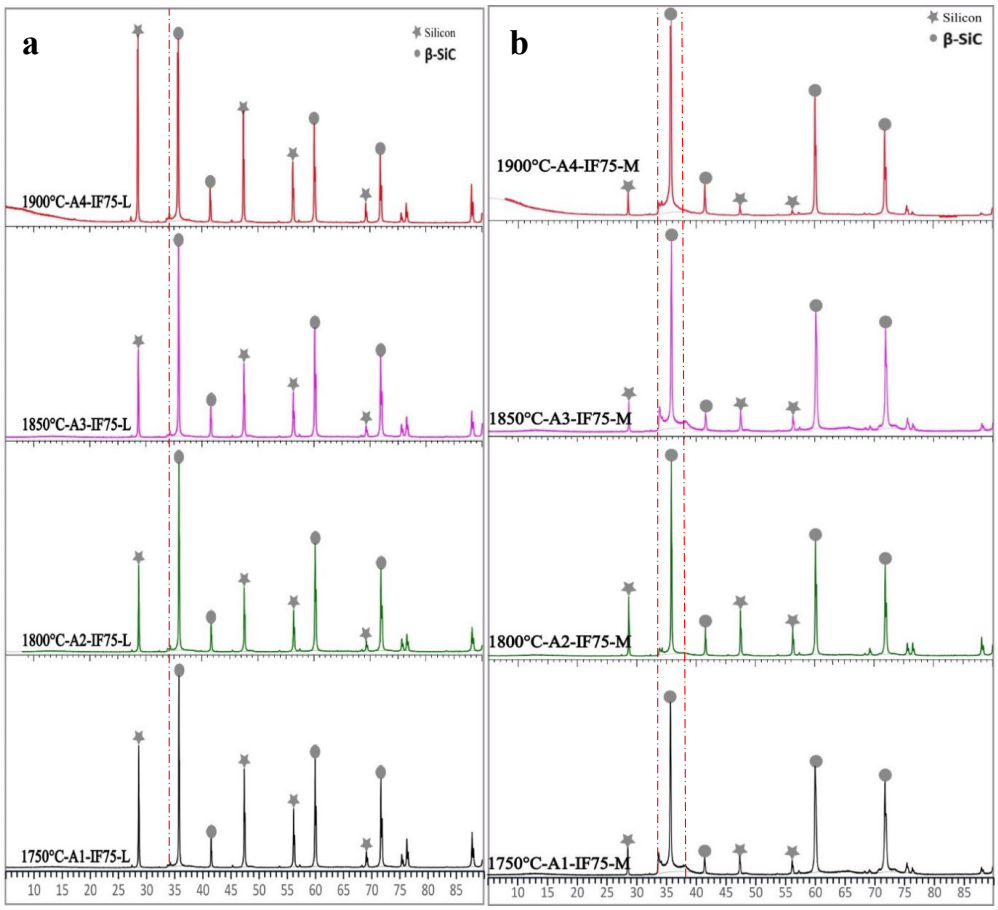

Figure 4.1.23. X-ray diffractograms of charcoal-converted SiC samples from (a) lower (L) and (b) middle (M) layers, from constant volume experiments conducted at 1750, 1800, 1850, and 1900 °C. Only 3C-SiC polytype (100%), which is β-SiC phase, is present in the SiC.

The results described above are all from the constant volume experiments. Similar results were found in samples collected from the constant weight experiments too, as expected. **Figure 4.1.24** depicts the X-ray diffractograms of SiC samples from the middle and lower regions, from the constant weight experiments conducted at 1750 and 1800 °C. The cubic form 3C-SiC polytypes (β-SiC) were identified in the SiC particles. Elemental Si was also present at all temperatures. No carbon peak (broad peak at around 2θ = 26°) is present in these SiC particles.

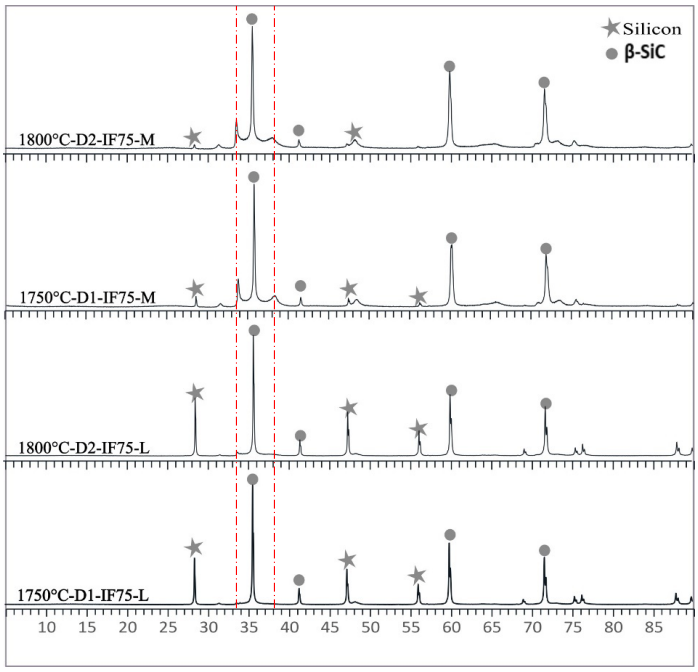

Figure 4.1.24. X-ray diffractograms of SiC samples from lower (L) and middle (M) regions, from constant weight experiments conducted at 1750 and 1800 °C. Cubic form 3C-SiC polytypes (β-SiC) were identified in the SiC particles.

Figure 4.1.25 shows the X-ray diffractogram of SiC particle from the constant volume experiment that used (SiO_2 + SiC) pellets as the source for SiO gas at 1750 °C. The SiC phase is identified as the cubic form, the β-SiC. The Si peaks are hardly noticeable. The (111) peak of 3C-SiC in all the samples, and the elevated background under the peak from $2\theta \geq 33.6°$, are due to the intensity that arises from the stacking faults in the samples. There is a higher crystallinity in SiC samples with Si, and a much lower level of stacking faults in the 3C-SiC polymorph. It is also evident that the scattering (peak broadening at the (111) 3C-SiC) due to stacking faults is reduced in the SiC samples produced at temperatures > 1750 °C. Chemical

analysis of the SiC samples gave information regarding the amount of Si, β-SiC, and free carbon (unreacted carbon) in them, which is presented in the next section.

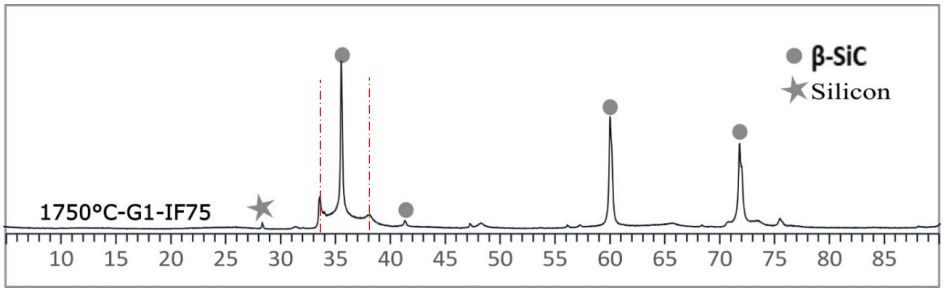

Figure 4.1.25. X-ray diffractogram of SiC particle from constant volume experiment conducted at 1750 °C using (SiO_2 + SiC) pellets. The SiC phase is identified as the cubic form, which is β-SiC. Si peaks are not present in the SiC samples.

4.1.1.4 Chemical analysis

Chemical analysis was carried out to quantify free carbon, β-SiC, and Si in the SiC samples. **Figure 4.1.26** shows the chemical analysis of SiC samples from the middle layer, produced at different temperatures. Less than 10 wt.% of free carbon is left in all the samples, which indicates that some of the SiC particles have not completely converted to SiC. **Figure 4.1.27** shows that in samples from the lower layer, the amount of free carbon is less than 1 wt.%, and the quantity of Si is higher compared with SiC samples from the middle layer. Both these samples are from the constant volume experiments. **Figure 4.1.28** shows samples from the constant weight experiments, displaying similar results as the constant volume experiment samples. Hardly any temperature trend is present in the charcoal-converted SiC samples. This could be expected, as it is the amount of particles in each layer that is changing, not their elemental properties. This indicates that the properties of carbon are the most deciding factors than the temperature, in the formation of SiC. Elemental Si is present in most samples at temperatures ≥ 1750 °C.

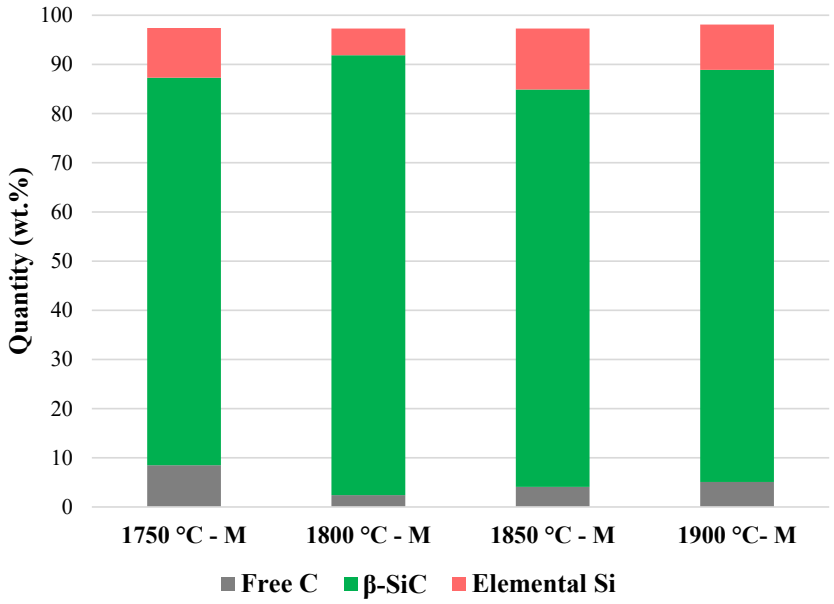

Figure 4.1.26. Chemical analysis of charcoal-converted SiC samples collected from middle layer, after constant volume experiments.

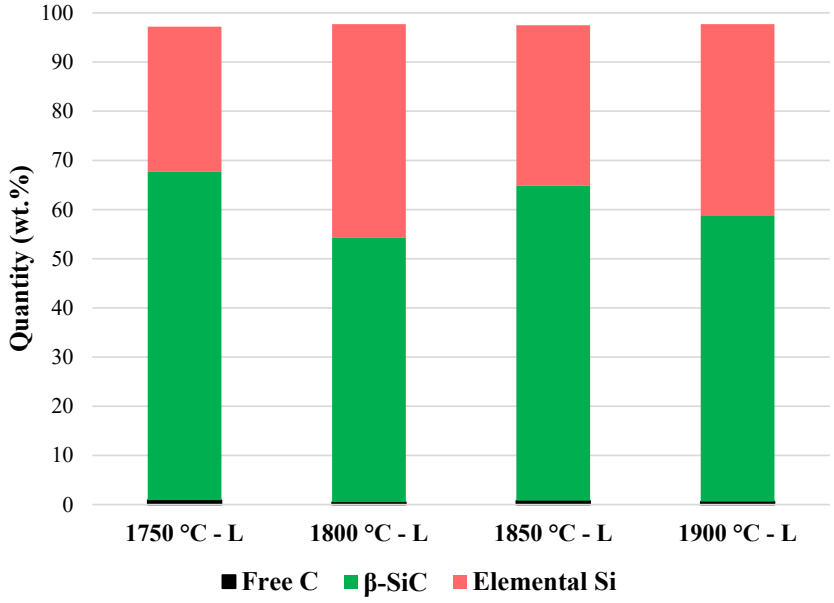

Figure 4.1.27. Chemical analysis of SiC samples from lower layer, collected after constant volume experiments.

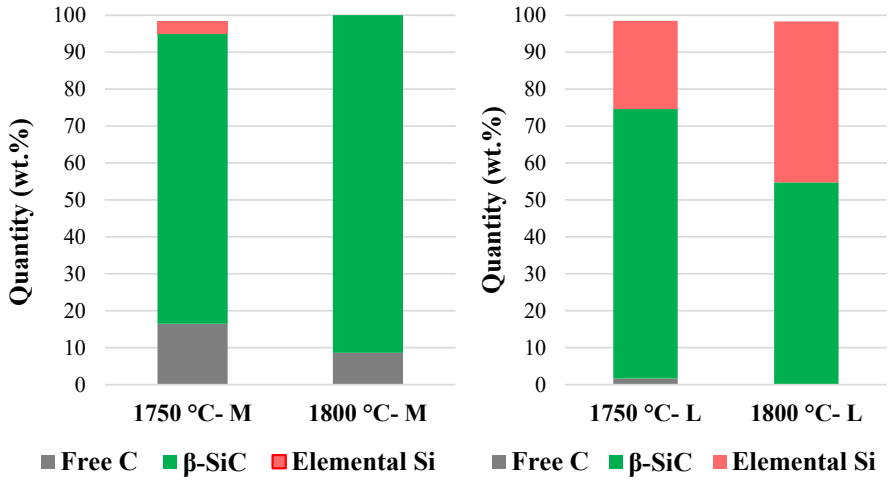

Figure 4.1.28. Chemical analysis of samples from middle (M, left side) and lower (L, right side) layers, collected after conducting constant weight experiments at 1750 and 1800 °C.

Quantities of free carbon, β-SiC, and Si in the SiC particles produced using (SiO_2 + SiC pellets) in the constant volume experiments are shown in **Figure 4.1.29**. The analysis showed that Si has not formed at 1750 °C. However, ~42 wt.% of Si has formed in the SiC samples at 1850 °C.

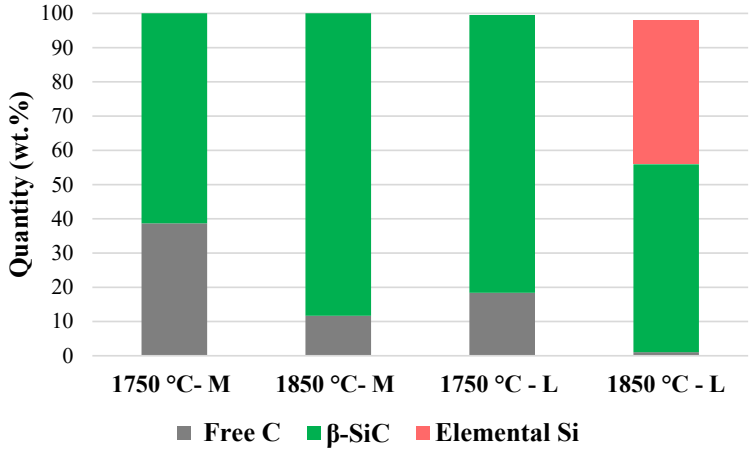

Figure 4.1.29. Chemical analysis of SiC particles produced in middle (M) and lower (L) layers, from the constant volume experiments conducted using (SiO_2 + SiC) pellets.

4.1.1.5 TEM characterization

The TEM characterization of SiC particles produced at 1750 °C was performed to ensure the polytype distribution in the sample. **Figure 4.1.30** shows the BF image and the corresponding SAD pattern of the SiC particle. The SAD pattern was taken from the position marked by the

red circle in **Figure 4.1.30a**. A few particles were analyzed, and all indexed SAD patterns were identified as cubic 3C-SiC polytype growing in [111] direction. No hexagonal SiC phase was found in these samples. The TEM results are in good agreement with the quantitative XRD polytype analysis.

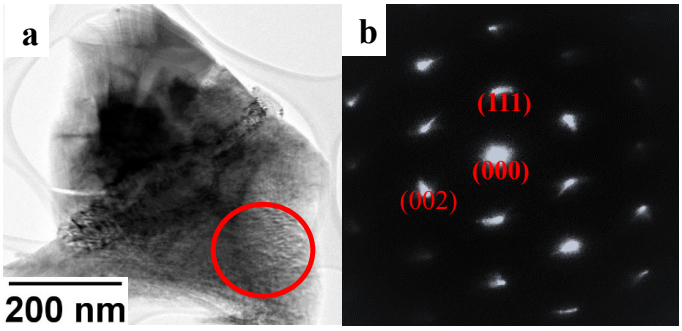

Figure 4.1.30. (a) BF image and (b) corresponding SAD pattern of SiC at 1750 °C. Red circle indicates position from where the SAD pattern was taken. It was identified as cubic 3C-SiC polytype grown in [111] direction.

SiC crystals of different shapes and sizes were observed in the SEM investigation of SiC particles. Interestingly, SiC micro-bullets with six facets, formed in clusters, had grown on the charcoal substrate of some of the selected SiC samples. The shape suggests that these crystals might have the hexagonal SiC phase. To confirm crystallinity of these SiC micro-bullets, their morphology and crystal structure were analyzed using SEM, STEM/TEM, and HAADF-STEM. The overview shown in **Figure 4.1.31a** demonstrates the formation of flower-shaped crystals of SiC with specific bullet-shaped facets. The particles have six regular facets (i.e., hexagonal cross-section) and they grow either solitary (**Figure 4.1.31b**) or in clusters, forming micro-flowers (**Figure 4.1.31c**). Steps and bands are observed on the surface, and in the secondary images, the bands display a strong alternating contrast. These contrasts alter between facets and sometimes even within a band on a facet (marked by red arrow in **Figure 4.1.31b**). The length of the micro-bullets ranges 15–140 µm and their width varies from the bottom to top in a decreasing manner, ranging from 70 to 4 µm. These structures were observed at a reaction temperature of 1700–1800 °C. This suggests that the local reaction conditions play an important role in controlling the morphology.

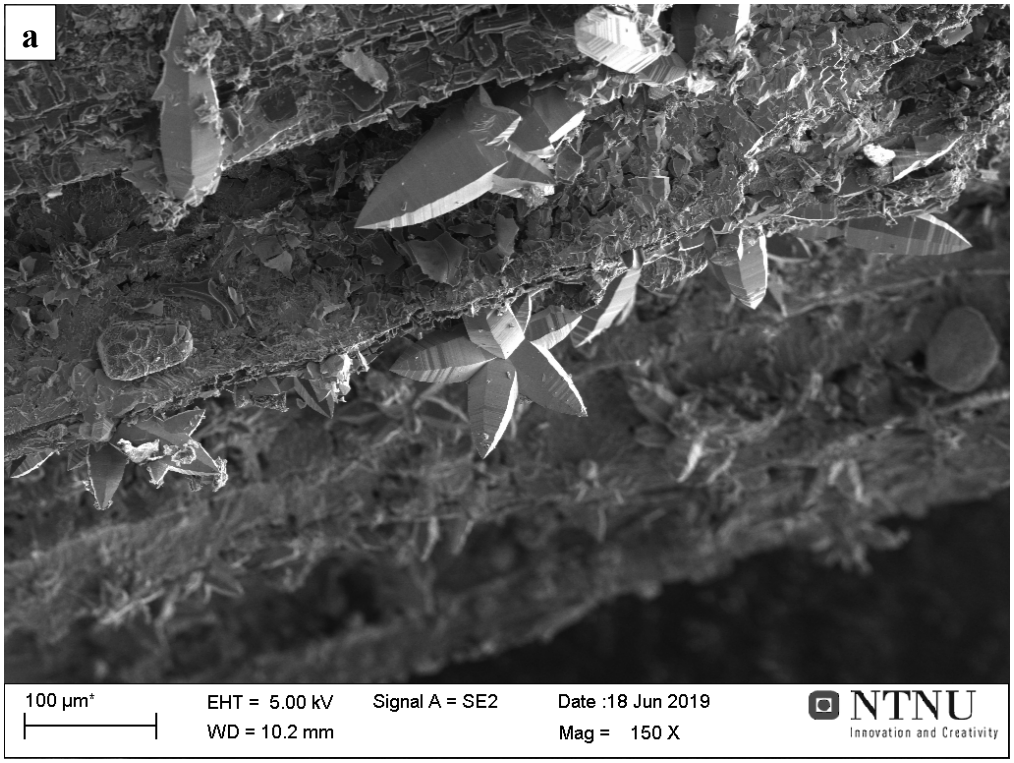
a
100 µm*
EHT = 5.00 kV
WD = 10.2 mm
Signal A = SE2
Date :18 Jun 2019
Mag = 150 X
NTNU
Innovation and Creativity

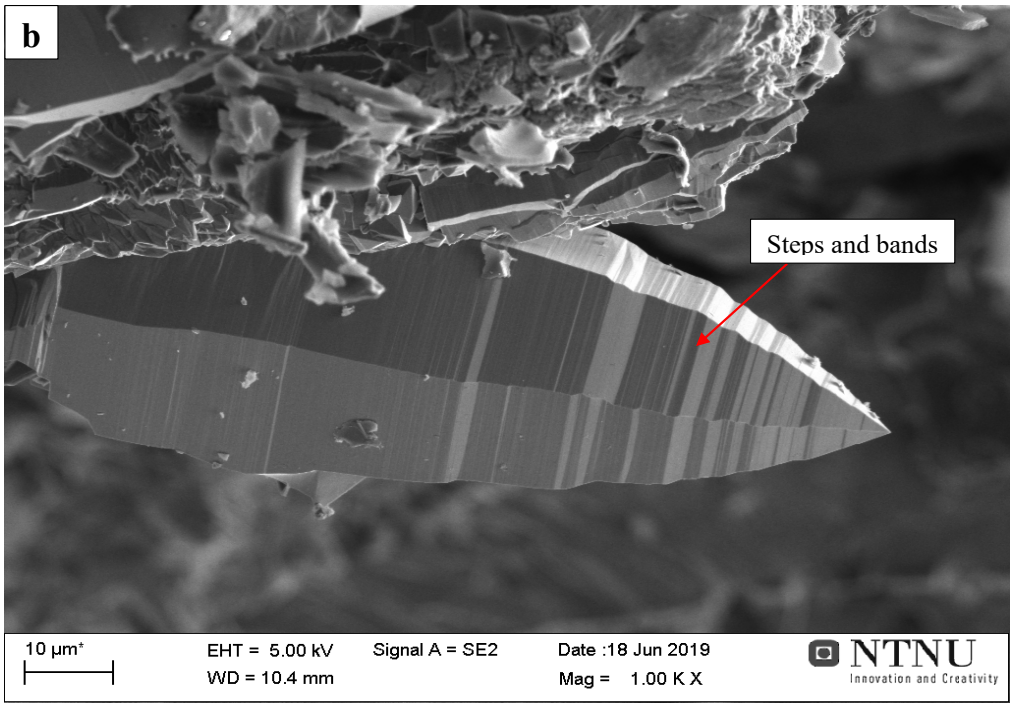
b
Steps and bands
10 µm*
EHT = 5.00 kV
WD = 10.4 mm
Signal A = SE2
Date :18 Jun 2019
Mag = 1.00 K X
NTNU
Innovation and Creativity

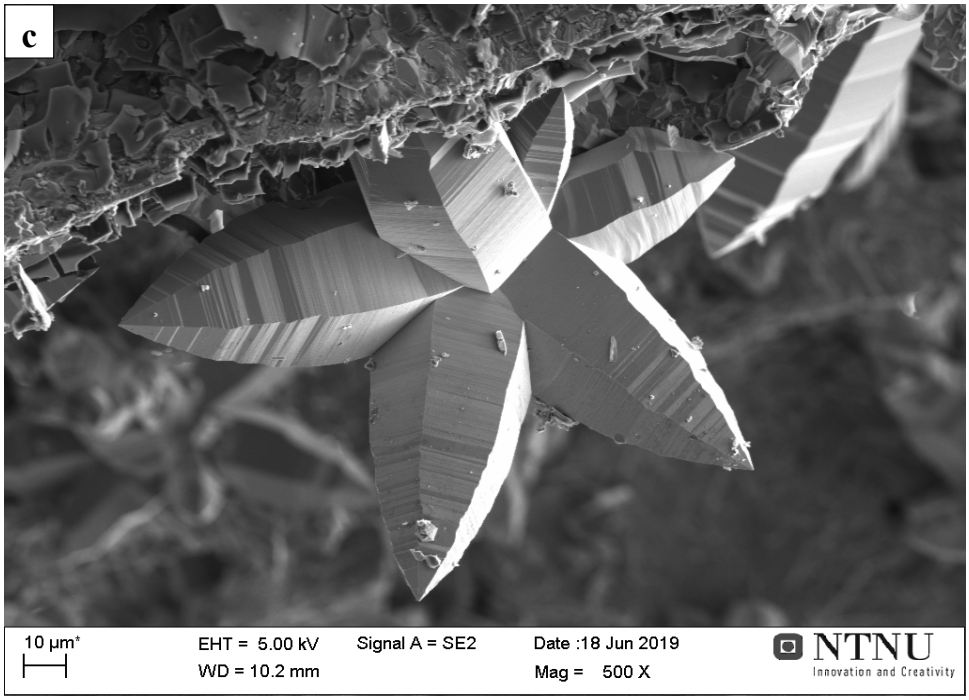

Figure 4.1.31. (a) Overview; secondary electron image of SiC micro-bullets grown on charcoal surface. (b) Micro-bullet with six faces. Red arrows indicate steps and bands. (c) SiC-flower formed by six micro-bullet petals.

To study the microstructures in detail, especially to deduce the crystal phases and lattice defects, and link them to the observed morphology, a TEM lamella of a micro-bullet was extracted using FIB. The chemical compositions of the SiC micro-bullet were investigated by elemental mapping and quantitative analysis using EDX. The elemental mapping was performed along the length of the micro-bullet lamella. Both the spectra and maps show that Si and carbon are uniformly distributed in a nearly 1:1 ratio along the length of the bullet, as shown in **Figure 4.1.32.** This clearly indicates that Si and carbon atoms were readily available throughout the process of crystal growth.

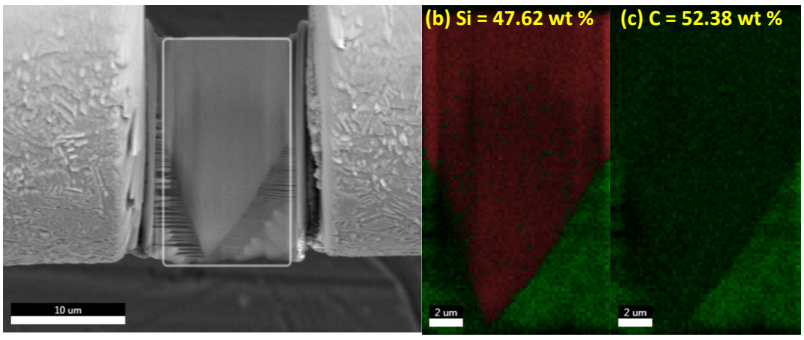

Figure 4.1.32. Elemental mapping and quantitative analysis using EDX. Si and carbon are uniformly distributed in ~1:1 ratio along the length of the bullet.

Figure 4.1.33a, **b**, and **c** show TEM BF cross-section images of respectively the top, middle, and bottom parts of the SiC micro-bullet. The micro-bullet has a high density of planar defects along the entire length of the SiC micro-bullet. The electron diffraction patterns are similar everywhere across the TEM sample up to a depth of ~20 µm, from the top to bottom of the micro-bullet. The indexed diffraction pattern is that of 2H-SiC, and the structure is similar along the bullet. Based on the diffraction patterns, the lattice parameters measured were ***a* = *b* = 3.06 Å** and **c** = **5.04** (+/- 1%), which defines the basic hexagonal unit cell. The streaks or striations in the diffraction pattern along the [0001] direction (**c**-axis) of **Figure 4.1.33d** are due to the high density of non-periodic stacking faults. As they are not periodic, it does not belong to a particular SiC polytype. This shows that the lamella from the SiC micro-bullet might consist of a mixture of different polytypes with a high density of stacking sequence. The author recently published the crystallographic details of these SiC micro-bullets in Jayakumari et al. [112].

The vertical lines seen in the lamella in contrast variation is caused by the minor but abrupt changes in its thickness. Preparing a lamella of even thickness by FIB was challenging due to the morphology of the bullet. Carbon was deposited on either side of the bullet to achieve a flat surface morphology. However, the carbon protection layer, primarily on either side, sputters much faster than the SiC. Additional sputtering was done iteratively with decreasing width to achieve an even lamella thickness.

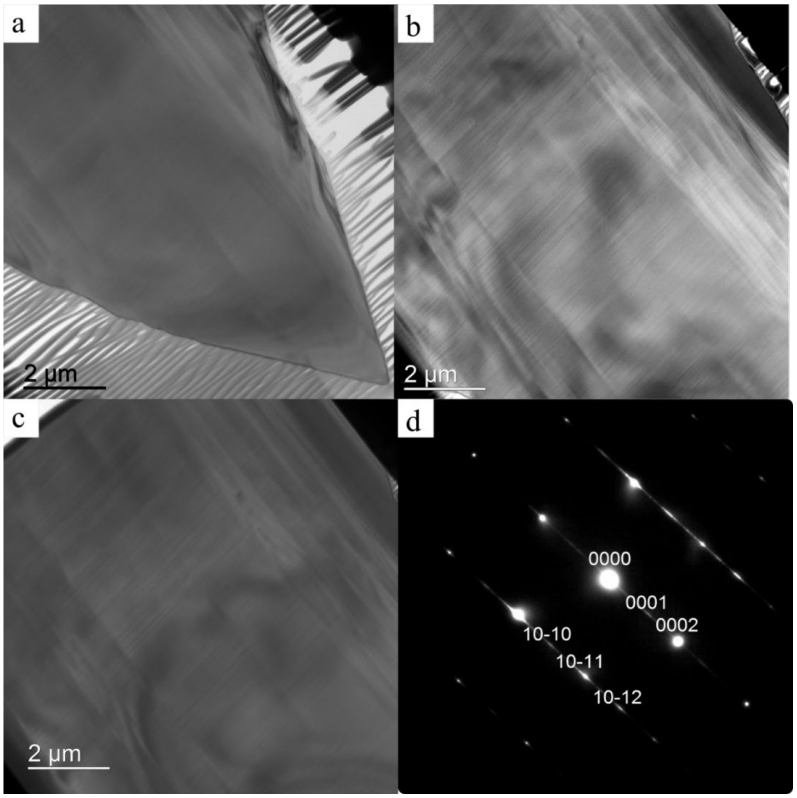

Figure 4.1.33. TEM BF images from (a) top, (b) middle, and (c) bottom parts of micro-bullet. (d) Diffraction pattern taken along [1-210] zone axis from the SiC micro-bullet identified it as 2H-SiC. Streaks in [0001] direction are due to stacking fault density in the growth direction.

The HAADF-STEM technique images a sample on contrast scales of Z^2 (Z = atomic number), which gives an accurate chemical composition of the sample. The HAADF-STEM image shown in **Figure 4.1.34** confirms that the micro-bullet has an even contrast for an even thickness and hence, an even atomic number indicating that only SiC is present. The lack of contrast from any chemical compositions other than SiC is a clear indication of a single-phase material. The variation in the stacking is also visible in the lattice images. The high-resolution TEM (**Figure 4.1.35a**) and the HAADF-STEM (**Figure 4.1.35b**) images reveal that the SiC bullet has a high density of stacking faults, which are common inherent characteristics of SiC bulk and nanomaterials [113, 24]. The steps and bands in the micro-bullets (**Figure 4.1.31b**) observed under SEM could not be found in the TEM BF images of its lamella. Inclusions of non-periodic stacking of planes, i.e., stacking faults, along the unique **c**-axis are present in the whole sample in similar densities. The HAADF-STEM contrast from the lamella proves that the contrast variations

observed on the surface of the SiC micro-bullet are not due to any variations in the chemical composition, such as Si or carbon-rich regions within the SiC.

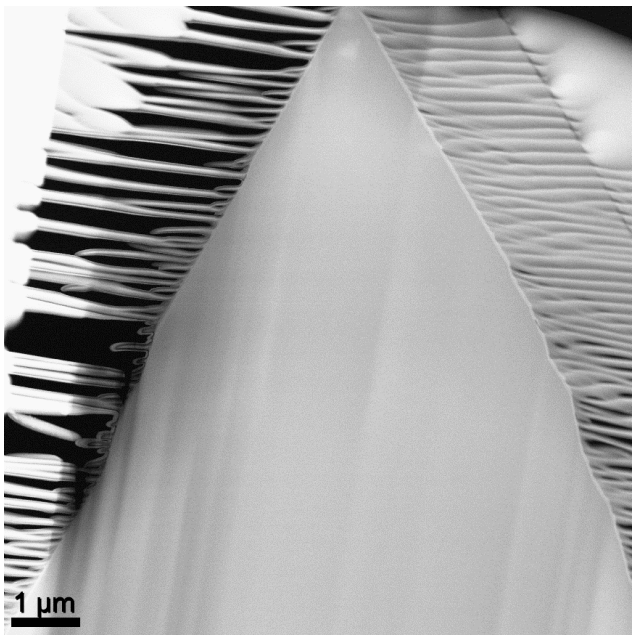

Figure 4.1.34. HAADF-STEM image of SiC micro-bullet. Additional outward protuberance on conical edges of the lamella was created while preparing the sample with FIB.

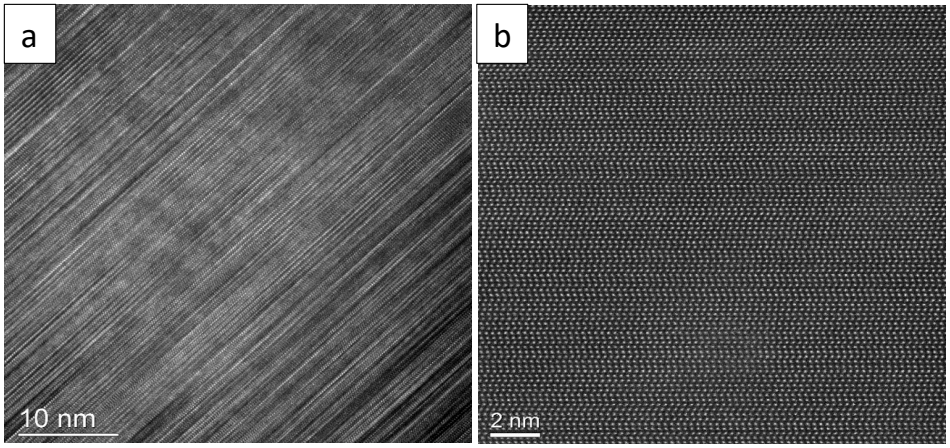

Figure 4.1.35. (a) High-resolution TEM and (b) HAADF-STEM lattice images taken along [1-210] zone axis. SiC micro-bullet has a very high density of stacking faults.

4.1.2 β-SiC production: Graphite tube furnace validation experiments

SiC production experiments were performed in a graphite tube furnace, to validate the results from induction furnace experiments. The experiments in the graphite tube furnace were performed in a controlled manner in a closed environment. The quantities of raw materials used and the target temperatures set for these experiments are detailed in **Table 3-13**. The extraction of samples was effortless, and no fines had formed from the SiC particles. They were collected from the top, middle, and lower layers of the final materials inside the crucibles. **Figure 4.1.36** shows the approximate amounts of the collected samples, from the experiments conducted at 1674, 1755, and 1822 °C. A mixture of (SiO_2 + Si) was used to generate SiO(g) in these experiments. The quantities of charcoal and the final products obtained from the experiments conducted at 1756 °C using pellets of (SiO_2 + SiC) are also presented in **Figure 4.1.36**. These graphs give an approximation of SiC produced by the two different SiO(g) producing materials at various temperatures. In all experiments, the samples in the lower layer of crucibles, where temperatures were higher, show an increase in SiC formation with increasing temperatures. The figure also shows that with pellets of (SiO_2 + SiC), which produce a lower SiO pressure, SiC production was lesser in the lower layer.

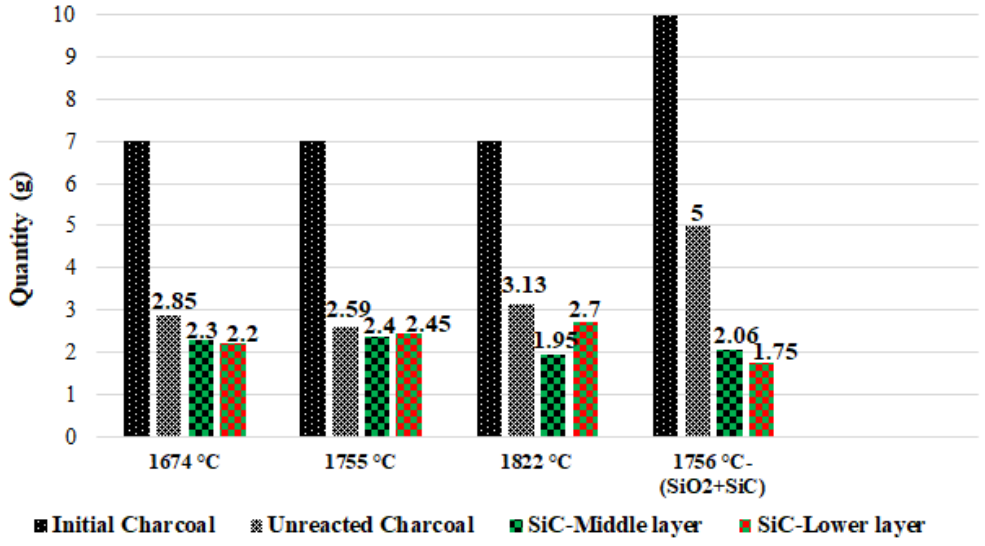

Figure 4.1.36. Quantities of initial charcoal and final products collected after conducting graphite tube furnace experiments at 1674, 1755, 1822, and 1756 °C. First three experiments used a mixture of (SiO_2 + Si) to generate SiO(g). Experiment conducted at 1756 °C used pellets of (SiO_2 + SiC) to generate SiO(g).

These samples, collected from the three different layers at four different temperatures, from the experiments conducted using (SiO_2 + Si) and pellets of (SiO_2 + SiC), were further analyzed as described in the following sections.

4.1.2.1 SEM morphology

SEM morphologies of the SiC samples collected from the different layers of the crucibles, after conducting the experiments at 1674, 1755, and 1822 °C are shown in **Figure 4.1.37** to **Figure 4.1.39**, respectively. A mixture of (SiO_2 + Si) was used to generate SiO(g) in these three experiments. Fine whiskers and only a few seed crystals of SiC have formed in the charcoal pores of the samples in the top layer. The particles in middle layer have thicker whiskers compared with those in the top layer. This confirms that the carbon materials in the top layer was exposed to comparatively lower temperatures and lesser amounts of SiO(g) than those in the middle and the lower layers. However, the charcoal structure is clearly visible in particles from both top and middle layers. In particles from the lower layer, the original charcoal structure disappears, and the particle becomes denser. An increase in crystal size and growth are also observed with an increase in temperature.

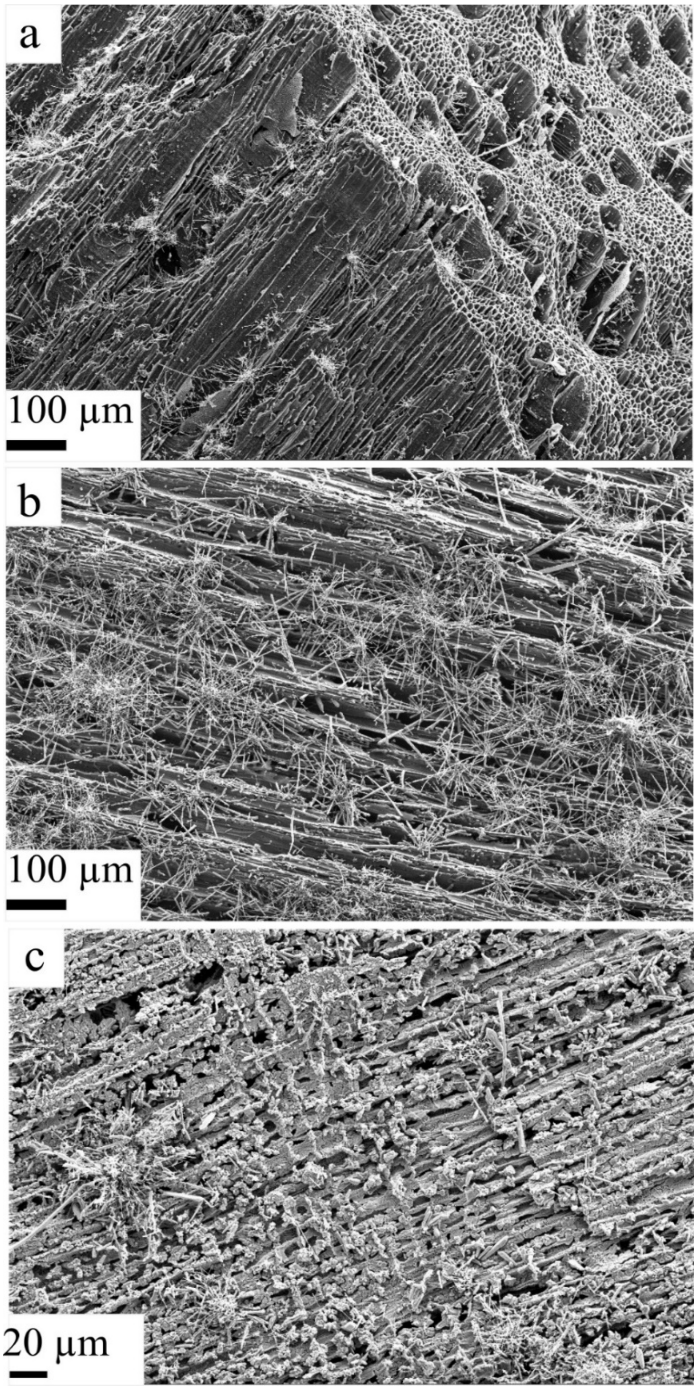

Figure 4.1.37. SEM morphologies of charcoal-converted SiC samples from (a) top, (b) middle, and (c) lower layers, collected after conducting experiments in graphite tube furnace at 1674 °C. Charcoal structure is clearly visible in particles in top and middle layers.

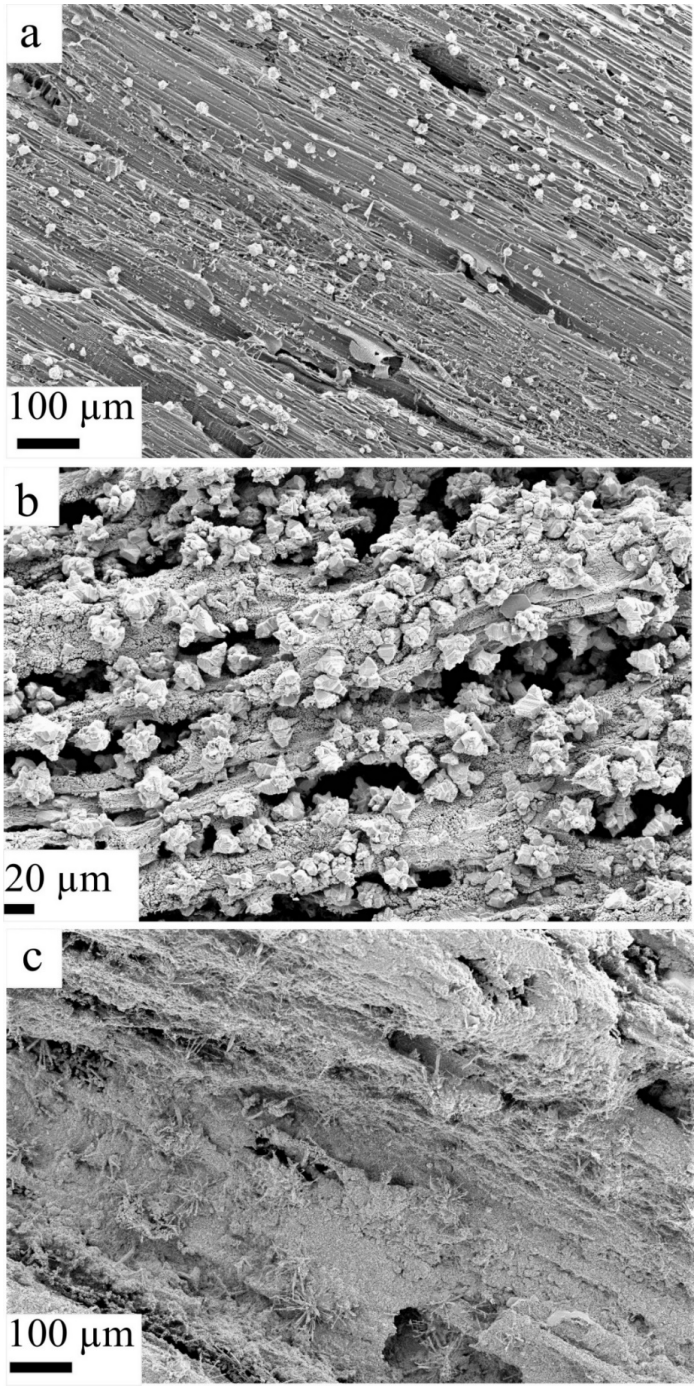

Figure 4.1.38. SEM morphologies of charcoal-converted SiC samples from (a) top, (b) middle, and (c) lower layers, collected after conducting experiments in graphite tube furnace at 1755 °C.

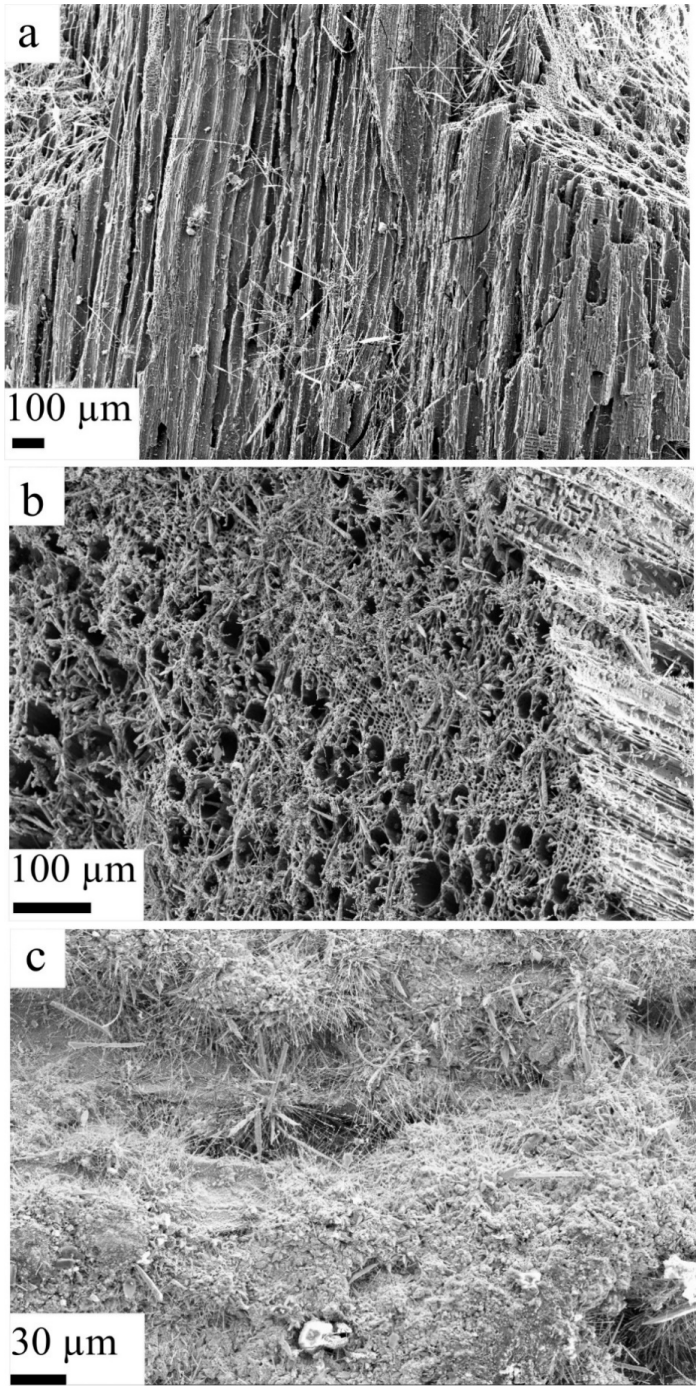

Figure 4.1.39. SEM morphologies of charcoal-converted SiC samples from (a) top, (b) middle, and (c) lower layers, from experiments conducted in graphite tube furnace at 1822 °C. Charcoal structure is clearly visible in particles in top and middle layers.

The SEM morphologies of SiC samples from the middle and lower layers of the experiments conducted at 1756 °C are presented in **Figure 4.1.40**. Pellets of (SiO_2 + SiC) were used in this experiment to generate SiO(g). The characteristics of SiC particles are similar to their counter parts from the experiments conducted with (SiO_2 + Si). Fine whiskers of SiC crystals have formed in the middle layer, while retaining the original structure of charcoal. In the lower layer, the whiskers have become thicker, and more SiC crystals have developed as the charcoal structure disappears.

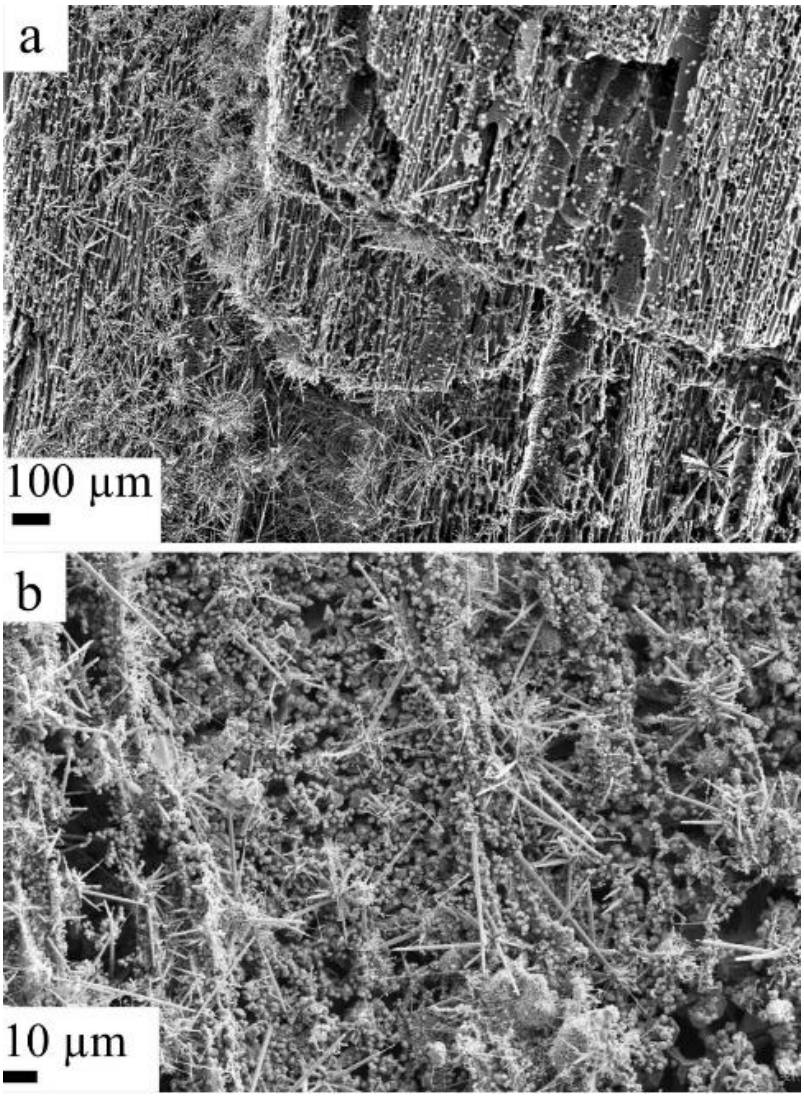

Figure 4.1.40. SEM morphologies of charcoal-converted SiC samples collected from (a) middle and (b) lower layers of graphite tube furnace. These experiments were conducted at 1756 °C, using pellets of (SiO2 + SiC) to generate SiO(g).

There is a condensation chamber in the graphite tube furnace to collect the off-gas products. No condensates were observed in the chamber after conducting the experiments using a mixture of (SiO_2 + Si). However, white and light bluish colored condensates were observed on the surfaces of the particles filled in the condensation chamber, after conducting experiments with pellets of (SiO_2 + SiC). The condensates observed on the surfaces of the particles are shown in **Figure 4.1.41** and their SEM image is shown in **Figure 4.1.42**. **Figure 4.1.43** shows the EDX from the condensates and it confirms that these white layers mainly consist of Si and O, i.e., SiO_2 and Si. Some carbon is also visible, which indicates that some (SiO_2 + SiC) might also be present.

Figure 4.1.41. White and light bluish condensates observed on surfaces of particles used for filling the condensation chamber, from experiments performed with pellets of (SiO_2 + SiC).

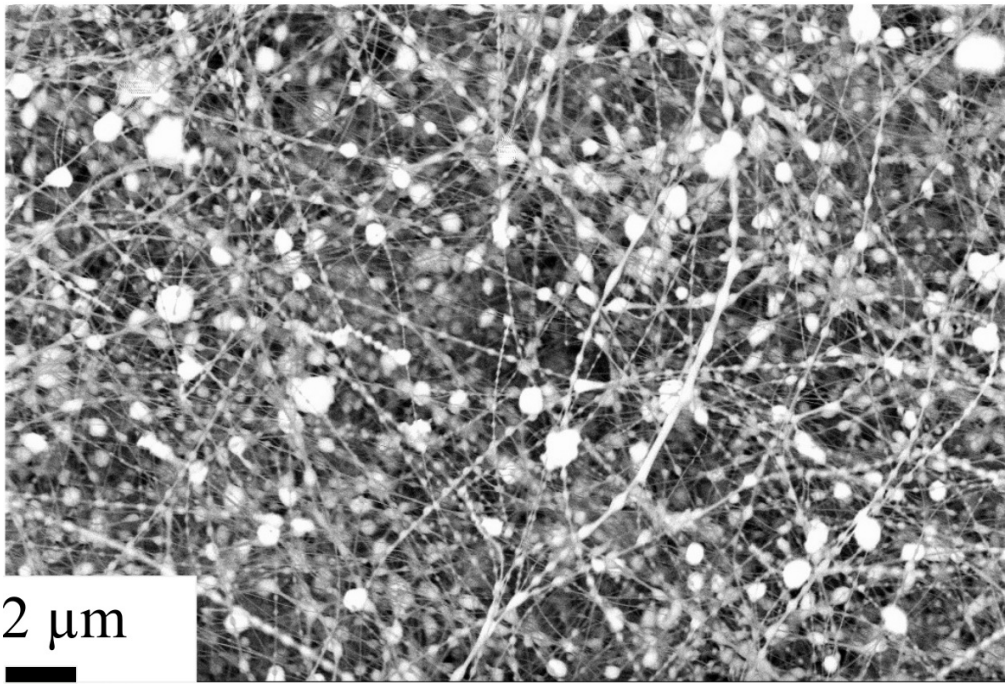

Figure 4.1.42. SEM image of condensates observed on surfaces of particles filled in the condensation chamber.

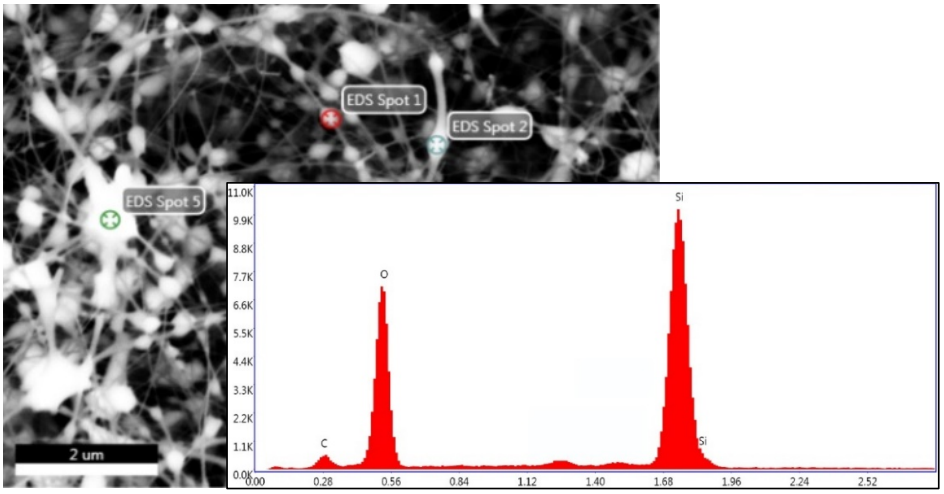

Figure 4.1.43. EDX of condensates on surfaces of particles in the condensation chamber. White layers mainly consist of Si and O, i.e., SiO_2 and Si. Some carbon is also visible, therefore it is assumed that some (SiO_2 + SiC) might also be present.

4.1.2.2 Chemical analysis and EPMA-BSE imaging

Chemical and EPMA-BSE analyses of the SiC particles were performed to evaluate their elemental characteristics. A higher amount of carbon in the samples increases the uncertainty in measurements, hence the amount of elemental Si in the SiC particles could not be calculated. Only the amount of SiC formed in the different layers could be calculated, which is presented in **Figure 4.1.44**. At 1755 °C, twice the amount of SiC was produced by (SiO_2 + Si), compared with pellets of (SiO_2 + SiC) at 1756 °C (bars in magenta color), which proves that more SiC production is possible with (SiO_2 + Si) at a higher SiO(g) pressure.

EPMA analysis of samples from the lower layer was carried out to confirm the formation of elemental Si in the SiC particles at temperatures lower than the theoretical value of 1811 °C. As **Figure 4.1.45** and **Figure 4.1.46** show, elemental Si has formed in the SiC particles in the lower layer in the experiments conducted at 1674 and 1755 °C using (SiO_2 + Si). However, no traces of elemental Si is present in the SiC particles formed from (SiO_2 + SiC) at 1756 °C (**Figure 4.1.47**).

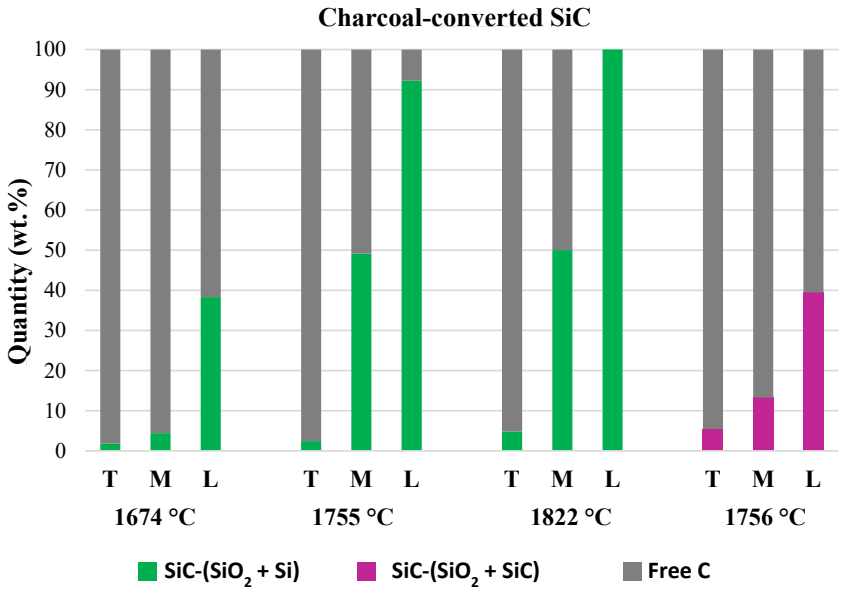

Figure 4.1.44. Quantities of SiC and unreacted carbon in SiC samples collected from top (T), middle (M), and lower (L) layers. Samples from experiments conducted using pellets of (SiO_2 + SiC) at 1756 °C are presented on the right end (magenta color bars). Other samples are from experiments conducted using (SiO_2 + Si) at 1674, 1755, and 1822 °C.

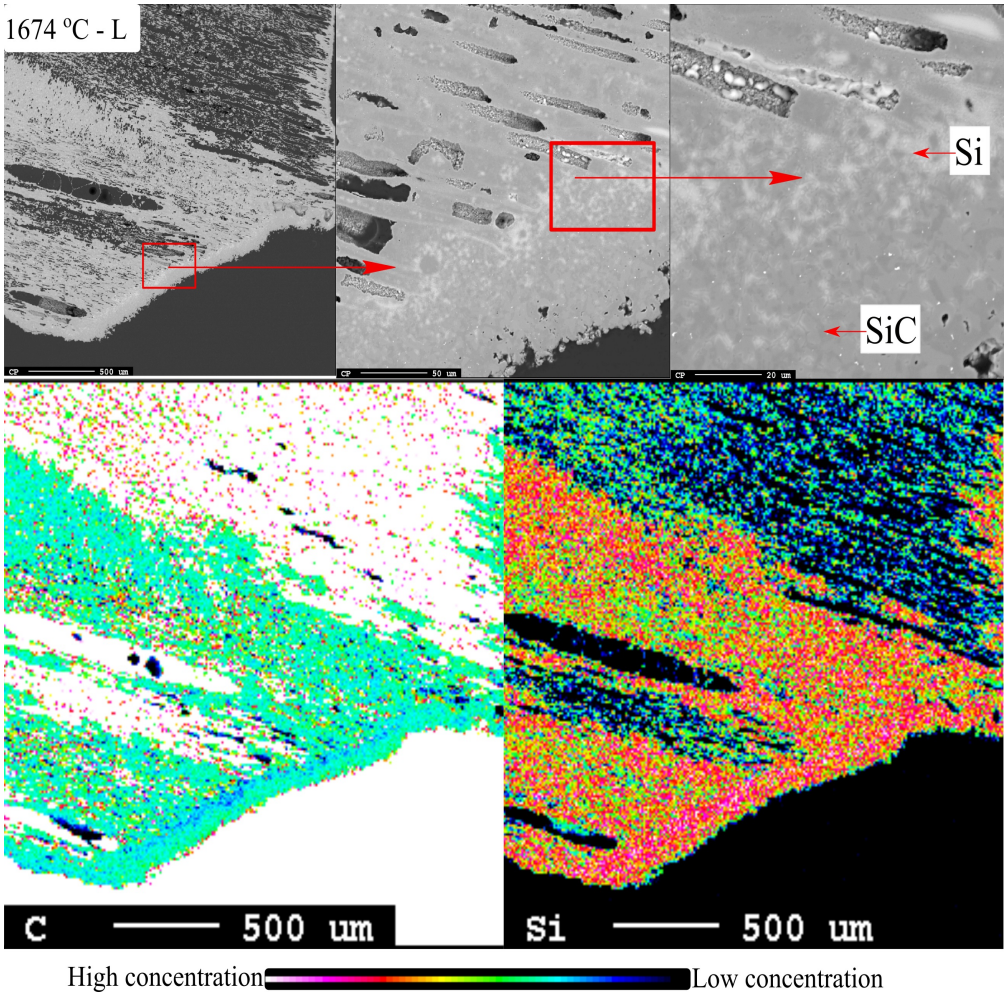

Figure 4.1.45. EPMA of SiC particle from lower (L) layer, produced at 1674 °C using (SiO_2 + Si). Magnified picture shows formation of Si in SiC. Elemental mapping of carbon and Si show traces of elemental Si in SiC particle.

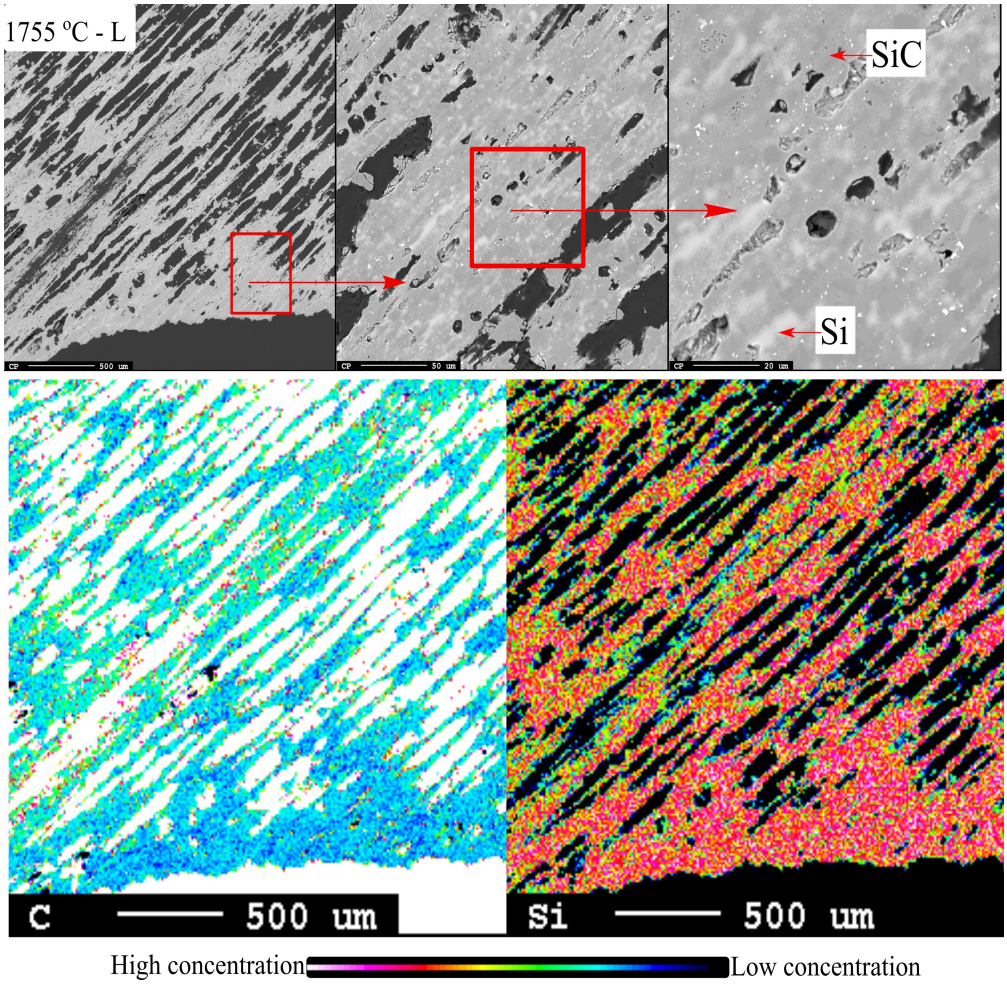

Figure 4.1.46. EPMA of SiC from lower layer (L), produced at 1755 °C using (SiO_2 + Si). Elemental distributions of carbon and Si show traces of elemental Si in SiC particle.

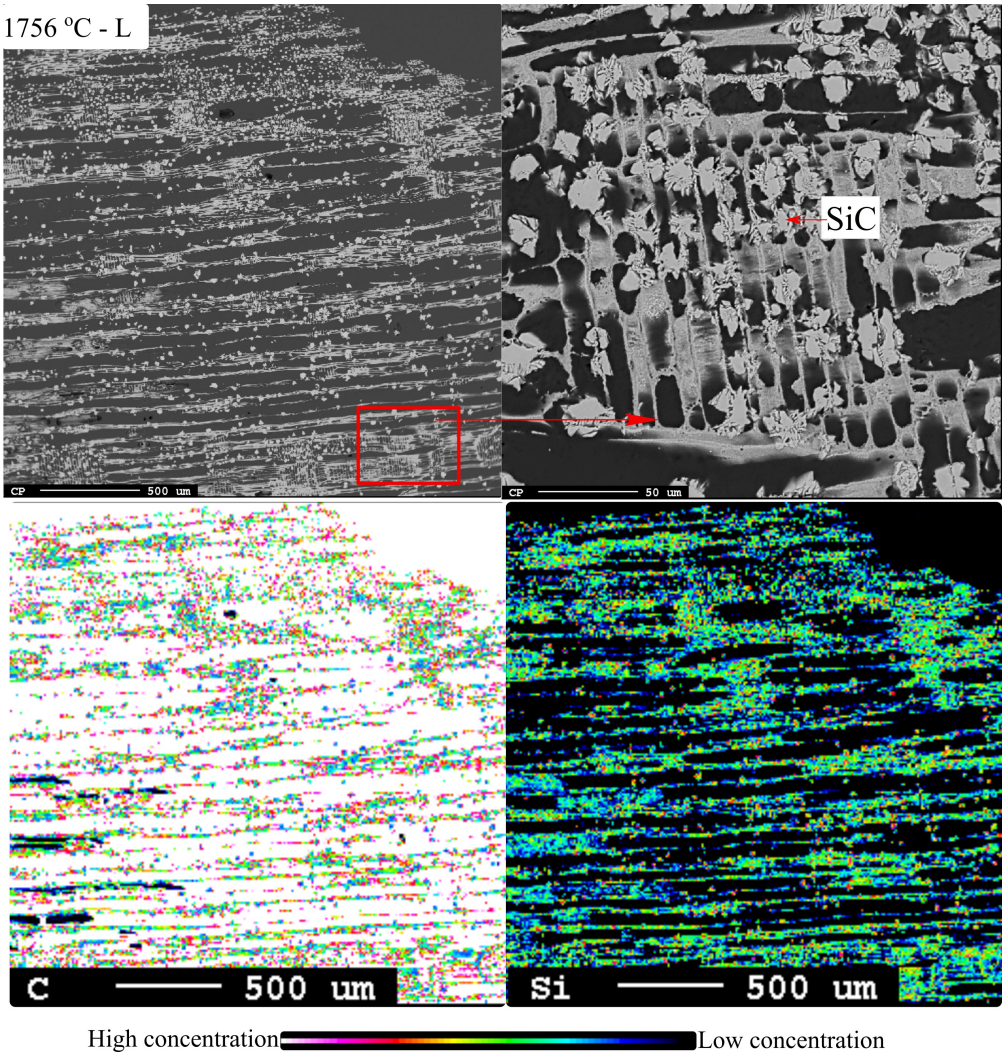

Figure 4.1.47. EPMA of SiC from lower layer (L), produced at 1756 °C using pellets of (SiO_2 + SiC). Elemental distributions of carbon and Si show no traces of elemental Si in SiC particle.

4.1.3 Transformation to α-SiC: Graphite tube furnace experiments

The graphite tube furnace was used again for this set of experiments to study the changes materializing in the structure of β-SiC, when it is exposed to extreme heat. β-SiC particles collected from the middle (with 9 wt.% elemental Si) and lower (with 39 wt.% Si) layers of the initial carbon layer, from the induction furnace experiments conducted at 1900 °C, were used in these experiments, to convert them to α-SiC. The samples were heated at 2100, 2300, and 2450 °C. Details of these experiments are presented in **Table 3-14**. **Figure 4.1.48** shows the β-SiC samples from the middle and lower layers, before and after the heat-treatment. The heat-treated SiC changes its color from greenish-blue to black, and its surface roughens compared with the β-SiC particles before heating. Precipitation of small crystals on the particle surface is also visible, especially on the heat-treated β-SiC samples that had a higher quantity of elemental Si (39 wt.%) in them.

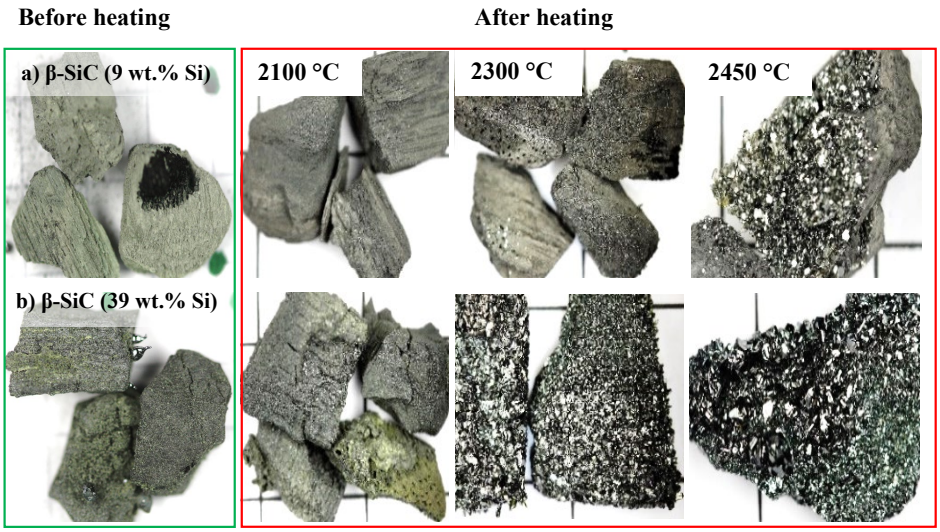

Figure 4.1.48. Charcoal-converted β-SiC samples collected from (a) middle (M, with 9 wt.% Si) and (b) lower (L, with 39 wt.% Si) layers of induction furnace, before and after they were heat-treated at 2100, 2300, and 2450 °C in graphite tube furnace.

A few β-SiC samples collected from the induction furnace experiments conducted at 1750 °C, which had no elemental Si present in them, were also heated in the graphite tube furnace. Details of these experiments are presented in **Table 3-17**. The samples obtained after the experiments in the graphite tube furnace were further analyzed as described in the following sections to evaluate the formation of α-SiC in them.

4.1.3.1 SEM morphology

Figure 4.1.49 depicts the SEM morphologies of β-SiC samples containing 39 wt.% Si (images on the left) and 9 wt.% Si (images on the right) that were heat-treated to 2100, 2300, and 2450 °C. Both the macroscopic and microscopic structures show changes occurring during the transformation from β-SiC to α-SiC. Crystals shaped as hexagonal-plates have formed after the heat-treatment. More such crystals form as the temperature increases. These new SiC crystals are very dense, and the original carbon structure exists no more in these samples.

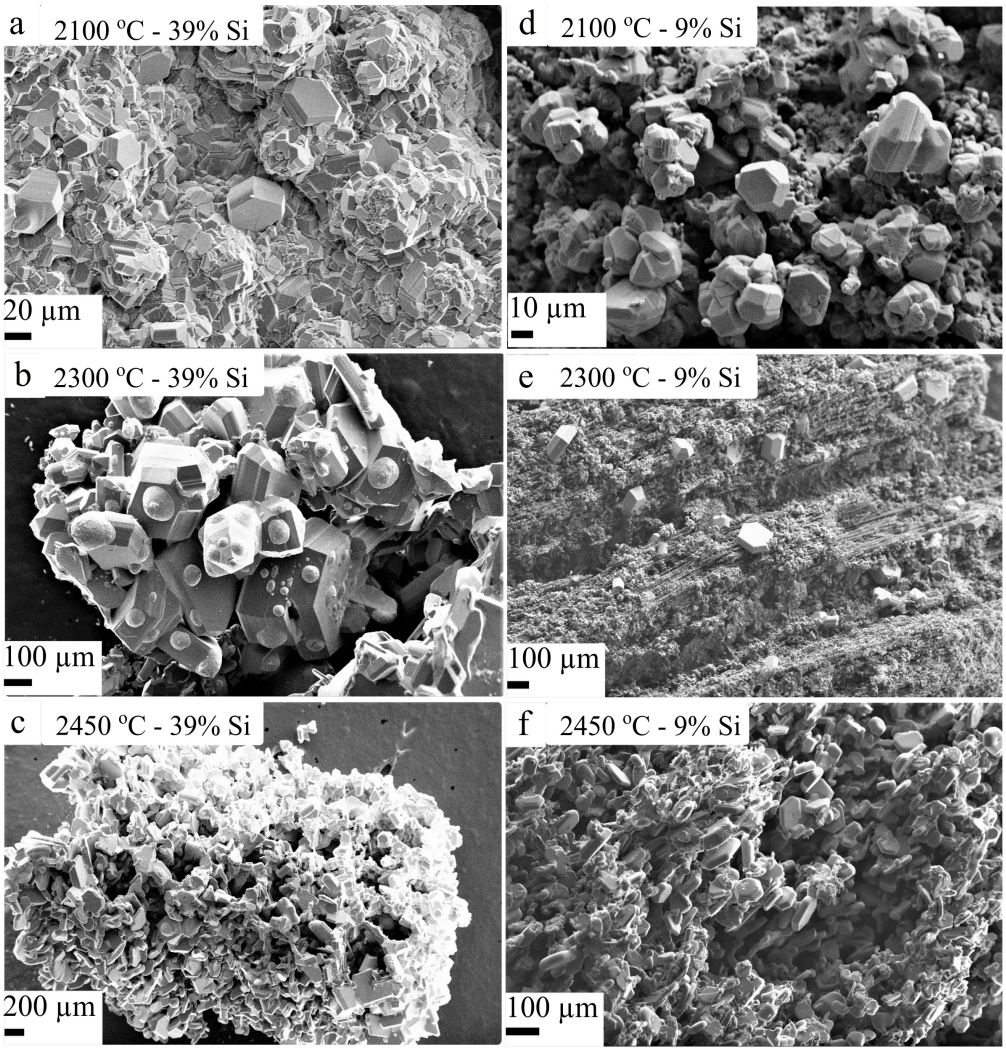

Figure 4.1.49. SEM morphologies of β-SiC samples heat-treated at 2100, 2300, and 2450 °C in graphite tube furnace. β-SiC samples with (a–c) 39 wt.% Si and (d–f) 9 wt.% Si were collected respectively from lower and middle layers from induction furnace.

4.1.3.2 EPMA-BSE imaging

Figure 4.1.50 shows the corresponding EPMA-BSE images of the heat-treated β-SiC samples with 9 and 39 wt.% Si. The hexagonal-plate like crystals observed in the SEM images (**Figure 4.1.49**) are visible in the EPMA images too, especially in the SiC sample at 2450 °C. These crystals are highlighted with red arrows in **Figure 4.1.50c** and **f**.

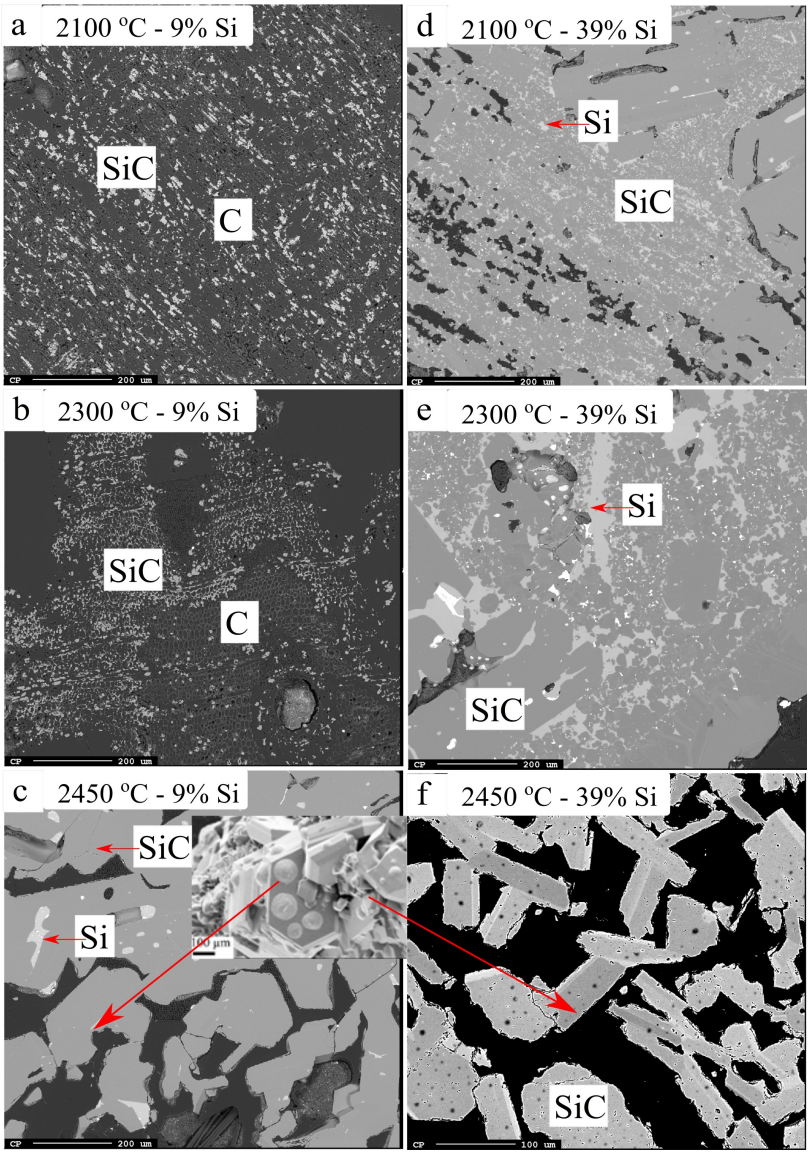

Figure 4.1.50. EPMA-BSE images of heat-treated β-SiC samples with (a–c) 9 wt.% Si and (d–f) 39 wt.% Si, after exposed to 2100, 2300, and 2450 °C. Inset in plot (c) shows corresponding SEM image of SiC particle.

4.1.3.3 XRD analysis

The X-ray diffractograms of the samples were analyzed using Topas. As β-SiC was the main constituent in the preliminary material used for the experiments, it was included in the Rietveld refinement by Topas. Besides the already identified phases, i.e., Si and SiC, several of the samples showed a broad peak at around 2θ = 26°. This could be arising from the unreacted carbon phase in the SiC particles and was not quantified in the analysis.

Figure 4.1.51 shows the different SiC phases formed in the β-SiC sample with 39 wt.% Si, after it was heated at 2450 °C. The most intense SiC peak is located at 2θ = 35.8°, overlapped with Bragg reflections 111-3C, 004-4H, 006-6H, 012-6H, 0015-15R, and 015-15R. The graph shows good agreement between the observed and calculated XRD patterns. The presence of α-SiC polytypes such as 4H, 6H, and 15R are established from their isolated peaks in the XRD data. The peaks are formed at 2θ = 46.26° and 49.7° for 4H, 2θ = 34.1° and 45.3° for 6H, and 2θ = 37.5° and 47.8° for the 15R polytypes.

Prior to heating, some samples had quite a higher amount of Si. However, upon heating, the number of Si peaks decreased gradually (**Figure 4.1.52** and **Figure 4.1.53**). The samples exhibited a variety of structural polymorphs of SiC, in particular the 3C and 6H versions. The SiC phases show considerable evidence of disorder/stacking faults, resulting in peak broadening in the 3C-SiC (111) position. Due to the defects in the SiC crystal, high intensities of stacking faults lead to extra peaks at 2θ = 33.7° and 38.3°. These high densities of defects in the starting material are also involved in the β to α transformation; the heavily twinned β-SiC provides a high density of sites for the α-SiC nucleation [114].

The quantitative phase composition analysis showed that the major polytypes identified from the diffractogram in **Figure 4.1.51** are 4H (18.6 wt.%), 6H (61.6 wt.%), and 15R (15.7 wt.%). The amount of Si was found to be 3.48 wt.%. The presence of α-SiC polytypes confirms that increasing temperature caused the transformation from β to α in the samples. The vertical bars close to the x-axis in **Figure 4.1.51** shows the angular position of the allowed Bragg reflections (d-spacings).

Figure 4.1.52 to **Figure 4.1.54** are the X-ray diffractograms of the heat-treated β-SiC with respectively 0, 9, and 39 wt.% Si in it. The fitted diffractograms show good agreement between the observed and calculated XRD patterns of all SiC samples that were quantitatively analyzed by Topas. From **Figure 4.1.54** it is evident that when a SiC particle with a high intensity Si peak (39 wt.% Si) is heat-treated at 2100 °C, peak broadening occurs and new peaks starts forming at the 3C (111) position. The quantity of Si in the SiC enhances the extent of α

transformation in this case. Whereas, **Figure 4.1.52** shows that in a SiC particle with a lesser amount of Si, the stacking fault reduces initially and the peak broadening disappears, as the temperature increases at 2100 °C. In this case, the α-SiC transformation requires a higher temperature. The fitted diffractograms of all SiC samples are provided in Appendix B. The summary of quantitative SiC polytypes in all heat-treated SiC samples identified by Topas are presented in **Figure 4.1.55** to **Figure 4.1.57**.

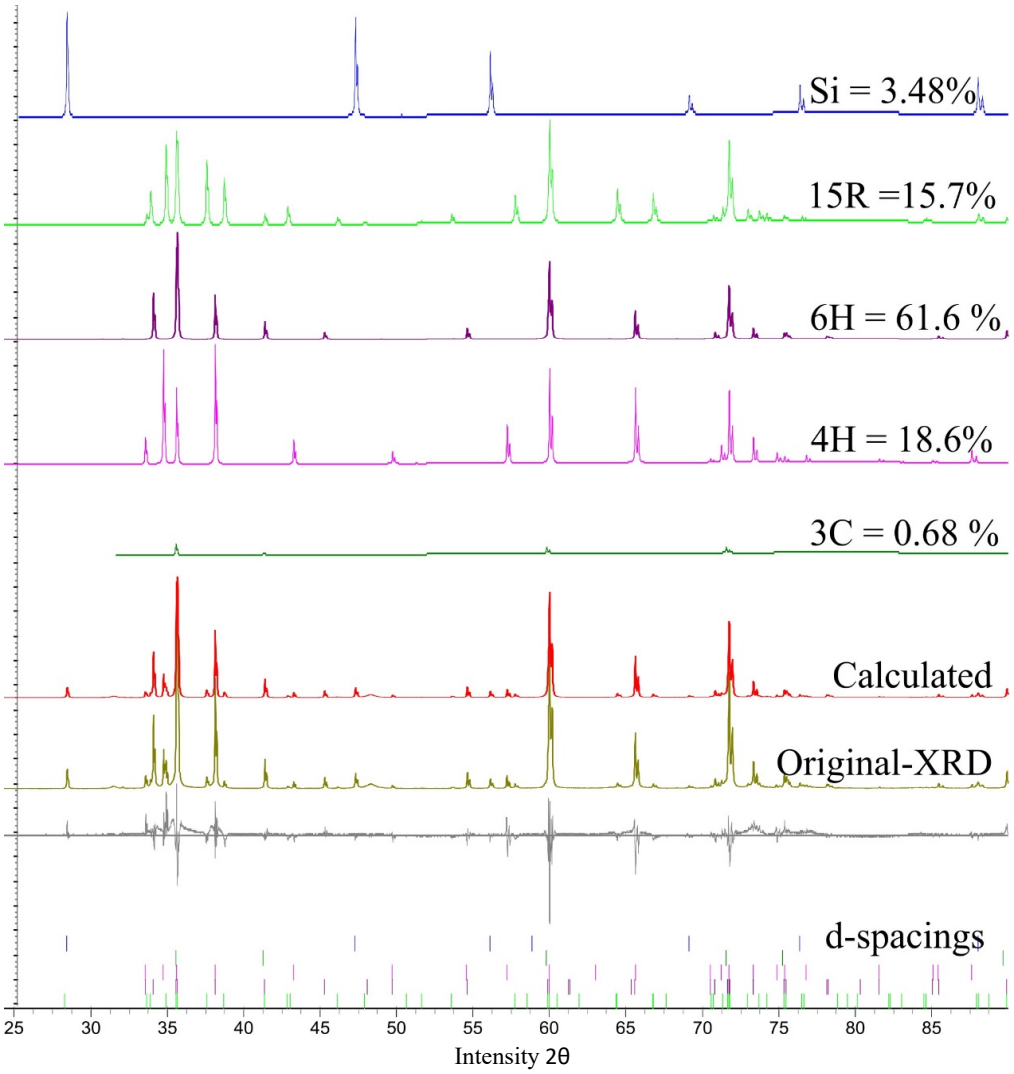

Figure 4.1.51. Different SiC phases formed after heating β-SiC sample with 39 wt.% Si at 2450 °C.

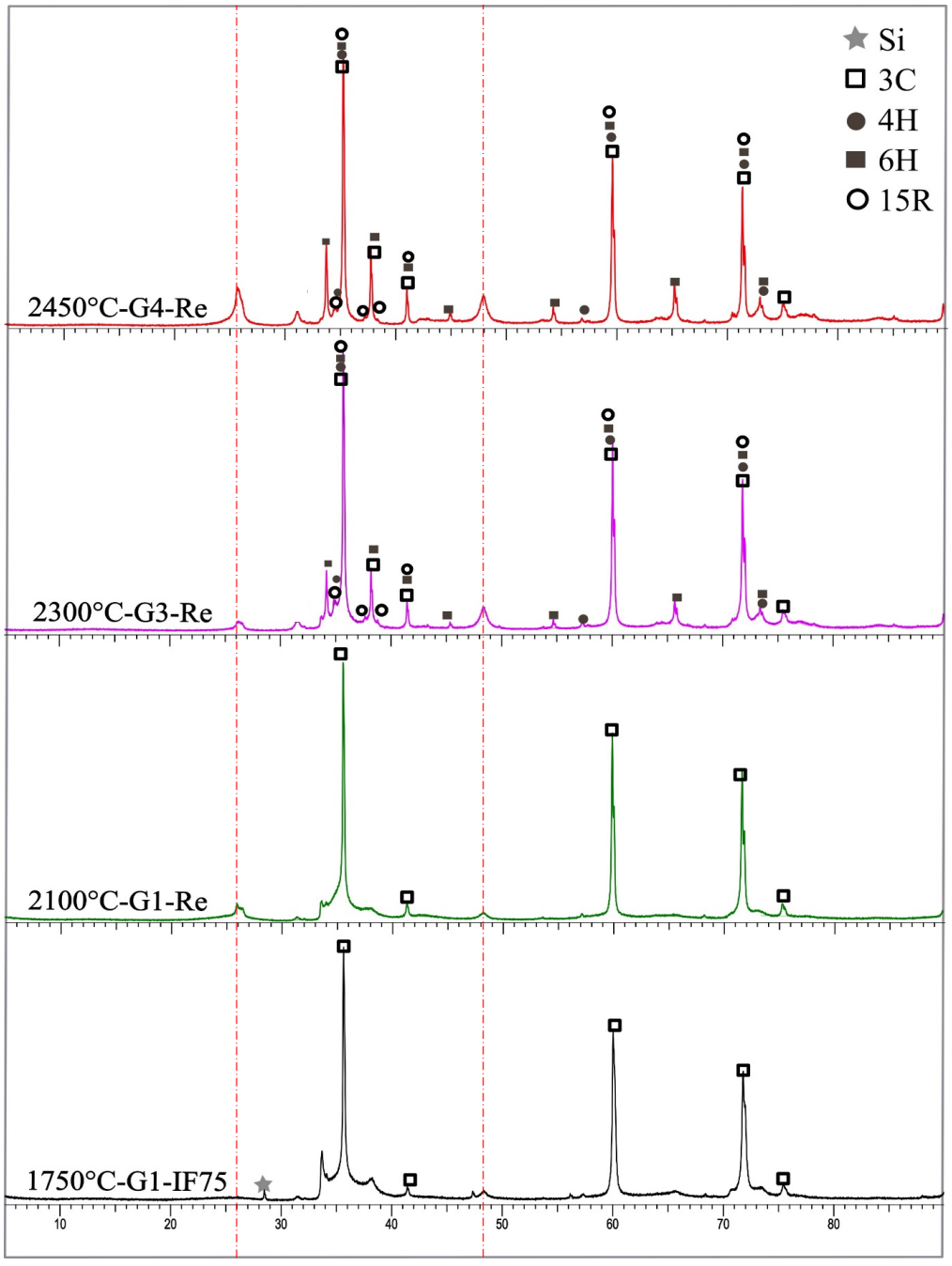

Figure 4.1.52. X-ray diffractograms showing SiC phases identified in β-SiC with 0 wt.% Si formed at 1750 °C, before and after heat-treatment at 2100, 2300, and 2450 °C.

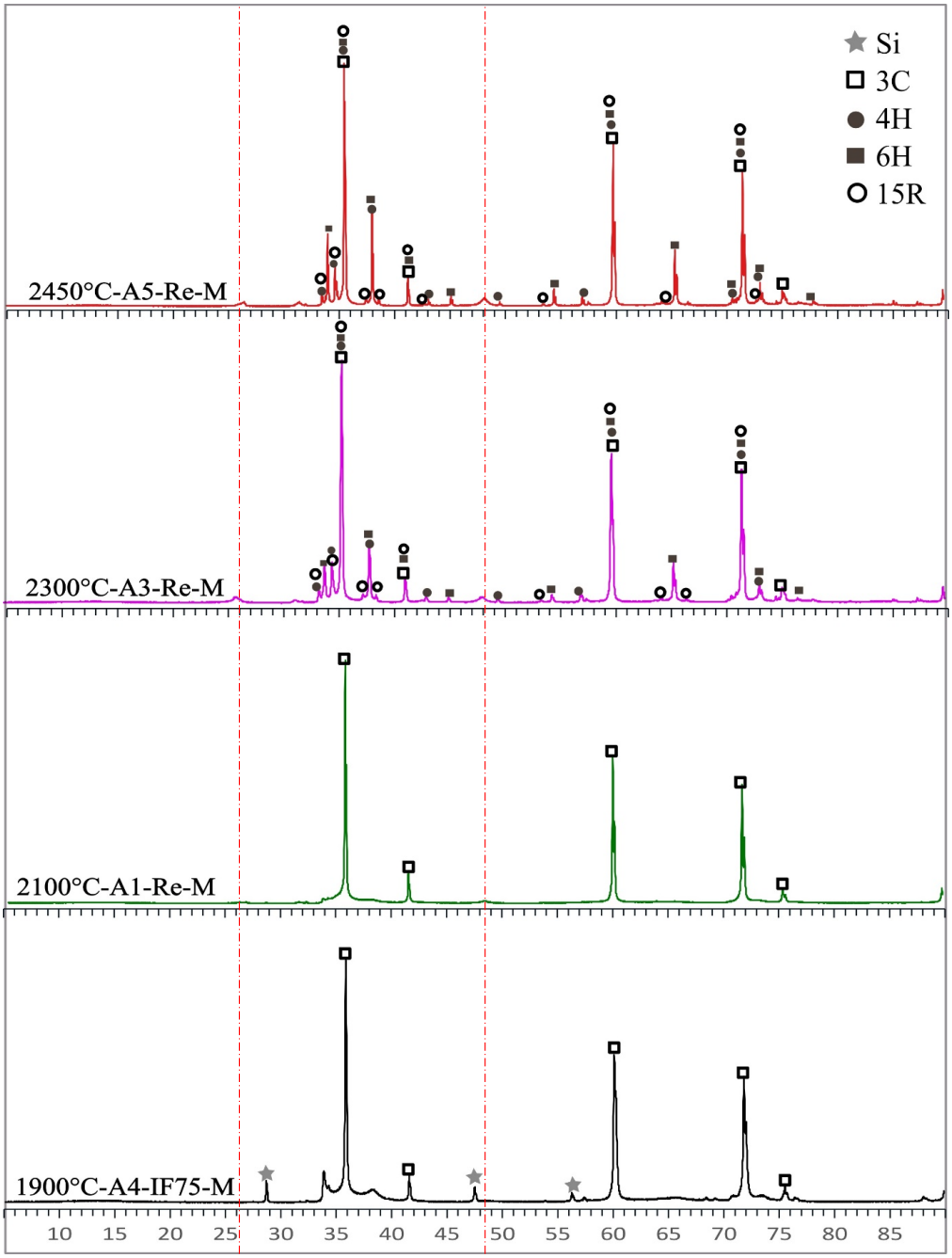

Figure 4.1.53. X-ray diffractograms showing SiC phases identified in β-SiC with 9 wt.% Si formed at 1900 °C, before and after heat-treatment at 2100, 2300, and 2450 °C.

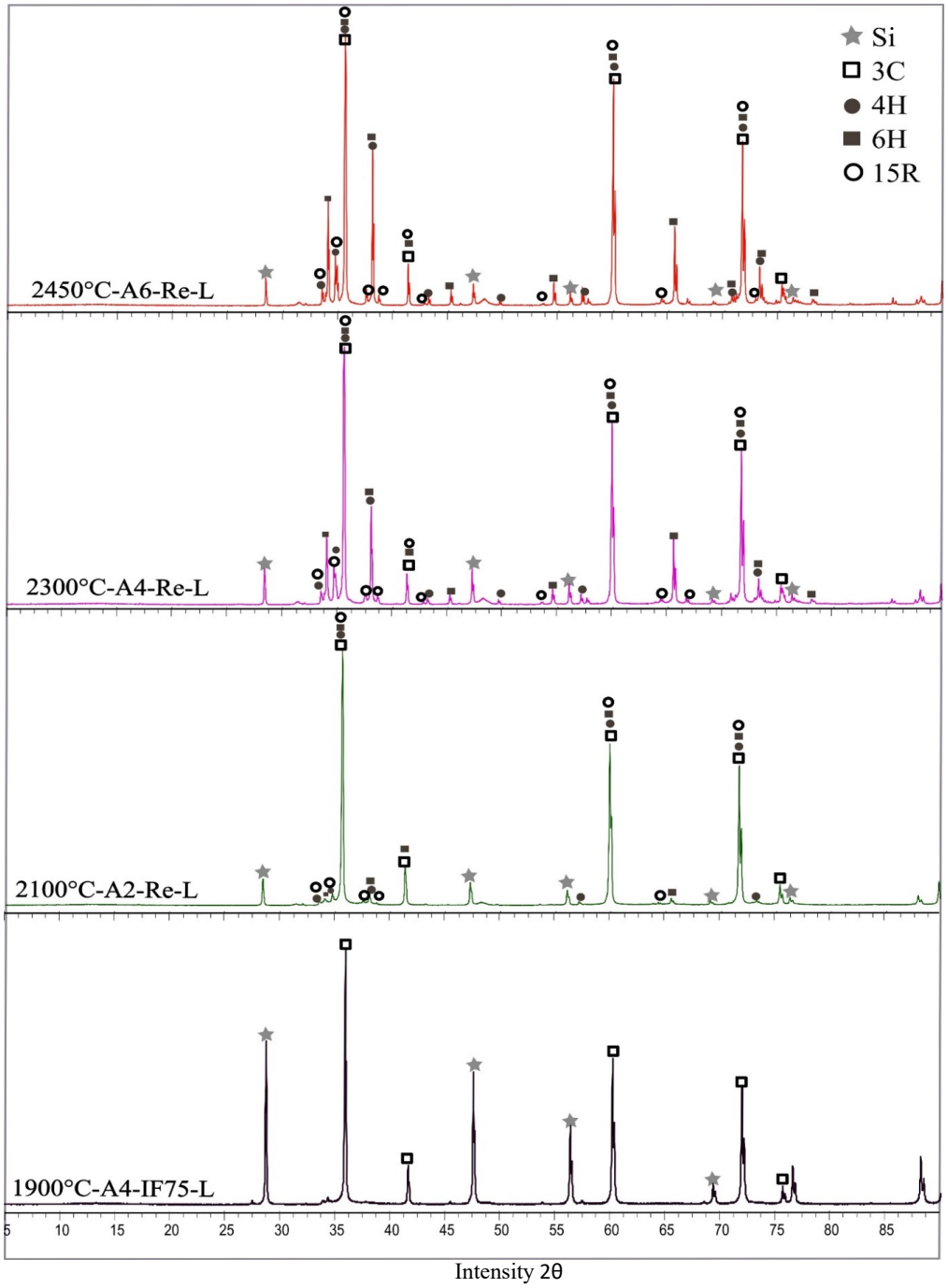

Figure 4.1.54. X-ray diffractograms showing SiC phases identified in β-SiC with 39 wt.% Si formed at 1900 °C, before and after heat-treatment at 2100, 2300, and 2450 °C.

The β-SiC with no additional amount of Si did not transform to α-SiC even at 2100 °C (**Figure 4.1.55**). However, 64 wt.% of the β-SiC converted to α-SiC after being held for 60 min at 2300 °C. The main α-SiC polymorphs such as 4H, 6H, and 15R have formed in this sample. When β-SiC particles with 9 wt.% elemental Si was heated at 2100 °C, no α-SiC conversion was observed (**Figure 4.1.56**). At 2300 °C, 78 wt.% of β-SiC transformed to α-SiC. On the other hand, 19 wt.% of the β-SiC with 39 wt.% elemental Si transformed to α-SiC at 2100 °C (**Figure 4.1.57**). This shows that β-SiC with no elemental Si and β-SiC with 9 wt.% of Si require a temperature of about 2300 °C for partial conversion to α-SiC. At 2450 °C, β-SiC with 9 and 39 wt.% of elemental Si transformed to 82.91 and 100 wt.% of α-SiC, respectively. There was hardly any 3C-SiC phase detected in the β-SiC with 39 wt.% elemental Si after it was heat-treated at 2450 °C, whereas around 4 wt.% of 3C phase was observed when it was heat-treated to 2300 °C. This indicates that the stability of different phases is dependent on the amount of Si present in the SiC particles.

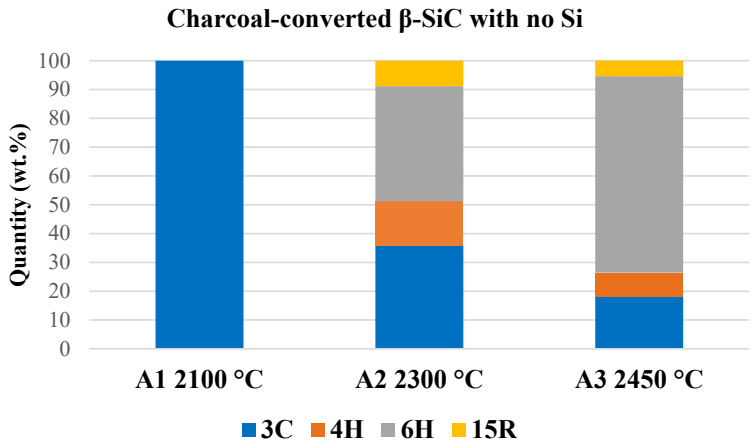

Figure 4.1.55. Summary of quantitative SiC polytypes in β-SiC with no additional amount of Si, heat-treated at 2100, 2300, and 2450 °C.

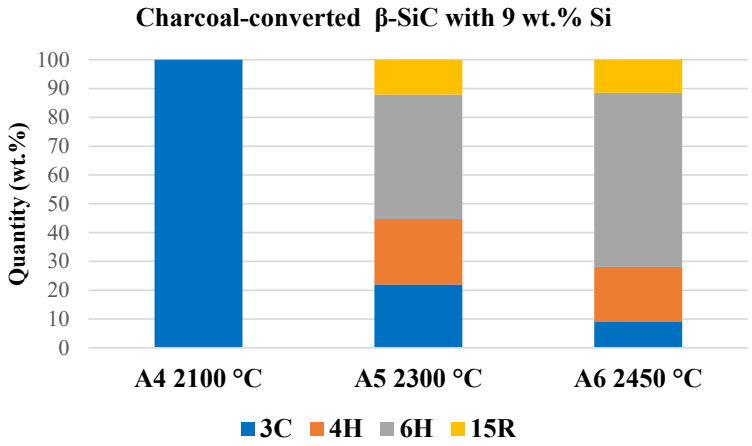

Figure 4.1.56. Summary of quantitative SiC polytypes in β-SiC with 9 wt.% Si, heat-treated at 2100, 2300, and 2450 °C.

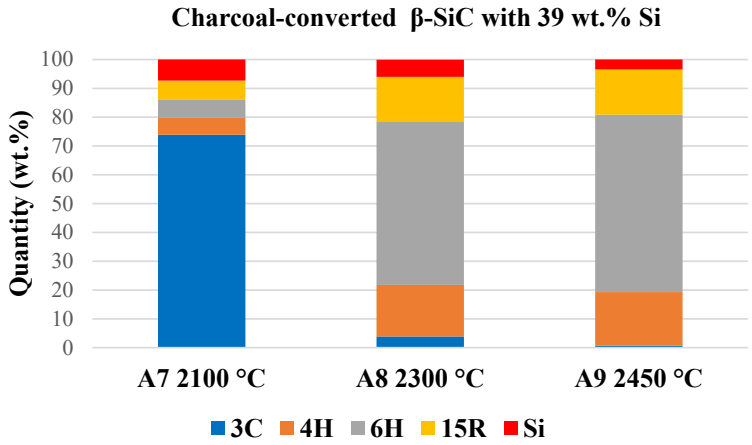

Figure 4.1.57. Summary of quantitative SiC polytypes in β-SiC with 39 wt.% Si, heat-treated at 2100, 2300, and 2450 °C.

Some experiments were repeated to validate the results of β-SiC to α-SiC conversion; their details are presented in **Table 3-18.** Only the Ar/He inert atmosphere was used in these experiments, whereas a mixture of inert gas with CO(g) was used in the other experiments. The purpose was to examine whether the gas atmosphere affects the conversion to α-SiC. **Figure 4.1.58** presents the X-ray diffractograms of SiC samples from these validation experiments, showing the phases identified in them. **Figure 4.1.59** shows the quantities of α-SiC in the sample of β-SiC with no Si, heated at 2100 and 2200 °C. No α-SiC transformation was found in sample that was heated to 2100 °C. The main α-SiC polymorph 4H (35 wt.%) was found in the β-SiC after heating the sample at 2200 °C.

There were not any β-SiC samples with 9 wt.% Si left for repeating the experiments, instead, SiC particles with 10 wt.% Si was used for the validation experiments. **Figure 4.1.60** shows summary of quantitative polytypes present in these β-SiC particles after heating them at 2100 and 2200 °C. At 2100 °C, around 24 wt.% of the sample has transformed to α-SiC, and 4H was the main polytype present in it. When heated at 2200 °C, around 81 wt.% of it transformed to α-SiC, and the presence of main SiC polytypes such as 4H, 6H, and 15R are detected.

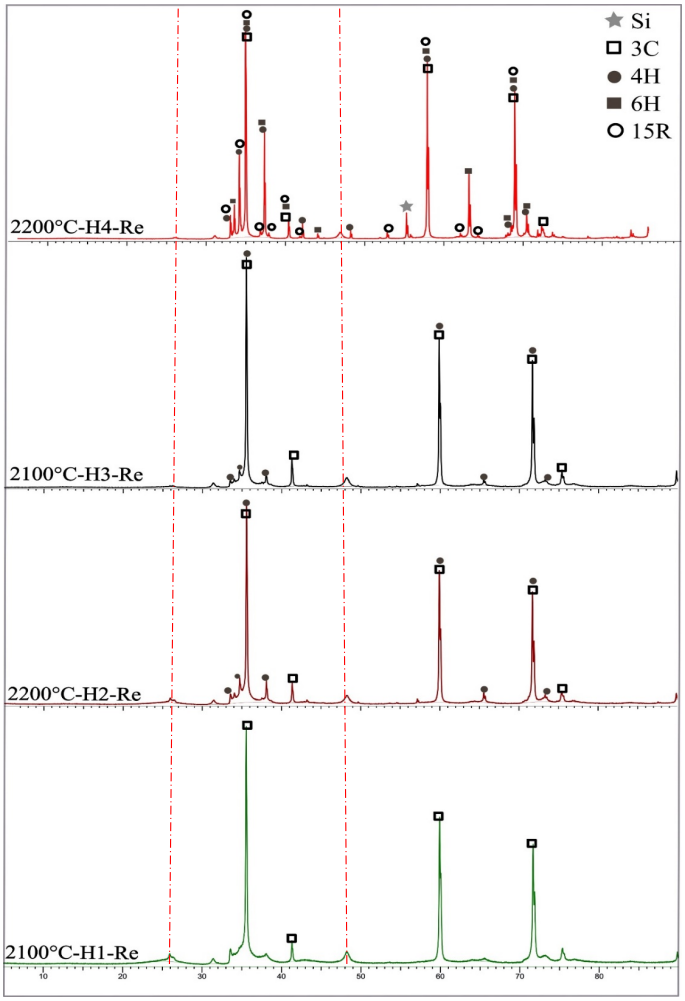

Figure 4.1.58. X-ray diffractograms showing SiC phases identified in β-SiC with no Si (H1-Re and H2-Re) and β-SiC with 10 wt.% Si (H3-Re and H4-Re) heat-treated at 2100 and 2200 °C for validation experiments.

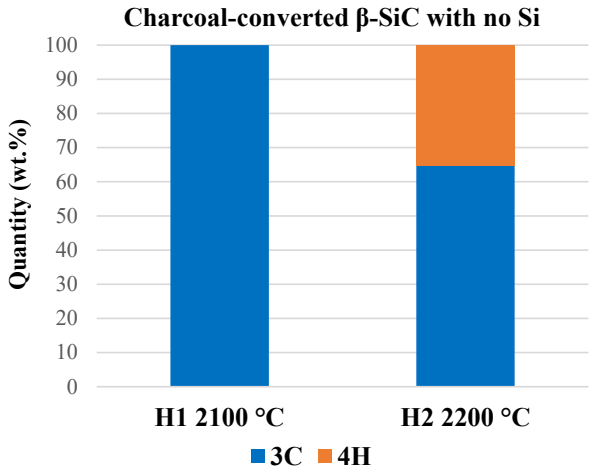

Figure 4.1.59. Summary of quantitative SiC polytypes in β-SiC with no Si, heat-treated at 2100 and 2200 °C for validation experiments.

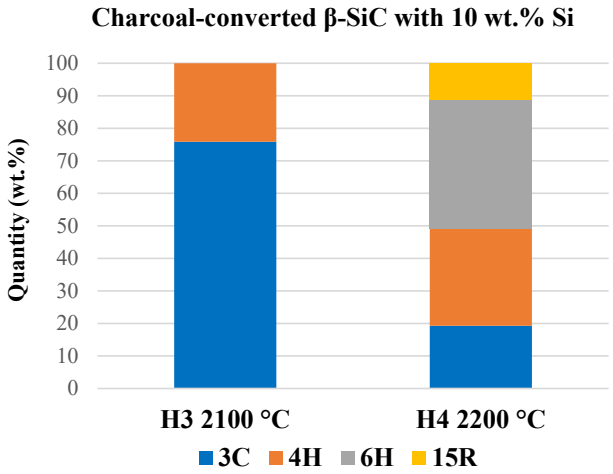

Figure 4.1.60. Summary of quantitative SiC polytypes in β-SiC with 10 wt.% Si, heat-treated at 2100 and 2200 °C for validation experiments.

4.1.3.4 TEM characterization

The sample heated at 2450 °C was characterized under TEM to ensure the polytype distribution present in the sample. This sample (Exp. no. **A6-Re-L**) was also characterized using XRD and polytype quantitative analysis (**Figure 4.1.57**). The BF images and the corresponding SAD pattern from the selected sample are presented in **Figure 4.1.61**. Red circles in the BF images indicate the locations of the diffraction patterns. The diffraction patterns indexed are the cubic 3C-SiC polytypes grown in [111] direction (**Figure 4.1.61b**). The diffraction patterns (**d** and **f**) are indexed, and they are of the hexagonal form 4H and 6H, respectively, grown in $[11\bar{2}0]$ direction. The diffraction pattern (**h**) taken from the BF image (**g**) is indexed and was identified as the rhombohedral form of SiC polytype, 15R, also grown in the $[11\bar{2}0]$ direction. The obtained TEM results are in good agreement with the XRD quantitative analysis of the sample (**Figure 4.1.54** and **Figure 4.1.57**).

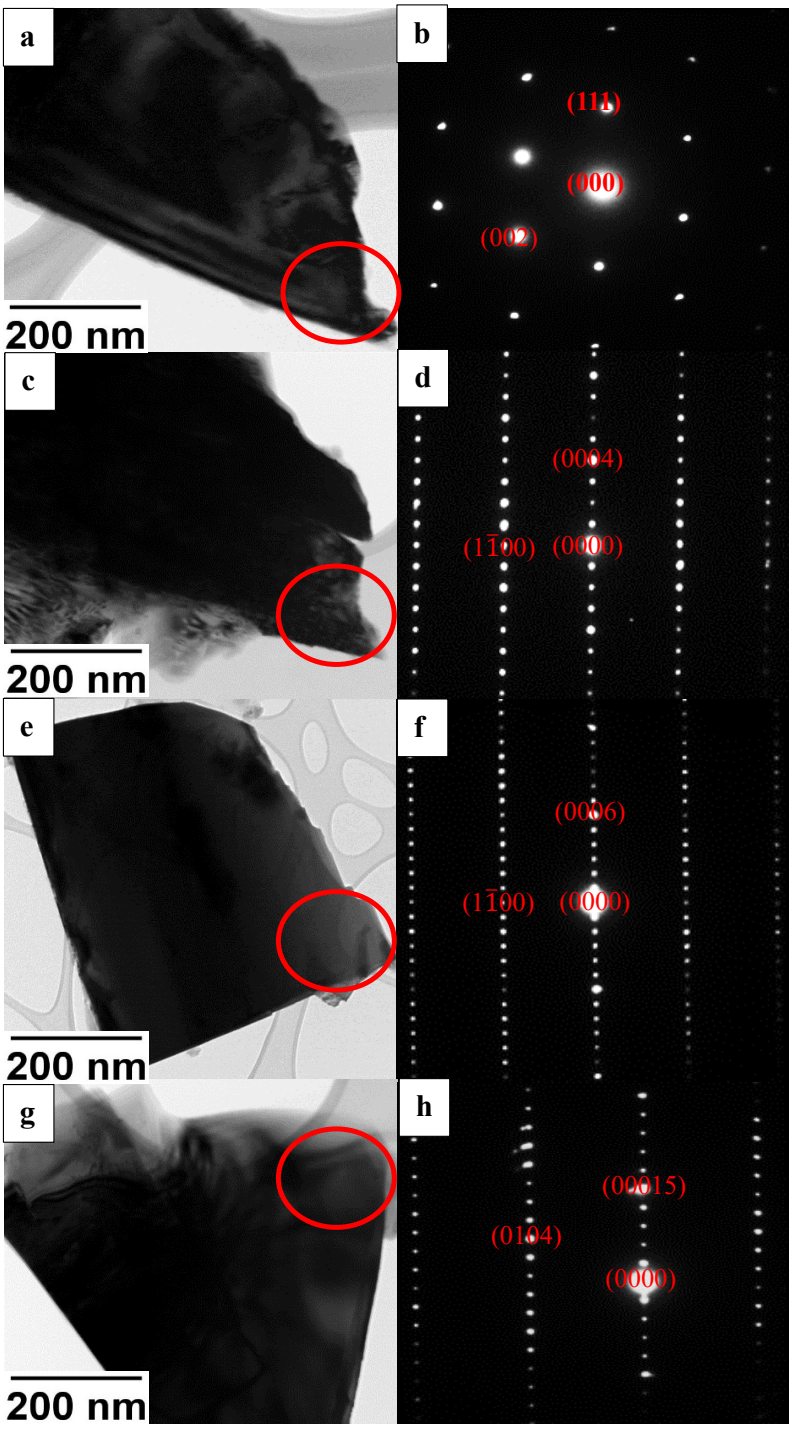

Figure 4.1.61. BF images and corresponding SAD patterns of β-SiC heated at 2450 °C. Most common polytypes such as 3C, 4H, 6H, and 15R are detected.

4.1.4 Transformation to α-SiC: Hot-press furnace experiments

The hot-press furnace used in this study is a resistively heated graphite furnace. This experiment was performed to check whether temperature, time, and pressure have any influence on the transformation to α-SiC. The β-SiC with 9 wt.% Si was used for the experiments and were tested for 1 h (at 20 MPa), 30 min (at 20 MPa), and 4 h (35 MPa), at 2000, 2100, and 2000 °C, respectively. **Figure 4.1.62** shows the XRD data before and after the experiments. No transformation to α-SiC takes place at these conditions. Therefore, it is concluded that pressure does not affect the extent of transformation of β-SiC to α-SiC. Experiments at temperatures above 2100 °C cannot be performed in the in situ hot-press furnace.

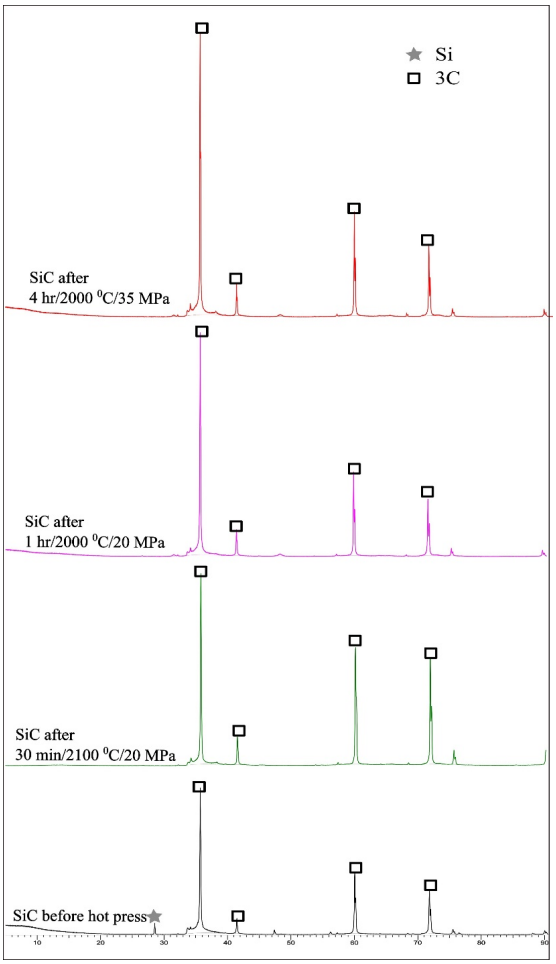

Figure 4.1.62. X-ray diffractograms showing SiC phases identified in β-SiC with 9 wt.% Si, heat-treated by varying time and pressure at 2000 and 2100 °C.

4.2 Coal

The results from experiments conducted with coal are detailed in this section. SiC was produced from coal in both induction and graphite tube furnaces. Both constant volume and constant weight experiments were conducted in the induction furnace. The mixture of (SiO_2 + Si) and pellets made from (SiO_2 + SiC) were used to generate SiO(g). Experiments were performed in the graphite tube furnace in a more controlled environment to validate the induction furnace experiments. Samples were collected from the top, middle, and lower layers of the crucibles after these experiments. The coal-converted β-SiC samples were further heat-treated in the graphite tube furnace to evaluate their transformation to α-SiC. Observations from these experiments and analyses of the coal-converted SiC particles are presented in the following sections.

Figure 4.2.1 shows the visual appearance of SiC samples collected from the top, middle, and lower layers, from the induction furnace experiments. The samples collected from the graphite tube furnace experiments are presented in **Figure 4.2.2**. The samples collected from the three separate layers were similar in appearance, in both the experiments. The samples from the top layer mainly consisted of unreacted carbon material that resembled the original coal, the middle layer contained coal that had partly and completely transformed to SiC, and in the lower layer, the particles had mostly transformed to SiC, with droplets of Si on them. The SiC particles from the middle layer are green in color, whereas particles taken from the lower layer are hard, dark bluish in color, and droplets of Si are visible on some of these particles (**Figure 4.2.1**).

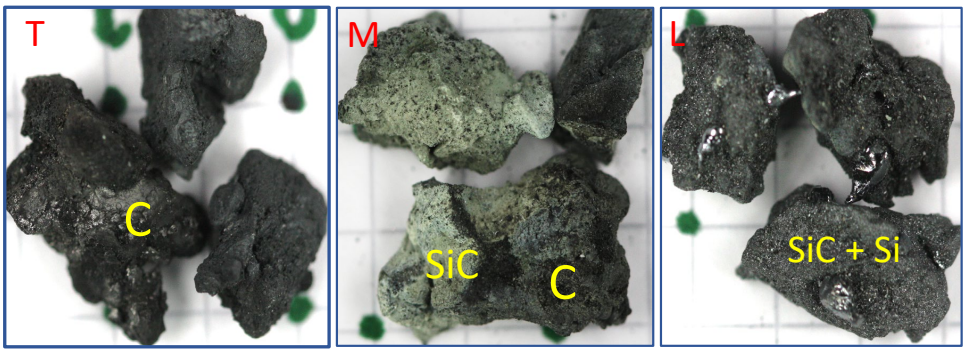

Figure 4.2.1. SiC samples collected from top (T), middle (M), and lower (L) layers, after induction furnace experiments.

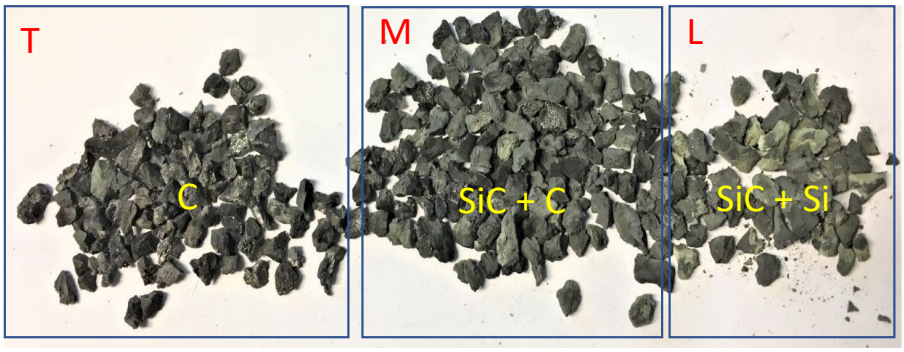

Figure 4.2.2. SiC samples collected from top (T), middle (M), and lower (L) layers, after graphite tube furnace experiments.

4.2.1 β-SiC production: Induction furnace experiments

A mixture of (SiO_2 + Si) was used as the source for SiO(g). As in the case of charcoal, some of the SiC was lost as fines, while retrieving the samples from the crucible. Approximate quantities of samples collected from the three different layers after the constant volume and constant weight experiments are illustrated in **Figure 4.2.3** and **Figure 4.2.4**, respectively. The graphs represent experiments conducted at 1750 and 1800 °C. The approximate quantities of SiC in the samples are almost identical in both the experiments. The increasing temperature has caused an increase in the quantities of SiC at 1800 °C, especially in the lower layers of both the experiments. In the constant volume (weight) experiments ~15.75% (13.85%) and ~27.5% (24.0%) of the total coal have transformed to SiC at 1750 and 1800 °C, respectively. There was no significant difference in the production of SiC between both the constant volume and constant weight experiments.

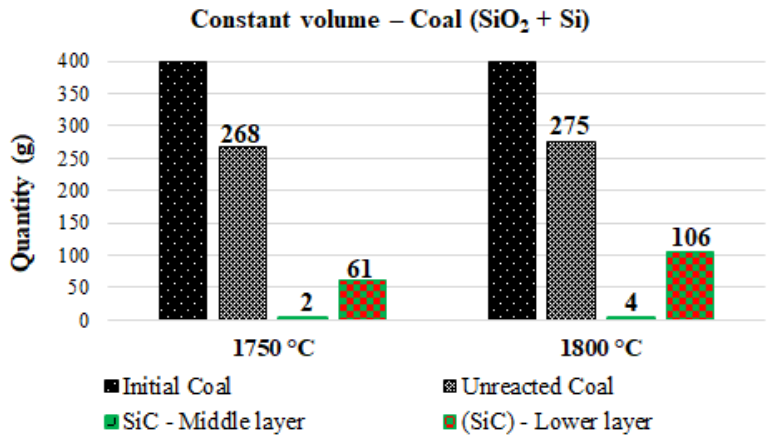

Figure 4.2.3. Quantities of initial coal and final products collected from constant volume experiments, conducted at 1750 and 1800 °C in induction furnace.

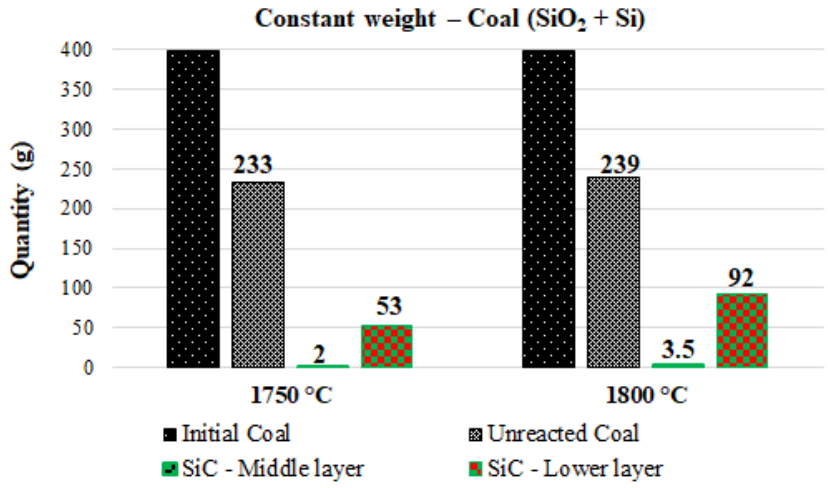

Figure 4.2.4. Quantities of initial coal and final products collected from constant weight experiments, conducted at 1750 and 1800 °C in induction furnace.

The experiments conducted using pellets of (SiO_2 + SiC) malfunctioned, as the pellets started foaming upon heating. As in the experiments with charcoal, here too the pellets were foaming upwards to the coal materials and could not be pushed down towards the charge mix. Therefore, the experiments with (SiO_2 + SiC) were not successful with coal. **Figure 4.2.5** shows cross-sections of the crucibles displaying unconsumed pellets after conducting the experiments with coal at 1750 and 1850 °C. Only the samples from experiments performed using (SiO_2 + Si) were analyzed further, as detailed in the following sections.

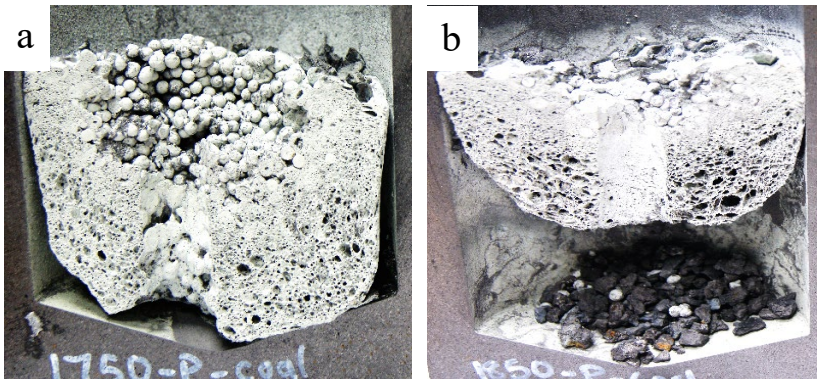

Figure 4.2.5. Cross-sections of crucibles displaying interior conditions, after conducting experiments with coal and pellets of (SiO_2 + SiC), at (a) 1750 and (b) 1850 °C.

4.2.1.1 SEM morphology

Surface morphologies of coal-converted SiC particles from the constant volume experiments were analyzed to study the SiC crystal growth in coal. These experiments were conducted at 1750, 1800, 1850, and 1900 °C. SiC particles from the lower and middle layers of these experiments were selected for the morphological characterization. **Figure 4.2.6** displays the SiC crystal formation in coal particles, in these two layers at the four temperatures.

SiC crystals of varying sizes and shapes have formed on the surface of coal. In some regions, long SiC crystals of length of ~100 µm are visible (**Figure 4.2.6c, d,** and **g**). SiC crystals in the form of thick and long nanowires have formed in the particles collected from the experiment conducted at 1800 °C. As the temperature increases, concentration of the SiC crystals also increases. The SiC particles become denser as Si starts forming in them, especially in the lower layers. (**Figure 4.2.6b, d, f,** and **h**).

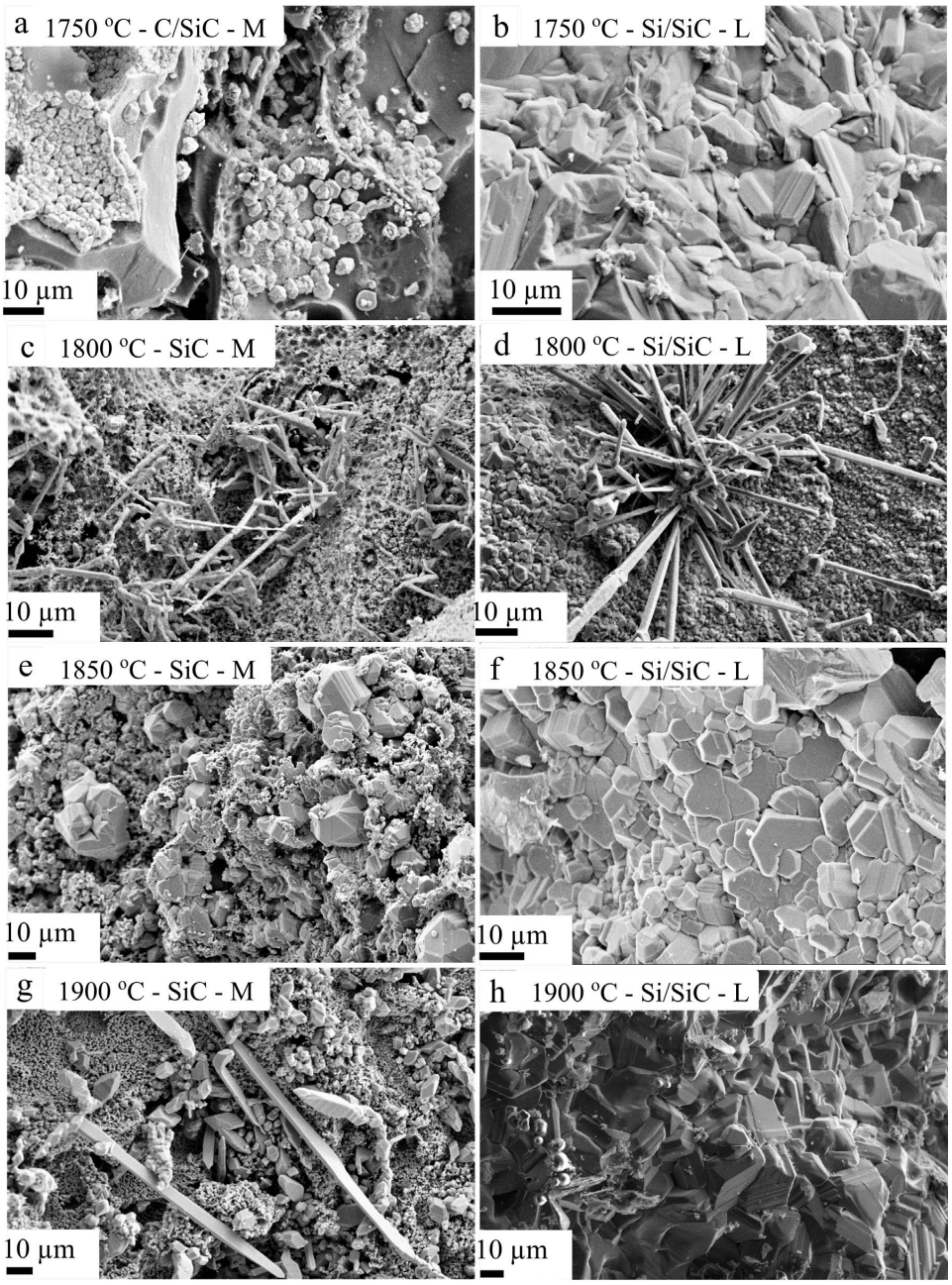

Figure 4.2.6. SEM surface morphologies of coal-converted SiC particles collected from the (a, c, e, g) middle (M) and (b, d, f, h) lower (L) layers of induction furnace. Experiments were conducted at 1750, 1800, 1850, and 1900 °C.

4.2.1.2 EPMA-BSE imaging

Figure 4.2.7 shows the EPMA-BSE images of SiC particles collected from the lower and middle regions, after conducting the experiments at 1750, 1800, 1850, and 1900 °C. All these samples are from the constant volume experiments. SiC is visible as dark gray region in the images. The light gray or nearly-white portion in images from the lower region is the elemental Si formed along with SiC. Pure carbon and epoxy are almost black in color.

The EPMA of SiC samples from the lower layer (images on the left side) reveal that as the temperature increases, more elemental Si forms in the SiC particles (**Figure 4.2.7a**, **c**, **e**, and **g**). Also, the particles become denser and the original coal structure disappears. The samples from the middle region (**Figure 4.2.7b**, **d**, **f** and **h**) were exposed to slightly lower temperatures compared with samples in the lower layer. Si phase was not present in these samples, and the original coal structure is prominent, even after being exposed to SiO(g). The original coal structure is not conspicuous in the SEM morphology investigation (**Figure 4.2.6**); however, it is clearly visible in the EPMA-BSE images.

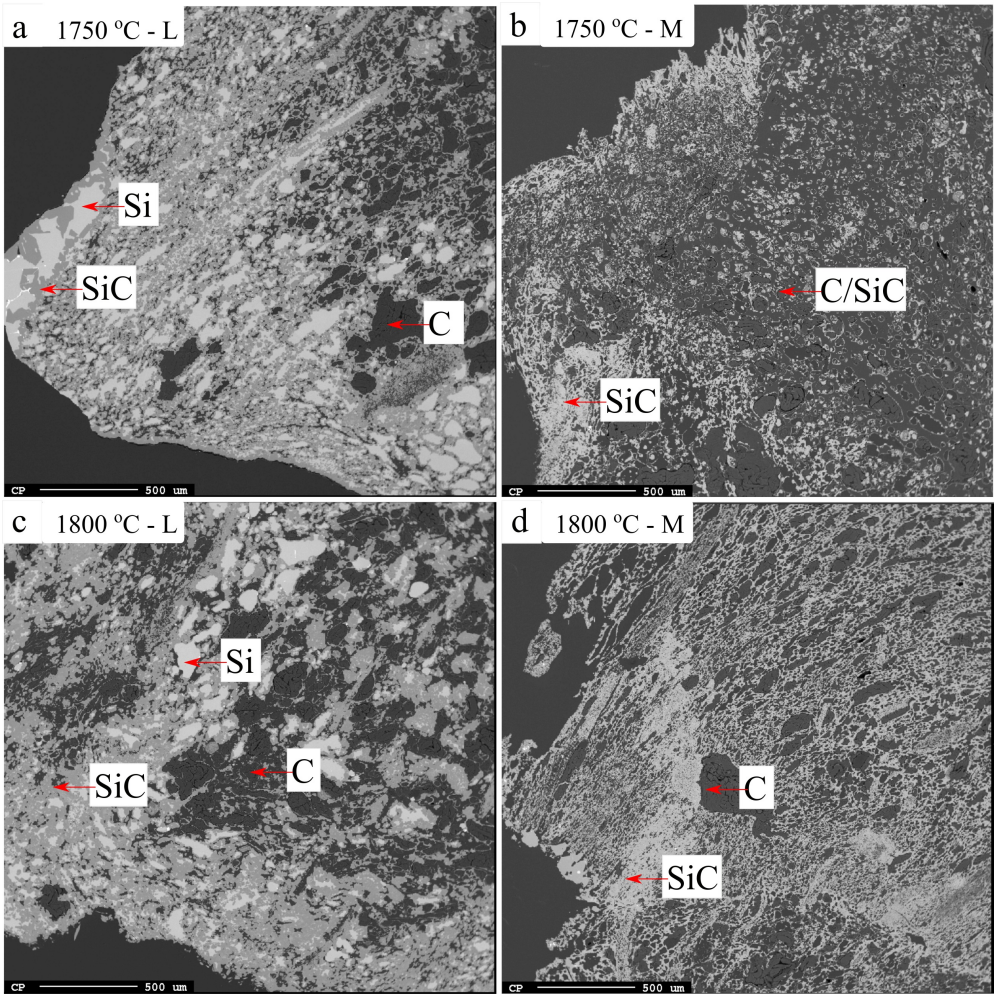
a
1750 °C - L
Si
SiC
C
CP
500 um
b
1750 °C - M
C/SiC
SiC
CP
500 um
c
1800 °C - L
Si
C
SiC
CP
500 um
d
1800 °C - M
C
SiC
CP
500 um

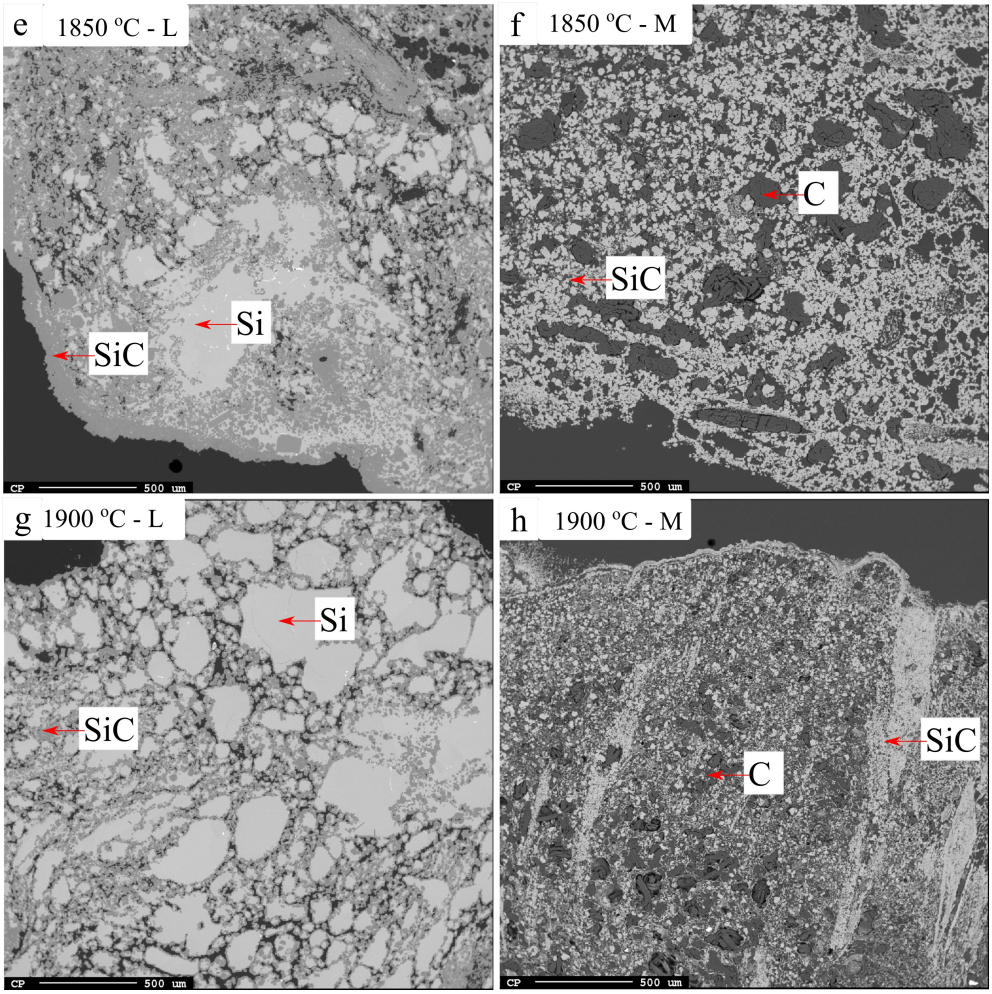

Figure 4.2.7. EPMA images of SiC particles collected from (a, c, e, g) lower (L) and (b, d, f, h) middle (M) layers of induction furnace, after conducting constant volume experiments at 1750, 1800, 1850, and 1900 °C.

Figure 4.2.8 and **Figure 4.2.9** show the elemental distribution of carbon and Si in the coal-converted SiC particle, collected respectively from the middle and lower layers of the experiments conducted at 1750 °C. Again, elemental Si is not present in the middle layer. However, formation of elemental Si in SiC along with some unreacted carbon is detectable in the lower layer (**Figure 4.2.9**). The pores disappear as molten Si fills them up, and the original carbon structure also disappears. If Si does not form in SiC, the particle would reveal the structure of coal. Interestingly, in some particles, once SiC starts forming in the outer surface, elemental Si also forms in them. It happens regardless of the extent of transformation to SiC. This could be observed in the EPMA images as well (**Figure 4.2.7a**, **c**, and **e**). The topochemical reaction,

showing formation of SiC and Si together on the outer surface, along with the unreacted carbon in the middle, is clearly visible in **Figure 4.2.9**. Similar phenomenon was observed in the EPMA of samples from the constant weight experiments as well, conducted at 1750 and 1850 °C (images not shown). Traces of Iron (Fe) are also visible in the sample from the lower layer.

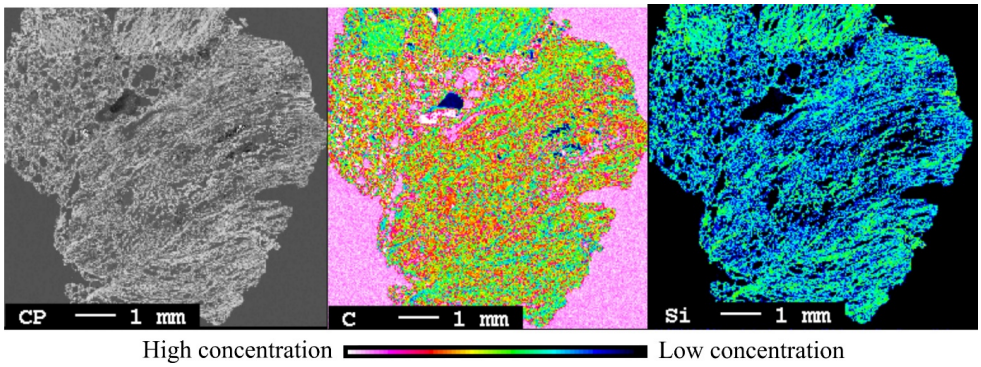

Figure 4.2.8. EPMA elemental mapping of SiC particle from middle layer of experiment conducted at 1750 °C, and elemental distribution of carbon and Si in it.

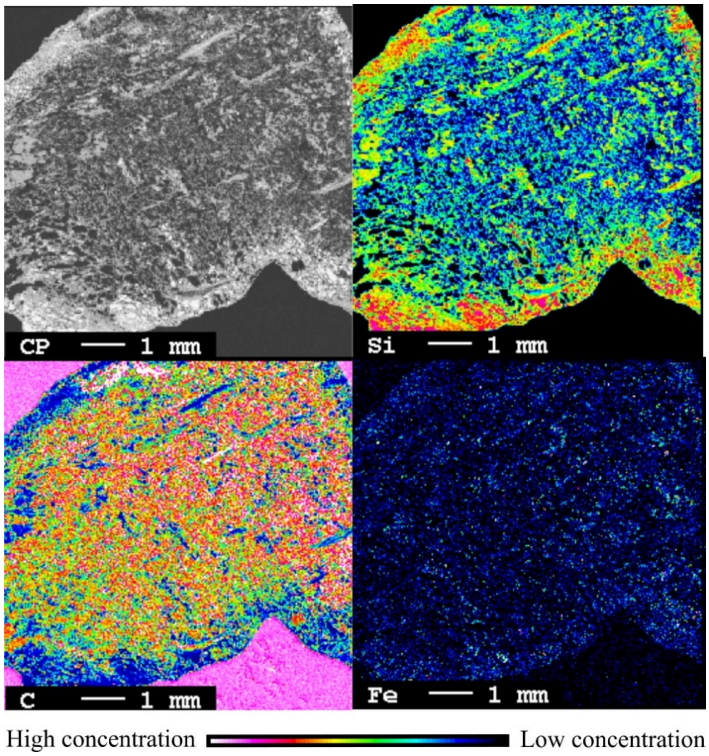

Figure 4.2.9. EPMA elemental mapping of SiC particle from lower layer of experiment conducted at 1750 °C, and elemental distribution of Si, carbon, and Fe in it.

4.2.1.3 XRD analysis

Figure 4.2.10 shows X-ray diffractograms of SiC samples from the middle and lower layers of the constant volume experiments, conducted at 1750, 1800, 1850, and 1900 °C. These experiments used a mixture of (SiO_2 + Si), at a higher SiO pressure. The quantitative XRD analysis identified the SiC particles obtained from coal as the cubic 3C-SiC polytype (100%), which is the β-SiC phase. Elemental Si is mostly found in the lower layer, forming sharp peaks (images on the left side). A few Si peaks are also visible in the middle layer at 1900 °C. The EPMA-BSE investigation, however, had no elemental Si phase in the SiC particles from middle layer. The XRD sample preparation needs crushing the SiC particles to a fine powder, and the selected SiC particles could have had some Si in it. However, the EPMA analysis uses only a portion of the particle, which might not have had Si present in that particular sample. This could be the reason for detection of Si in the XRD and not in EPMA.

Carbon peaks are present in the middle layer, at all four temperatures. Similar results could be found in the sample collected from the constant weight experiments, conducted at 1750 and 1800 °C (**Figure 4.2.11**). The SiC phase was identified as β-SiC. The Si peaks are also present in these samples. The stacking faults in the sample have caused the (111) peaks of 3C-SiC and the elevated background under the peaks for $2\theta \geq 33.6°$. The SiC samples with Si showed higher crystallinity than those without Si and a much lower level of stacking faults in the 3C-SiC polymorph. It is also evident that the scattering (peak broadening at the (111) 3C-SiC) due to stacking faults is reduced in the SiC samples produced at temperatures > 1750 °C.

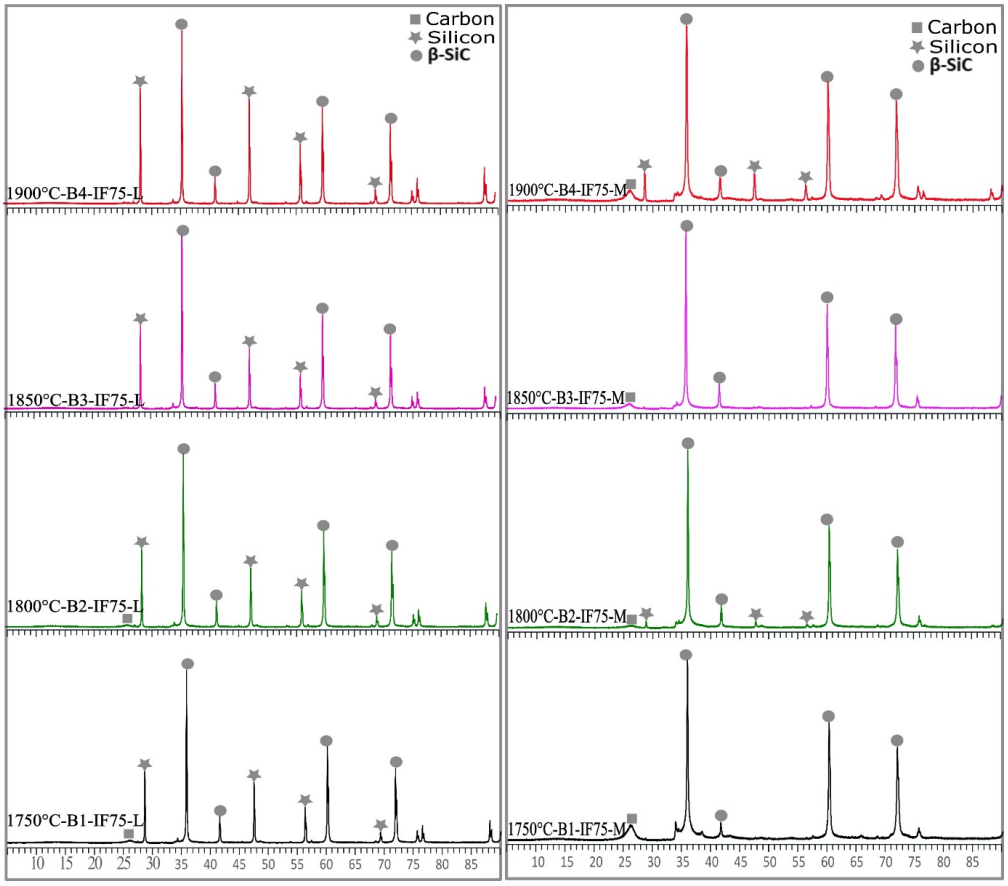

Figure 4.2.10. X-ray diffractograms identifying different phases in coal-converted SiC samples from lower (L) and middle (M) layers of constant volume experiments, conducted at 1750, 1800, 1850, and 1900 °C.

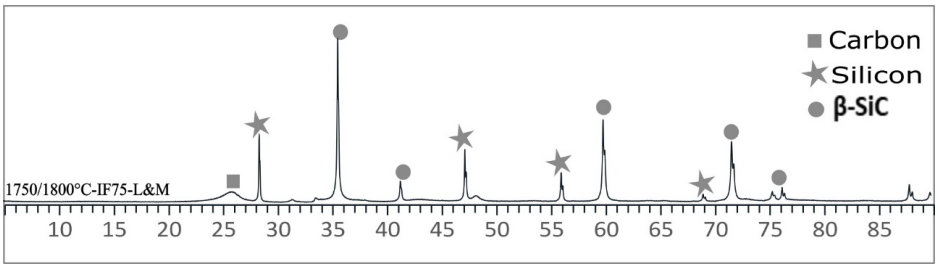

Figure 4.2.11. X-ray diffractograms of coal-converted SiC samples from the constant weight experiments conducted at 1750 and 1800 °C.

4.2.1.4 Chemical analysis

The amounts of free carbon, SiC, and Si in the SiC samples were estimated by chemical analysis. **Figure 4.2.12** shows SiC samples from the middle layer, collected after conducting the constant volume experiments at 1750, 1800, 1850, and 1900 °C. Over 20% of free carbon is left in most of the samples. This shows that not all carbon particles have completely converted to SiC. All samples have elemental Si present in them. The EPMA-BSE analysis, however, did not show any elemental Si phase in SiC particles from the middle layer. A minimum of 4 g of sample was needed for the chemical analysis; therefore, among the selected SiC particles, some might have had Si in them, which could have led to the detection of elemental Si in the analysis.

Figure 4.2.13 shows similar parameters for samples from the lower layer. The experiments conducted at 1750 and 1800 °C have free carbon close to 10% and at higher temperatures, the amount of free carbon is less than 10%. The amount of unreacted carbon is comparatively lesser in the lower layers at all temperatures. The analysis shows that the temperature has a great influence on the formation of SiC and Si in coal. The maximum amount of Si is produced in the lower layer at 1900 °C. **Figure 4.2.14** presents chemical analysis of the samples collected from both the lower and middle layers of the constant weight experiments conducted at 1750 and 1800 °C. There are no significant differences between the quantities of SiC and Si formed in both the constant volume and constant weight experiments, under the same experimental conditions.

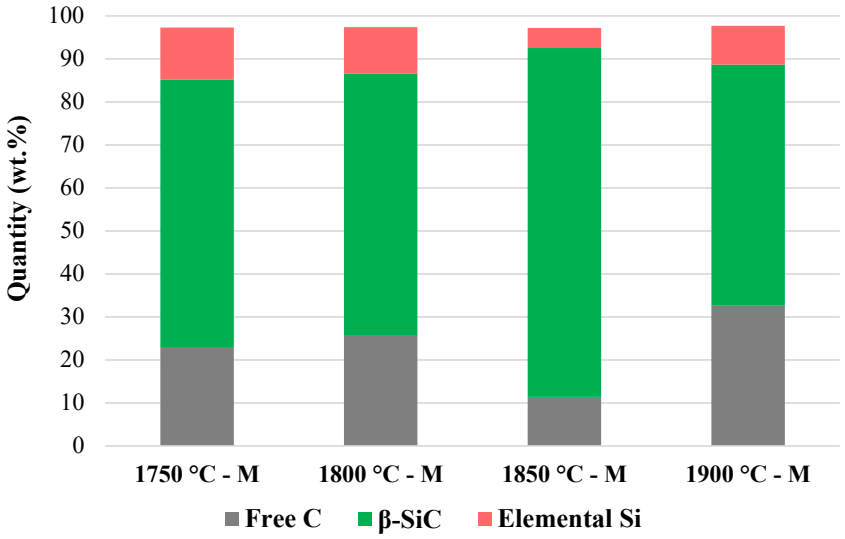

Figure 4.2.12. Chemical analysis of coal-converted SiC samples from middle (M) layers of constant volume experiments, conducted at different temperatures.

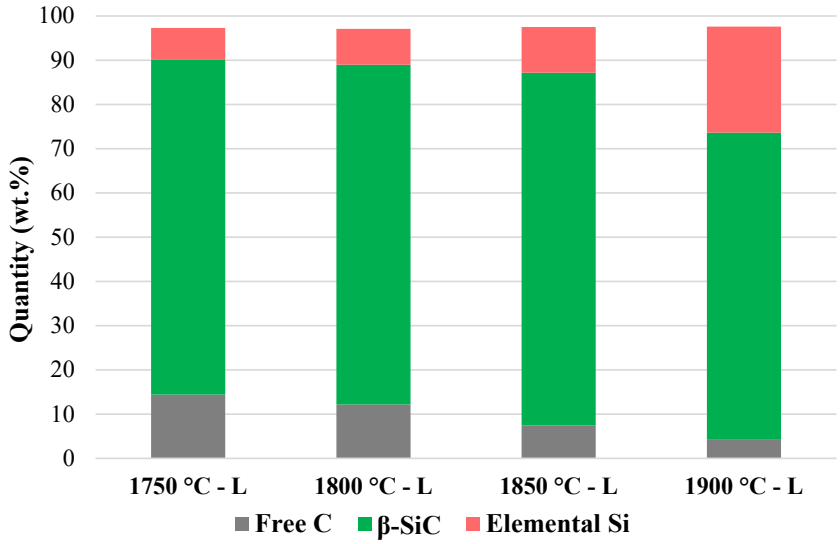

Figure 4.2.13. Chemical analysis of SiC samples from lower (L) layers of constant volume experiments, conducted at different temperatures.

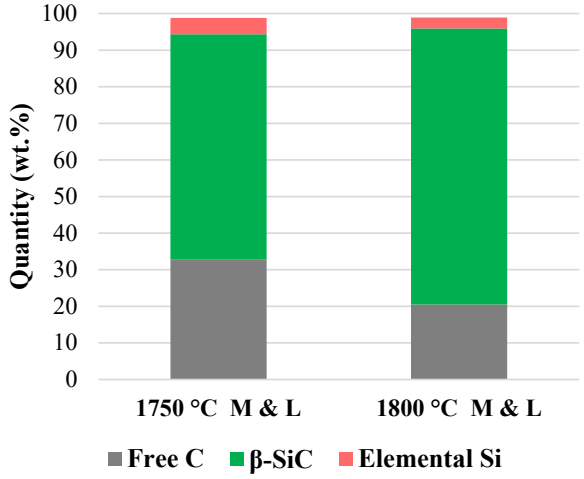

Figure 4.2.14. Chemical analysis of coal-converted SiC samples from middle (M) and lower (L) layers of constant weight experiments, conducted at different temperatures.

4.2.2 β-SiC production: Graphite tube furnace validation experiments

To validate the results from the induction furnace experiments, SiC production experiments were performed in the graphite tube furnace. **Figure 4.2.15** shows quantities of the initial coal and the samples collected from the three layers. The first two experiments were conducted at 1686 and 1765 °C, using (SiO_2 + Si) mixture as SiO(g) source, and the final experiment was conducted

at 1750 °C, using pellets made from (SiO_2 + SiC). This would elucidate the effectiveness of the two SiO(g) producing methods, at various temperatures. A few SiC particles obtained from all three experiments were hard solids and it was assumed that they might have Si them. Further analyses performed on samples from each layer would later confirm the presence of elemental Si in them. **Figure 4.2.15** shows that the final product from the crucible weighed less than the initial product, which could be due to; (a) carbon particles from the top layer falling out of the crucible upon vacuuming the furnace chamber, and (b) removal of volatiles from the carbon particles upon heating. A total amount of ~50 ± 6% of SiC was obtained from all experiments.

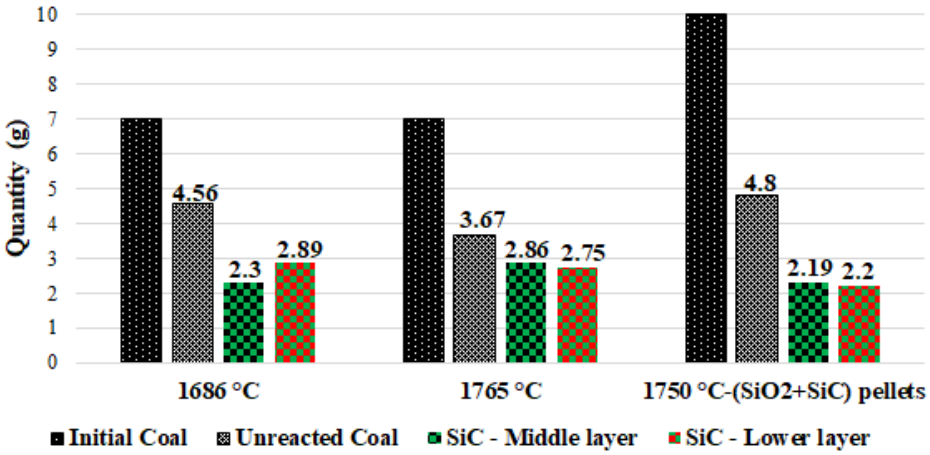

Figure 4.2.15. Quantities of initial coal and final samples collected from three layers. Experiments conducted at 1686 and 1765 °C used (SiO_2 + Si) mixture, and that conducted at 1750 °C used pellets of (SiO_2 + SiC) as SiO(g) source.

4.2.2.1 SEM morphology

Figure 4.2.16 and **Figure 4.2.17** show surface morphologies of samples collected from the top, middle, and lower layers of the experiments conducted at 1686 and 1765 °C, that used (SiO_2 + Si) mixture as source of SiO(g). **Figure 4.2.18** shows similar images of particles from the experiment conducted at 1750 °C, which used (SiO_2 + SiC) pellets. Tiny SiC seed crystals are deposited on the pore walls of particles in the top layer, and needle-shaped SiC crystals are formed on particles from the middle layer, at all temperatures. The images from the lower region show clusters of needle-shaped SiC crystals at 1686 °C (**Figure 4.2.16c**). At 1765 °C, dense crystals are formed in the lower layer, and the original structure of coal vanishes completely (**Figure 4.2.17c**). This indicates that Si might have formed in the SiC particles at 1765 °C, when (SiO_2 + Si) was used. Only needle-shaped crystals are formed on particles from the middle and

lower layers at 1750 °C that used pellets of (SiO_2 + SiC) (**Figure 4.2.18b** and **c**). The original structure of coal is visible in all images, except in those from the lower layer (**Figure 4.2.16** and **Figure 4.2.17**).

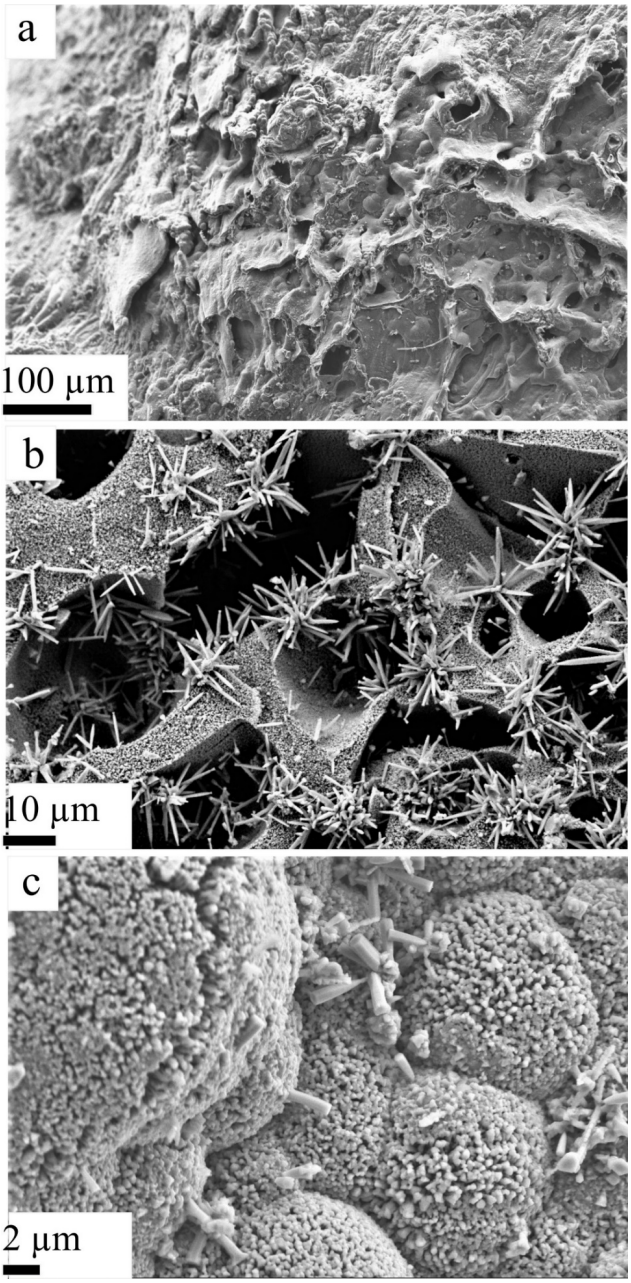

Figure 4.2.16. SEM morphologies of samples collected from (a) top, (b) middle, and (c) lower layers of experiment conducted at 1686 °C, using (SiO_2 + Si) mixture.

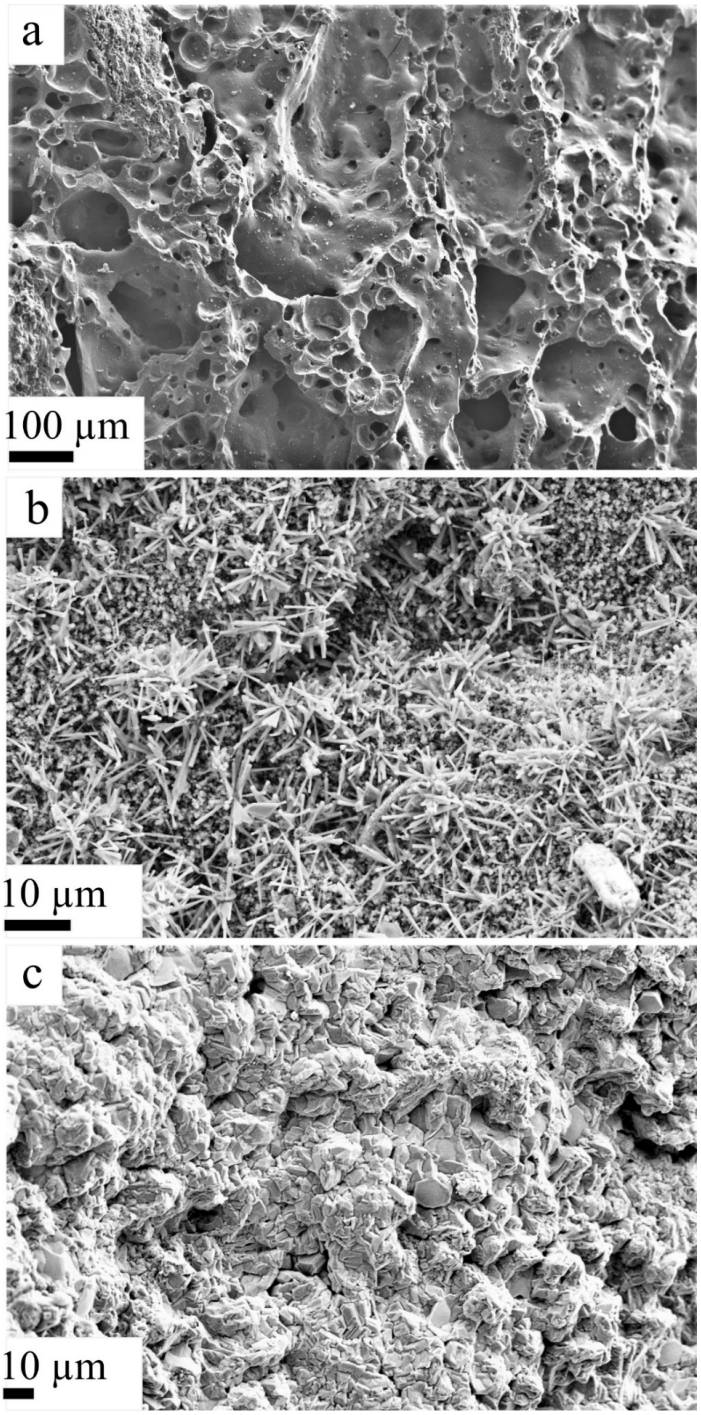

Figure 4.2.17. SEM morphologies of samples collected from (a) top, (b) middle, and (c) lower layers of experiment conducted at 1765 °C, using (SiO_2 + Si) mixture.

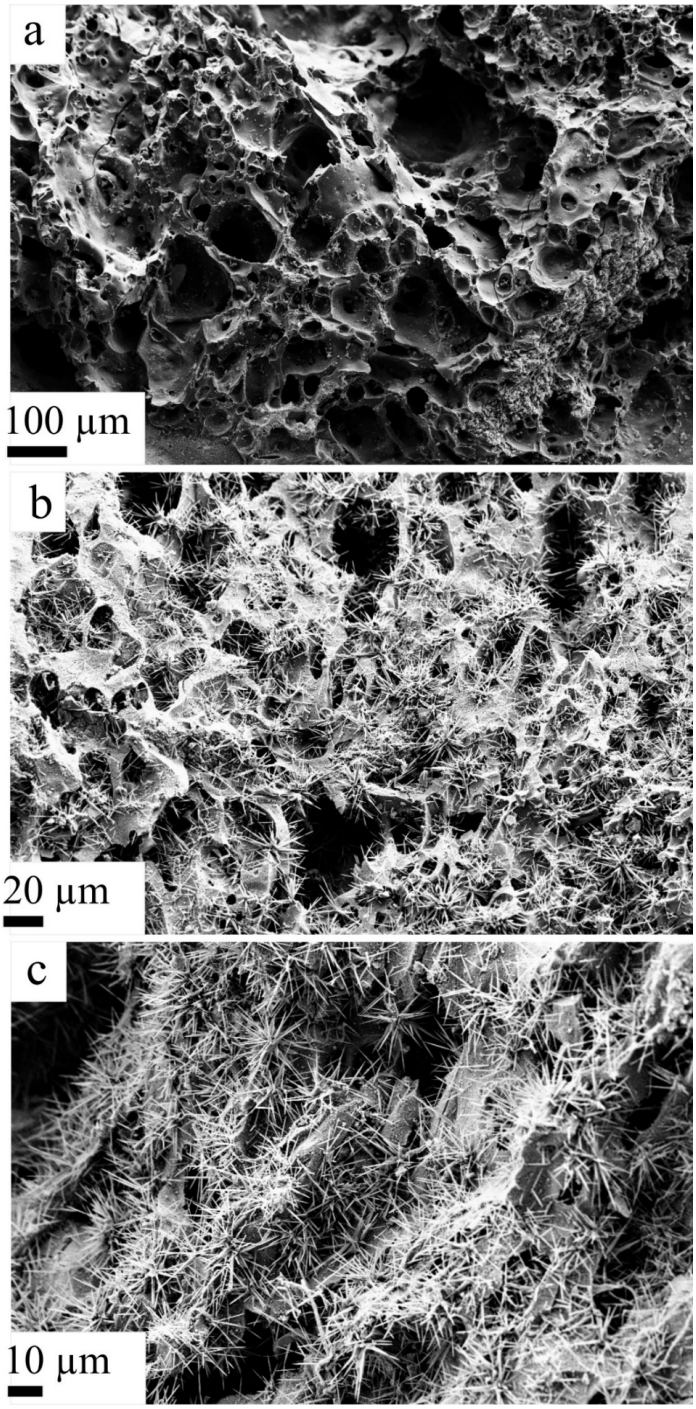

Figure 4.2.18. SEM morphologies of samples collected from (a) top, (b) middle, and (c) lower layers of experiment conducted at 1750 °C, using pellets of (SiO_2 + SiC).

4.2.2.2 Chemical analysis and EPMA-BSE imaging

Chemical analysis of the coal-converted SiC samples was also performed for particles from the top, middle, and lower layers of the crucible, collected from the same three experiments. However, as with the validation experiments of charcoal, here too, the quantity of elemental Si could not be measured, and only the SiC content was measured. The amounts of SiC formed in the different layers are presented in **Figure 4.2.19**. At 1756 °C, a 10% more amount of SiC was produced by (SiO_2 + Si), compared with pellets of (SiO_2 + SiC) at 1750 °C (bars in magenta color), which proves that more SiC production is possible with (SiO_2 + Si) at a higher SiO(g) pressure. The EPMA-BSE analysis of SiC formed at 1686 and 1765 °C using (SiO_2 + Si), revealed formation of elemental Si in the lower layers, as shown in **Figure 4.2.20** and **Figure 4.2.21**, respectively. No elemental Si could be observed in the lower layer particles that were formed from (SiO_2 + SiC) at 1750 °C (**Figure 4.2.22**).

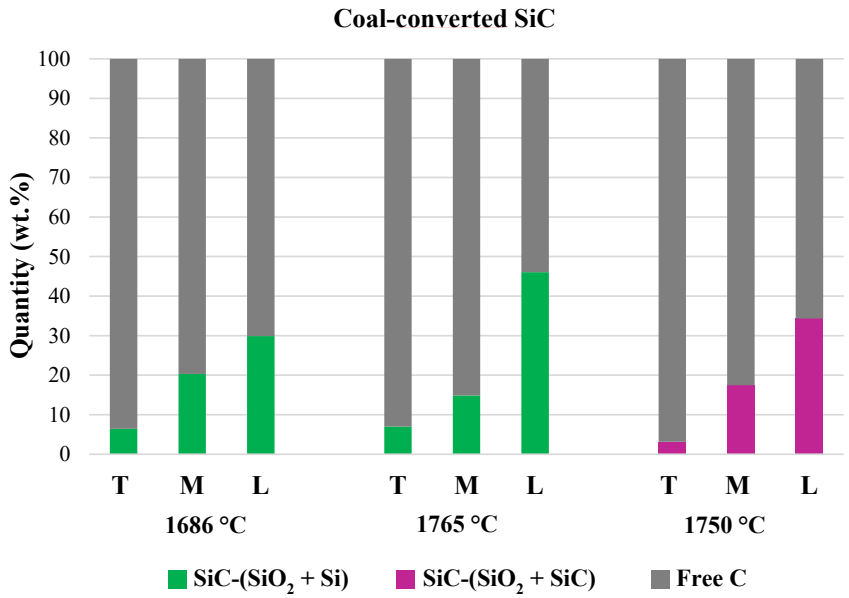

Figure 4.2.19. Amounts of SiC and unreacted carbon in coal in top (T), middle (M), and lower (L) layers. Experiments were conducted in graphite tube furnace at 1686 (SiO_2 + Si), 1765 (SiO_2 + Si), and 1750 °C (SiO_2 + SiC) (magenta colored bars).

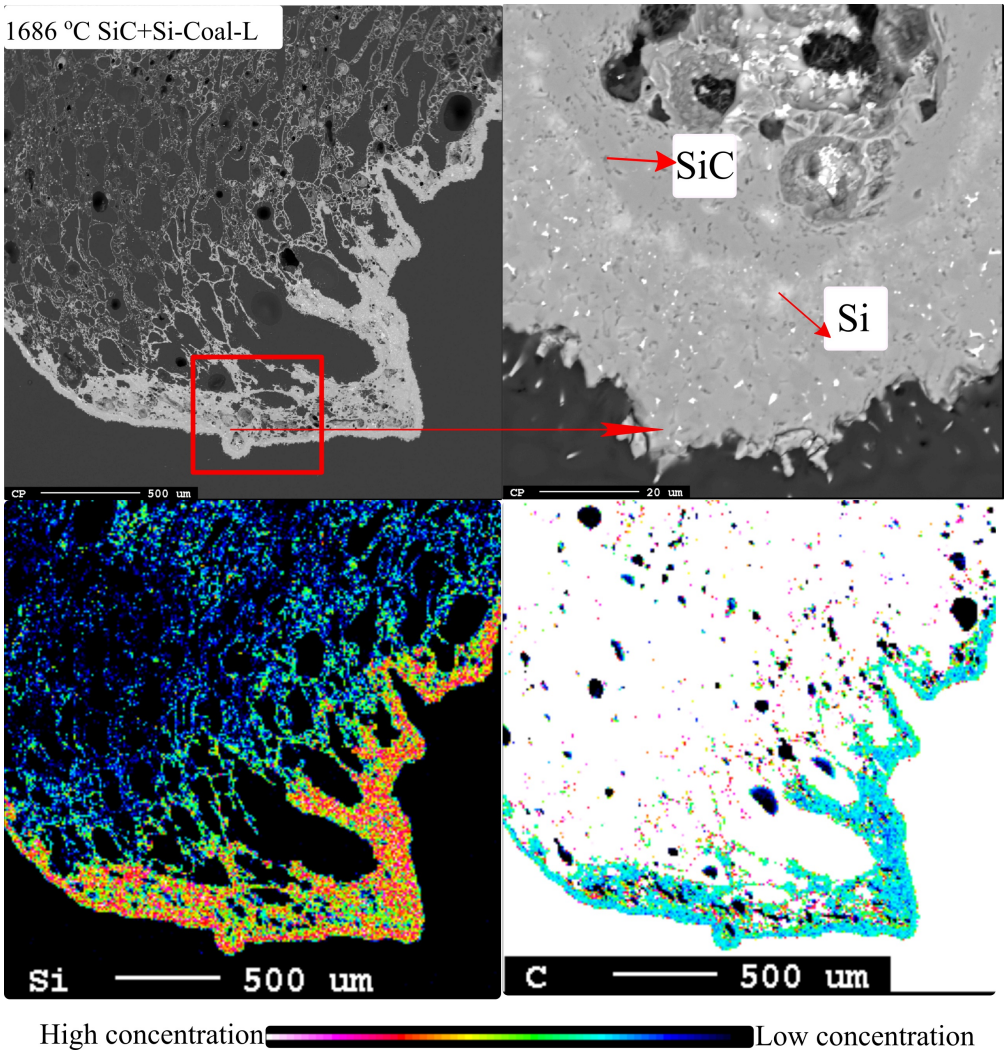

Figure 4.2.20. EPMA of SiC produced in lower (L) layer at 1686 °C using (SiO_2 + Si), and elemental mapping of Si and carbon in SiC sample. Traces of elemental Si are visible in the SiC particle.

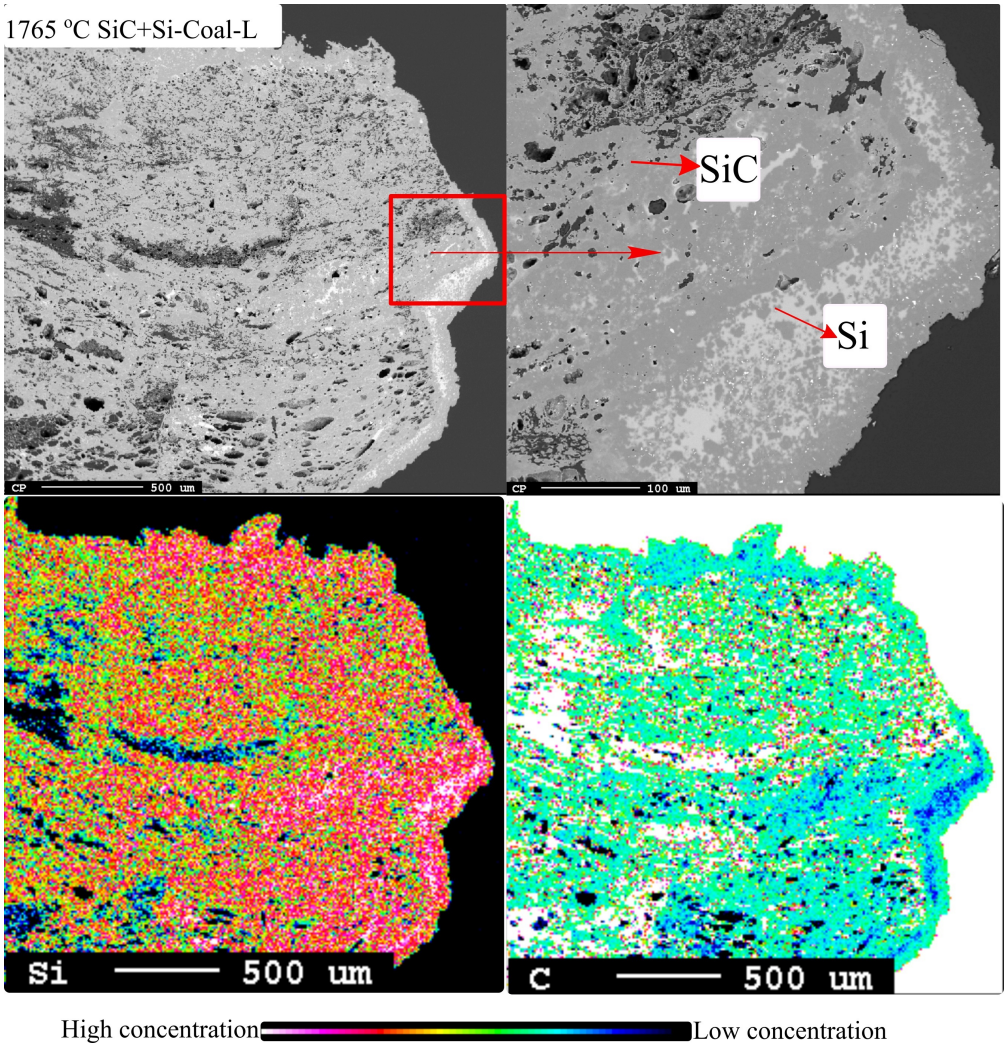

Figure 4.2.21. EPMA of SiC particle produced in lower (L) layer at 1765 °C using (SiO_2 + Si), and elemental mapping of Si and carbon in it. Traces of elemental Si are visible in the SiC particle.

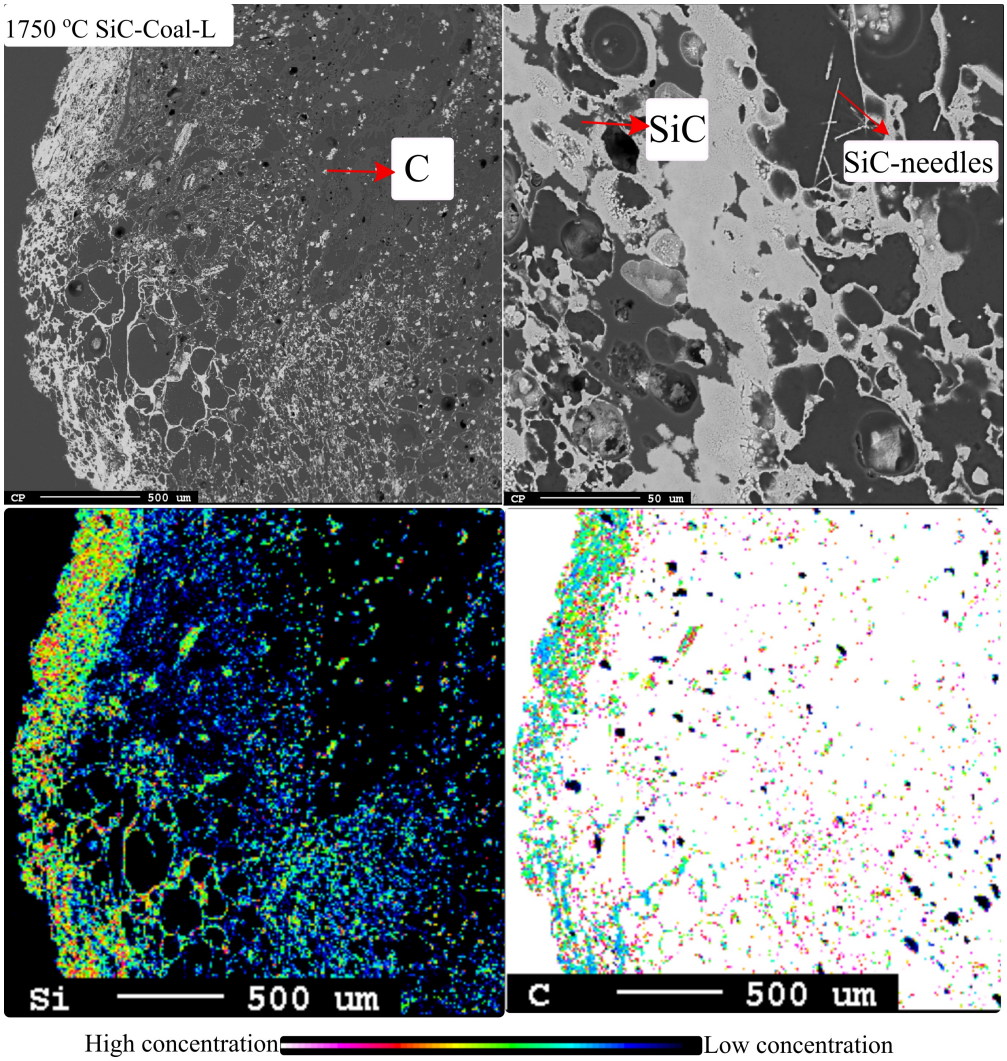

Figure 4.2.22. EPMA of SiC produced in lower (L) layer at 1750 °C using (SiO_2 + SiC), and elemental mapping of Si and carbon in it. No traces of elemental Si could be observed in the SiC particle.

4.2.3 Transformation to α-SiC: Graphite tube furnace experiments

The graphite tube furnace was used to study the modifications developing in the structure of coal-converted β-SiC, when it is exposed to temperatures > 2000 °C. β-SiC particles collected from the induction furnace experiments with (SiO_2 + Si), conducted at 1900 °C, were converted to α-SiC. The particles collected from the middle (with 9 wt.% elemental Si) and lower (with 24 wt.% Si) layers were used, and they were heated at 2100, 2300, and 2450 °C. Details of these experiments are presented in **Table 3-15. Figure 4.2.23** shows the coal-converted β-SiC samples before and after they were heated at 2100, 2300, and 2450 °C. The SiC changes its color as the temperature increases. Precipitation of crystals on the surface of the particle is also visible, especially in the heat-treated β-SiC samples that had a higher content of Si.

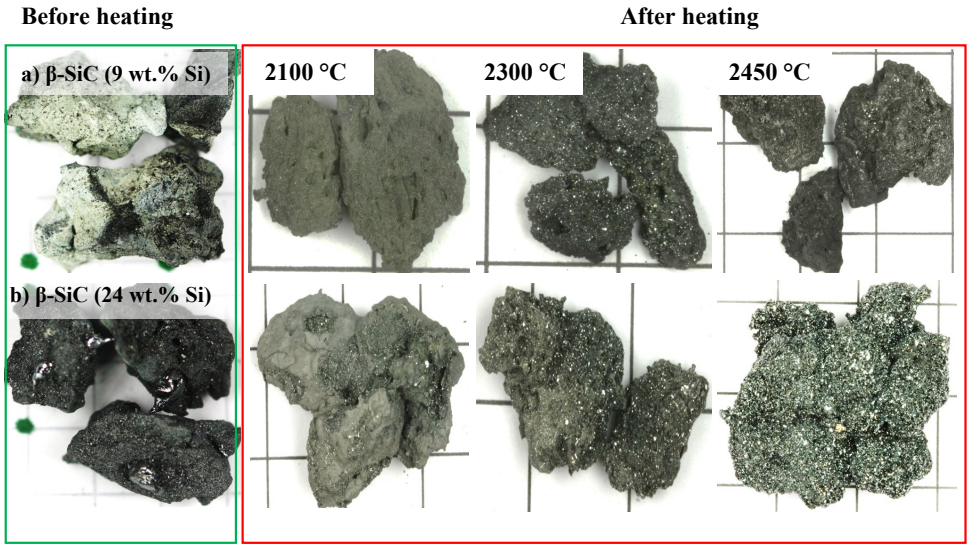

Figure 4.2.23. Coal-converted β-SiC samples from (a) middle (9 wt.% Si) and (b) lower (24 wt.% Si) layers, before and after they were heated at 2100, 2300, and 2450 °C.

4.2.3.1 SEM morphology

Figure 4.2.24 depicts SEM morphologies of β-SiC samples with 9 and 24 wt.% Si, after being heat-treated at 2100, 2300, and 2450 °C. Hexagonal plate-shaped crystals have formed in most samples, and more crystals form as the temperature increases. There are no hexagonal plate-shaped crystals in the SiC samples heat-treated at 2100 °C (**Figure 4.2.24a** and **d**), whereas, very prominent hexagonal-shaped crystals are present in the SiC samples heated at

temperatures ≥ 2300 °C, indicating the formation of α-SiC phase. The results reveal that a temperature above 2100 °C is required to form α-SiC in coal-converted SiC particles. The new SiC particles are very dense, and the original coal structure has disappeared completely. The images show that when partly converted SiC are heated to temperatures > 2000 °C, the SiC crystals gather, come outside of the pores, and aggregate on the surface of coal.

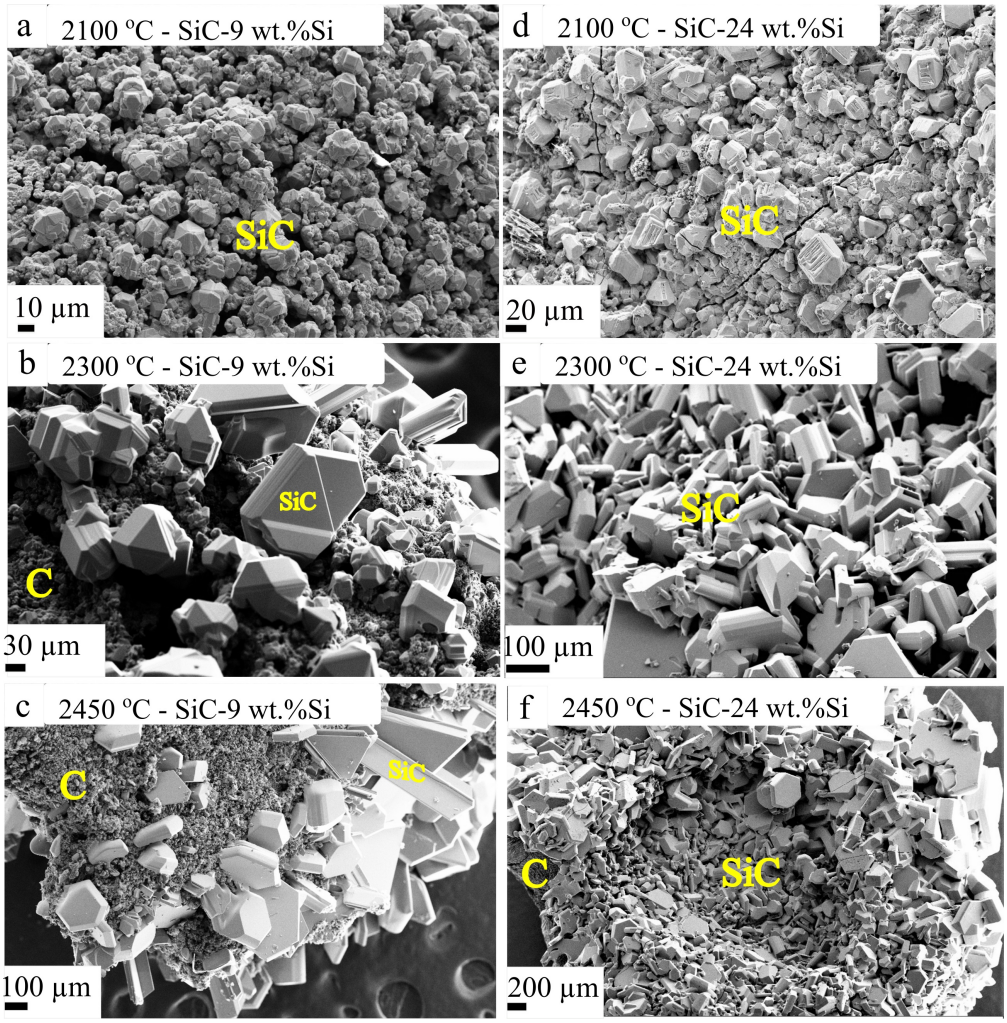

Figure 4.2.24. SEM morphologies of β-SiC samples with (a–c) 9 wt.% Si and (d–f) 24 wt.% Si, after heat-treated at 2100, 2300, and 2450 °C.

4.2.3.2 EPMA-BSE imaging

Figure 4.2.25 shows the corresponding EPMA-BSE images of the heat-treated β-SiC samples with 9 and 24 wt.% Si, after they were exposed to 2100, 2300, and 2450 °C. The hexagonal plate-shaped structures observed in the SEM (**Figure 4.2.24**) are visible in the EPMA images as well, especially at 2450 °C. They are highlighted with red arrows in **Figure 4.2.25c** and **f.**

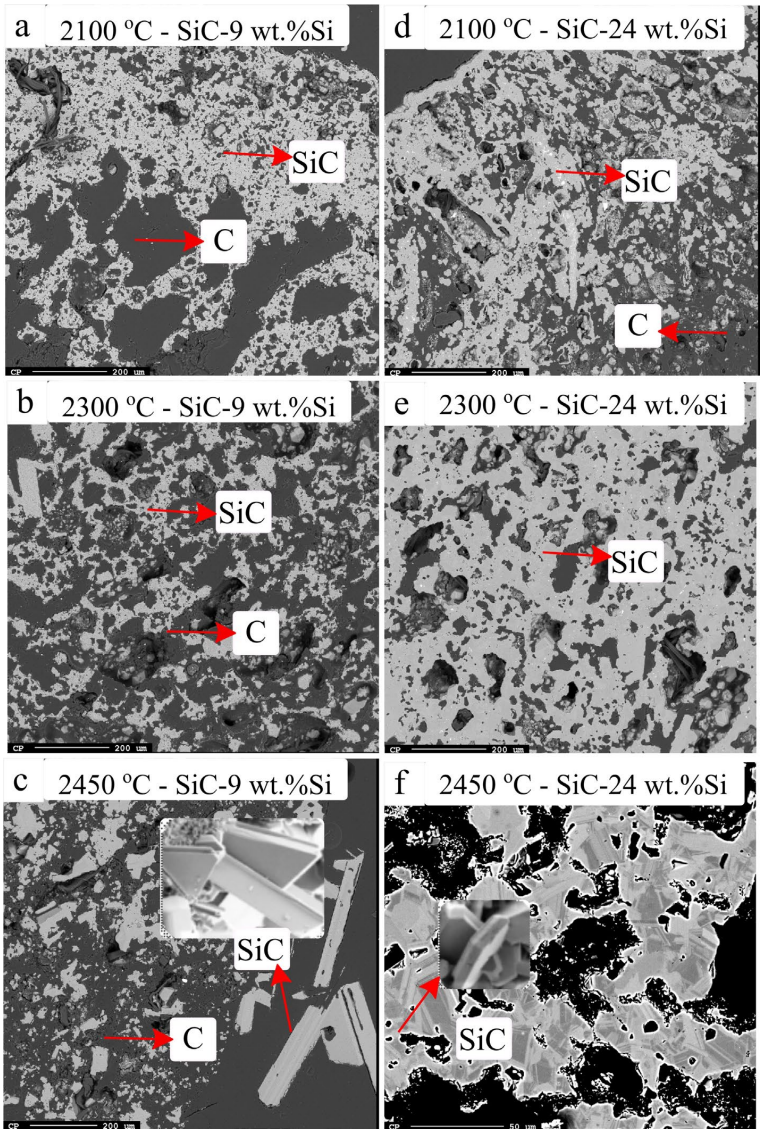

Figure 4.2.25. EPMA-BSE images of β-SiC samples (a–c) with 9 wt.% Si and (d–f) with 24 wt.% Si, after heat-treated at 2100, 2300, and 2450 °C.

4.2.3.3 XRD analysis

X-ray diffractograms of the samples were collected, and the data were analyzed using the Bruker Topas v5 software. As β-SiC was the main constituent of the starting material, it was included in the Rietveld refinement by Topas. The unreacted carbon phase in the SiC particles was not quantified in the analysis.

Figure 4.2.26 and **Figure 4.2.27** show the formation of different SiC phases in β-SiC samples with respectively 9 and 24 wt.% Si in them, after they were heated at 2300 °C. The most intense SiC peak is observed in SiC with 9 wt.% Si, located at 2θ = 35.8°, being the overlap of Bragg reflections 111-3C and 006-6H. Additional 004-4H, 012-6H, 0015-15R, and 015-15R have formed in SiC with 24 wt.% Si. The graph shows good agreement between the observed and calculated XRD patterns. The presence of α-SiC polytypes such as 4H, 6H, and 15R are established from their isolated peaks in the XRD data.

Besides the peaks formed at 2θ = 34° and 38.1°, some additional peaks have formed at 45.2°, 54.5°, and 65.6° for 6H, marked by red circles **in Figure 4.2.26**. The figure clearly shows that no additional peak has formed in SiC with 9 wt.% Si at 2300 °C. In **Figure 4.2.27**, in addition to the peaks formed for 4H, 6H, and 15R due to the overlapping at (111)-3C, the isolated peaks in each phase also confirm the presence of α-SiC polytypes. The isolated peaks are at 2θ = 33.5°, 43.2°, and 57.2° for 4H, 2θ = 45.2° and 54.6° for 6H, and 2θ = 42.85° and 57.7° for 15R. The results from the Rietveld quantitative phase composition analysis (**Figure 4.2.26**) show that the major SiC polytypes are 72 wt.% of 3C, and the rest transformed to 6H. The lesser amount of Si in SiC could be the reason that the other polytypes such as 4H and 15R did not develop in it. More α-SiC polytypes are detected in the β-SiC sample with 24 wt.% Si at 2300 °C, indicating that the presence of Si in SiC is the main reason for β-SiC transforming to α-SiC. The vertical bars in **Figure 4.2.26** and **Figure 4.2.27** show the angular position of the allowed Bragg reflections (d-spacings).

Figure 4.2.28 and **Figure 4.2.29** show the X-ray diffractograms of β-SiC samples with 9 and 24 wt.% Si, respectively, showing the SiC phases in them, both before and after they were heat-treated at 2100, 2300, and 2450 °C. The fitted diffractograms show good agreement between the observed and calculated XRD patterns of all SiC samples that were analyzed quantitatively by Topas. The fitted diffractograms of all SiC samples are presented in Appendix B. Two additional experiements were performed using SiC with 24 wt.% Si at 2100 and 2200 °C. The X-ray diffractograms of the samples collected from these two experiments

presented in **Figure 4.2.30** show that, upon increasing the temperatures to 2100 °C, the particle initially started to reduce its stacking fault, and the extra peaks at 2θ = 33.7° and 38.3° disappear.

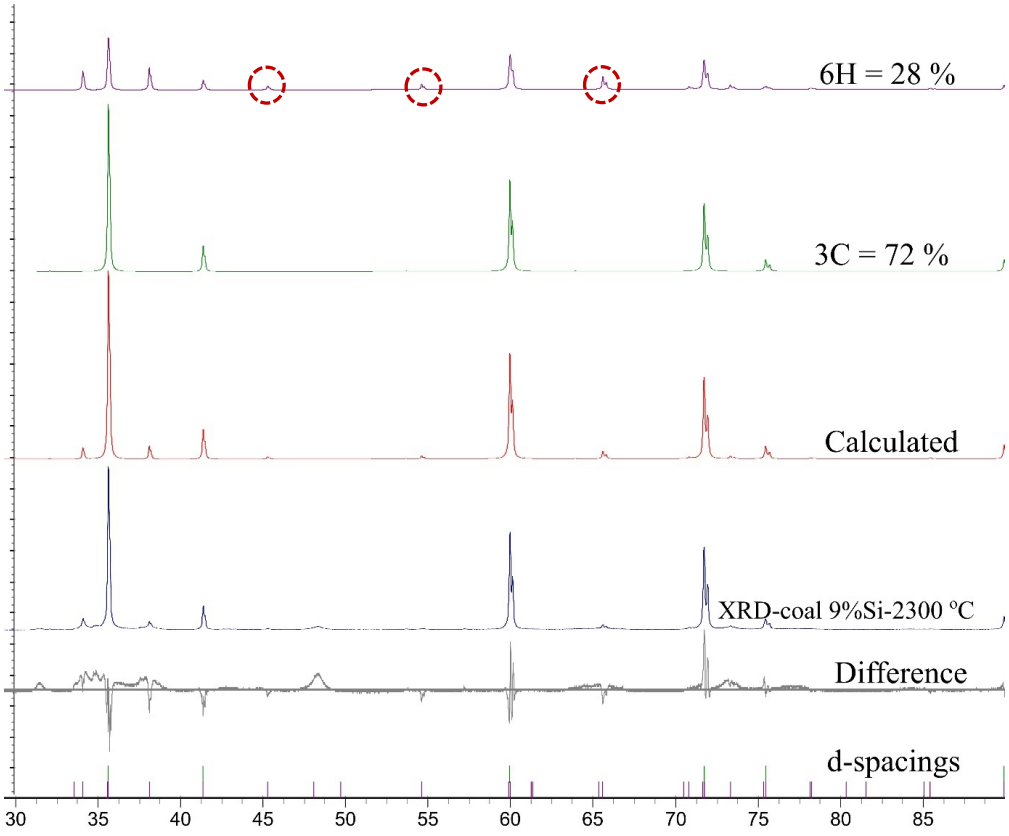

Figure 4.2.26. Formation of different SiC phases in β-SiC sample with 9 wt.% Si at 2300 °C.

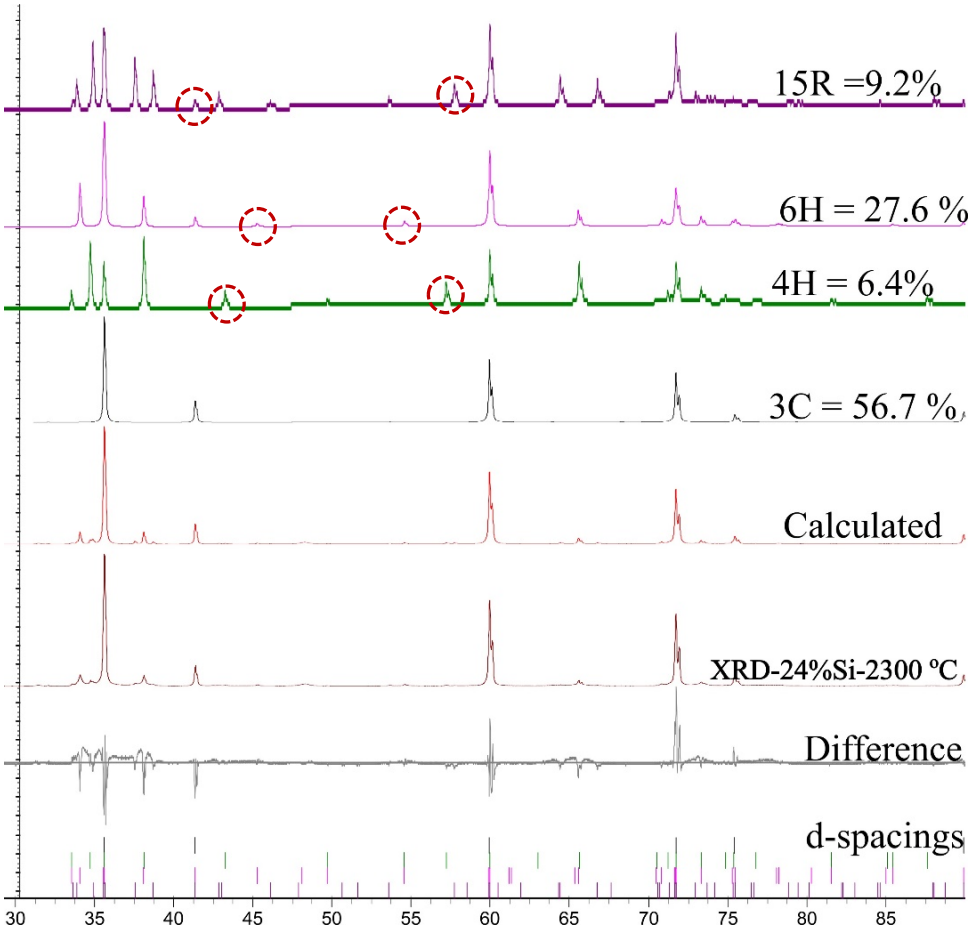

Figure 4.2.27. Formation of different SiC phases in β-SiC sample with 24 wt.% Si at 2300 °C.

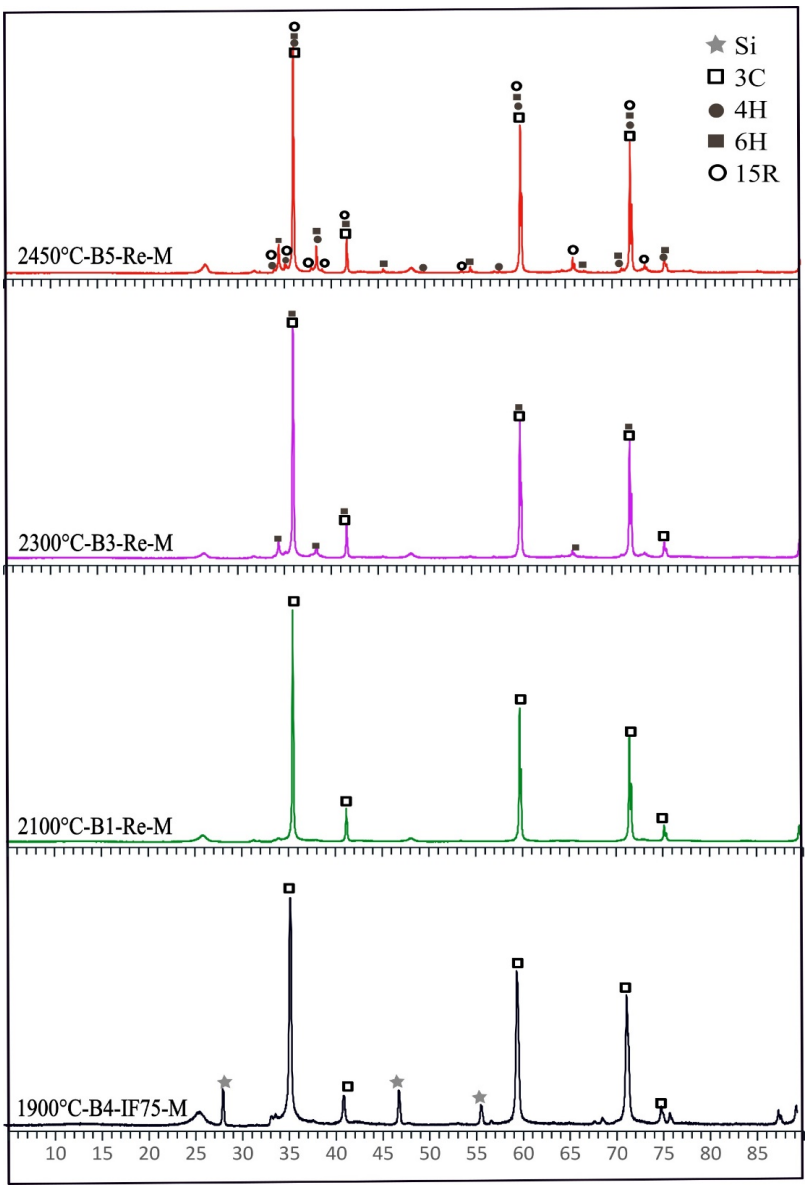

Figure 4.2.28. X-ray diffractograms identifying SiC phases in β-SiC with 9 wt.% Si formed at 1900 °C, and heat-treated at 2100, 2300, and 2450 °C.

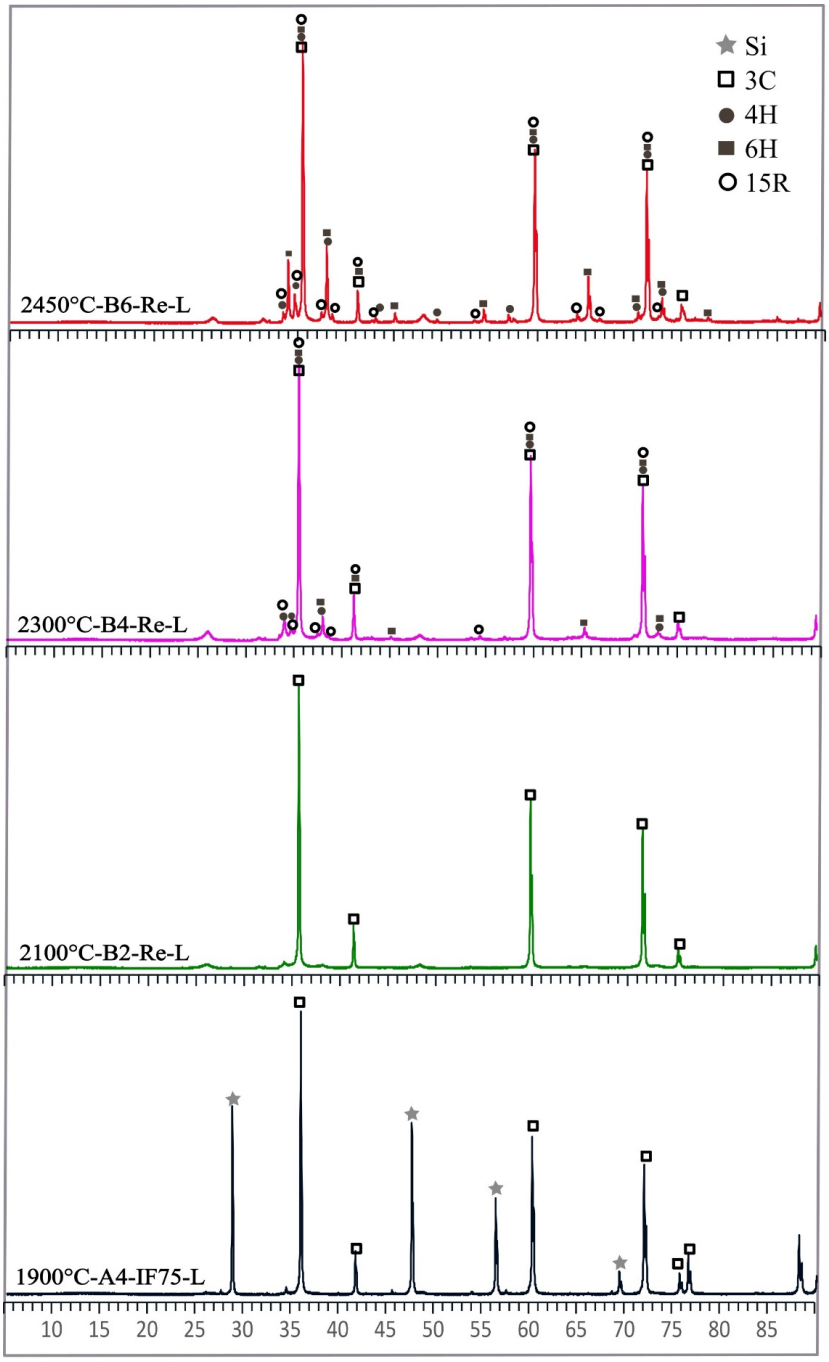

Figure 4.2.29. X-ray diffractograms of SiC phases in β-SiC with 24 wt.% Si formed at 1900 °C, and after heat-treated at 2100, 2300, and 2450 °C.

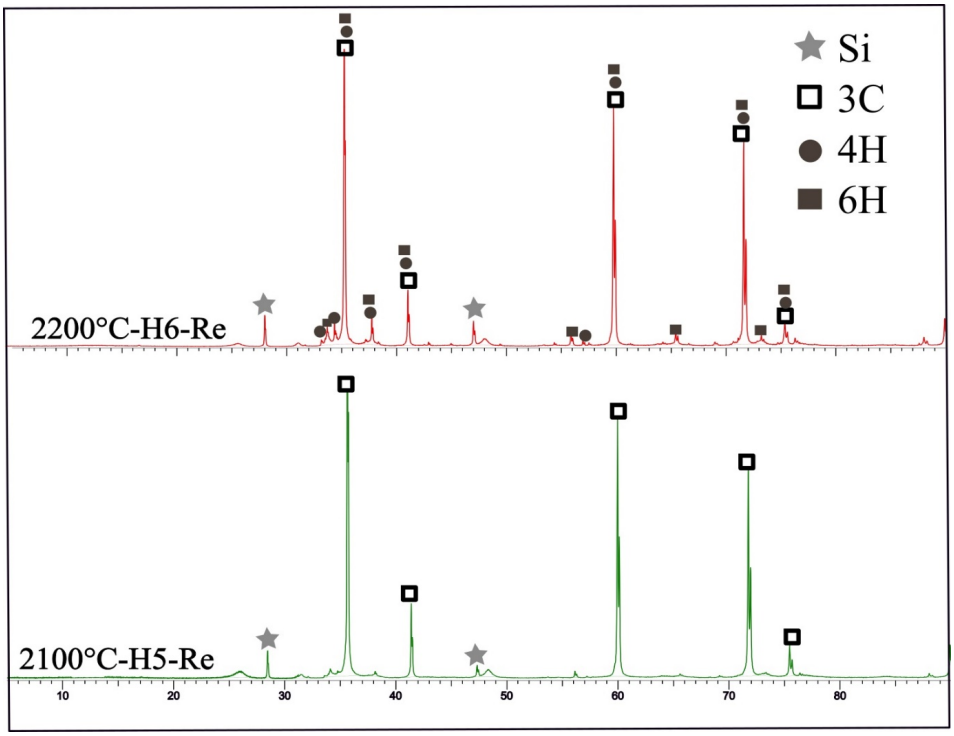

Figure 4.2.30. X-ray diffractograms identifying SiC phases in β-SiC with 24 wt.% Si, heat-treated at 2100 and 2200 °C for validation experiments.

Figure 4.2.31 and **Figure 4.2.32** show the quantitative polytype analysis of the coal-converted β-SiC samples with varying amounts of Si, heated at 2100, 2300, and 2450 °C. At 2100 °C, the β-SiC samples containing 9 and 24 wt.% of pure Si, did not transform to α-SiC. However, at 2300 °C, β-SiC sample with 9 wt.% Si has partly transformed to α-SiC, and 6H was the main polytype detected in it. The β-SiC sample with 24 wt.% Si has transformed to 43 wt.% of α-SiC, at 2300 °C. The most common polytypes such as 4H, 6H, and 15R are found in it. At 2450 °C, β-SiC samples with 9 and 24 wt.% Si have transformed to 50 and 86.6 wt.% of α-SiC, respectively. **Figure 4.2.32** also shows samples from the two additional experiments, heat-treated at 2100 and 2200 °C. No transformation to α-SiC took place at 2100 °C, whereas at 2200 °C, around 37 wt.% transformed to α-SiC, forming mostly the polytypes 4H and 6H, and 4.9 wt.% of Si has left in it.

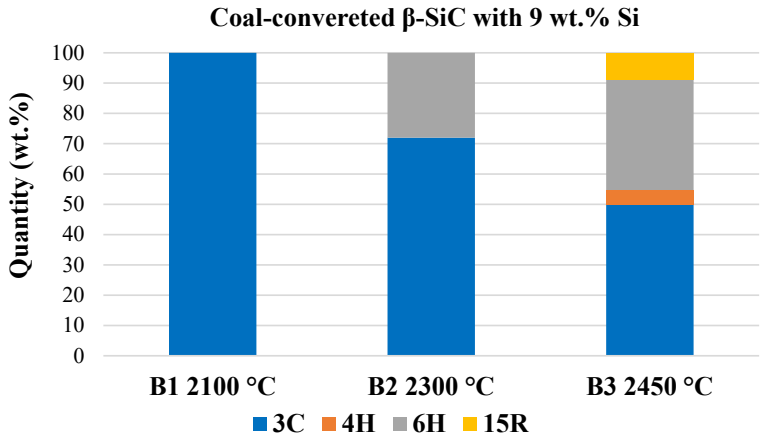

Figure 4.2.31. Quantitative polytype analysis of coal-converted β-SiC samples with 9 wt.% of Si, heated at 2100, 2300, and 2450 °C.

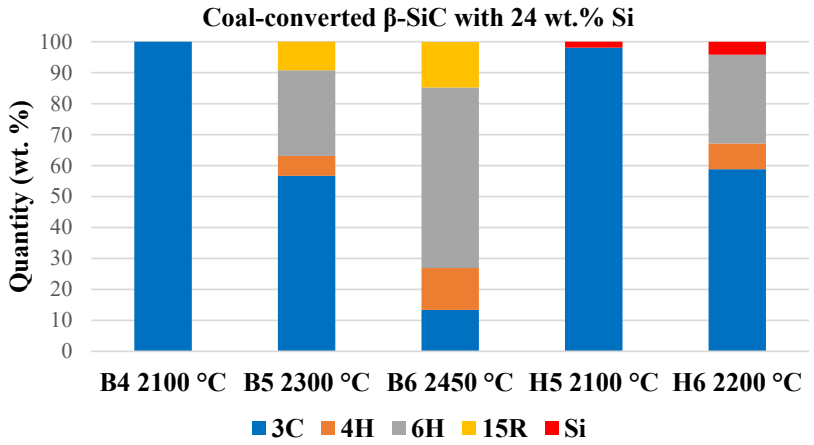

Figure 4.2.32. Quantitative polytype analysis of coal-converted β-SiC samples with 24 wt.% of Si, heated at 2100, 2300, and 2450 °C. Last two samples are from additional experiments conducted at 2100 and 2200 °C, which also contained 24 wt.% Si.

4.3 Petroleum coke

Pet-coke was the third and final carbon source used in this research, to produce SiC and Si. As with charcoal and coal, both induction and graphite tube furnaces were used to produce SiC in the laboratory, and to validate these results, experiments were conducted in the graphite tube furnace in a more controlled environment. To generate SiO(g), either a mixture of (SiO_2 + Si) or pellets made from (SiO_2 + SiC) were used. The graphite tube furnace was also used to transform the β-SiC converted from pet-coke, to α-SiC. Visual observation, EPMA, SEM, XRD, and chemical analysis of the SiC samples obtained from both the furnaces are presented in the following sections.

Figure 4.3.1 and **Figure 4.3.2** show the type of samples collected from the top, middle, and lower sections of the final product (initial pet-coke) layer, from the induction and graphite tube furnaces, respectively. In both cases, the unreacted particles from the top layer resembled the original carbon material, pet-coke. The particles from the middle layer consisted of both completely and partly transformed SiC particles. In the lower layer, the particles had completely transformed to SiC. There were no droplets of Si on the surfaces of the particles. SiC particles from the middle layer were green in color, whereas those from the lower layer were hard and dark bluish in color.

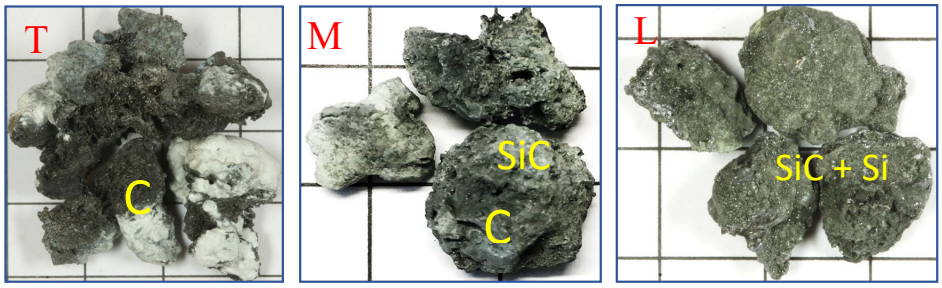

Figure 4.3.1. Samples from top (T), middle (M), and lower (L) layers of final product, collected from induction furnace.

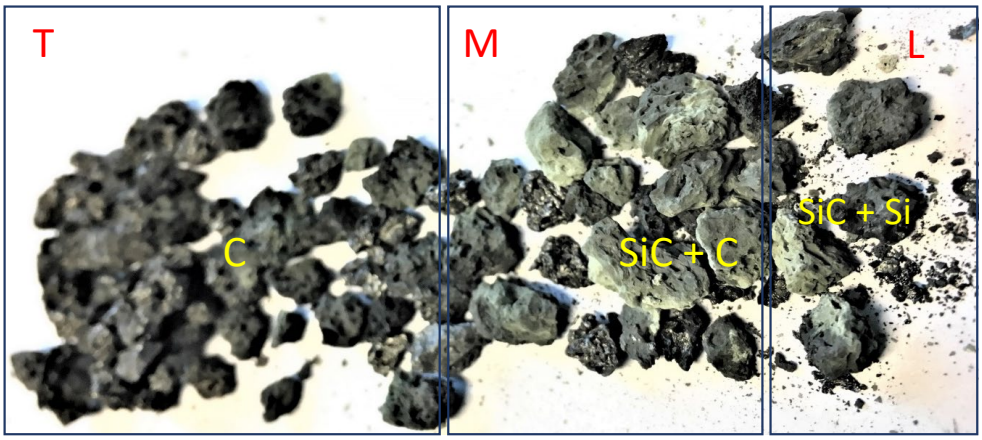

Figure 4.3.2. Samples from top (T), middle (M), and lower (L) layers of final product, from graphite tube furnace.

4.3.1 β-SiC production: Induction furnace experiments

Only (SiO_2 + Si) was used as charge mix in the induction furnace experiments. Both constant volume and constant weight experiments were performed in the induction furnace. The quantities of raw materials used in both sets of experiments are presented in **Table 3-7** and **Table 3-11**,and the experimental conditions set for them are presented in **Table 3-8** and **Table 3-12**, respectively. Retrieving samples from the middle and lower layers of the crucible, after the experiments, was a laborious task. The cross-section of the crucible along with samples in the lower layer is shown in **Figure 4.3.3.** The pet-coke and the transformed SiC particles stuck together, especially in the lower layer close to the (SiO_2 + Si) charge. Therefore, the approximate amounts of SiC produced in each layer could not be measured after the induction furnace experiments. The samples collected were further analyzed to characterize and quantify the SiC and Si formed in them. The following sections describe the results from these analyses.

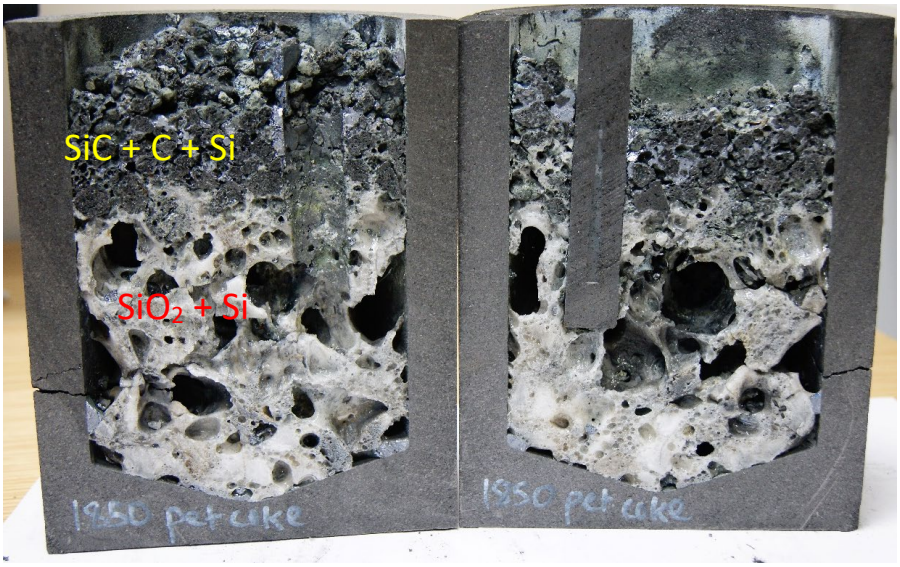

Figure 4.3.3. Cross-section of crucible after conducting experiment with pet-coke.

4.3.1.1 SEM morphology

SEM characterizations were performed on SiC particles randomly selected from the different experiments. The SEM images of samples from the middle and lower layers, exposed to a temperature < 1750 °C (**Figure 4.3.4**) and ~1800 °C (**Figure 4.3.5**) are presented. SiC crystals in the shape of whiskers have formed on the samples in the middle layer (**Figure 4.3.4**). Pores in the form of cracks on the pet-coke surface are also visible. In the lower layer (**Figure 4.3.5**), pet-coke has completely transformed to SiC. The pores and cracks have disappeared, and the particle has become denser. Therefore, it is assumed that Si has formed, filling up pores in the SiC particle.

Figure 4.3.4. SEM images of SiC from middle layer, exposed to a temperature < 1750 °C. SiC crystals in the shape of whiskers have formed.

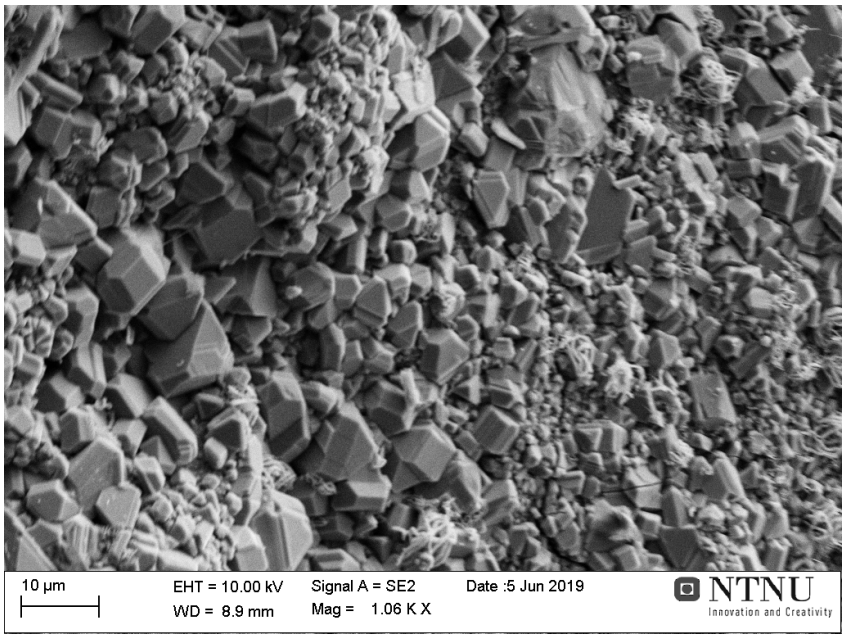

Figure 4.3.5. SEM images of SiC from lower layer, exposed to a temperature of ~1800 °C. Particle is densely filled with crystals, assumed to be from Si formation in them.

4.3.1.2 EPMA-BSE imaging

EPMA-BSE imaging was carried out to determine the phases, composition, and elemental distribution in the SiC particles produced at different temperatures. **Figure 4.3.6** shows EPMA images of SiC particles from the lower and middle regions of the initial pet-coke layer, collected after conducting the constant volume experiments at 1750, 1800, 1850, and 1900 °C. The dark gray regions in the images are SiC, and the light gray or nearly-white regions are the elemental Si in SiC. Pure carbon and epoxy are nearly-black in color. In the SiC samples from the lower layers (images on the left side), more Si forms in them as the temperature increases (**Figure 4.3.6**). In the middle region, the carbon particles were exposed to slightly lower temperatures compared with the lower layer. Si phase is not present in samples from the middle, and the structure of pet-coke is visible, even after it is exposed to SiO(g). It was difficult to see the pet-coke structure in the SEM morphology investigation, whereas the structure is clearly visible in the EPMA images. **Figure 4.3.6c** shows the sharp boundary between the SiC formed in the pores and the unreacted carbon region. This confirms that the pores are important for the transformation to SiC, when it is exposed to SiO(g).

Also, the pores are not distributed homogeneously; a mixture of small and large pores with thick and thin cell walls could be observed. Therefore, during the conversion to SiC, SiO(g) is retained longer on the surface of pet-coke. This could be the reason for Si forming simultaneously, once SiC has formed on the surface of pet-coke. **Figure 4.3.7**shows the elemental distribution of Si and carbon in a SiC particle from the lower layer, formed at 1800 °C. High concentrations of elemental Si are present in the imaged particle. The molten Si formed is surrounded by SiC crusts in the lower layers, at all temperatures (**Figure 4.3.6a**, **c**, **e**, and **g**), which was observed also in both charcoal and coal.

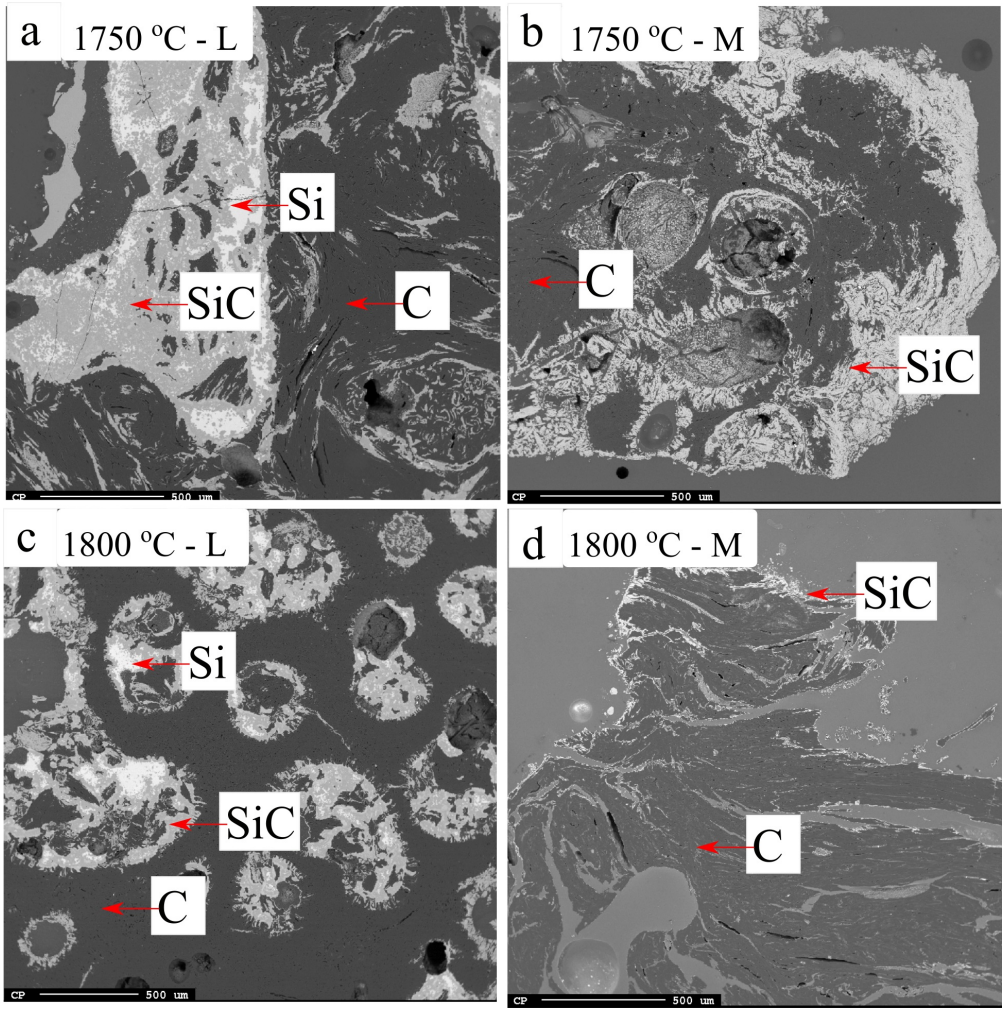
a
1750 °C - L
Si
SiC
C
b
1750 °C - M
C
SiC
c
1800 °C - L
Si
SiC
C
d
1800 °C - M
SiC
C

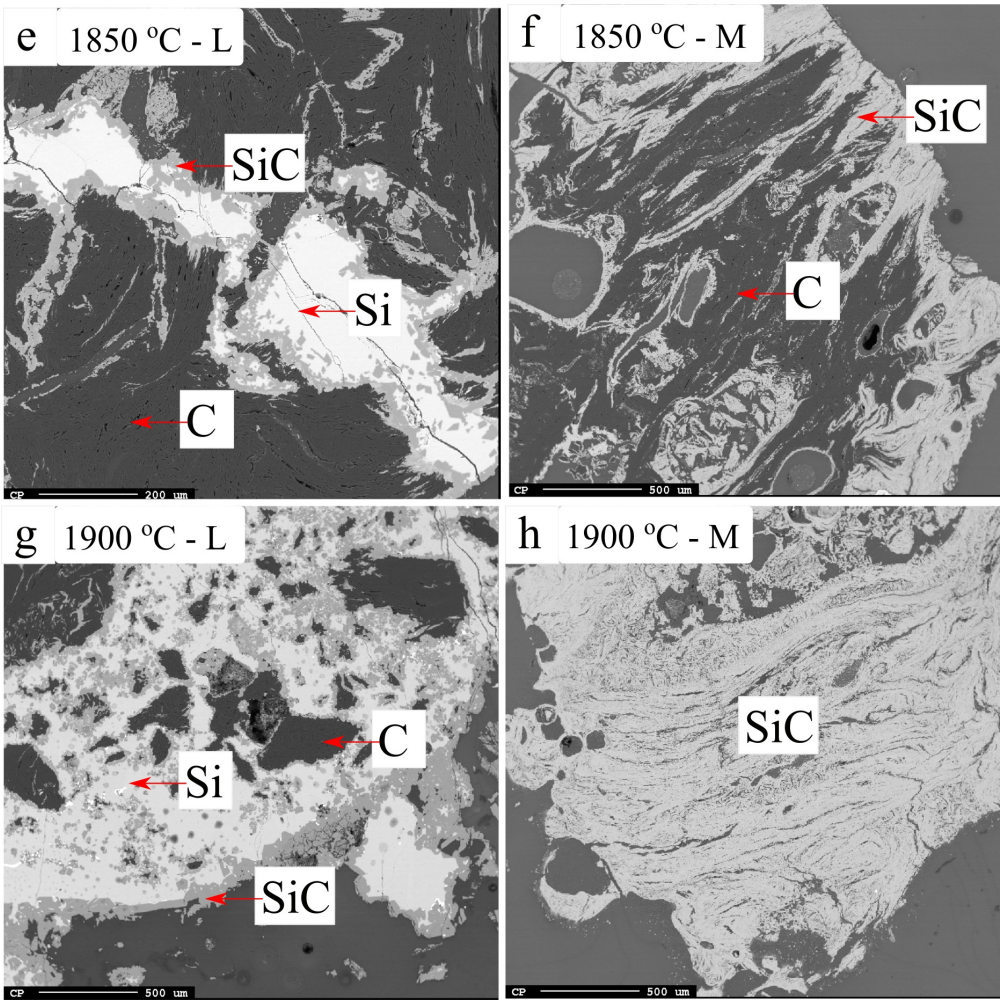

Figure 4.3.6. EPMA images of SiC particles formed in (a, c, e, g) lower (L) and (b, d, f, h) middle (M) regions of initial pet-coke layer, after conducting constant volume experiments at 1750, 1800, 1850, and 1900 °C. Molten Si surrounded by SiC crust is clearly visible in lower layers.

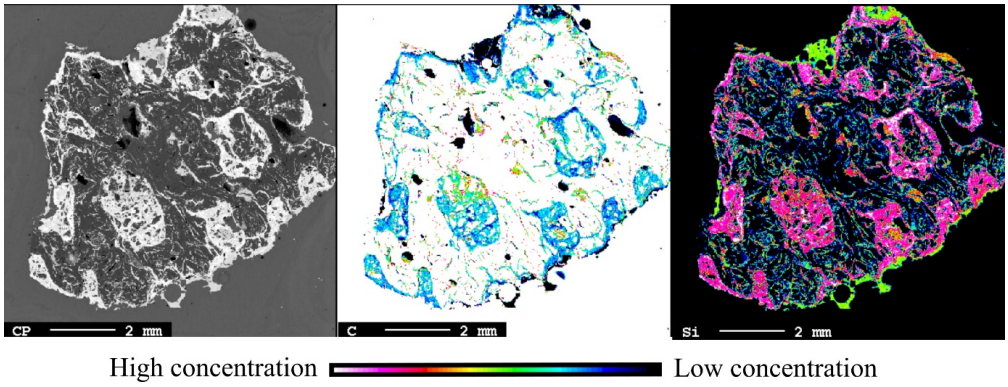

Figure 4.3.7. EPMA of SiC particle from lower layer, formed at 1800 °C, and elemental distribution of carbon and Si in it. High concentrations of elemental Si are visible in the particle.

4.3.1.3 XRD analysis

The XRD analysis of SiC particles collected from the middle and lower layers was carried out, to identify the different crystal phases, as shown in **Figure 4.3.8**. The samples are from the constant volume experiments, conducted at 1750, 1800, 1850 and 1900 °C, using a mixture of (SiO_2 + Si), at high SiO pressure. The quantitative XRD analysis identified that only the 3C-SiC polytype (100%), which is the β-SiC phase, is present in the samples. Elemental Si peaks are mostly present in the SiC particles from the lower layer (**Figure 4.3.8**). Here too, the stacking faults are causing the (111) peaks of 3C-SiC in all samples, along with the elevated backgrounds under them, for $2\theta \geq 33.6°$.

The samples from the middle layer did not show any Si peak in the diffractograms. The intensities of the β-SiC peaks are extremely low in samples from the middle layer, at both 1750 and 1800 °C. This is due to the high carbon content, which arises from the high intensity Bragg reflection from the carbon phase ($2\theta = 26°$). This shows that the intensity is very much dependent on the amount of elemental distribution in the samples. The XRD data from all samples have high intensity peaks that arise from the carbon phase. This gives an indication that pet-coke has not reacted well with SiO(g), causing reduced levels of conversion to SiC. The results obtained from the XRD data are in good agreement with the EPMA images of the samples at all temperatures. The presence of unreacted carbon in the SiC particles indicates that along with the temperature, the type of carbon particle is also a significant factor that influences the conversion to SiC. Similar results were obtained from the XRD analysis of samples collected from the constant weight experiments, conducted at 1750 and 1800 °C (**Figure 4.3.9**). Here too, only the 3C cubic form, the β-SiC phase, could be identified both in the lower and middle layers, at all temperatures.

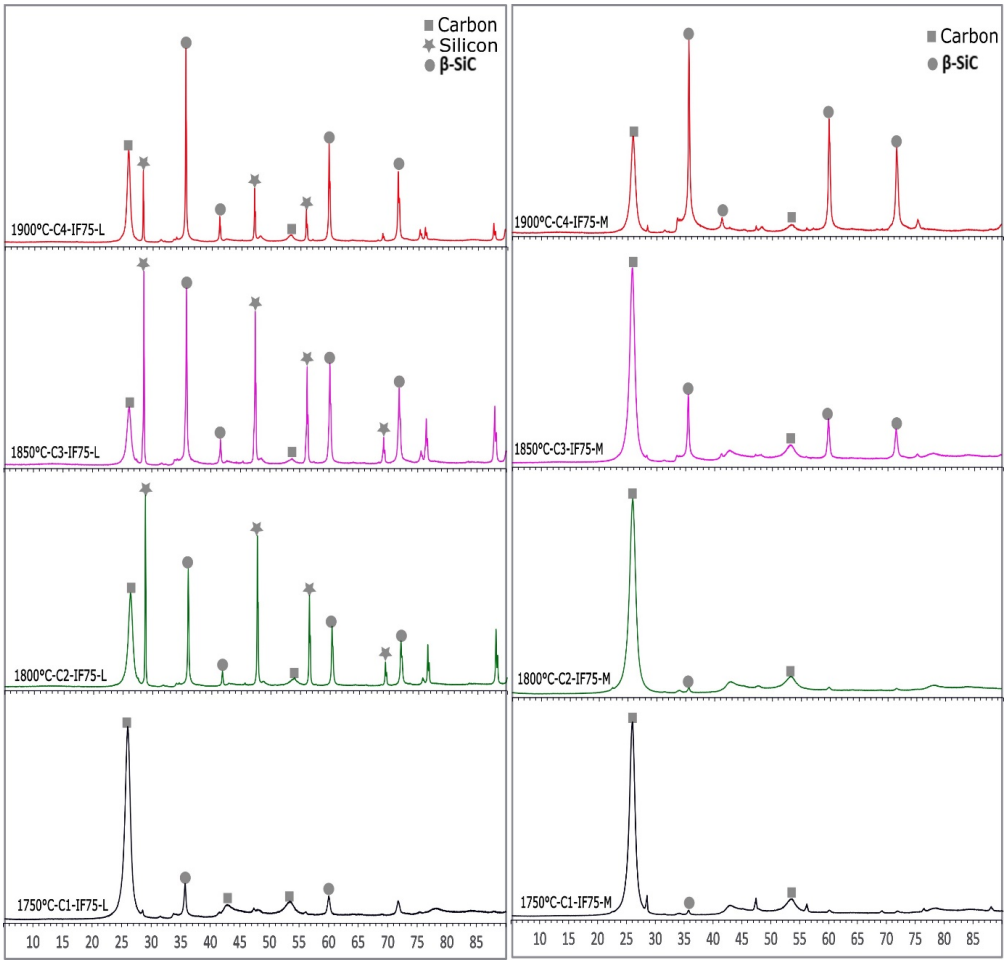

Figure 4.3.8. X-ray diffractograms of pet-coke-converted SiC samples from middle (M) and lower (L) layers. Samples are from constant volume experiments conducted at 1750, 1800, 1850, and 1900 °C.

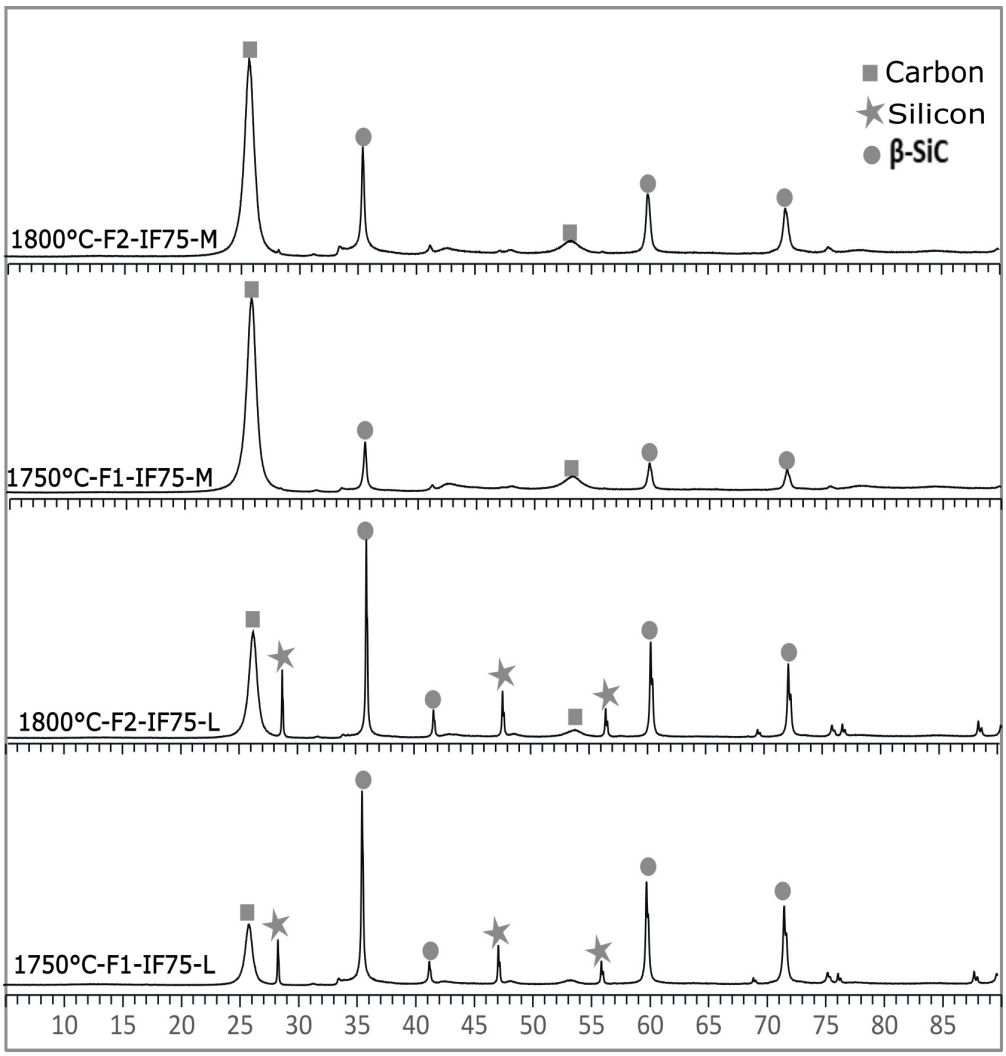

Figure 4.3.9. X-ray diffractograms of pet-coke-converted SiC samples from middle (M) and lower (L) layers, collected from constant weight experiments conducted at 1750 and 1800 °C. SiC present has only 3C-SiC polytype (100%), which is β-SiC phase.

4.3.1.4 Chemical analysis

The amount of free carbon, SiC, and elemental Si in pet-coke-converted SiC samples from the middle and lower layers are determined by chemical analysis. **Figure 4.3.10** and **Figure 4.3.11** show the chemical analysis of samples taken respectively from the middle and the lower layers of SiC, produced at different temperatures in the constant volume experiments. The samples formed at 1750, 1800, and 1850 °C had higher amounts of free carbon in them, which increase uncertainty in the measurements. Therefore, the amount of elemental Si could not be calculated

for the samples that had more than 40% free carbon in them. The amount of SiC is calculated according to equation (23). At 1750 °C, ~3 and ~11 wt.% of pet-coke transformed to SiC in the middle and lower layers, respectively. The amount of Si in SiC samples was calculated only for samples from the lower layer at 1850 °C and for those from both middle and lower layers at 1900 °C (equation (20) and (22)). Elemental Si is present in both layers at 1900 °C, and in the lower layer at 1850 °C (**Figure 4.3.10** and **Figure 4.3.11**). The amount of unreacted carbon is high in all SiC samples. The results from both EPMA and XRD analysis confirm the presence of unreacted carbon, which is in good agreement with the chemical analysis results. However, the EPMA analysis shows formation of elemental Si in the lower layer, even at 1750 and 1800 °C (**Figure 4.3.6a** and **c**).

Figure 4.3.12 shows chemical analysis of samples from the constant weight experiments. The amount of free carbon is higher (> 50%) in both layers at 1750 °C and in the middle layer at 1800 °C. Therefore, the amount of SiC is calculated based on the total carbon content based on equation (23). The amount of Si in SiC is calculated only for samples from the lower layer at 1800 °C (equations (20) and (22)). Around 10 wt.% of elemental Si has formed in SiC particles in the lower layer at 1800 °C. Both the constant volume and constant weight experiments show a similar trend in producing SiC.

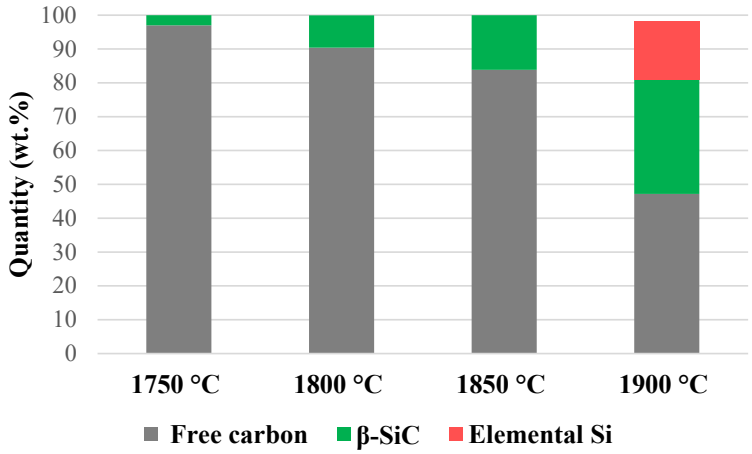

Figure 4.3.10. Chemical analysis of SiC samples from middle layer, produced at different temperatures.

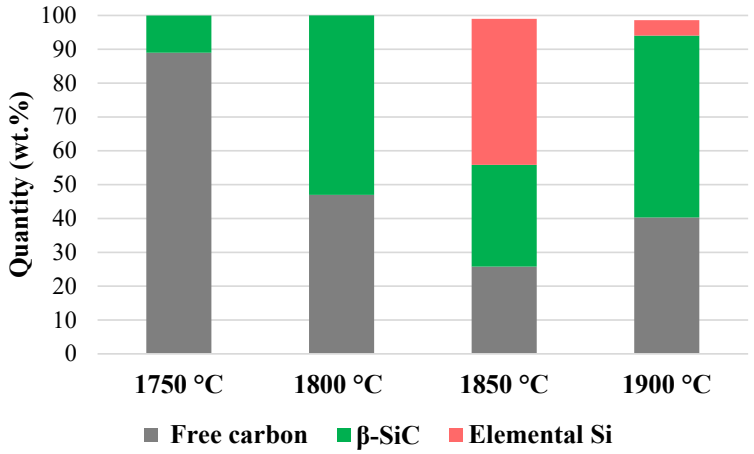

Figure 4.3.11. Chemical analysis of SiC samples from lower layer, produced at different temperatures.

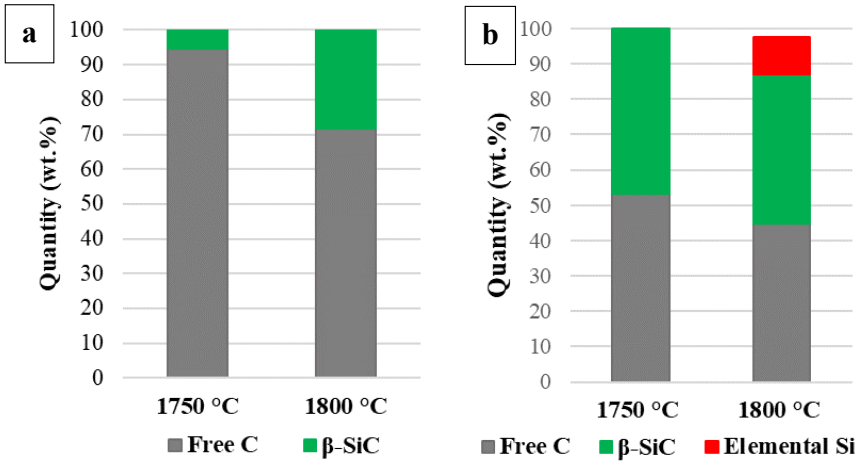

Figure 4.3.12. Chemical analysis of SiC samples from (a) middle and (b) lower layers, produced in constant weight experiments, at 1750 and 1800 °C.

4.3.2 β-SiC production: Graphite tube furnace validation experiments

Graphite tube furnace experiments were carried out to validate the induction furnace experiments. Three experiments at 1694, 1748, and 1836 °C using a mixture of (SiO_2 + Si), and another experiment at 1752 °C using (SiO_2 + SiC) pellets were performed. **Figure 4.3.13** gives the approximate quantities of initial pet-coke and the final products collected from the graphite tube furnace experiments. SiC production increases with an increase in temperature.

More details of the samples are revealed from their characterization analyses by SEM, EPMA, and chemical analysis, which are described in the following sections.

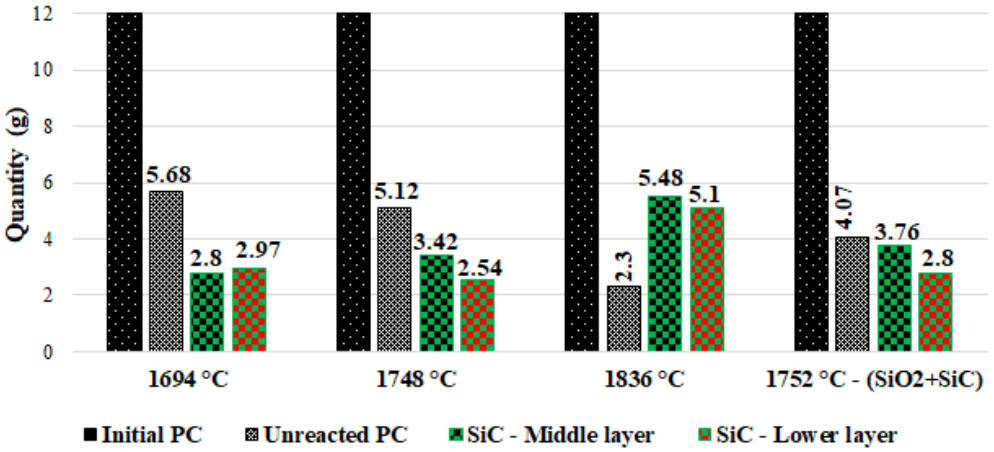

Figure 4.3.13. Quantities of initial pet-coke and final products collected from graphite tube furnace experiments. Last experiment at 1752 °C used pellets of (SiO_2 + SiC), whereas, rest of the experiments used (SiO_2 + Si) mixture as source of SiO(g).

4.3.2.1 SEM morphology

Figure 4.3.14 and **Figure 4.3.15** show SEM morphologies of the samples collected from top, middle, and lower layers, after the experiments were conducted at 1694 and 1748 °C, respectively. The (SiO_2 + Si) mixture was used as charge in these experiments. SiC in the shape of whiskers have formed in samples from the top and middle layers. In the middle layer (**Figure 4.3.14b** and **Figure 4.3.15b**), more SiC whiskers form as the temperature increases, and they get thicker. In the lower layers, SiC formation becomes dense, and the carbon surface is no longer visible, especially in the SiC particle formed at 1748 °C (**Figure 4.3.15**).

Figure 4.3.16 shows similar images of a sample from the experiment conducted at 1752 °C using (SiO_2 + SiC) pellets. There is no SiC formation in the particle from the top layer, and the structure of pet-coke is clearly visible in the image. In the middle layer, whiskers of SiC have formed on the pores, and in the lower layer, needle-shaped thin SiC crystals have formed.

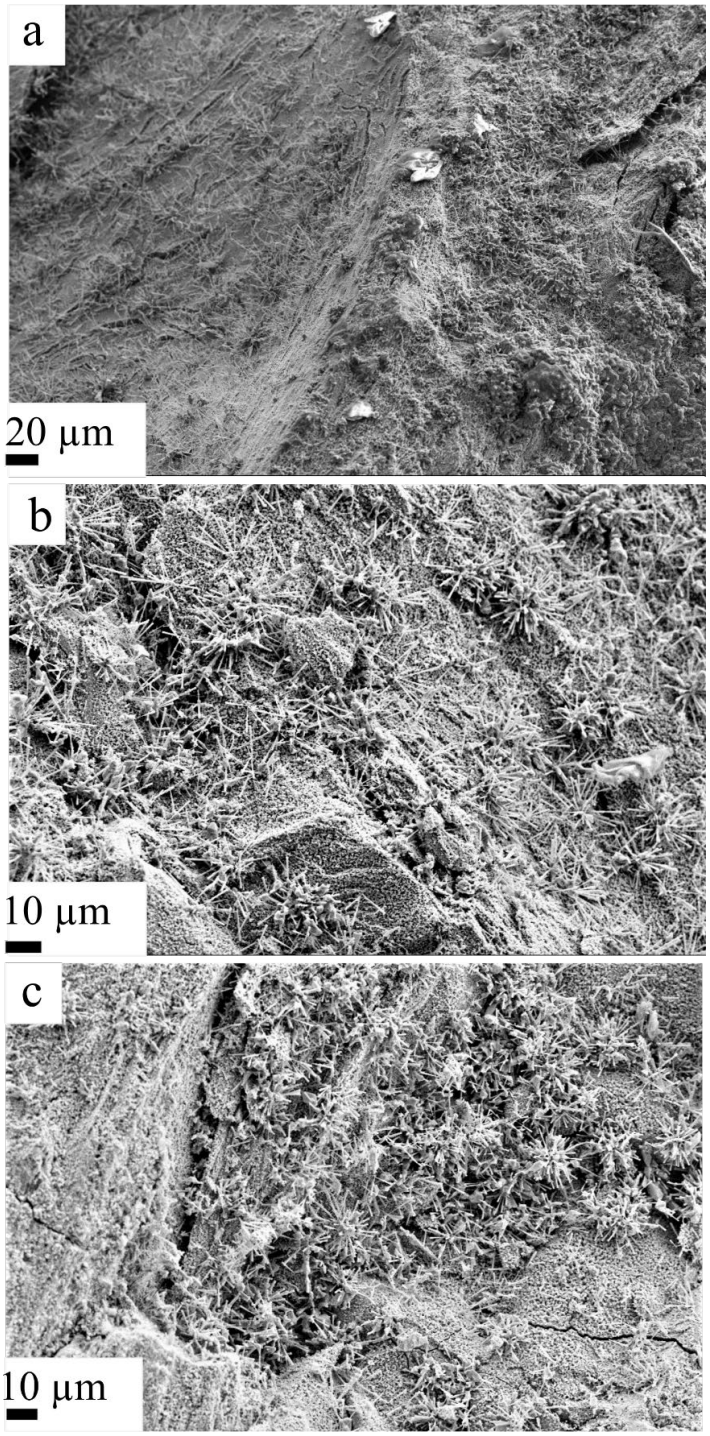

Figure 4.3.14. SEM morphologies of pet-coke-converted SiC from (a) top, (b) middle, and (c) lower layers. Experiment was conducted at 1694 °C using (SiO_2 + Si) mixture.

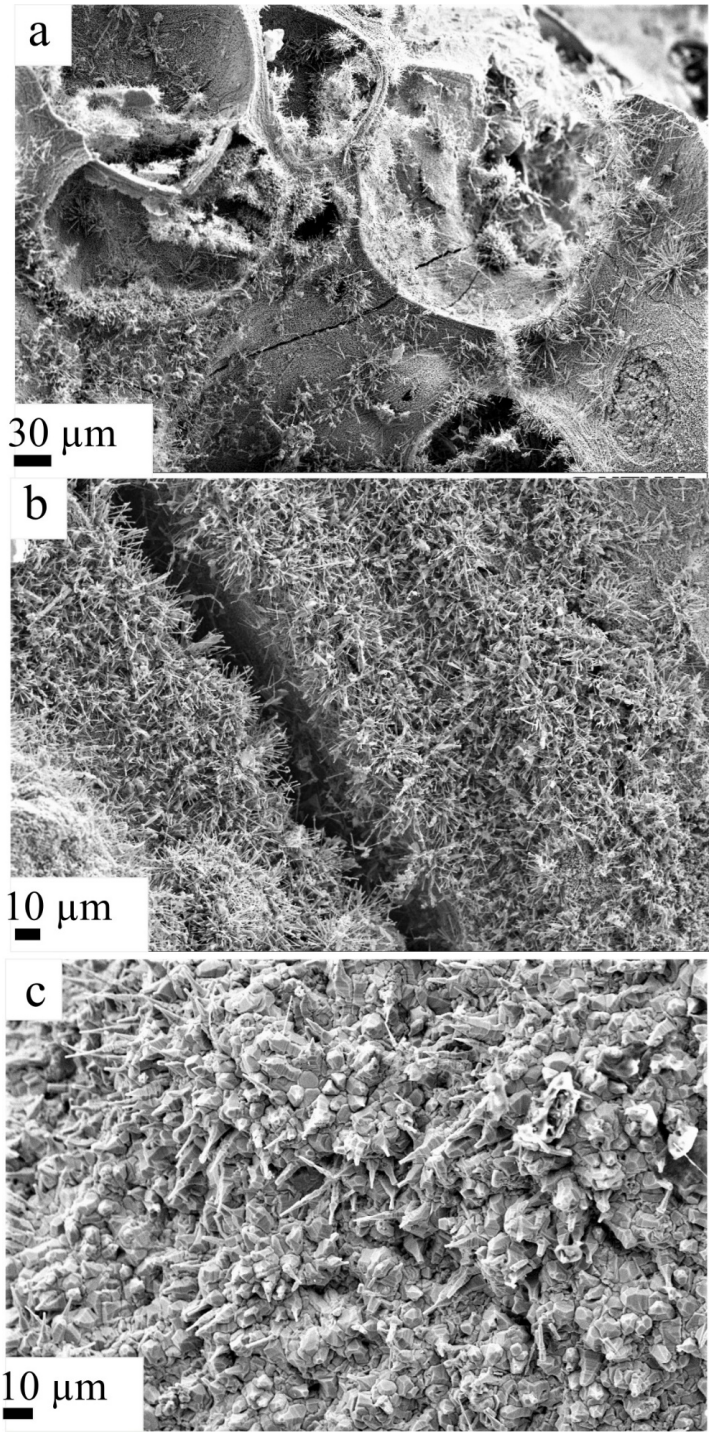

Figure 4.3.15. SEM morphologies of pet-coke-converted SiC from (a) top, (b) middle, and (c) lower layers, from experiment conducted at 1748 °C using (SiO_2 + Si) mixture.

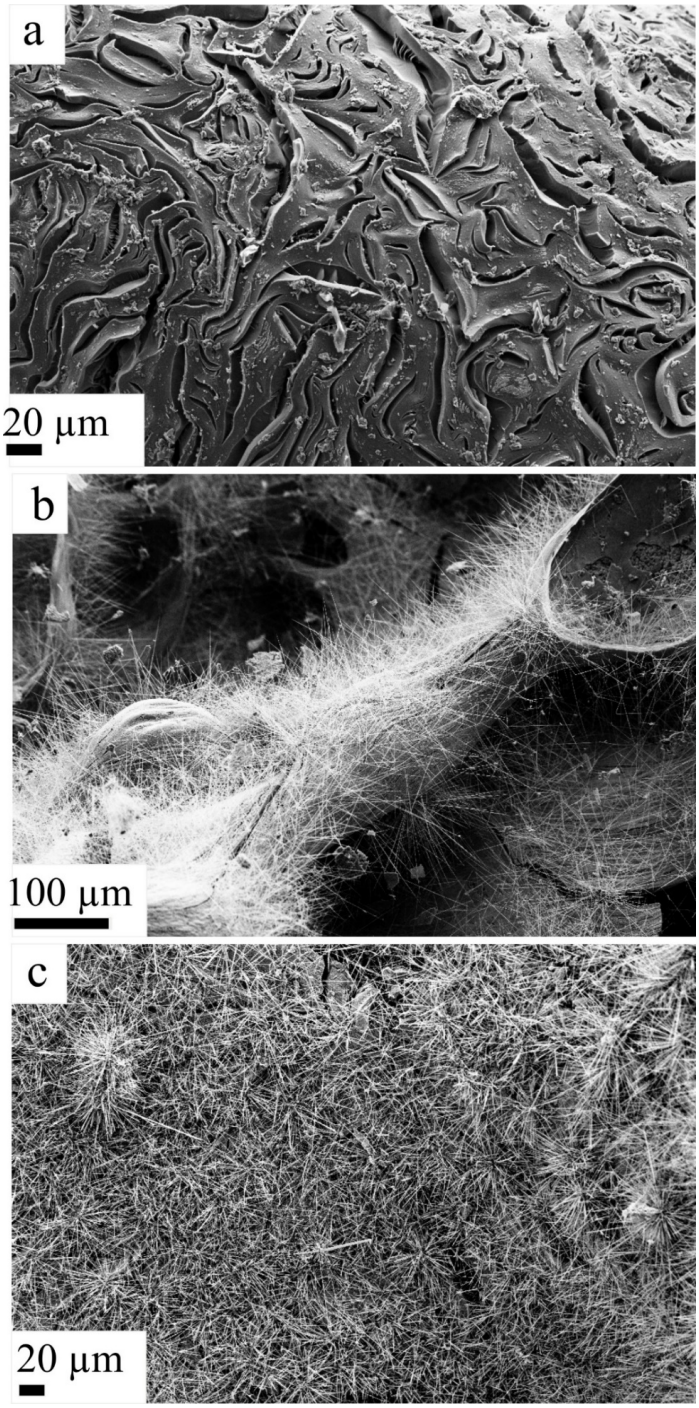

Figure 4.3.16. SEM morphologies of pet-coke-converted SiC from (a) top, (b) middle, and (c) lower layers, from experiment conducted at 1752 °C using (SiO_2 + SiC) pellets.

4.3.2.2 Chemical analysis and EPMA-BSE imaging

To form SiC samples from pet-coke, experiments were conducted at 1694, 1748, and 1832 °C using a mixture of (SiO_2 + Si). The experiment using (SiO_2 + SiC) pellets was performed at 1752 °C. As mentioned earlier, only the amount of SiC could be calculated, as the amount of free carbon was higher in most samples. The result from the chemical analysis, presented in **Figure 4.3.17**, shows that for the pet-coke experiments, SiC production was slightly higher with (SiO_2 + Si) as the charge mix, than it was with (SiO_2 + SiC).

Figure 4.3.18 and **Figure 4.3.19** show the EPMA investigation of particles collected from the lower layer at 1694 and 1748 °C, respectively, which used (SiO_2 + Si) as charge mix. As expected, elemental Si has formed in the SiC particles, whereas, no elemental Si is visible in the SiC particles formed at 1752 °C, which used (SiO_2 + SiC) as source of SiO(g) (bars in magenta), as shown in **Figure 4.3.20**. These results also confirm that Si production is possible at temperatures lower than 1811 °C, even in SiC derived from pet-coke.

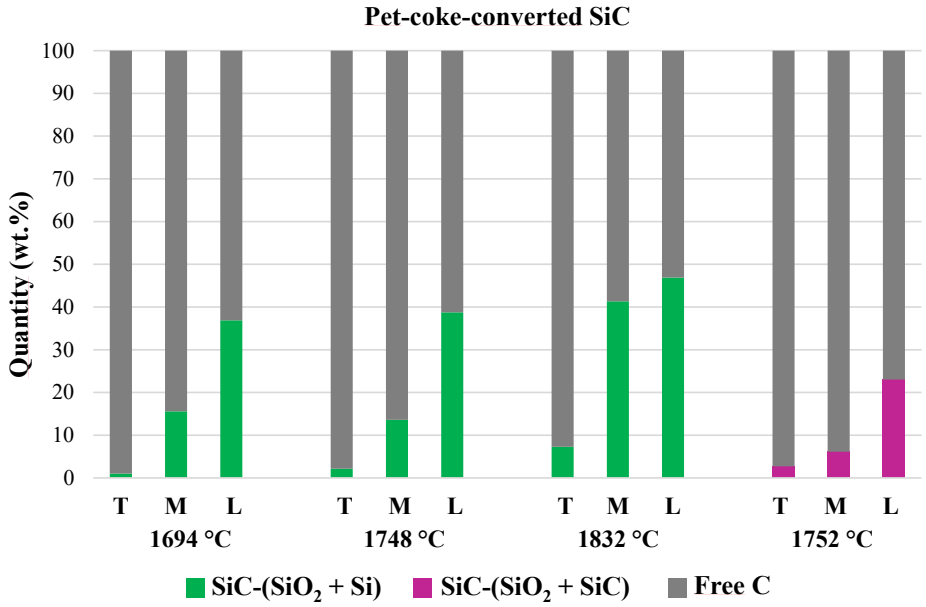

Figure 4.3.17. Quantities of SiC and unreacted carbon in top (T), middle (M), and lower (L) layers, from experiments conducted in graphite tube furnace. Experiment at 1752 °C used (SiO_2 + SiC) as charge mix, whereas rest of the experiments used (SiO_2 + Si).

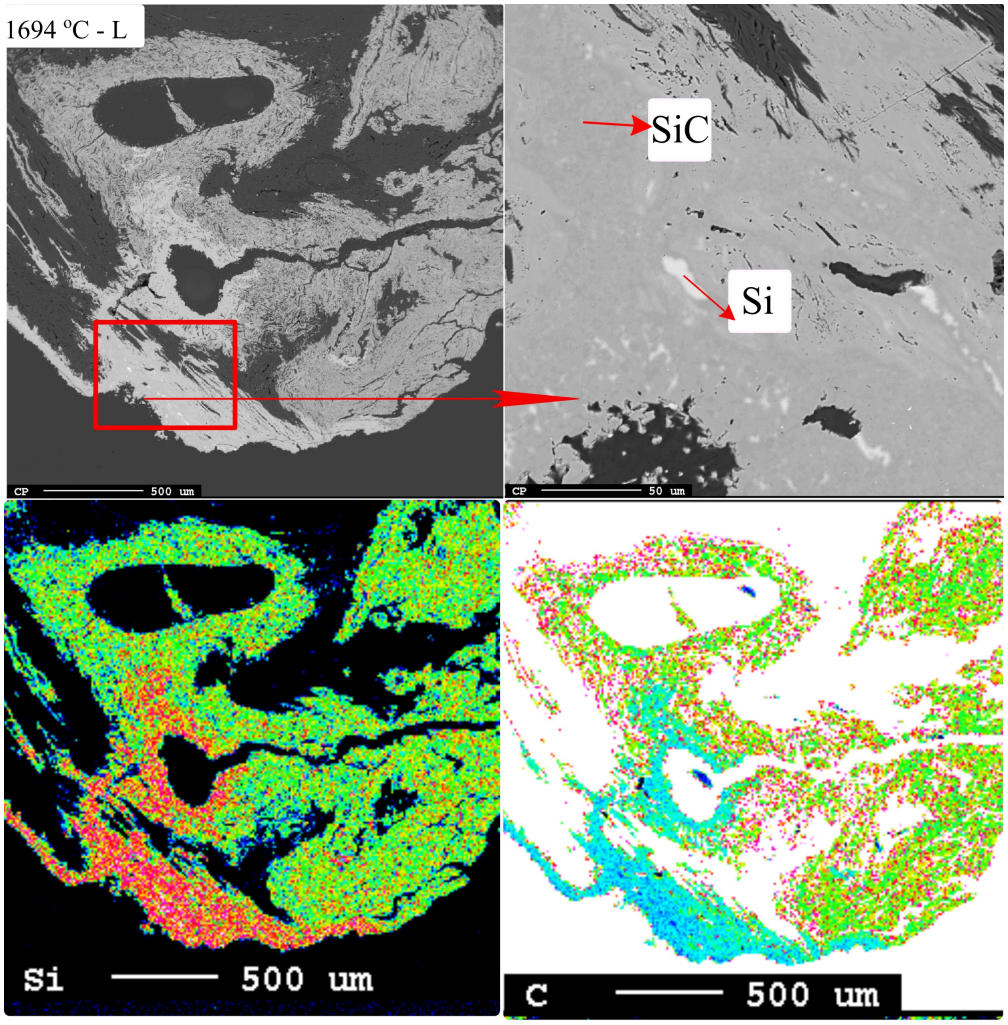

Figure 4.3.18. EPMA of SiC produced in lower layer at 1694 °C using (SiO_2 + Si), and elemental mapping of Si and carbon in it. Traces of elemental Si are visible in the SiC particle.

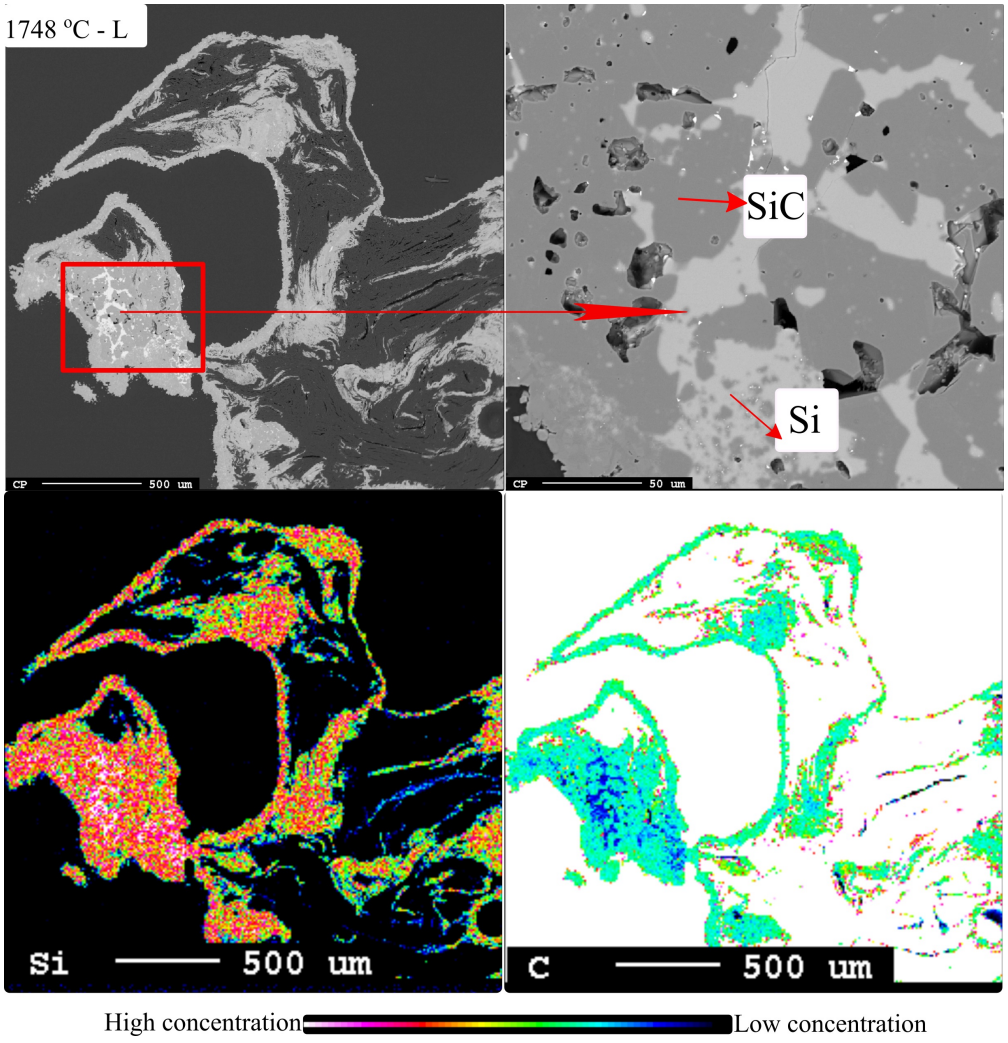

Figure 4.3.19: EPMA of SiC produced in lower layer at 1748 °C using (SiO_2 + Si), and elemental mapping of Si and carbon in it, showing traces of elemental Si forming in the particle.

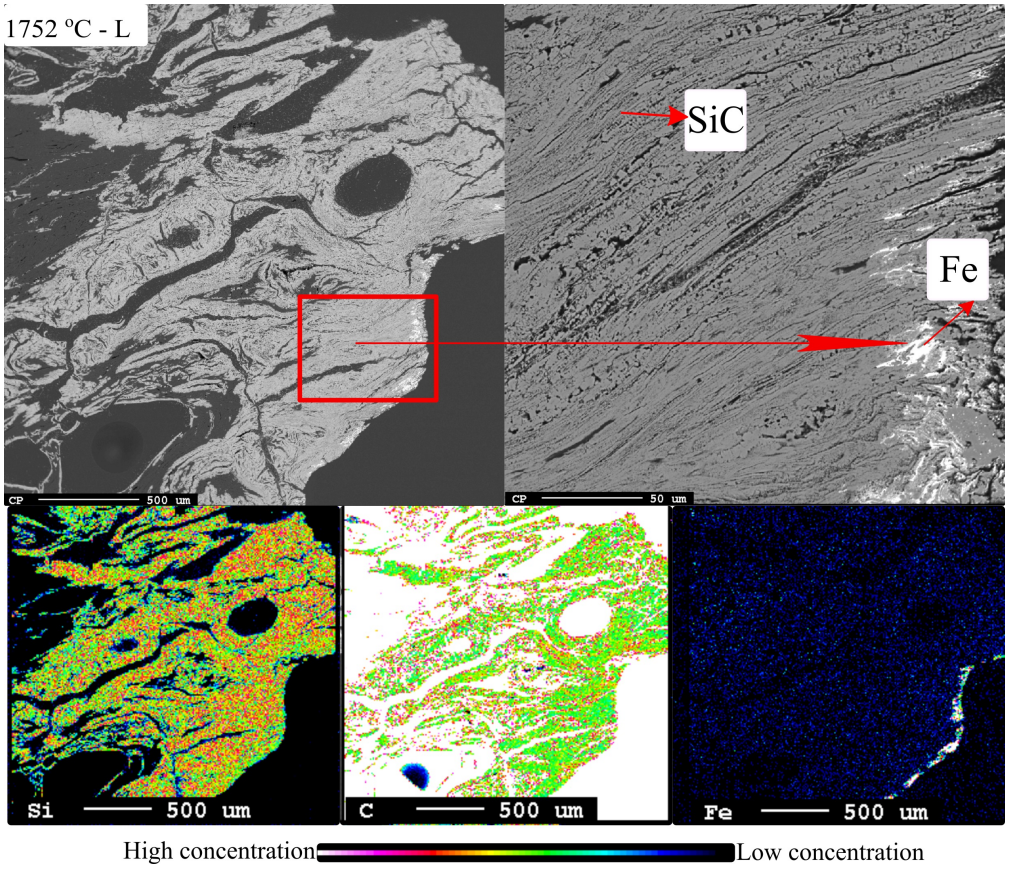

Figure 4.3.20. EPMA of SiC produced in lower layer at 1752 °C using (SiO_2 + SiC), and elemental mapping of Si, carbon, and Fe in it. No trace of elemental Si is present in the SiC particle.

4.3.3 Transformation to α-SiC: Graphite tube furnace experiments

β-SiC samples produced from pet-coke were further converted to α-SiC in the graphite tube furnace, to study the structural changes evolving in SiC exposed to temperatures > 2000 °C. Only a moderate amount of SiC samples could be obtained after the induction furnace experiments; hence, only β-SiC samples from the middle and lower layers, formed at 1850 and 1900 °C, were used to produce α-SiC. The %Si in the β-SiC samples were determined as the %Si of both experiments (1850 and 1900 °C) combined for each layer, and they were 8.7 wt.% Si in the middle and 18.8 wt.% Si in the lower layers. **Figure 4.3.21** shows the visual appearance of the pet-coke-converted β-SiC samples before and after the heat-treatment at 2100, 2300, and 2450 °C. As the temperature increases, the SiC changes its color. Precipitation

of crystals on the surfaces of the particles is also visible at higher temperatures, especially on the β-SiC samples with 18.8 wt.% Si.

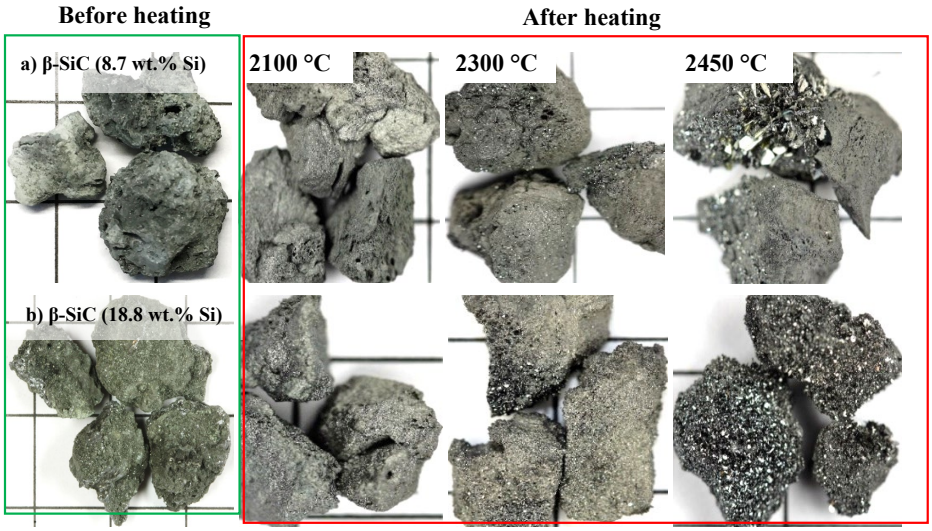

Figure 4.3.21. β-SiC samples with (a) 8.7 wt.% Si and (b) 18.8 wt.% Si, before and after heat-treatments at 2100, 2300, and 2450 °C.

4.3.3.1 SEM morphology

Figure 4.3.22 depicts the SEM morphologies of β-SiC samples with 8.7 (images on the left) and 18.8 (images on the right) wt.% Si, after they were heat-treated at 2100, 2300, and 2450 °C. The hexagonal plate-shaped crystals have formed at temperatures ≥ 2300 °C, which indicates the formation of α-SiC phase. Their accumulation increases with increasing temperature. No such crystals are visible in the SiC samples heat-treated at 2100 °C. The results reveal that a temperature above 2100 °C is required for the formation of α-SiC phase in pet-coke-converted SiC particles. The new SiC particles are highly dense, and the original carbon structures have completely disappeared.

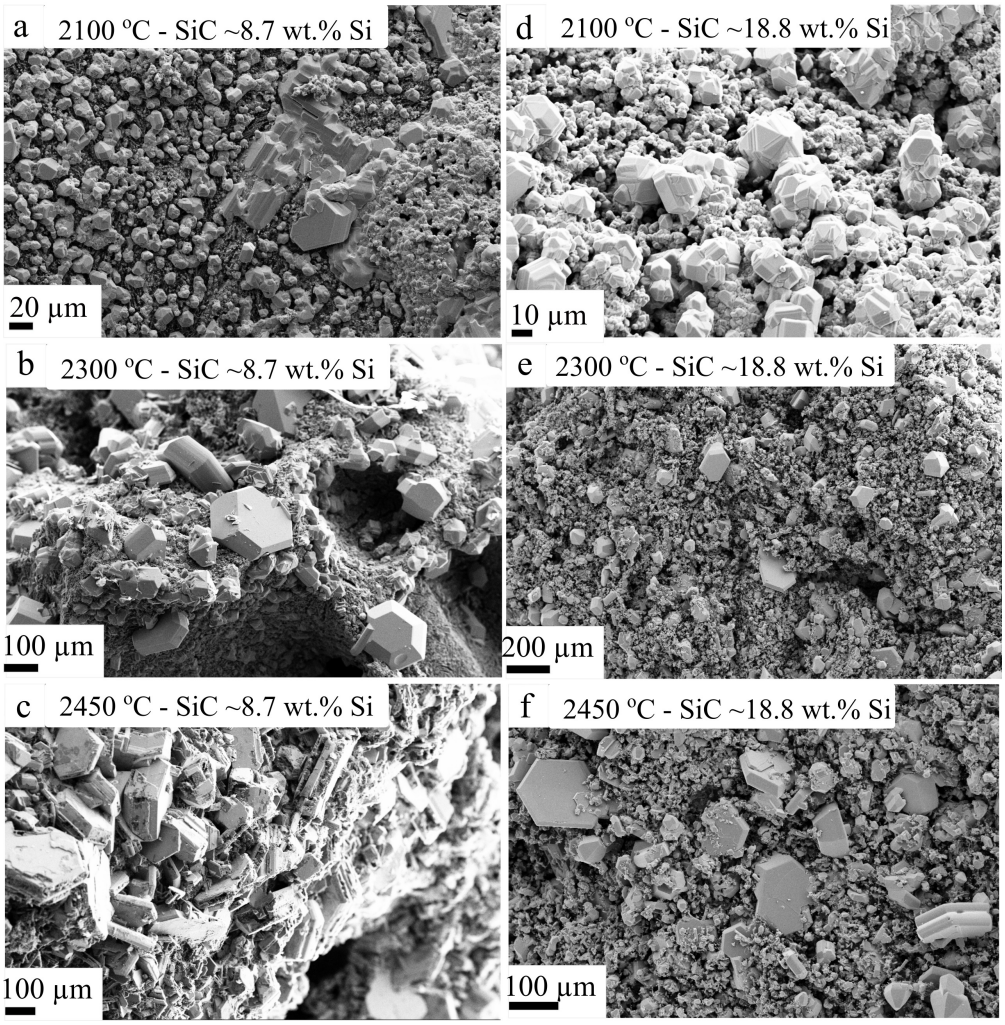

Figure 4.3.22. SEM morphologies of β-SiC samples with (a–c) 8.7 wt.% Si and (d–f) 18.8 wt.% Si, after heat-treated at 2100, 2300, and 2450 °C.

4.3.3.2 EPMA-BSE imaging

Figure 4.3.23 shows the EPMA images of heat-treated β-SiC samples with 8.7 (images on the left) and 18.8 (images on the right) wt.% Si, heat-treated at 2100, 2300, and 2450 °C. The hexagonal plate-shaped structure observed in the SEM (**Figure 4.3.22**) is visible in the EPMA images as well, especially in the SiC samples heat-treated at temperatures ≥2300 °C.

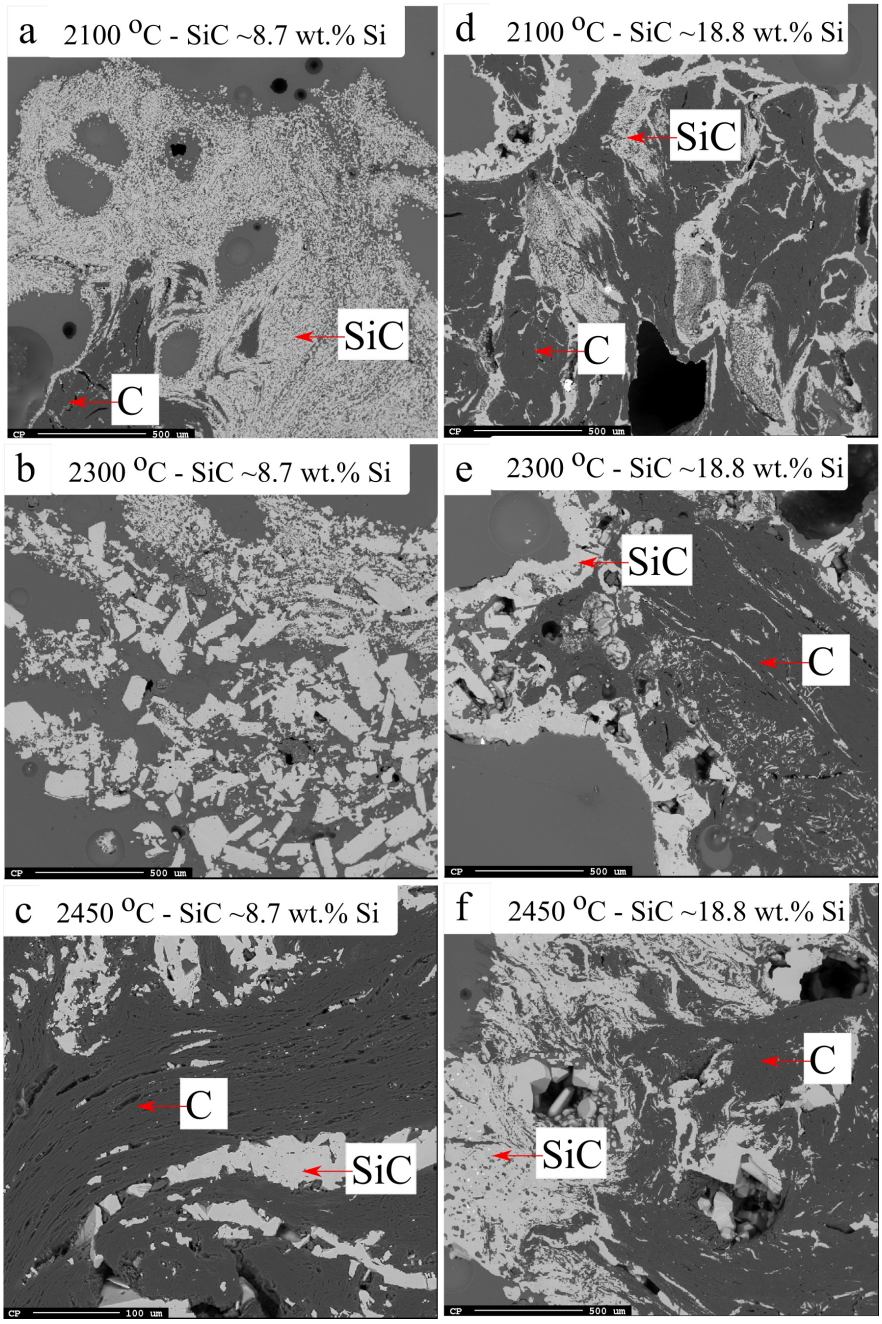

Figure 4.3.23. EPMA images of β-SiC samples with (a–c) 8.7 wt.% Si and (d–f) 18.8 wt.% Si, after heat-treated at 2100, 2300, and 2450 °C.

4.3.3.3 XRD analysis

X-ray diffractograms of the heat-treated β-SiC samples were collected and the data were analyzed by including the initial material, i.e., β-SiC, in the Rietveld refinement by Topas. In addition to the identified phases of Si and SiC, several samples showed a broad peak at around 26°, which could be arising from the unreacted carbon phase in the SiC particles. Only the existing SiC polytypes and the elemental Si left in the samples after heating are considered for the quantitative XRD analysis; the carbon phase is excluded.

Figure 4.3.24 shows the formation of different SiC phases when β-SiC sample with 8.7 wt.% Si was heat-treated at 2450 °C. The most intense SiC peak is located at 2θ = 35.8°, overlapped with Bragg reflections of 111-3C and 006-6H. The peaks formed at 2θ = 33.5°, 38°, and 65.5° for 6H are marked by red circles. No other additional peaks have formed in β-SiC with 8.7 wt.% Si.

Figure 4.3.25 shows SiC phases identified in the β-SiC sample with 18.8 wt.% Si, after it is heated at 2450 °C. In addition to the intense SiC peak at 2θ = 35.8° (3C), additional 006-6H and 015-15R have also formed. In the XRD data, the presence of α-SiC polytypes such as 6H and 15R are established from their isolated peaks. In addition to these two peaks formed due to the overlapping at 111-3C, the presence of α-SiC polytypes are also confirmed by the other isolated peaks of each phase. These isolated peaks are at 2θ = 34°, 38.1°, 45.3°, 54.6°, and 65.2° for 6H, and 2θ = 34.9°, 37.5°, and 38.7° for 15R. The vertical bars at the bottom in both the figures show the angular position of the allowed Bragg reflections (d-spacings). The graphs show good agreement between the observed and calculated XRD pattern. The 4H-SiC phase is not present in both the samples.

Figure 4.3.26 and **Figure 4.3.27** show the X-ray diffractograms with identified SiC phases in β-SiC with 8.7 and 18.8 wt.% Si, respectively, which were heat-treated at 2100, 2300, and 2450 °C. The fitted diffractograms show good agreement between the observed and calculated XRD patterns, for all SiC samples that were analyzed quantitatively by Topas. These additional fitted diffractograms are presented in Appendix B.

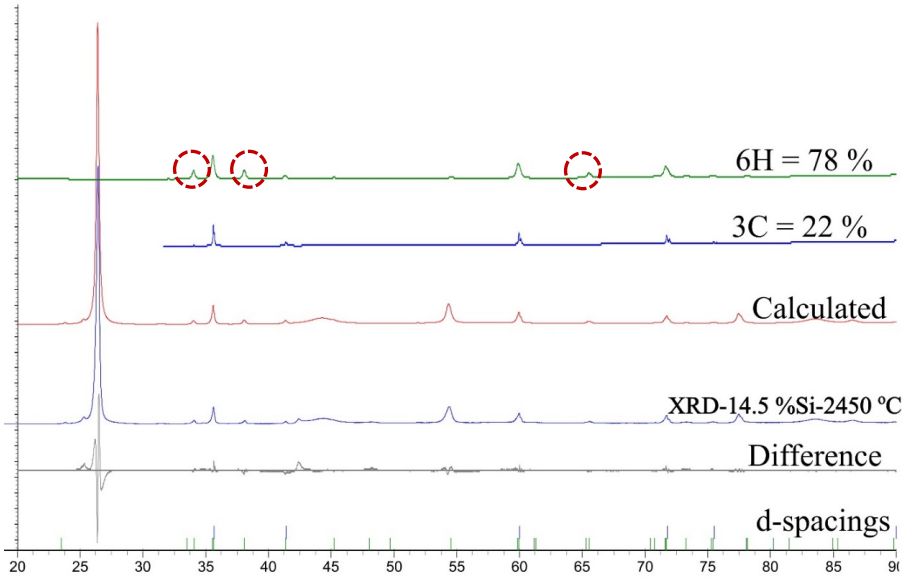

Figure 4.3.24. Formation of different SiC phases in β-SiC sample with 8.7 wt.% Si, heat-treated at 2450 °C.

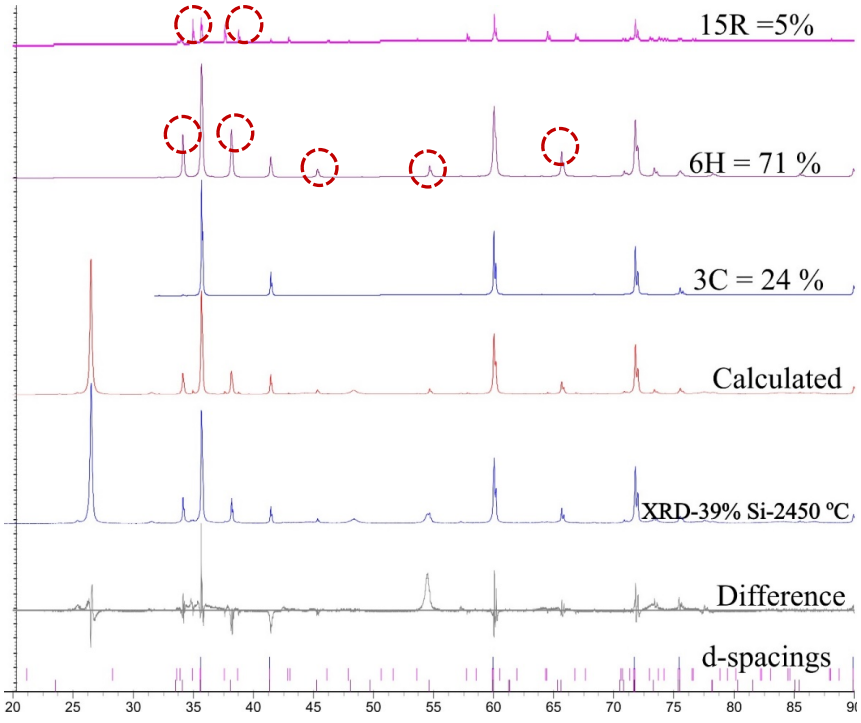

Figure 4.3.25. Formation of different SiC phases in β-SiC sample with 18.8 wt.% Si, heat-treated at 2450 °C.

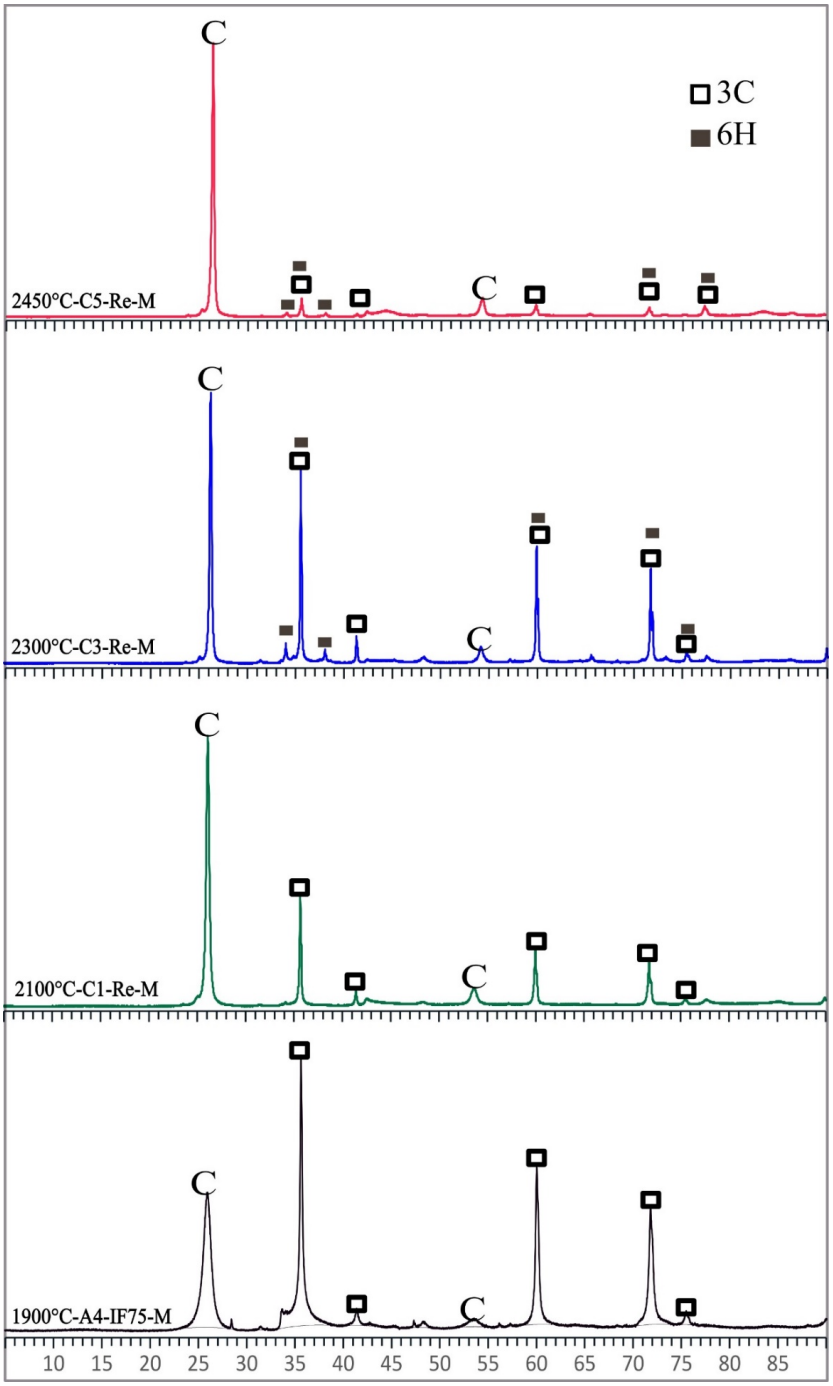

Figure 4.3.26. X-ray diffractograms of identified SiC phases in β-SiC with 8.7 wt.% Si formed at 1850 and 1900 °C (middle layer), and after it is heat-treated at 2100, 2300, and 2450 °C.

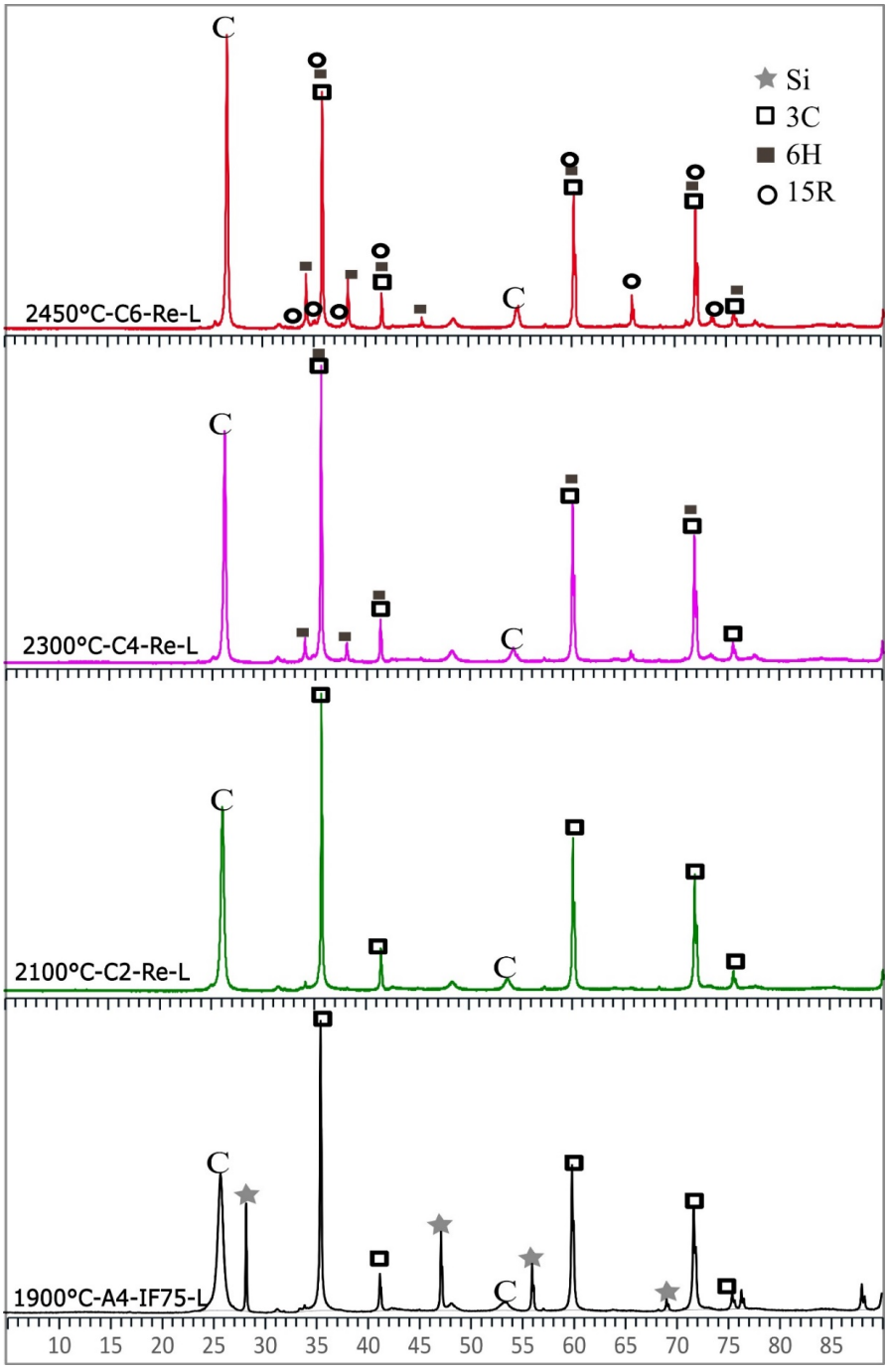

Figure 4.3.27. X-ray diffractograms with identified SiC phases in β-SiC with 18.8 wt.% Si formed at 1850 and1900 °C (lower layer), and after it is heat-treated at 2100, 2300, and 2450 °C.

Figure 4.3.28 and **Figure 4.3.29** show the quantitative polytype analysis of the β-SiC samples respectively with 8.7 and 18.8 wt.% elemental Si, heated at 2100, 2300, and 2450 °C. No α-SiC has formed at 2100 °C. At 2300 °C, samples have partly converted to α-SiC and only 6H phase is present. At 2450 °C, β-SiC samples with 18.8 wt.% of pure Si contain 6H as the dominating polytype. A minor percentage of 15R is also present. However, β-SiC samples with 8.7 wt.% of elemental Si, heated at 2450 °C, do not show any polytypes other than 3C and 6H. The major SiC polytype in β-SiC with 8.7 wt.% Si is 22 wt.% of 3C. The rest has transformed to 6H. The main SiC polytypes of 24 wt.% 3C, 71 wt.% 6H, and 5 wt.% 15R have formed in β-SiC with 18.8 wt.% Si.

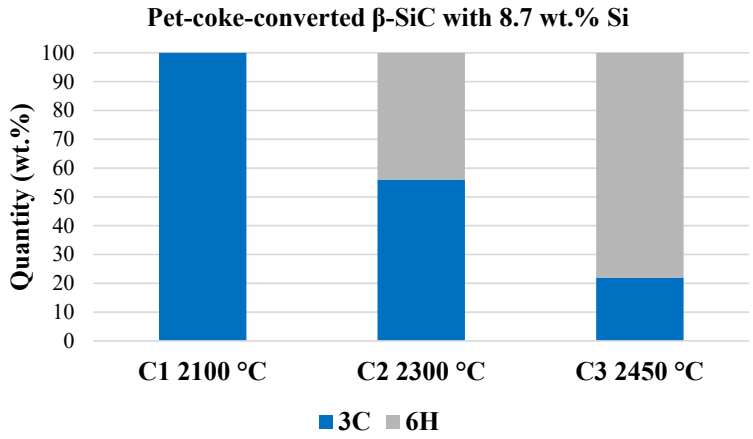

Figure 4.3.28. Quantitative polytype analysis of β-SiC with 8.7 wt.% Si, after it is heated at 2100, 2300, and 2450 °C.

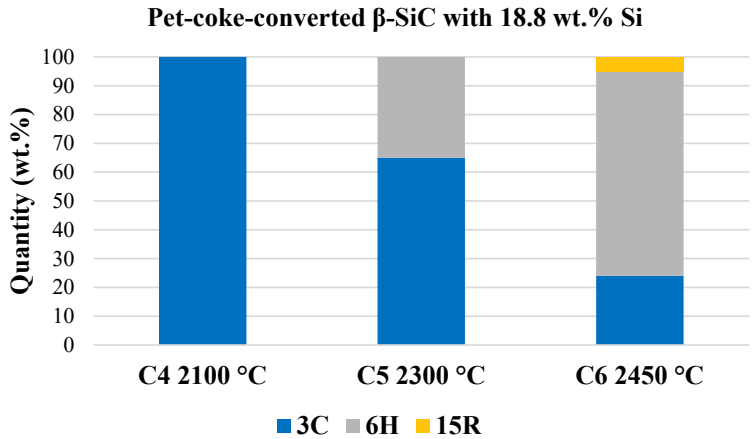

Figure 4.3.29. Quantitative polytype analysis of β-SiC 18.8 wt.% Si, after it is heated at 2100, 2300, and 2450 °C.

Two additional experiements were performed in the graphite tube furnace using β-SiC with 11.29 and 11.89 wt.% of elemental Si in it, which were heat-treated at 2300 °C. The carbon phase is high in these samples as well (**Figure 4.3.30**). In addition to the 3C phase, 6H was the dominating polytype, with a minor percentage of 15R in both the samples (**Figure 4.3.31**).

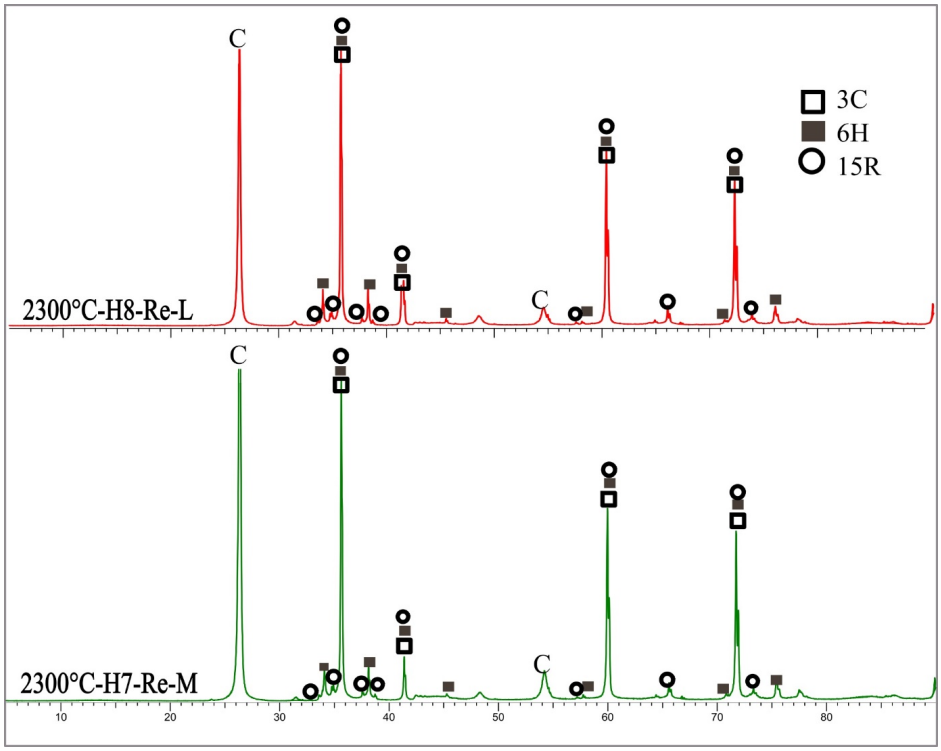

Figure 4.3.30. X-ray diffractograms with identified SiC phases in β-SiC with 11.29 (H7-Re-M) and 11.89 (H8-Re-L) wt.% of elemental Si in it, after heat-treated at 2300 °C.

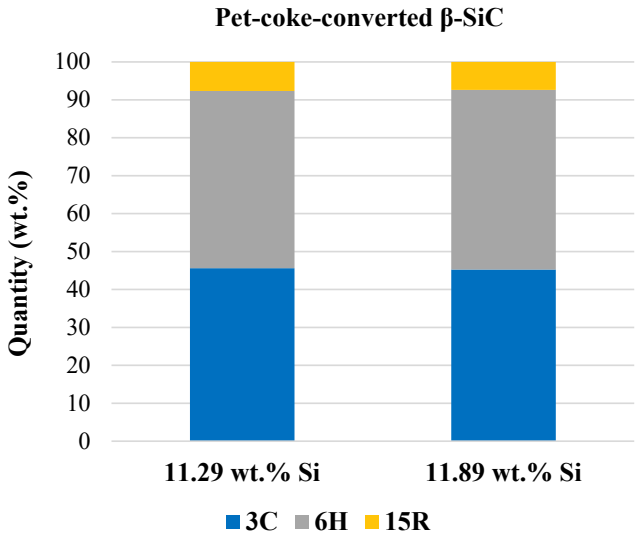

Figure 4.3.31. Quantitative polytype analysis of β-SiC with 11.29 and 11.89 wt.% Si, after heat-treated at 2300 °C.

4.4 SiC from industrial Si processes

Samples of SiC were procured from three industrial furnaces to validate the laboratory-scale production of SiC accomplished in this research. These samples were also scrutinized under SEM, EPMA, and XRD. The details of the SiC samples and their analyses are described below.

4.4.1 SiC-ELT

The first sample, SiC-ELT, was obtained from the Elkem Thamshavn furnace 2. Coal was the main source of carbon in this furnace. The original position of the SiC sample inside the furnace is unknown. There had been a built-up of SiC heap in the center of the furnace. Upon stoking the charge from the top, a block of SiC fastened on to the stoker. This block of SiC was procured for this study and is shown in **Figure 4.4.1**. It has tiny dense grains and does not have the original carbon structure.

Figure 4.4.1. SiC-ELT obtained from Elkem Thamshavn furnace 2.

The SEM and EPMA-BSE images of SiC-ELT are shown in **Figure 4.4.2** and **Figure 4.4.3**, respectively. SEM gives the surface morphology and shows the SiC crystals in the form of thick hexagonal plates. The elemental mapping in **Figure 4.4.3** shows that the main phases in the samples are Si and SiC, with less than 1% traces of Fe, Ca, and Al.

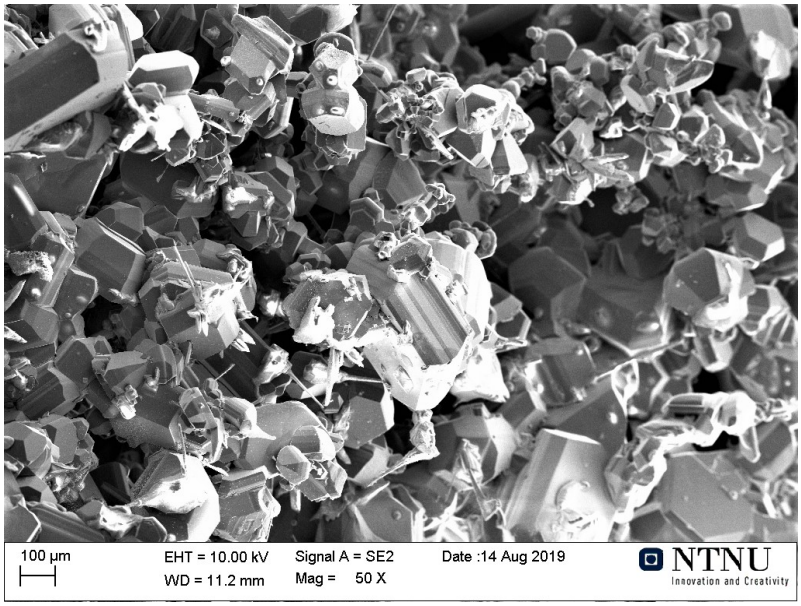

Figure 4.4.2. SEM morphology of SiC-ELT. SiC crystals formed are in the form of thick hexagonal plates.

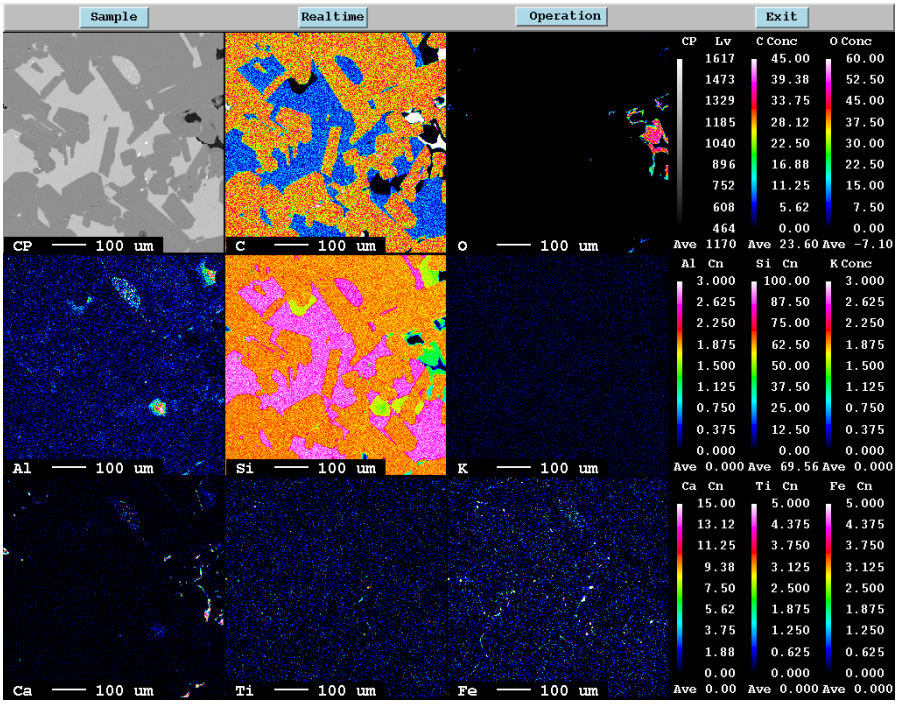

Figure 4.4.3. EPMA of SiC-ELT and its elemental mapping showing main phases, i.e., Si and carbon. Less than 1% traces of Fe, Ca, and Al are also present.

4.4.2 SiC-ELB

This sample was obtained during the furnace excavation at Elkem Bremanger, which is operated for producing Silgrain®. The accurate position of the samples was not known. It was observed as SiC crust and was assumed to be formed at the crater wall near the electrode. **Figure 4.4.4** shows SiC-ELB, with big pores clearly visible on the SiC crust. The magnified picture shows SiC inside the big pore, in the form of small particles sticking together to form SiC agglomerates. They were extremely hard and blackish-green in color. Coal was the main source of carbon in this furnace.

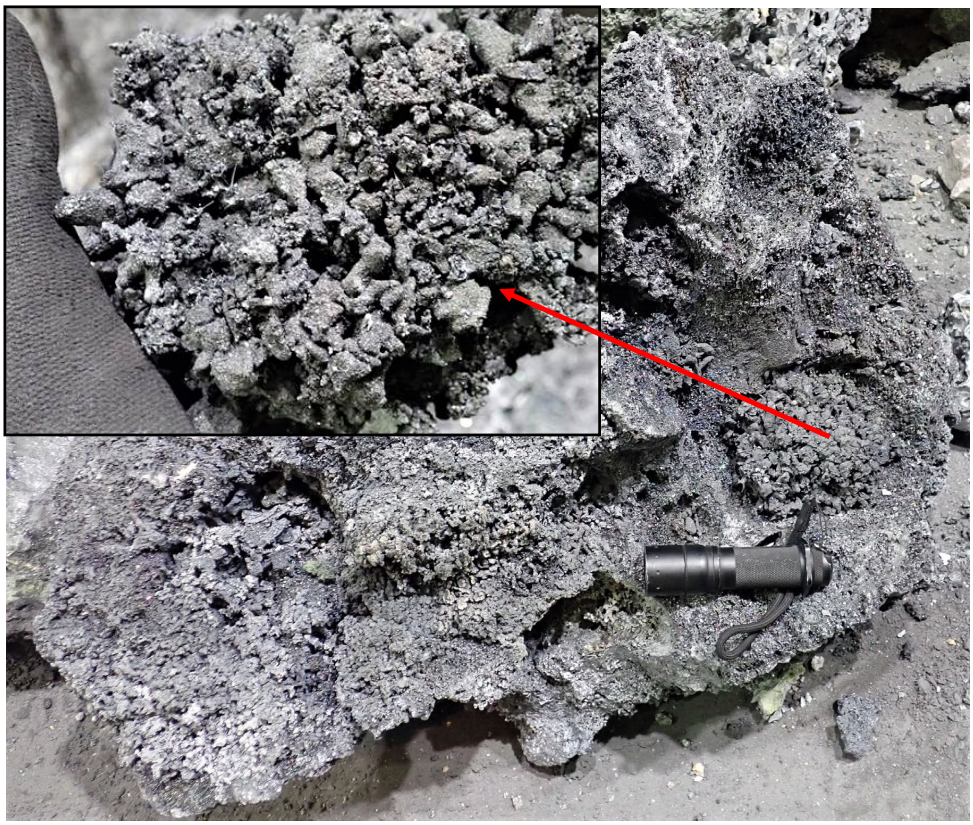

Figure 4.4.4. SiC-ELB obtained after furnace excavation from Elkem Bremanger. Magnified picture on top left shows SiC in the form of agglomerates inside the big pore marked by red arrow.

The SEM and EPMA images of SiC-ELB are presented in **Figure 4.4.5** and **Figure 4.4.6**, respectively. SEM shows SiC crystals in the form of dense hexagonal plates. EPMA and elemental mapping of the sample (**Figure 4.4.6**) show that the main phases in the sample are carbon and Si, with considerably higher contents of Al, Ca, and O.

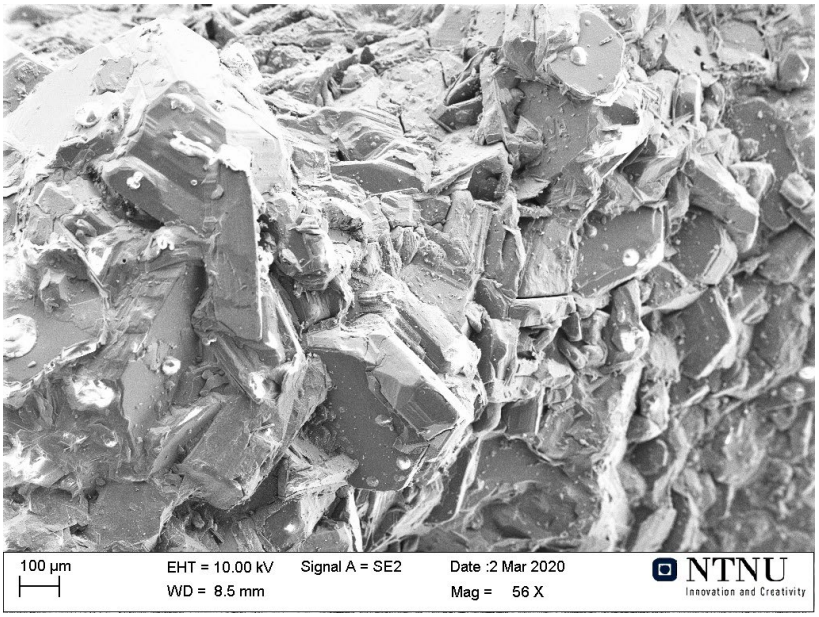

Figure 4.4.5. SEM image of SiC-ELB showing dense, hexagonal plate-shaped SiC crystals.

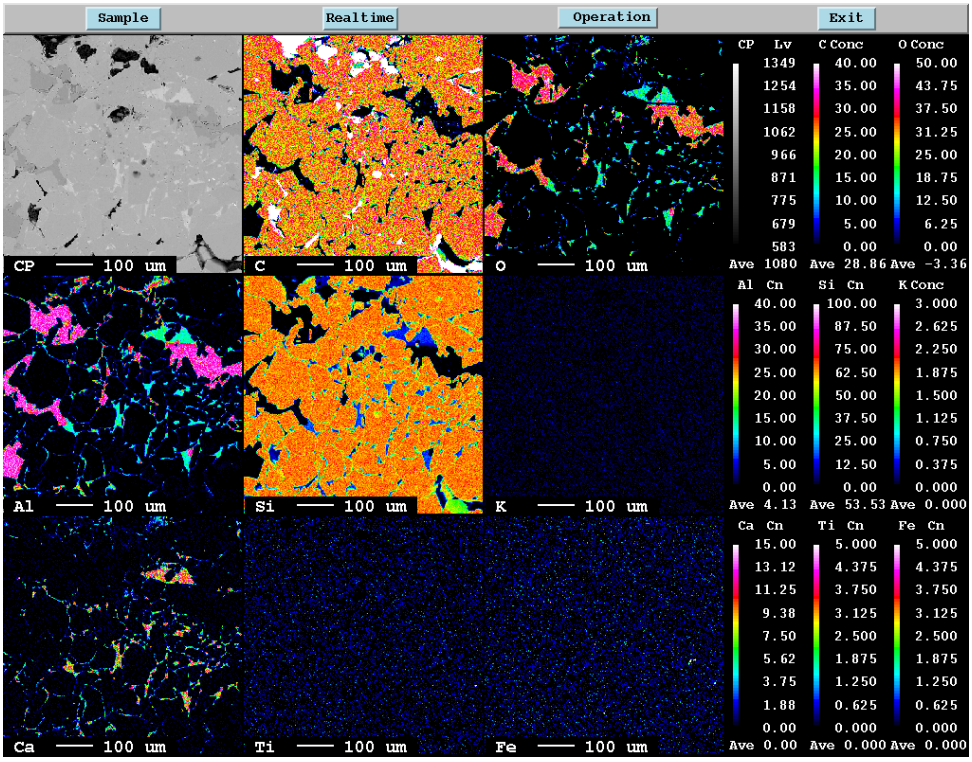

Figure 4.4.6. EPMA of SiC-ELB and its elemental distribution. Main phases in the sample are Si and carbon, with reasonably higher contents of Al, Ca, and O.

4.4.3 SiC-ELK

SiC-ELK was obtained from one of the furnaces at Elkem Kristiansand. Coal was the main carbon source in this furnace. The furnace operators noticed a heap of charge mix at the center of the furnace, during the operation. They managed to push the top of the heap out of the furnace using the stoking car while recharging. Upon stoking, the charge heap was broken, and a big piece was taken out for analysis. The charge heap (marked as yellow) and the region where the big SiC sample, SiC-ELK, was located (A and B) are shown in **Figure 4.4.7**. The sample consisted of brown condensates on the top, followed by molten quartz (both at region A), and black-SiC at the bottom (region B). Small samples were taken out from these three parts for further analyses. **Figure 4.4.8** shows the black-SiC taken from the furnace hearth, with large crystals on its surface, which were partly filled with Si. The SiC crystals from the top (region A) and the black-SiC (region B) were analyzed by SEM and EPMA.

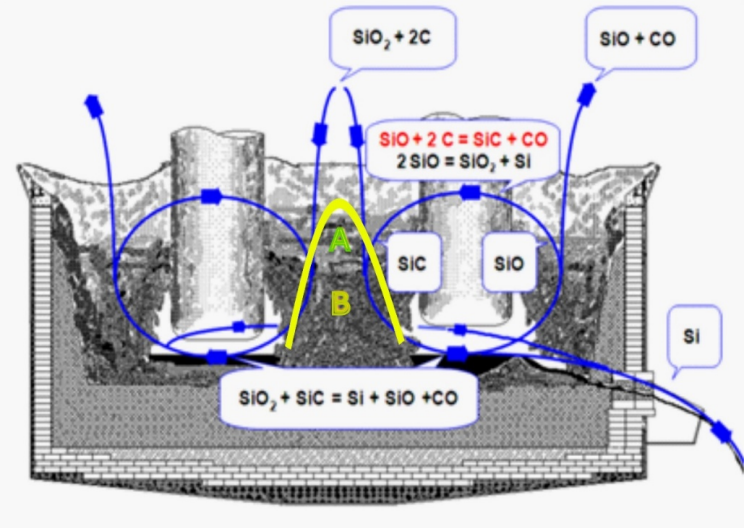

Figure 4.4.7. Schematic of furnace at Elkem Kristiansand provided by Heidi Sæverud Hauge at REC Solar. Charge heap (yellow arc) and position where the big SiC sample, SiC-ELK, was located (A and B) are marked.

Figure 4.4.8. Black-SiC sample (SiC-ELK, from region B).

Figure 4.4.9 and **Figure 4.4.10** show SEM morphology of the two SiC samples close to the condensate region (region A, **Figure 4.4.7**). The structure of the sample is similar to the structure of coal, and SiC in the form of whiskers have grown on the pore walls. **Figure 4.4.11** shows the SEM of coal-converted SiC particle taken from a region near the molten quartz (region A). This particle has completely transformed to SiC; dense SiC crystals of varying sizes have formed on it, and the carbon structure has disappeared. **Figure 4.4.12** shows the SEM morphology of the black-SiC (region B); big plate-shaped SiC crystals of ~0.6 mm have formed on this particle. EPMA elemental mapping in **Figure 4.4.13** shows that the main phases in the samples are Si and carbon, with traces of Al and Ca.

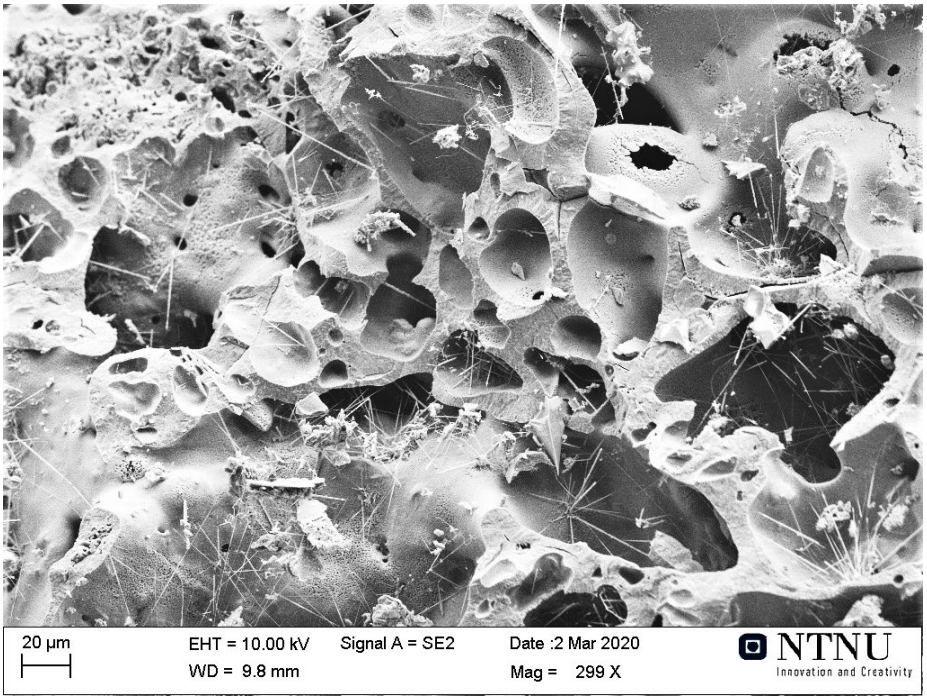

Figure 4.4.9. SEM morphology of part of SiC-ELK, close to condensate region (region A).

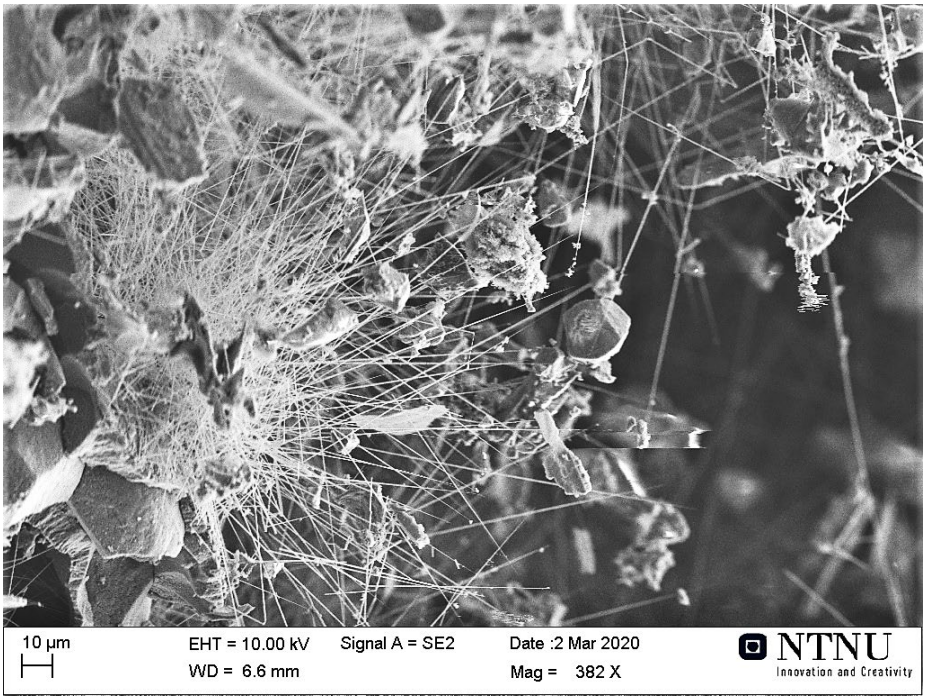

Figure 4.4.10. SEM morphology of part of SiC-ELK, close to condensate region (region A).

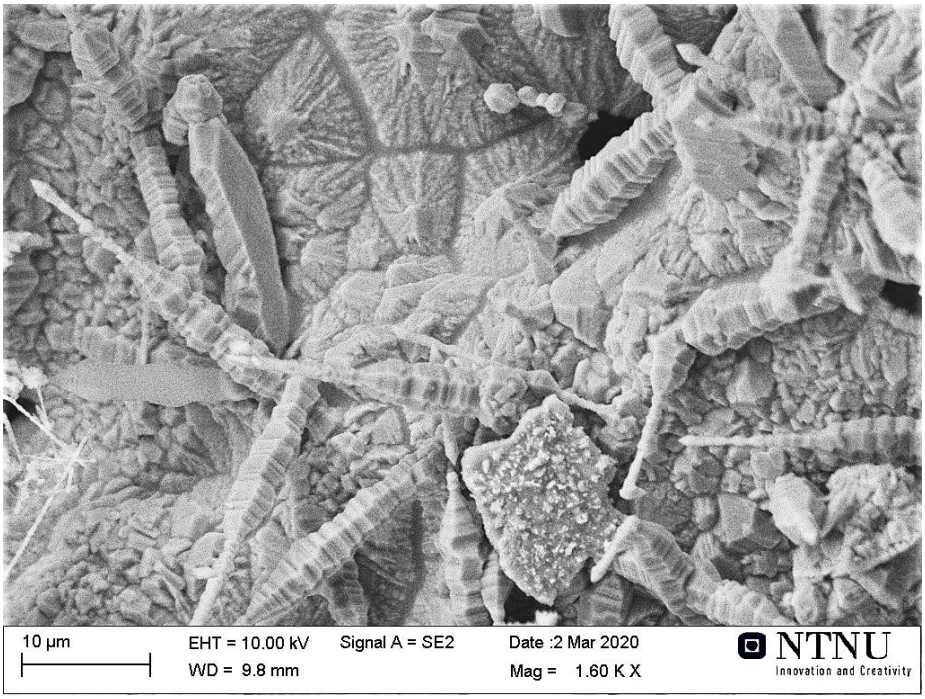

Figure 4.4.11. SEM morphology of part of SiC-ELK, near molten quartz region, just below region A.

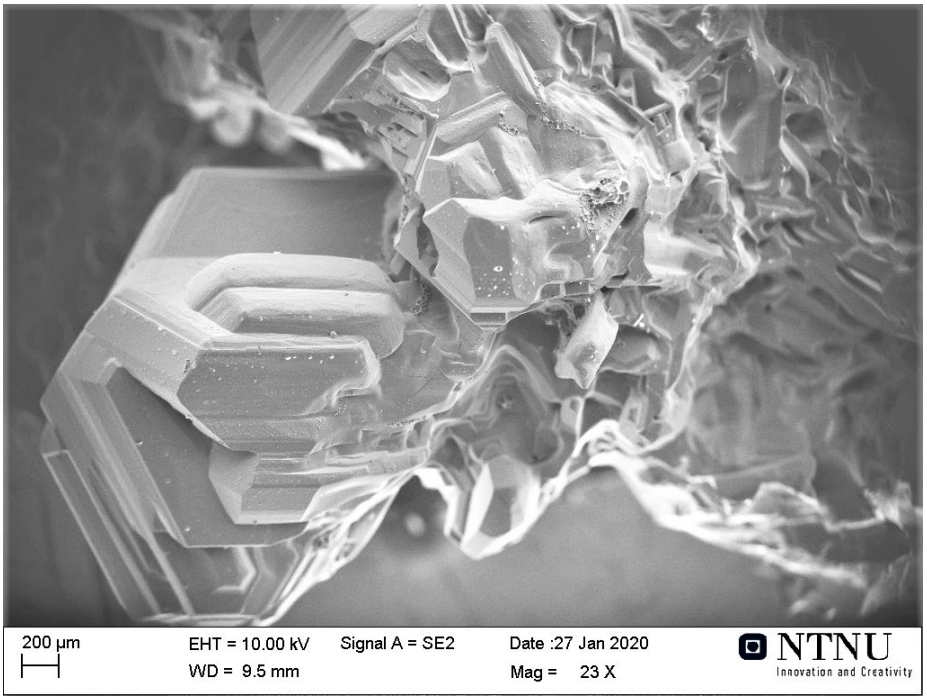

Figure 4.4.12. SEM morphology of the black-SiC sample from region B.

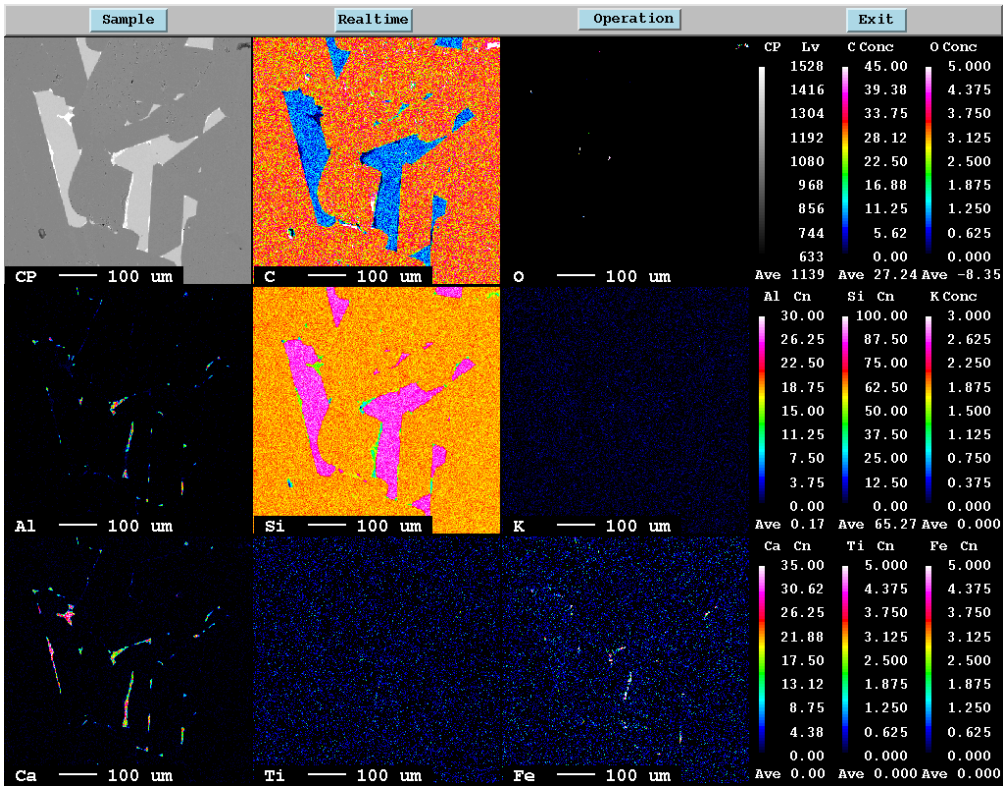

Figure 4.4.13. EPMA and elemental mapping of black-SiC (region B). Main phases in the samples are Si and carbon, with traces of Al and Ca.

4.4.4 XRD analysis of industrial SiC samples

X-ray diffractograms of the three SiC samples (samples shown in **Figure 4.4.1**, **Figure 4.4.4**, and **Figure 4.4.8**) were collected using a Bruker D8 Focus X-ray diffractometer, running in Bragg Brentano collection mode with Cu-Kα radiation. Data were then analyzed using the Bruker Topas v5 software and summarized in **Figure 4.4.14**. All samples consist of the major SiC polytypes such as 3C, 4H, 6H, and 15R, with 6H being the main polytype. The amount of α-SiC was calculated as 78, 87, and 95 wt.% in SiC-ELB, SiC-ELT, and SiC-ELK, respectively. Hardly any cubic form of SiC, i.e., 3C, was present in the SiC-ELK sample and it had completely transformed to α-SiC crystal. The major phase in it was 6H (86 wt.%), followed by ~3 wt.% of 4H and ~6 wt.% of 15R. Elemental Si of around 1–4 wt.% was found in all samples.

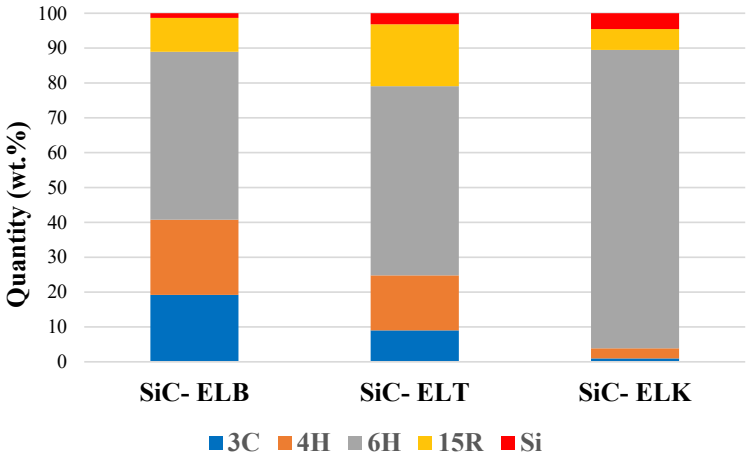

Figure 4.4.14. SiC polytypes present in three industrial SiC samples.

5 Discussion

The results described in the previous chapter are interpreted and discussed in this chapter. The chapter is divided into four parts: (i) production of β-SiC from charcoal, coal, and pet-coke; (ii) formation of elemental Si in β-SiC; and (iii) transformation of β-SiC to α-SiC. SiC formation in the industrial Si furnaces is explained in the fourth (iv) section.

5.1 Production of β-SiC from charcoal, coal, and petroleum coke

SiC was produced from charcoal, coal, and pet-coke in the induction furnace, using (SiO_2 + Si) and pellets of (SiO_2 + SiC) as sources of SiO(g), at temperatures ranging from 1750 to 1900 °C. The XRD analysis confirmed that the SiC produced at this temperature range was β-SiC. The SEM and EPMA analyses revealed the bulk structures, surface morphologies, and elemental composition of the β-SiC particles produced from charcoal, coal, and pet-coke. These analyses revealed that SiC forms through two different mechanisms; (a) SiC surface crystals of varying sizes and shapes form on the pore wall surfaces, and (b) the carbon pore walls themselves transform to SiC. The formation and morphologies of the SiC surface crystal structures are discussed first, followed by elaborating the SiC transformation of the carbon pore walls.

5.1.1 Formation of SiC surface crystals

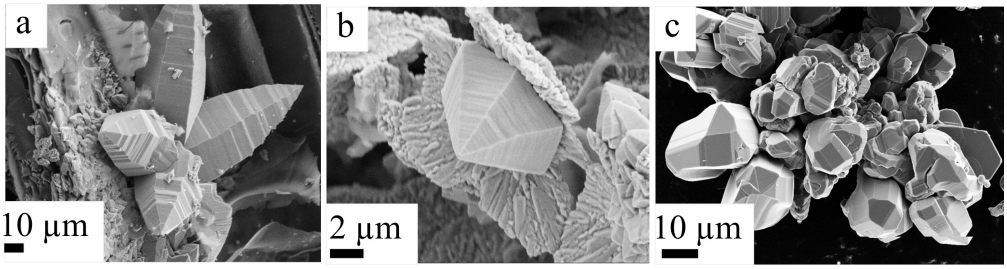

Figure 5.1.1. SiC crystals of different sizes and shapes grown on surfaces of charcoal particles.

Figure 5.1.1 shows the commonly found SiC surface crystals of different sizes, formed on the surfaces of charcoal particles at temperatures of 1700–1800 °C. The SiC crystals visible on the surface of charcoal have lengths in the ranges of 15–348 µm. Their widths vary from bottom to top in a decreasing manner, ranging from 206 to 18 µm. Surface crystals formed on the different carbon materials differed in their shapes. The surface crystals formed on charcoal walls were

mostly shaped as hexagonal micro-bullets of varying sizes, and the crystal growth increased with an increase in temperature (refer results in **section 4.1.1.1**, **Figure 4.1.6** to **Figure 4.1.15**).

The SiC surface crystals formed on coal and pet-coke were different from those formed on charcoal. Long SiC crystals with length ranges of 60–588 µm and widths in the range of 10–36 µm (**Figure 5.1.2a**), and SiC whiskers of lengths ~58–70 µm and widths of ~2 µm (**Figure 5.1.2b** and **c**) were found on coal. In pet-coke, SiC surface crystals mostly in the form of whiskers were noticed, as shown in **Figure 5.1.3.**

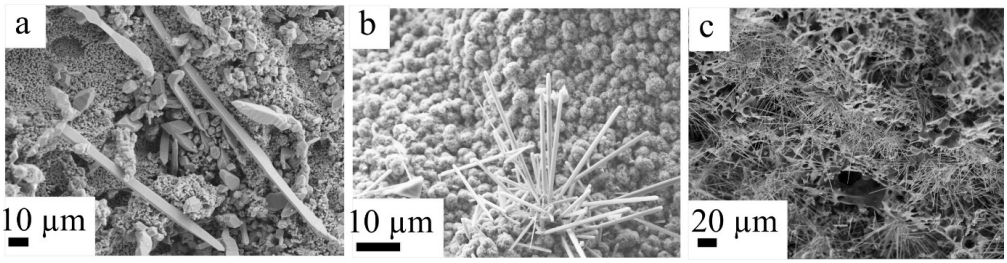

Figure 5.1.2. SiC crystals of different sizes and shapes grown on surfaces of coal particles.

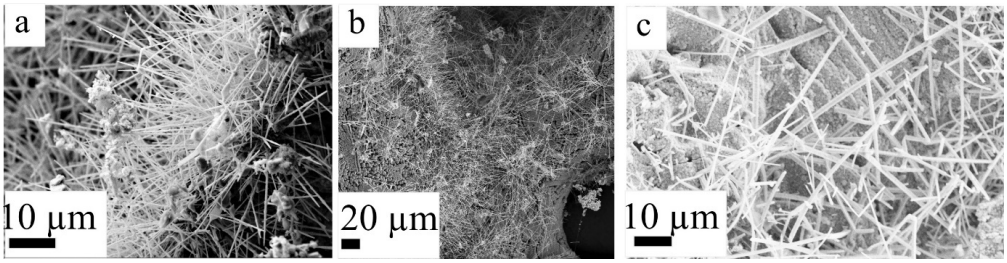

Figure 5.1.3. SiC crystals of different sizes and shapes grown on surfaces of pet-coke particles.

The surface SiC crystal formation in the form of whiskers has been studied extensively by many researchers [115, 116, 117, 118]. The prevailing theories propose that the gaseous species react with the activated carbon atoms both on the carbon surface and on the pore walls, according to **reaction (13)**, and this Vapor-Solid (VS) process forms the SiC particles initially. The surface and pores of the carbon material serve as nucleation sites for the formation of SiC whiskers. The SiO(g) then continuously adsorb on the initially formed SiC nucleus and the SiC whiskers grow preferentially from the gaseous phase as follows:

$$SiO\ (g) + 3CO\ (g) = SiC\ (\text{whiskers/surface crystals}) + 2CO_2\ (g) \qquad (24)$$

$$CO_2(g) + C = 2CO(g) \qquad (25)$$

The CO_2 reacts with carbon to form CO (**reaction (25)**), and SiC would further form as long whiskers/surface crystals, via this CO(g) and SiO(g).

The SINTEF SiO-reactivity test for the reduction materials shows that different types of cokes including pet-coke have the lowest reactivity towards SiO(g). Also, the CO_2 reactivity is higher in charcoal compared with pet coke [22, 39]. Therefore, **reaction (25)** is assumed to be taking place at a slower rate in the case of pet-coke. This might reduce the amount of CO(g) available to further react with SiO(g) (**reaction (24)**, which could be the reason for thin whiskers forming on the surface of pet-coke.

The SiC crystals observed on the surfaces of charcoal and coal are also formed by the mechanism described above. SiC crystals of varying sizes and shapes form at various growth rates, depending on the interface and orientation of the substrate [3]. The flow rate and the amount of SiO(g) that reaches the surface of the substrate where the crystal is growing, also determine the variations in crystal size. The crystal growth continues until the amount of available SiO(g) diminishes.

The SiC surface crystals on charcoal substrates, which were shaped as hexagonal micro-bullets, were selected to extract their crystallographic details (**Figure 5.1.1a**). Only the sample formed at 1750 °C was investigated. Nevertheless, crystals with similar structures had formed at the temperature ranges of 1700–1800 °C as well. It is assumed that the mechanism of crystal formation is the same at these temperatures. The high-resolution TEM analysis and lattice imaging revealed that the SiC micro-bullet had a high density of stacking faults in the growth direction. The density of defects was similar across the studied sample. Steps and bands observed on the facets of the micro-bullet, as shown in the SEM images (**Figure 5.1.1a**), were not directly related to the stacking sequence or their defects. The HAADF-STEM contrast confirmed that these bands were not because of any variations in the chemical composition, such as the presence of Si or carbon-rich regions. This confirmed that the micro-bullet crystals consist of only SiC. These micro-bullet shaped crystals were observed only on the charcoal substrate.

A study of the β-SiC crystal orientation, based on SiC ceramics from wood, has suggested that both the SiC nucleation and the subsequent crystal growth might be influenced by the molecular structure and orientation of carbon on the pore surface [4]. As crystals are anisotropic in nature, the formation of a crystal surface always depend on the Gibbs energy [119, 120]. The surface energies of crystals differ based on their types, which control the equilibrium shape of the crystals. If the Gibbs energy is lower, the crystal keeps growing, whereas it reaches its equilibrium shape, if the Gibbs energy is high.

More prominent, dense SiC crystals had formed on surfaces of the three carbon materials as the temperature increased (refer results in **section 4.1.1.1**, **4.2.1.1**, and **4.3.1.1**). However, these surface crystals were disappearing once the temperature rose above 1800 °C, which is associated with the formation of Si at higher temperatures. At a temperature above 1800 °C, SiO(g) with a higher pressure reacts with the already formed SiC crystals, producing additional Si in the SiC, according to **reaction (18)**. The formation of SiC surface crystals thus diminishes gradually, and the particle will transform to elemental Si. **Figure 5.1.4** shows the morphological changes occurring in SiC particles on the surfaces of charcoal, coal, and pet-coke, when elemental Si forms in them at higher temperatures (1900 °C).

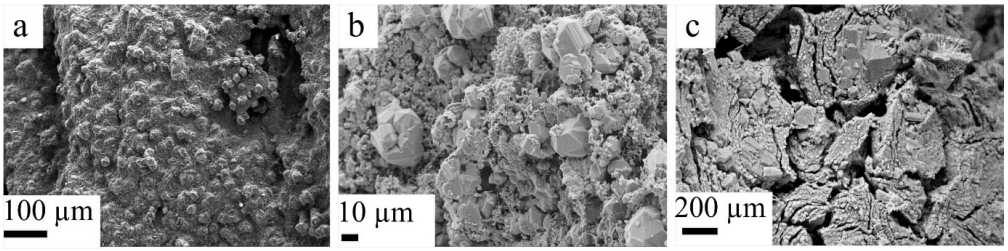

Figure 5.1.4. SEM images of Si formation in SiC particles produced from (a) charcoal, (b) coal, and (c) pet-coke.

5.1.2 Transformation of carbon pore walls to SiC

Though a lot of SiC surface crystals had formed on the carbon surface, another SiC formation mechanism, i.e., the carbon materials directly transforming to SiC, was also observed in the present study This could be the main reaction of β-SiC formation which happens through the following reaction:

$$SiO\ (g) + 2C = SiC + CO\ (g) \qquad (13)$$

The transformation of pore walls takes place via a solid-gas reaction method according to **reaction (13)**, where a gas source (SiO(g)) reacts on the carbon surface and diffuse through the pores of the solid. **Figure 5.1.5** shows EPMA images of the pore walls that had transformed to SiC (highlighted in red color in magnified images on the right side) in charcoal, coal, and pet-coke. The brighter areas in the images are the carbon that reacted to form SiC (**reaction (13)**). The porous structure is also clearly visible in the images where charcoal has thin cell walls, which are distributed homogeneously. Pores are not distributed homogeneously in coal and pet-coke, and they both have thicker cell walls. The SiC surface crystals observed in the pores of charcoal and coal are highlighted in green in the images (**Figure 5.1.5**). The SEM analysis also clearly showed the pore walls of charcoal that had transformed to β-SiC (**Figure 5.1.6**).

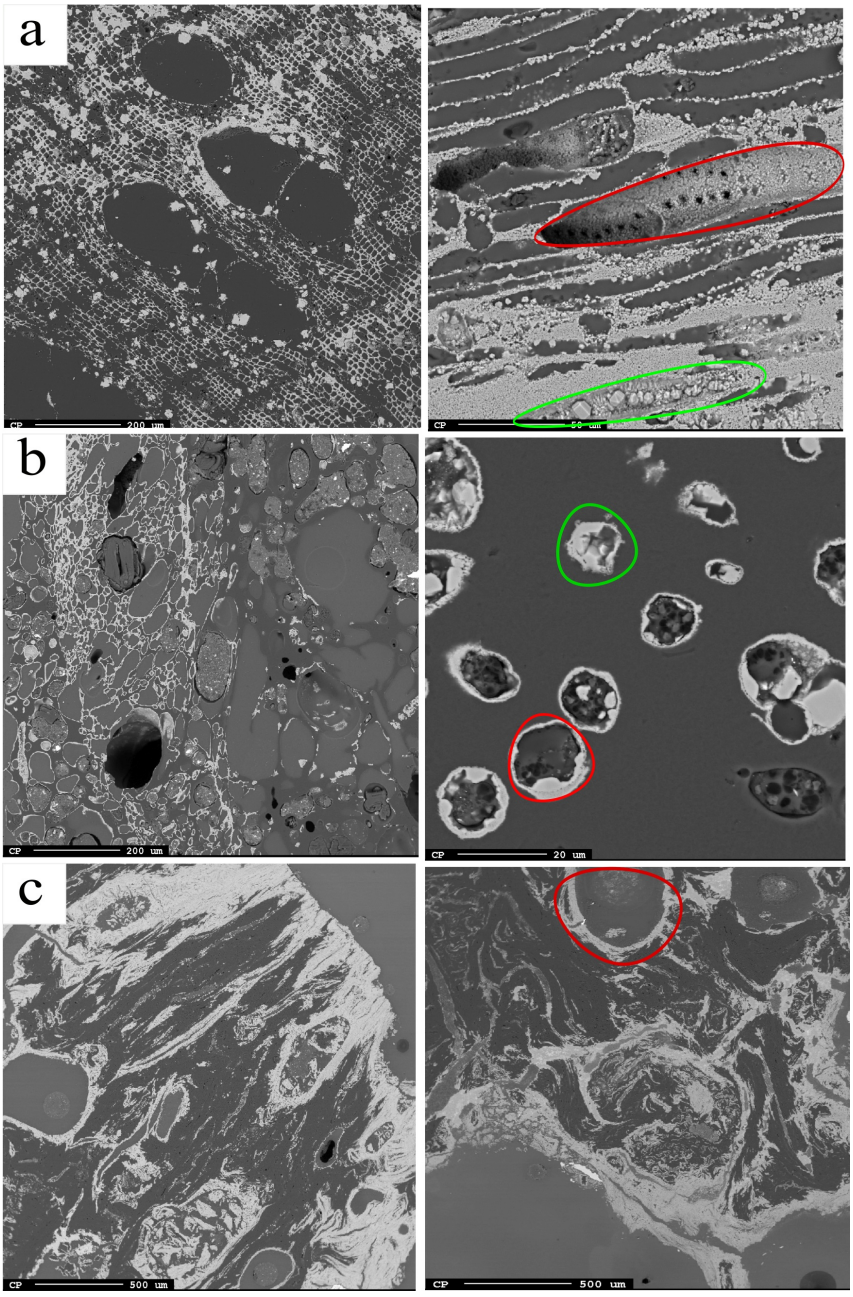

Figure 5.1.5. EPMA images of SiC particles formed from (a) charcoal, (b) coal, and (c) pet-coke, showing pore walls that have transformed to SiC. Their corresponding magnified images are presented on the right side. Pore walls transformed to SiC are highlighted in red and surface crystals visible inside pores of charcoal and coal are highlighted in green.

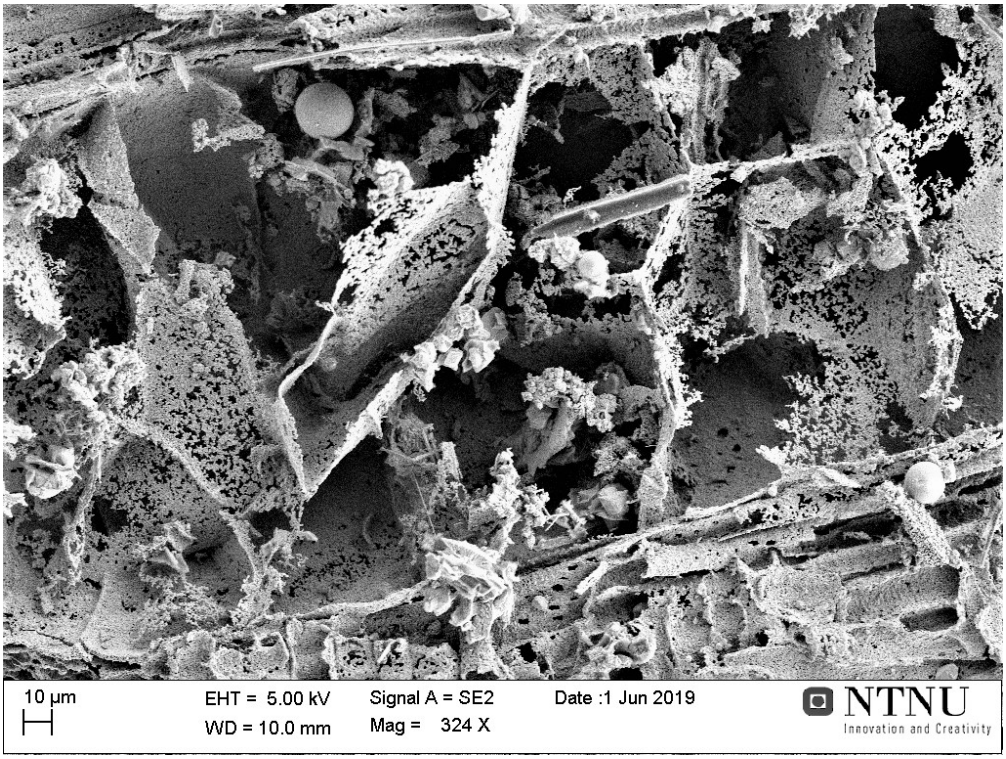

Figure 5.1.6. SEM image of charcoal-converted SiC particles, showing pore walls that have transformed to SiC.

The EPMA-BSE analysis gave an insight into the diffusional behavior of SiO(g) in charcoal, coal, and pet-coke. **Figure 5.1.7** shows the EPMA images of cross-sections of SiC particles partly transformed from charcoal, coal, and pet-coke. The gray regions are SiC converted from the carbon particles and the blackish regions are the unreacted carbon.

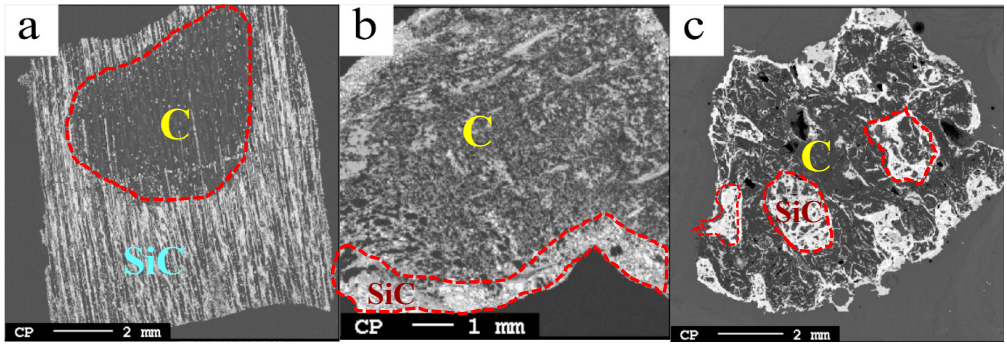

Figure 5.1.7. EPMA-BSE images of cross-sections of SiC particles partly transformed from (a) charcoal, (b) coal, and (c) pet-coke. Boundaries between SiC and unreacted carbon are marked by red dashed-lines.

In charcoal, the SCM closely approximates the real particles as shown in **Figure 5.1.7a**. During the conversion of charcoal to SiC, the reaction starts on the surface of the particle, initially forming a peripheral layer of SiC. The thickness of the SiC layer increases as the reaction proceeds. According to Schei and Halvorsen [95], the reaction rate slows down as the thickness of the SiC layer increases because the SiO(g) has to diffuse through the already formed SiC layer, to reach the unreacted carbon to complete the conversion. This work, hence, shows that the SCM can explain the transformation from carbon to SiC in charcoal.

However, coal and pet-coke used in this study behave differently, they does not follow the SCM mechanism. The EPMA image of charcoal partly converted to SiC shows a sharp boundary between the SiC formed in the pores and the unreacted carbon in the middle (marked with red dotted lines in **Figure 5.1.7a**). The coal particle too shows SiC forming mostly on its outer layer, and the SiC formation is more spatially distributed in its middle region (gray region **Figure 5.1.7b**). Therefore, it is not easy to differentiate a sharp boundary between the reacted and the unreacted regions of the partly transformed coal particle. However, in the SiC particle formed from pet-coke, a sharp boundary is clearly visible between the pore walls that transformed to SiC and the unreacted region (**Figure 5.1.7c**). These differences in the transformation mechanisms between each of the carbon materials could be related to the properties of the initial carbon materials. Kinetics of SiO(g) reacting with different types of carbon material have been studied previously [40, 20, 21, 22]. Myrhaug [20] also studied the SiO(g) reactivity of charcoal, coal, and metallurgical-coke, and proposed that the SCM does not give a detailed description of the topochemical conversion process in the inner structure of all carbonaceous particles. However, it predicts the overall conversion of the carbon particles.

5.1.3 Total transformation of carbon material to SiC

The current study also evaluated the extent of β-SiC formation in charcoal, coal, and pet-coke, in correspondence with the properties of the carbon materials. **Figure 5.1.8** shows the amount of β-SiC and unreacted carbon left after the SiC production at 1750 °C, with respect to porosities and cell wall thicknesses of charcoal, coal, and pet-coke. Among the three chosen carbon materials, charcoal exhibits the highest porosity with thinnest cell walls, leading to the formation of highest amount of SiC with no significant free carbon left in it. Coal and pet-coke follows charcoal. Pet-coke that has the maximum cell wall thickness and least porosity produced the least amount of SiC, leaving highest amount of unreacted carbon in it.

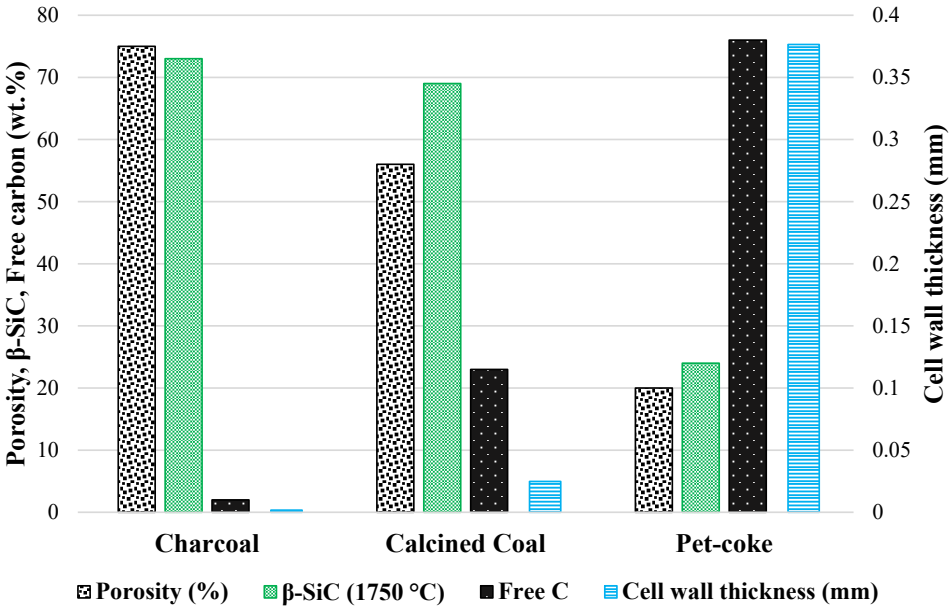

Figure 5.1.8. SiC production and its relation to properties of carbon materials, viz. porosity and cell wall (or pore wall) thickness (SiC data are from chemical analysis of SiC formed at 1750 °C in lower layer, from the three carbon materials).

The SiO-reactivity and conversion to SiC depend on the pore size distribution of the material and thus affect the effective diffusivity. The pore geometry and concentration of the gas that diffuses through the pores might also affect the size and shape of a crystal. **Figure 5.1.9** shows the SEM morphology revealing the pore wall distribution and pore sizes in charcoal (both in transverse and longitudinal directions), coal, and pet-coke. Charcoal has the highest porosity (75%) with thinnest cell walls (in the range 0.008–0.026 µm) compared with coal and pet-coke (**Figure 5.1.8**, **Figure 5.1.9a** and **b**). The high porosity in charcoal allows a higher concentration of SiO(g) to diffuse easily through the charcoal surface and its pores. It also has a lower distance to diffuse in the solid structure, as the cell walls are thinner. Hence the SiO(g) easily reacts with charcoal to form thick SiC surface crystals on the surface as well as transform the pore wall to SiC.

The pore size distribution in coal is not homogeneous; both small and large pores with thick and thin cell walls are present in it (**Figure 5.1.9c**). The porosity of coal is around 56% and its cell wall thickness ranges between 0.08 to 0.8 µm (**Figure 5.1.8**). In regions where the pores had thin cell walls, long and thick SiC crystals have formed (**Figure 5.1.2a**), whereas in regions where pore walls were thicker, SiC crystals have grown in the form of whiskers (**Figure 5.1.2b** and **c**). Based on petrographic analysis of coal and metallurgical-coke in the production of Si

alloys, Myrvågnes and Lindstad [101], and Myrvågnes [40] found that calcined coal showed a lot of depositional carbon in the pores of coal. It was assumed that the depositional carbon sealed the pore walls and blocked the reaction towards the SiO(g), resulting in a reduced reactivity.

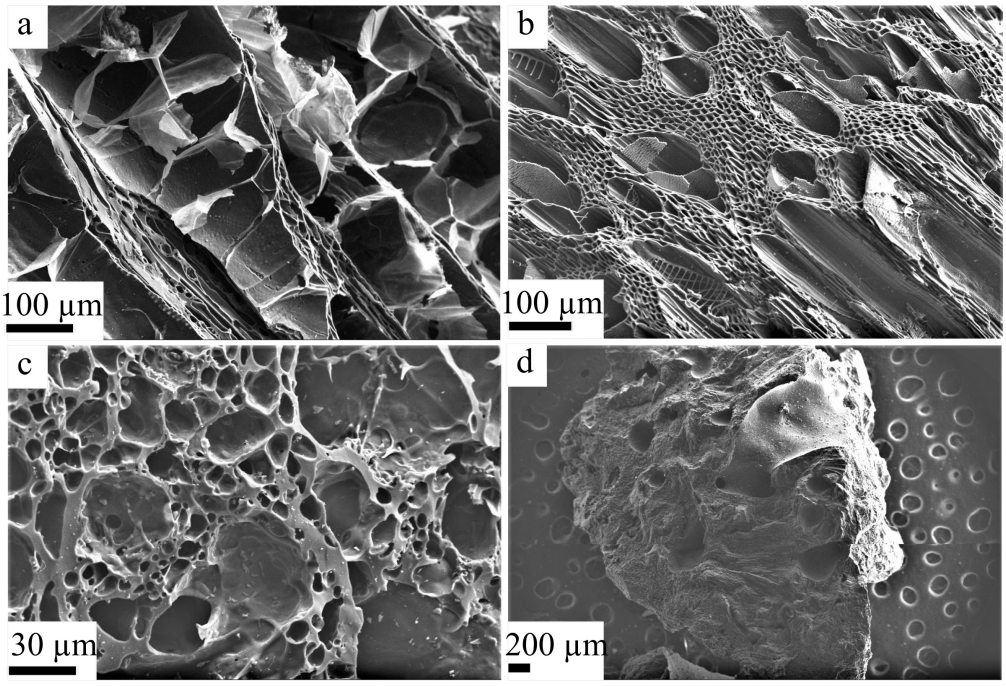

Figure 5.1.9. SEM morphology revealing pore wall distribution and pore sizes in (a) transverse direction in charcoal, (b) longitudinal direction in charcoal, (c) coal, and (d) pet-coke.

The porosity of pet-coke is around 20%, the least among the three carbon materials, and its cell wall thickness ranges from 1.84 to 8.79 µm, which is significantly higher than those of charcoal and coal (**Figure 5.1.8**). The diffusing path of SiO(g) is hindered by the low porosity and the large cell wall thickness in pet-coke (**Figure 5.1.9d**). Hence, it could be inferred that the formation of SiC in carbon particles depend on their physical properties, especially their porosity and cell wall thickness. Based on the results obtained in this study, charcoal has the highest formation of SiC followed by coal and pet-coke, which is in good agreement with the inference derived based on the structural properties of these carbon materials. Previous studies by Buø et al. [100] and Narciso-Romero et al. [98] have also confirmed the influence of the structural properties of different carbon materials on their SiO(g) reactivity. The results from current study are hence in good agreement with these previous findings.

5.1.4 Effect of SiO(g) pressure on SiC production

Two SiO(g) producing sources, a mixture of (SiO_2 + Si) and pellets of (SiO_2 + SiC), were utilized separately to produce SiC. These two sources produced SiO(g) at different pressures. Stoichiometrically, (SiO_2 + Si) would produce a partial pressure of SiO of 1 bar and (SiO_2 + SiC) would produce a partial pressure of SiO of 0.75 bar. Based on the chemical analysis data, charcoal produced the highest amount of SiC followed by coal and pet-coke, and the formation of SiC increased with an increase in temperature. The results from chemical analyses show that higher SiO pressures produced larger quantities of β-SiC, as expected. Here the pressure of SiO is higher than the equilibrium SiO pressure for the formation of SiC and it will provide a higher driving force, hence producing more SiC. The thermodynamics calculations demonstrating the pSiO(g) at which a carbon particle react with SiO(g) to form SiC is, shown in **Figure 5.1.10**.

A previous study has shown that at temperatures of 1550–1730 °C, a mixture of (SiO_2 + Si) reacted a maximum of 1.5 times faster than the mixture of (SiO_2 + SiC) [104]. The reactivity of (SiO_2 + Si) mixture as a function of time (30–180 min) and temperature (1650–1950 °C) in Ar atmosphere also showed that the reactivity of (SiO_2 + Si) increased with both time and temperature [103]. For the reaction between SiO_2 and Si, when the temperature reaches the melting temperature of Si, the liquid Si that forms enhances rate of the reaction. Hertl and Pultz [106] states that during the reaction between SiO_2 and SiC, CO(g) would form and at some point, it might get chemisorbed at the surface. It would block the reaction sites between the SiO_2 and SiC, which suppresses the reaction rate.

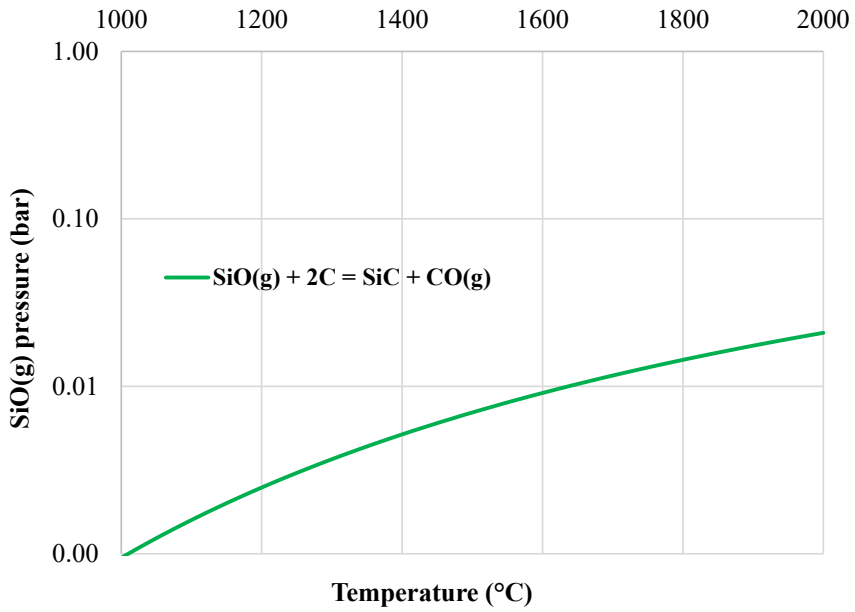

Figure 5.1.10. Effective partial pressure of SiO(g) in equilibrium with SiC as a function of temperature.

To obtain the exact amount of SiC and Si formed at different temperatures, calculations were performed, based on SiC and Si produced in each layer (wt.%) from the chemical analysis data (**section 4.1.1.4** and **section 4.2.1.4**) and their amounts (in grams) in the middle and lower layers (**Figure 4.1.3** and **Figure 4.2.3**). The values are taken form the constant volume experiments that used (SiO_2 + Si) as source for SiO(g). **Figure 5.1.11** and **Figure 5.1.12** show the total quantities of SiC and Si formed from charcoal and coal, respectively, both at 1750 and 1800 °C. The sample collection after pet-coke experiments was difficult and hence, this calculation was not performed for pet-coke. The figures show that as the temperature increases, more SiC and Si are formed both the carbon materials. At 1800 °C, 21.8% of SiC and 2.35% of Si have formed in coal, whereas, in charcoal at the same temperature, only 18.8% of SiC had formed. However, 12.8% of Si formed in charcoal at 1800 °C, which is higher compared with the %Si formed in coal. This shows that when using charcoal as the carbon source, once the SiC is formed, Si would also form rapidly in SiC, compared with SiC production using coal as the source of carbon (**Figure 5.1.11**).

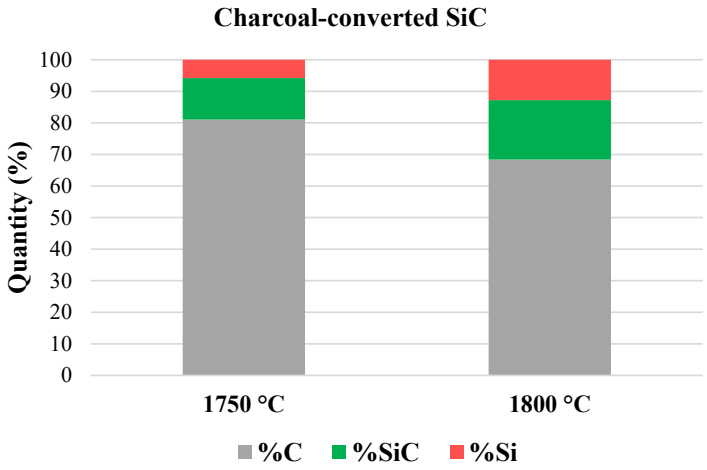

Figure 5.1.11. Total amounts of SiC, Si, and unreacted carbon formed at 1750 and 1800 °C, using charcoal as source of carbon, from constant volume experiments that used (SiO_2 + Si) as source of SiO(g).

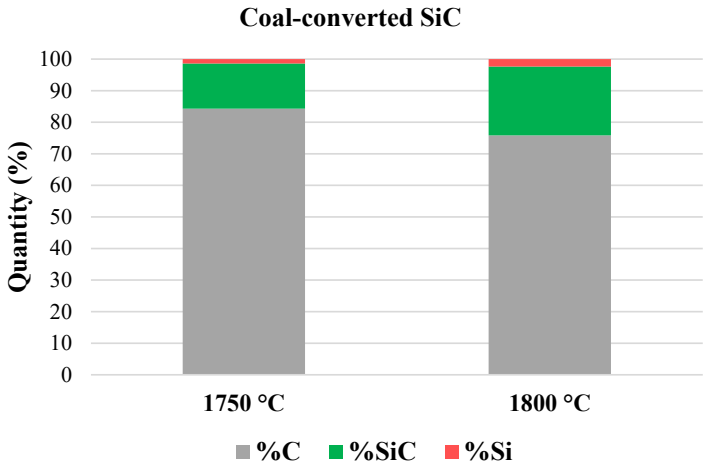

Figure 5.1.12. Total amounts of SiC, Si, and unreacted carbon formed at 1750 and 1800 °C, using coal as source of carbon, from constant volume experiments that used (SiO_2 + Si) as source of SiO(g).

5.2 Formation of elemental Si in β-SiC particles

Another important finding in this work is the formation of Si in SiC particles at a temperature range of 1674–1900 °C, especially in the lower region of the initial carbon layer. This study shows that the Si formation in SiC particles depends on the pSiO(g), and the quantity of Si formed is influenced by the type of the carbon source. Interestingly, Si was found in SiC particles even at 1674 °C at higher SiO pressures, and its quantity increased with an increase in temperature. The thermodynamic calculations suggest that Si can only be produced at a

temperature ≥ 1800 °C as it is postulated that the SiO gas pressure at lower temperatures will be too low due to condensation reactions. Nevertheless, the current study proved that it is possible to produce Si at temperatures < 1800 °C, when (SiO_2 + Si) was used to generate SiO(g), which creates a higher SiO(g) pressure.

The graphite tube furnace was utilized to validate the induction furnace experiments, especially, to verify the Si formation in SiC particles at temperatures below 1800 °C. **Figure 5.2.1** to **Figure 5.2.3** show the EPMA micrographs of SiC samples from the graphite tube furnace and elemental distributions of carbon and Si in them. The samples were collected from the lower layers of the experiments conducted with charcoal (1674 °C), coal (1686 °C), and pet-coke (1694 °C), using (SiO_2 + Si) as the source for SiO(g). The high concentrations of Si in the SiC particles confirm the formation of elemental Si in SiC, even at temperature ranges of 1674–1694 °C, which is much lower than the theoretical Si production temperature. The EPMA analysis also showed that SiC and Si forms homogeneously throughout the charcoal particle (**Figure 5.2.1**). In coal and pet-coke, Si forms mostly on the outer surface of the SiC sample and in lesser quantities (**Figure 5.2.2** and **Figure 5.2.3**), compared with the Si formed in charcoal. Hence, it is inferred that the properties of the carbon material also influence the amount of Si formed in the SiC particles.

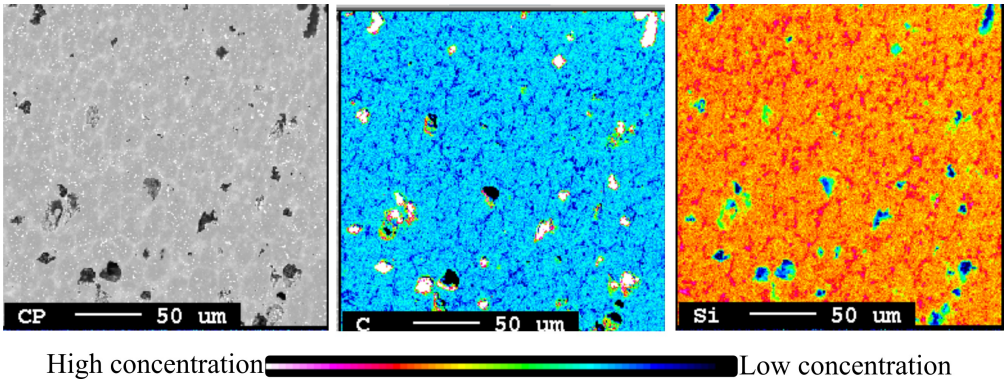

Figure 5.2.1. EPMA of charcoal-converted SiC sample in lower layer at 1674 °C, and elemental distribution of carbon and Si in it (dark red shows elemental Si and orange shows SiC). Mixture of (SiO_2 + Si) was source of SiO(g) in this experiment.

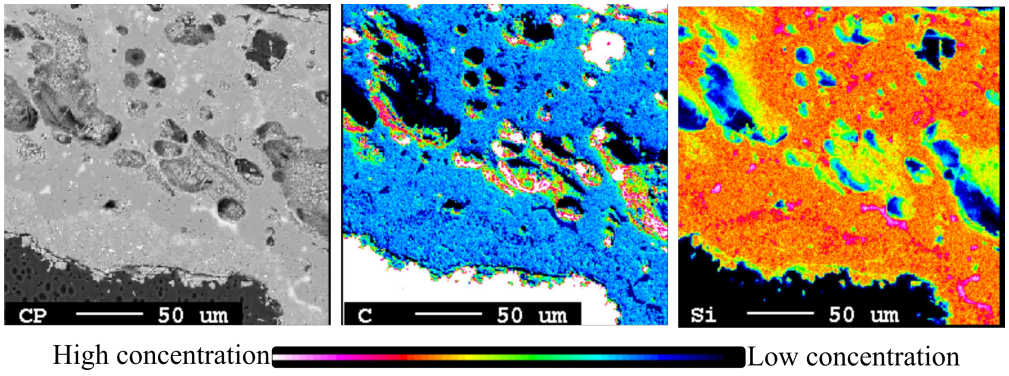

Figure 5.2.2. EPMA of coal-converted SiC sample in lower layer at 1686 °C, and elemental distribution of carbon and Si in it (dark red shows elemental Si and orange shows SiC). Mixture of (SiO_2 + Si) was source of SiO(g) in this experiment.

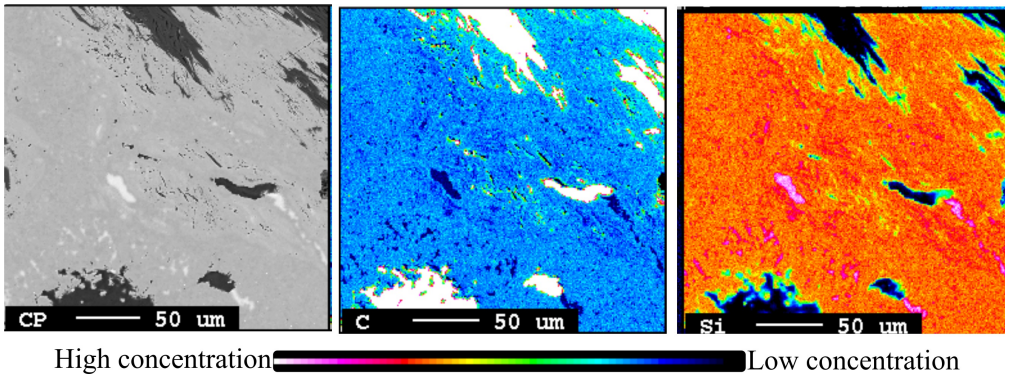

Figure 5.2.3. EPMA of pet-coke-converted SiC sample in lower layer 1694 °C, and elemental distribution of carbon and Si in it (dark red shows elemental Si and orange shows SiC). Mixture of (SiO_2 + Si) was source of SiO(g) in this experiment.

Figure 5.2.4 shows Si formed in SiC particles produced in the induction furnace at 1755 °C. Even though the formation of Si in SiC was observed at both 1674 (graphite tube furnace experiment) and 1755 °C (induction furnace experiment), quantity of Si produced in the graphite tube furnace was lower compared with those formed in the induction furnace. This could be due to the presence of inert gas while performing the experiments in the graphite tube furnace, which reduces the pSiO(g), thereby reducing the amount of Si formed in SiC particles. The amount of Ar used was 0.1 L/min for 1 h; 6 L of Ar was utilized for an experiment to produce SiC. Therefore, the total gas pressure was 2 moles of SiO(g) with 0.27 moles of Ar, which reduced the pSiO(g) to 88%.

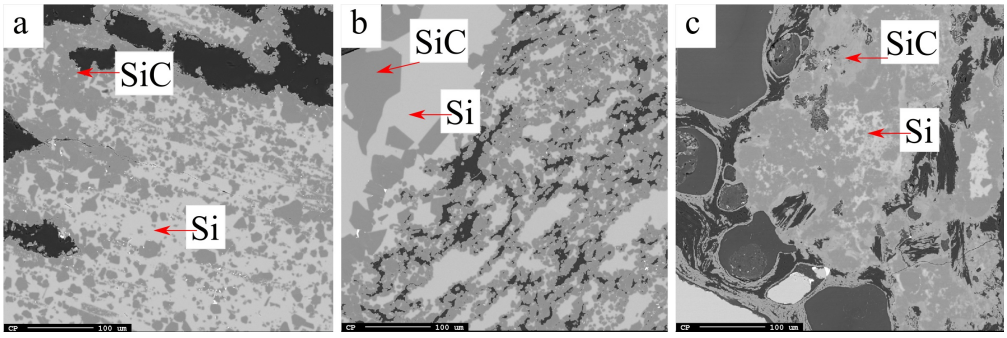

Figure 5.2.4. EPMA images of SiC particles produced from (a) charcoal, (b) coal, and (c) pet-coke in induction furnace at 1750 °C. Mixture of (SiO_2 + Si) was source of SiO(g) in this experiment.

Si did not form in the SiC particles when (SiO_2 + SiC) was used as the source for SiO(g). **Figure 5.2.5** shows the EPMA and elemental mapping of carbon and Si in the SiC samples produced in the lower layer using (SiO_2 + SiC) as the source for SiO(g). The samples were collected from the experiments conducted in the graphite tube furnace with charcoal at 1756 °C, coal at 1750 °C, and pet-coke at 1752 °C. Elemental mapping confirms that Si and carbon are distributed in a similar ratio, which indicates that only SiC has formed in the carbon particles and no elemental Si is present in them.

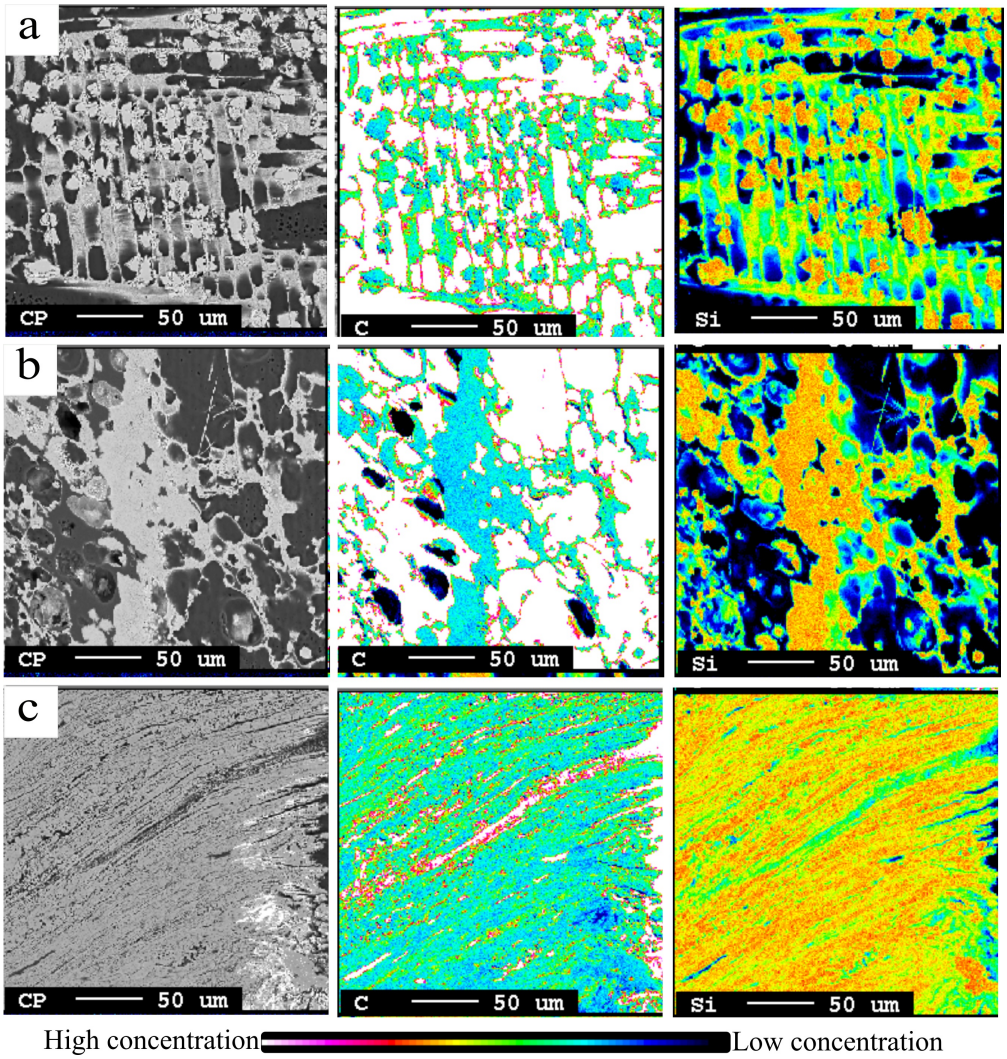

Figure 5.2.5. EPMA and elemental mapping of carbon and Si in SiC samples in lower layers, collected from graphite tube furnace experiments that used (SiO_2 + SiC) as source of SiO(g). (a) Charcoal at 1756 °C, (b) coal at 1750 °C, and (c) pet-coke at 1752 °C show that no elemental Si has formed in them at this SiO(g) pressure.

According to the thermodynamic calculation shown in **Figure 5.2.6**, Si is produced at higher SiO pressures (represented as red line) and needs a pSiO(g) of 0.68 bar at 1800 °C. The SiO pressure required to produce Si decreases with an increase in temperature. According to the thermodynamics, in the Si-O-C system where the gas phase contains both SiO and CO, a higher SiO pressure cannot be obtained at a lower temperature because the gas species would then transform to the condensed phases of SiO_2 and SiC, or SiO_2 and Si, as shown in **Figure**

5.2.6 Hence, to create a SiO pressure high enough to produce Si, the temperature should be higher than 1800 °C. Yet, elemental Si formed at lower temperatures in the present study; it shows that the condensation reactions are slow and hence they are not in thermodynamic equilibrium. Hardly any condensate formation was observed on the surfaces of the SiC particles in the EPMA-BSE images.

Broggi et al. [121] also showed that the condensation reactions was not in equilibrium and hence a higher SiO pressure was obtained during the experiments. Based on equilibrium calculations and temperature measurements, they showed that the condensates form at a temperature range of 1400–1780 °C at pSiO(g) = 0.534–0.742 bar. This pressure range is higher than the equilibrium pressure required for the condensation reaction, which verifies that the condensation reaction is kinetically hindered. This is also observed in the industrial furnaces where the Si yield is typically in the range of 80–90%. This Si loss indicates a much higher SiO pressure existing in the charge than the equilibrium pressure required for the condensation reactions.

The stochiometric SiO pressure for SiO formed from (SiO_2 + Si) and (SiO_2 + SiC) are 1 bar (red dotted line) and 0.75 bar (blue dotted line), respectively (**Figure 5.2.6**). If there are kinetic limitations on the condensation reactions, the SiO pressure might stay high. During the SiC production with (SiO_2 + Si), the total SiO(g) pressure created in the lower part of the carbon materials is assumed to be close to 1 atm, which is high enough to produce Si at lower temperatures. The elemental Si could also form through the condensation reaction: ((reverse) **reaction (14)**): [2SiO = SiO_2 + Si]. However, as no SiO_2 was found inside the SiC structure, it is presumed that the Si in SiC particles was produced through **reaction (18)**: [SiO (g) + SiC = 2Si + CO (g)].

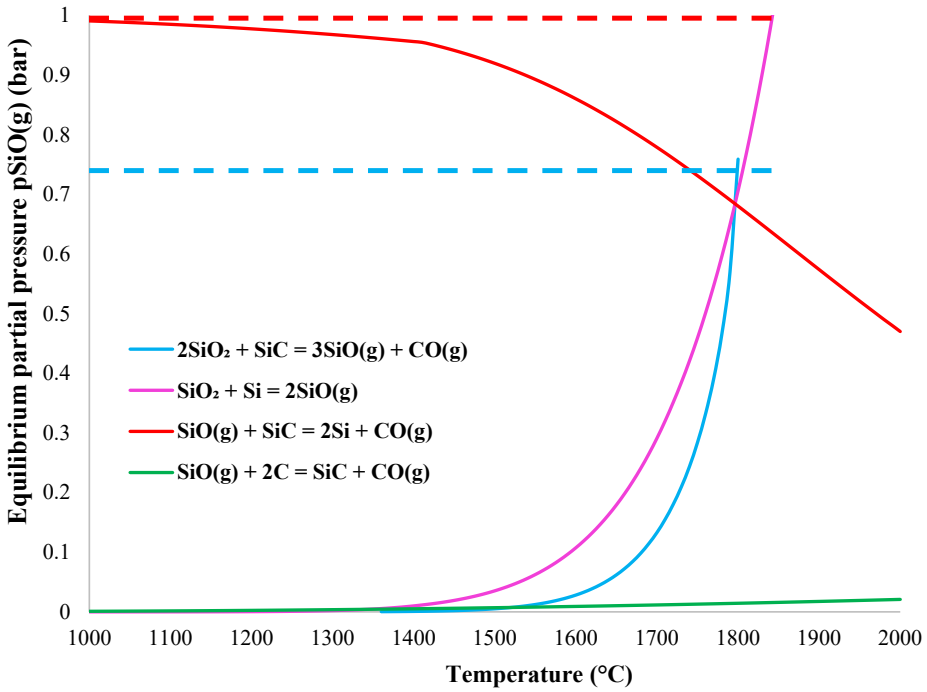

Figure 5.2.6. Equilibrium pSiO(g) required for SiO(g), SiC, and Si producing reactions.

The SiC structure become denser and loses the original carbon structure as elemental Si forms in them, as revealed by the SEM morphology and EPMA analyses of SiC particles with elemental Si in them (**Figure 5.1.4** and **Figure 5.2.4**). This could be because once Si forms in the SiC particles, pores of the carbon particles get filled with molten Si, which decreases the porosity of the particle. The production of elemental Si inside the SiC structure was also observed by Vangskåsen [32] in a pilot scale experiment. **Figure 5.2.7** shows cross-section of the pilot scale furnace, and the different zones where SiC particles with Si were found. Si was present in SiC particles collected from positions **5** and **6**, where the temperature was supposedly lower than the high temperature area. The results from the current study and previous studies indicate that if the SiO(g) pressure is high enough, around 10–15% (according to Vangskåsen [32]) of the total Si is produced in the SiC particles that are formed higher up in the Si furnace. Also, the quantity of Si production in SiC depends on selection of the carbon material source, as shown in **Figure 5.1.11** and **Figure 5.1.12**.

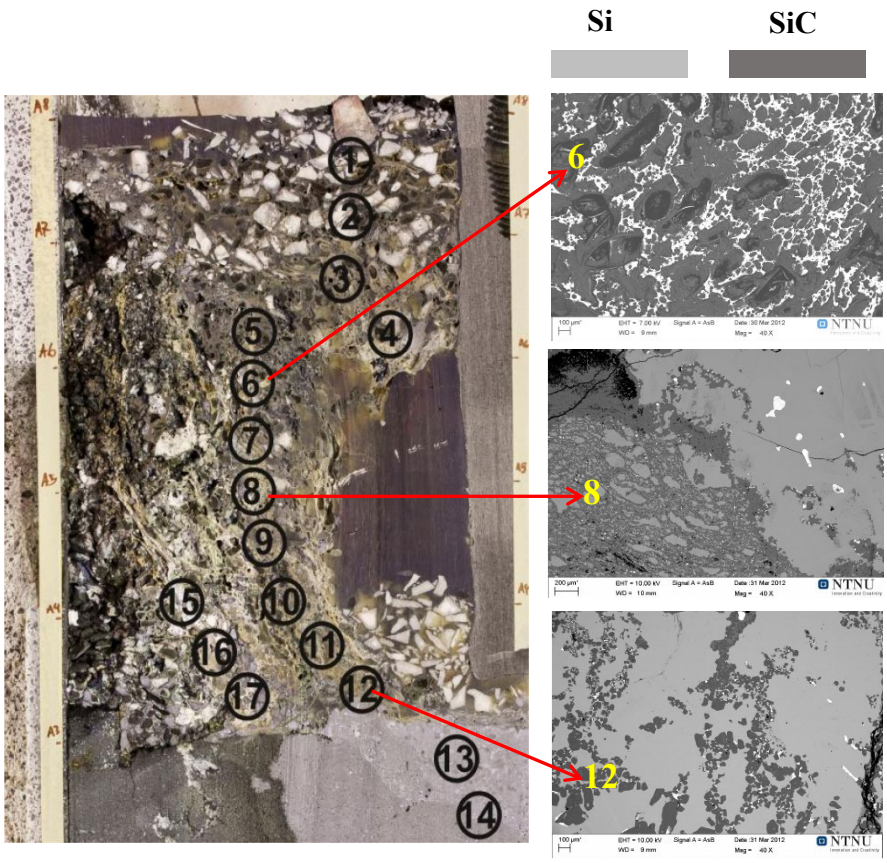

Figure 5.2.7. Cross-section of pilot scale furnace from Vangskåsen [32], showing different zones where Si was observed in SiC particles.

5.3 Transformation of β-SiC to α-SiC

The XRD analysis of SiC (with and without elemental Si) produced at 1750–1900 °C from charcoal, coal, and pet-coke, confirmed them as β-SiC with cubic modification 3C. Two types of SiC raw materials, i.e., β-SiC with 0% Si and β-SiC with varying amounts of Si, were used for their further transformation to α-SiC. The purpose was to study the behavior of SiC produced from different carbon materials, when they were exposed to higher temperatures. A temperature range of 2100–2450 °C was chosen for the heat-treating experiments. When the β-SiC with no elemental Si was heated at 2100 °C, it did not transform to α-SiC, however, increasing the temperature increased the formation of α-SiC in it. **Figure 5.3.1** shows the charcoal-converted β-SiC with no elemental Si, heat-treated at 2100–2450 °C. It shows that a

higher amount of α-SiC is produced at higher temperatures, indicating that temperature is one of the main factors determining the transformation to α-SiC. This is in accordance with previous literature stating that temperature is a main factor influencing the polytype transformation in SiC [25, 24]. An increase in temperature leads to a higher thermal diffusion of the atoms in the cubic β-SiC (3C). A rearrangement of atoms within the SiC would lead to the formation of different α-SiC polytypes [25, 69].

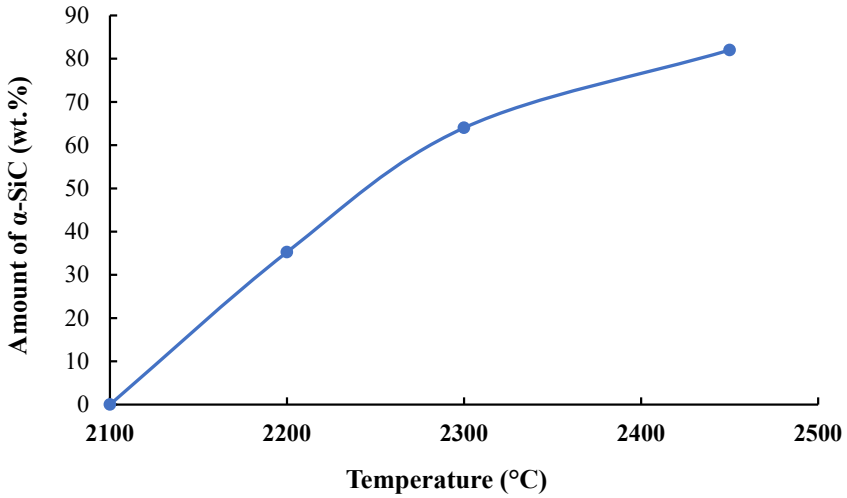

Figure 5.3.1. Charcoal-converted β-SiC with no elemental Si, heat-treated at 2100–2450 °C.

In addition to temperature, the results also reveal that elemental Si in the SiC particles enhances the extent of transformation of β-SiC to α-SiC. When the charcoal-converted β-SiC with 0, 9, and 39 wt.% of elemental Si was heat-treated at 2100–2450 °C, the amount of Si in the SiC particles increased their hexagonality, as shown in **Figure 5.3.2**. Ringdalen [18] studied the properties of SiC from coal at temperatures > 2000 °C; she used β-SiC derived from coal with no elemental Si in it and heat-treated it to 2000–2500 °C. Results showed that no transformation to α-SiC occurred until 2200 °C, and at 2350 °C, after a holding time of 1 h, 67 wt.% of the β-SiC transformed to α-SiC. The current study also shows that elemental Si in the β-SiC particles influences the transformation to α-SiC.

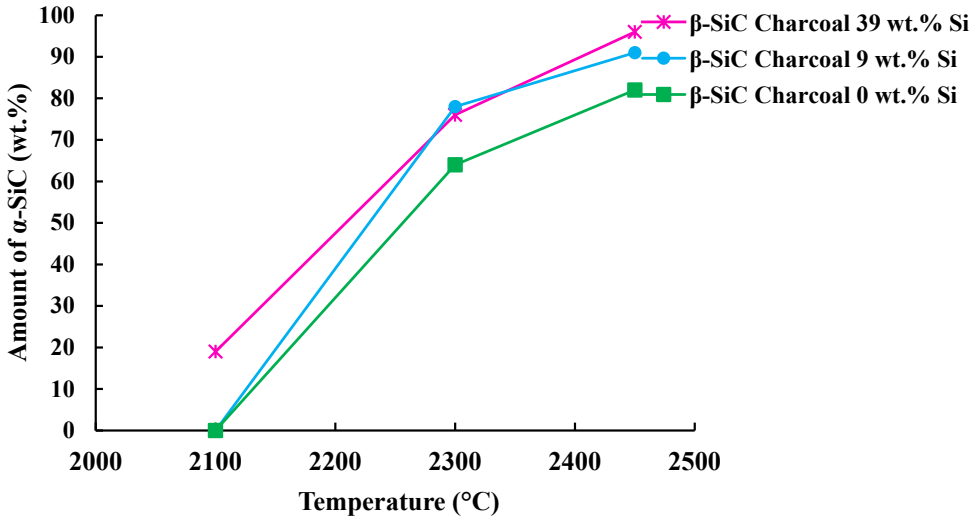

Figure 5.3.2. Charcoal-converted β-SiC particles with 0, 9, and 39 wt.% of elemental Si, heat-treated at 2100–2450 °C.

The current study shows that in addition to these two parameters, properties of the original carbon source are also factors determine the extent of transformation to α-SiC. **Figure 5.3.3** summarizes the effects of temperature, type of carbon material, and Si content in β-SiC on the transformation to α-SiC. It shows that both elemental Si and the original carbon source are essential factors determining the extent of α-SiC conversion. Charcoal-converted β-SiC with elemental Si had the highest extent of transformation to α-SiC, compared with coal and pet-coke. Charcoal has higher porosity and thereby a larger surface area compared with coal and pet-coke, as shown in **Table 3-5**. Larger surface area indicates a higher availability of nucleation sites for the α-SiC phases. The thermodynamic driving force for both nucleation and crystal growth increases with surface area [119], which could be the main reason for the increased transformation in charcoal-converted β-SiC.

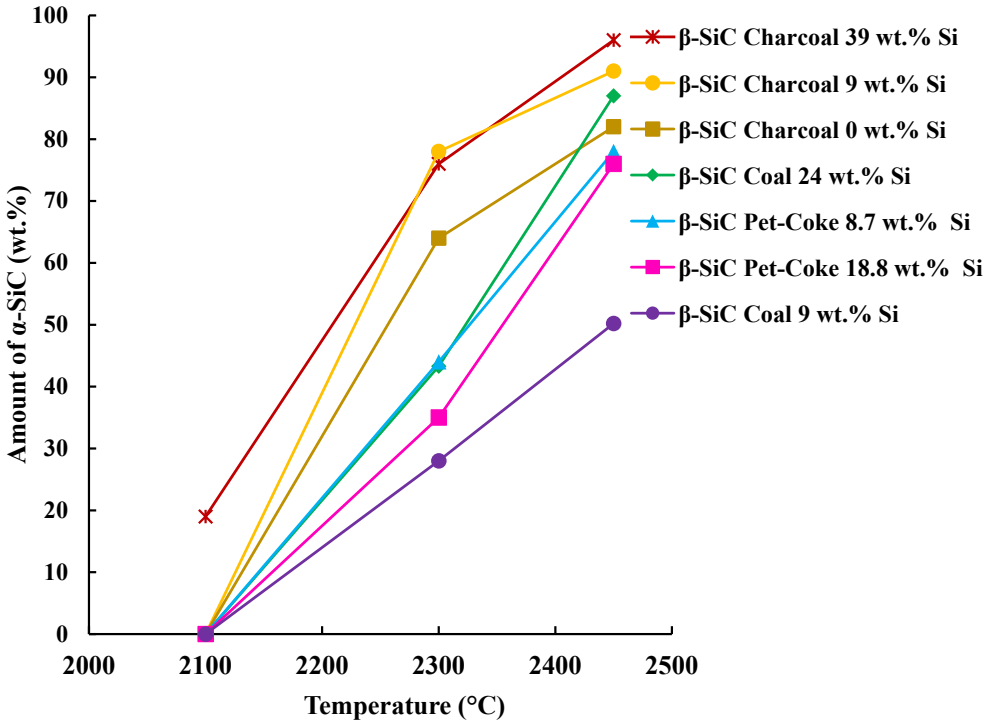

Figure 5.3.3. Effect of temperature, type of original carbon material, and Si content in β-SiC, on transformation to α-SiC.

Previous studies have shown that impurities such as N, Al, B, and O act as a catalyst for the rate of transformation of β-SiC to α-SiC [63, 59, 67]. The elemental analysis of ash composition in the carbon materials used here have shown that Al_2O_3 was one of the main impurities present in them, and the amount was higher in coal followed by pet-coke and charcoal (**Table 3-4**). However, results from the EPMA elemental mapping and XRD data did not show the presence of Al in the β-SiC particles from charcoal, coal, and pet-coke (**Figure 4.1.16**, **Figure 4.2.7**, and **Figure 4.3.6**). Only traces of Fe were observed in the samples. Therefore, it is presumed that in the present study, impurities in the chosen carbon materials did not play any significant role in the production of α-SiC.

Another interesting phenomenon observed was the differences in the distribution of various polytypes in the α-SiC produced from various β-SiC samples. At 2300 and 2450 °C, charcoal- and coal-converted β-SiC with 9 wt.% Si did show formation of 4H, 6H, and 15R, the most commonly occurring SiC polytypes (**Figure 5.3.4**). In β-SiC with 8.7 wt.% Si from pet-coke,

only the 6H polytype was present at 2300 and 2450 °C (**Figure 5.3.5**). Even though coal with 9 wt.% Si had the least amount of α-SiC in it (**Figure 5.3.3**), more α-SiC polytypes developed in it at 2450 °C, compared with pet-coke (**Figure 5.3.5**). Upon investigation of SiC surface crystal from charcoal, it showed a high intensity of stacking faults (**Figure 4.1.35**). The high density of defects in the starting material could also be involved in the β to α transformation; the heavily twinned β-SiC crystals provides a high density of nucleation sites for the α-SiC formation [114]. Not many SiC surface crystals were observed on the surfaces of β-SiC particles derived from pet-coke, which could also be the reason why different polymorphs of SiC had not formed in the α-SiC transformed from these particles (**Figure 5.3.4** and **Figure 5.3.5**).

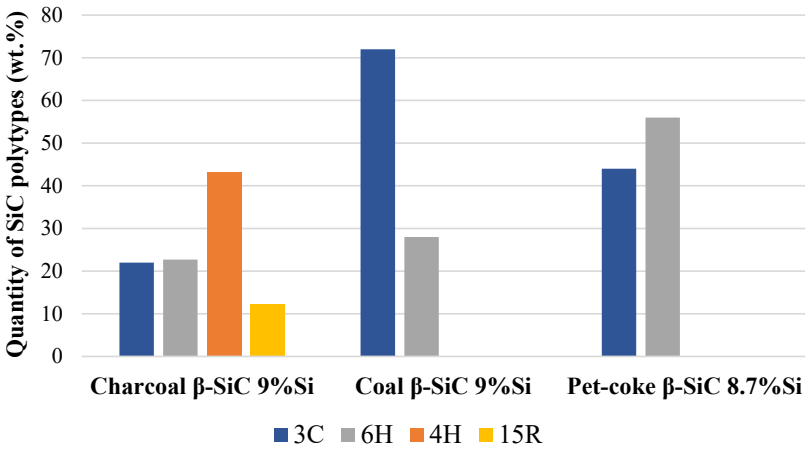

Figure 5.3.4. SiC polytype distribution in α-SiC formed at 2300 °C, from charcoal, coal, and pet-coke.

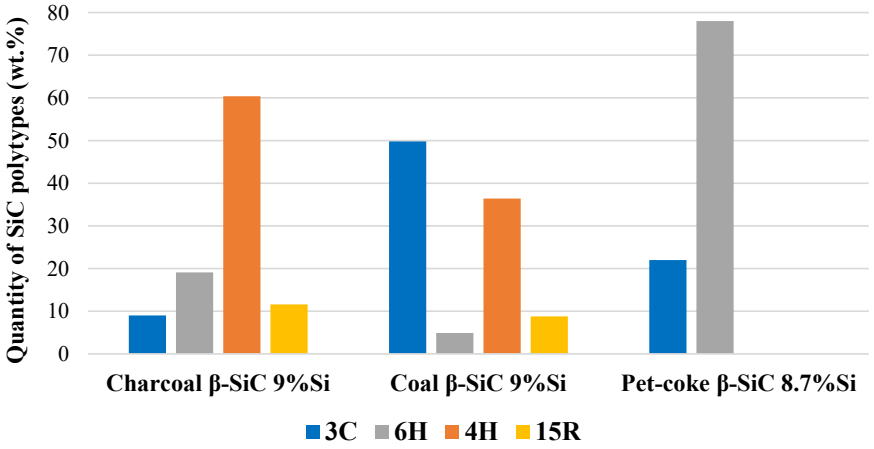

Figure 5.3.5. SiC polytype distribution in α-SiC formed at 2450 °C, from charcoal, coal, and pet-coke.

If elemental Si and β-SiC samples were exposed to a temperature near or above the SiC decomposition temperature, the Si and carbon rich species such as Si(g) and SiC_2(g) would appear at a higher partial pressure as shown in **Figure 5.3.6**. The partial pressures of Si(g) and SiC_2(g) are high compared with the partial pressure values of the other gas species. Kong et al. [89] performed a detailed study regarding the possible reactions responsible for the formation of SiC from the gas species. Based on the equilibrium concentration of the gas species and the free energy values of **reactions (5)** to **(10)** (**section 2.3.5**), it is probable that the SiC formation from the gas species is possible by the reactions between Si(g) and SiC_2(g), which are **reaction (7)** and **reaction (10)**.

$$SiC_2\ (g) = SiC\ (s) + C\ (s) \qquad (7)$$

$$SiC_2\ (g) + Si\ (g) = 2SiC\ (s) \qquad (10)$$

Among these two reactions, **reaction (10)** has the largest negative free energy, making it more stable than **reaction (7)**. **Figure 5.3.7** shows the evolution of free energy values of the **reactions (7)** and **(10)** with temperature, calculated using HSC chemistry 9. The reason why elemental Si might enhance the extent of transformation to α-SiC, could hence be the higher gas pressure of Si and SiC_2-species. This might facilitate the reaction between these two gas species to form α-SiC, in accordance to **reaction (10)**, and the equilibrium K value is the product of $\boldsymbol{p_{Si(g)} \cdot p_{SiC_2(g)}}$. Some of the gas species might precipitate as α-SiC at lower temperatures (~2000 °C), forming dendritic structures as found in the industrial α-SiC samples [15]. The formation of α-SiC through a gas phase will therefore be faster than the re-structuring of β-SiC, and hence, elemental Si will increase the extent of transformation at temperatures above 2000 °C.

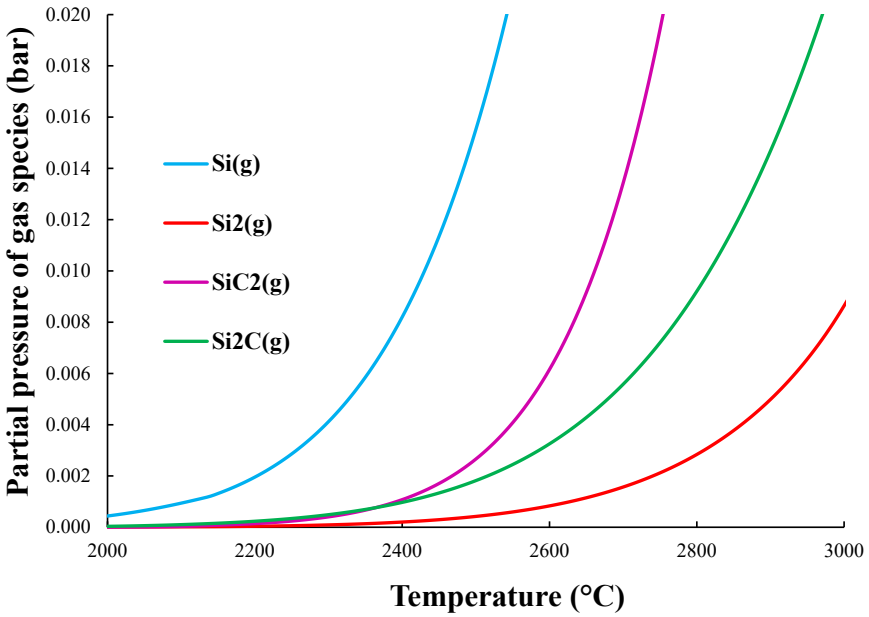

Figure 5.3.6. Equilibrium partial pressures of SiC gas species at 2000–3000 °C, calculated using HSC Chemistry 9 software.

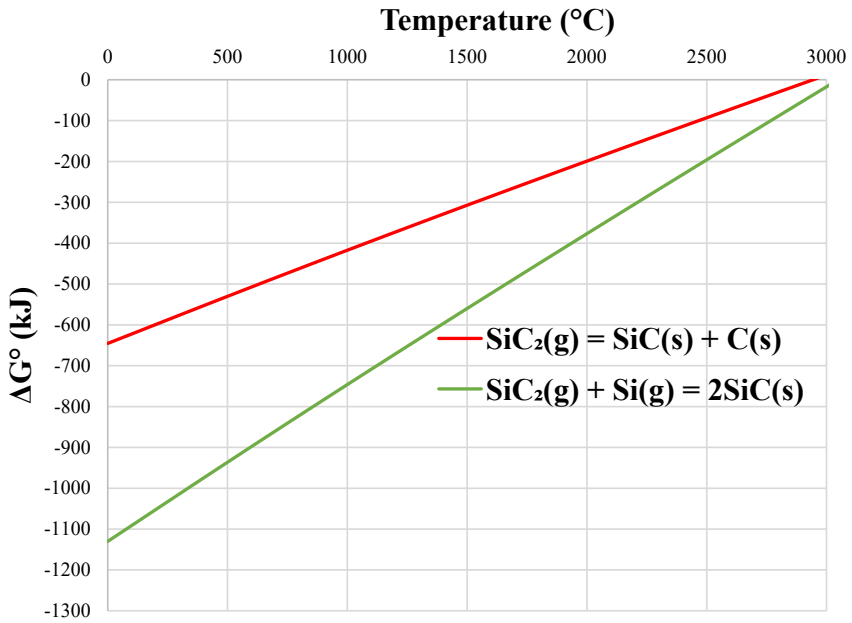

Figure 5.3.7. Free energy values of reactions (7) and (10) at temperatures up to 5000 °C.

5.4 SiC formation in industrial Si process

The laboratory-produced SiC samples were compared with three SiC samples obtained from the industry. Based on excavations and temperature distribution in the industrial furnaces, SiC would be located at different regions in different forms. The types of SiC produced in different zones of an industrial furnace are explained below. **Figure 5.4.1** shows the schematic illustration of an industrial Si furnace.

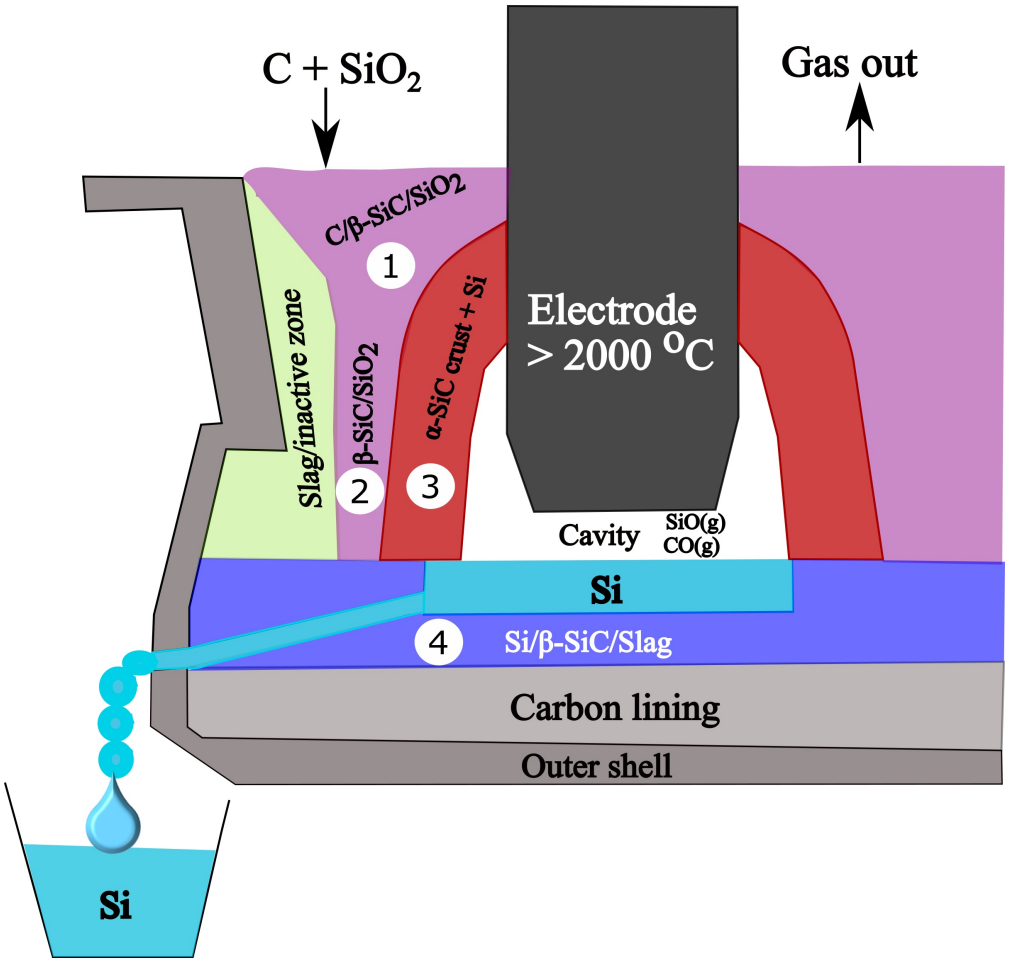

Figure 5.4.1. Schematic illustration of industrial Si furnace showing different zones where SiC is located (after excavations at Thamshavn [17] and Finnfjord [15]).

In the outer zone, where the charge materials are heated to temperature ranges of 700–1800 °C, most, if not all, of the carbon sources undergo a conversion to β-SiC as a result of its

interaction with SiO(g). The equilibrium pSiO(g) for different reactions (**Figure 2.4.1**) shows that SiC is produced when the temperature reaches 1512 °C at a pSiO(g) of 0.004 bar. However, as it is shown that the gas is not in equilibrium with the condensed phases, the SiC formation could take place at lower temperatures as well. In **Zone 1** in **Figure 5.4.1**, carbon particles are partly transformed to SiC, and are surrounded by condensates. The SEM morphology images of SiC produced in the laboratory from coal at a temperature < 1700 °C were similar to the SiC collected from this region (**Zone 1** in **Figure 5.4.1**). **Figure 5.4.2** shows the SEM morphologies of laboratory-produced SiC from coal at temperature < 1700 °C, confirmed as β-SiC, and the SiC procured from the industry, taken from **Zone 1**. SiC in the shape of whiskers have formed at temperatures below 1700 °C when coal was used as the main carbon source. As the structures of both the SiC particles were similar in appearence, it could be assumed that the temperature in **Zone 1** might have been < 1700 °C.

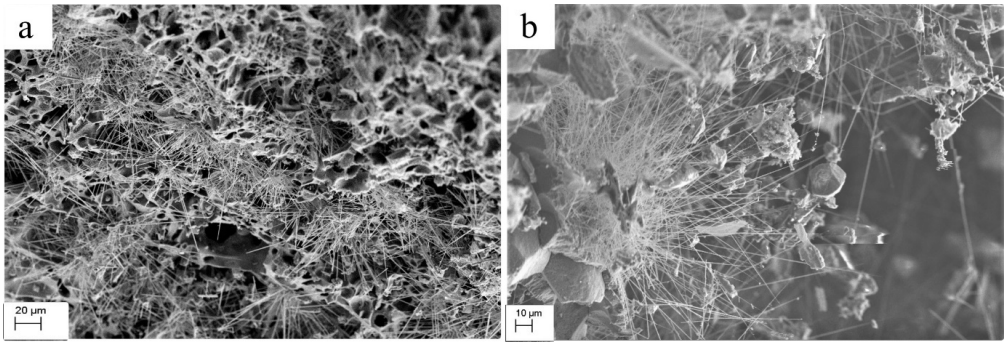

Figure 5.4.2. SEM morphology images of (a) laboratory-produced SiC from coal at temperatures < 1700 °C and (b) SiC from industry, from Zone 1.

In **Zone 2** (**Figure 5.4.1**), the temperature ranges from 1800 °C and above, and when the partly converted SiC enters that region, it would completely transform to SiC. **Figure 5.4.3** shows the SEM morphologies of laboratory-produced SiC at a temperature close to 1800 °C and SiC taken form **Zone 2**. Thick surface crystals of different sizes and shapes had formed in the pores of the coal particle. The SiC structure was dense, and it could also be an indication that elemental Si has also formed in the SiC particles, based on the SEM morphology of SiC particles formed at temperatures of 1750–1900 °C. Based on laboratory experiments (at 1750–1900 °C) that produced SiC from charcoal, coal, and pet-coke, the SiC produced by direct reaction of carbon with SiO(g) has been confirmed as β-SiC.

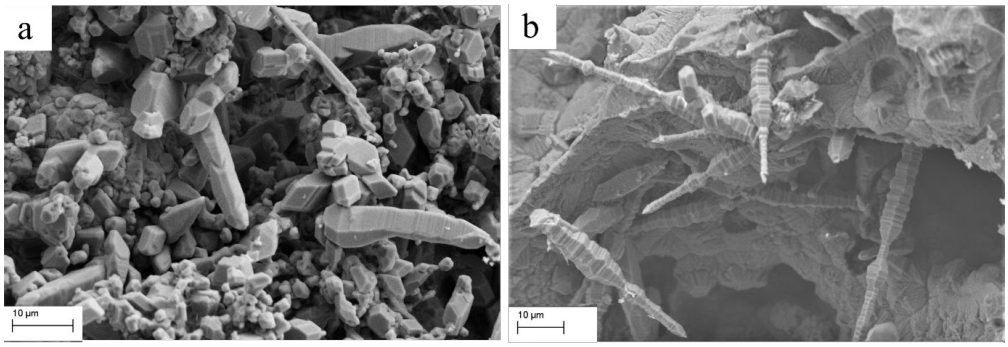

Figure 5.4.3. SEM morphologies of (a) laboratory-produced SiC from coal at ~1800 °C and (b) SiC from industry, formed at Zone 2, where temperature is assumed to be about 1800 °C.

In **Zone 3** (**Figure 5.4.1**), the lower part of the cavity walls consists of porous SiC, partly filled with molten Si, and was observed in some of the furnaces after excavations [24, 25]. These SiC crystals together with molten Si make the upper part of the deposits firm enough to create a wall. The β-SiC formed from carbon particles in the outer zone of the furnace (**Zones 1** and **2** in **Figure 5.4.1**) move to this inner zone, close to the cavity where the temperature ≥ 2000 °C. The SiC samples from **Zone 3** close to the electrode, collected after various excavations, were found to be denser with a structure different from the original carbon [35]. Hence it was assumed that the SiC found in the bottom portion near to the electrode was SiC from the original carbon particles that had further transformed to α-SiC.

Figure 5.4.4 shows the macroscopic and the corresponding SEM morphologies of β-SiC heat-treated in the laboratory at 2300 °C and the SiC sample obtained from **Zone 3**. Both the SiC samples have similar structures, hexagonal plate-shaped SiC crystals. In both these SiC samples, in addition to 3C, α-SiC polytypes of 6H, 4H, and 15R were observed, confirming that both of these samples, formed at temperatures > 2300 °C, were α-SiC. Based on the XRD quantitative SiC polytype analysis, more than 90 wt.% of the SiC excavated from industrial Si furnace crusts consisted of α-SiC. In the industrial SiC samples, 2H and 8H were also found, in addition to 6H, 4H, and 15R [18].

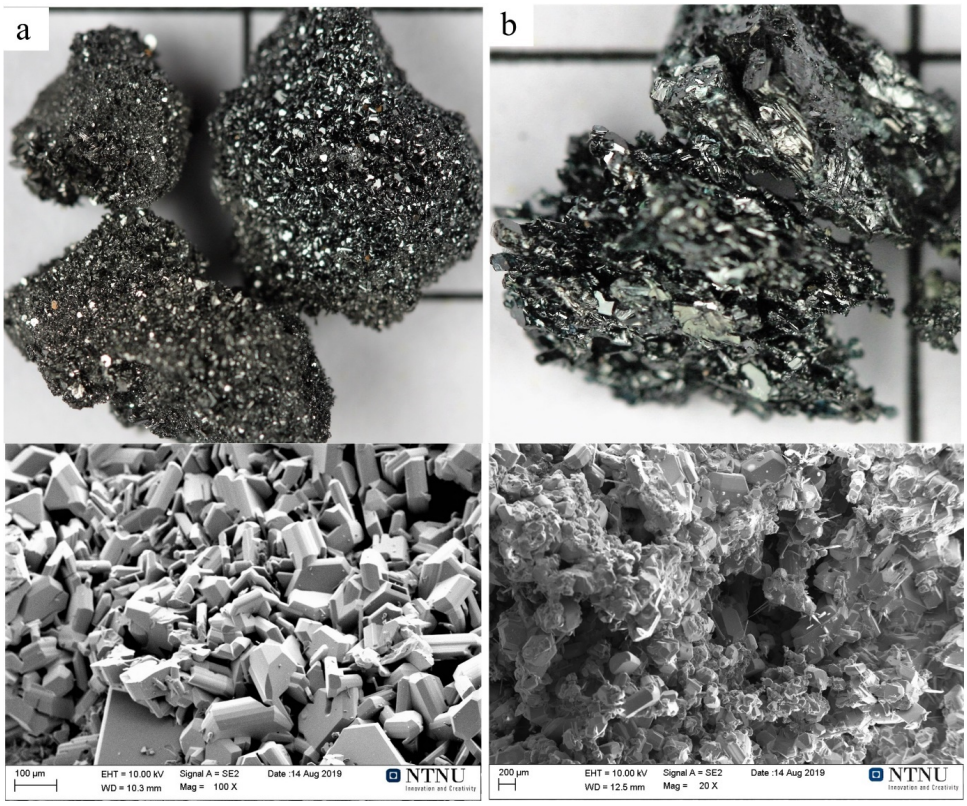

Figure 5.4.4. Original samples (top panel) and corresponding SEM morphologies (bottom panel) of (a) β-SiC heat-treated at 2300 °C in laboratory and (b) α-SiC obtained from industry.

The EPMA elemental mapping of the three industrial SiC samples showed the presence of Fe, Al, Ca, and O in them (**Figure 4.4.3, Figure 4.4.6**, and **Figure 4.4.13**). Therefore, during the industrial Si process, along with temperature and high amounts of elemental Si in the SiC, impurities might also have enhanced the extent of transformation to α-SiC. The laboratory-produced SiC samples were exposed only to CO(g) atmosphere, whereas the gas atmosphere in an industrial furnace is a combination of a higher partial pressure of SiO(g) along with CO(g). In addition, the industrial samples might have been exposed to higher temperatures for days and weeks, not just hours.

Myrhaug [20] excavated a 150 kW pilot scale Si furnace and analyzed the zones as well as various samples collected from different positions in the furnace. The illustration of the furnace is shown in **Figure 2.1.16**. He noticed a small crater wall filled with SiC particles precipitated from the gas phase (**Zone 3,** yellow region). In the SiC crust, large gas channels were also noticed, and precipitates of SiC in the shape of dendrites were observed inside these

gas channels. Tangstad et al. [15] proposed that the accumulated carbon or SiC exposed to much higher temperatures (> 2000 °C), formed gaseous compounds containing carbon or Si. During cooling, around 2000 °C, the gaseous products from carbon and Si are precipitated as α-SiC. The SiC crust from the gas species could also form in **Zone 3** (**Figure 5.4.2**) close to the arc. In the Si furnace, the arc near the electrode has temperatures above 2000 °C and it might be at this temperature region that the large amounts of $SiC_2(g)$ as well as Si(g) are produced, which might later condense on cooling and precipitate as α-SiC. Hence, the α-SiC in industrial furnaces might have been produced either directly by transformation of β-SiC, as investigated in this work, or from gas species. In either case, a temperature > 2100 °C is required, at least locally, for α-SiC to form.

Liquid silicon forms SiC by reacting with any available carbon [6]. As it cools, it precipitates SiC from carbon dissolved in the liquid Si, as the saturation limit of carbon decreases with temperature. This is represented as **Zone 4** in **Figure 5.4.2.** This SiC was however found to be β-SiC [29], and must again be exposed to higher temperatures for it to transform to α-SiC. In addition, β-SiC that was not consumed might also be found in **Zone 4.**

6 Conclusions

The formation of β- and α-SiC during Si/FeSi process and the features of Si formation in the β-SiC particles was studied in this thesis. The three carbon materials chosen for this study were charcoal, coal, and pet-coke, the commonly used carbonaceous reduction materials in the Si process.

The SEM and EPMA analyses revealed that SiC forms by two predominant mechanisms; they form as SiC surface crystals on the carbon surfaces, while the pore walls of carbon materials themselves simultaneously transform to SiC. SiC surface crystals of various sizes and shapes were observed on the carbon particles, which are assumed to be formed via a gas phase reaction where SiO(g) and CO(g) reacts to form SiC. The pore walls transform to SiC when SiO(g) meet the unreacted carbon, which is a gas-solid reaction mechanism. SiC surface crystals in the shape of hexagonal micro-bullets were observed on the surfaces of β-SiC particles formed from charcoal. The micro-bullet crystals formed only in charcoal, at the temperature ranges of 1700–1800 °C. The ease with which these could be produced from bio-carbon materials, in a limited temperature regime, could provide an attractive aspect to fabricate SiC micro/nano ceramics.

The material properties such as porosity and cell wall thickness of the selected carbon source had a substantial influence on the extent of SiC formation. Charcoal has the highest porosity and the lowest cell wall thickness when compared with coal and pet-coke, and it formed the largest quantity of SiC in this study. Pet-coke produced the least amount of SiC because it has the thickest cell walls and the lowest porosity, thus leaving the highest amount of unreacted carbon in it. The conversion of carbon to SiC broadly follows the mechanism explained by SCM in charcoal. The partly converted SiC particles obtained from charcoal had sharp boundaries between the SiC formed in their peripheries and the unreacted carbon in the middle regions of the particles. In coal, the SiC formation was more spatially distributed, and in pet-coke a sharp boundary was observed between the pores of reacted and unreacted regions.

The present study evidently confirmed the effect of the SiO pressure. Between the two SiO-sources used in this study, a mixture of (SiO_2 + Si) and pellets of (SiO_2 + SiC), larger quantities of β-SiC were produced on using (SiO_2 + Si), which provided a higher SiO pressure. For both SiO-sources, charcoal again produced more SiC compared with coal and pet-coke.

β-SiC was produced from charcoal, coal, and pet-coke at the temperature ranges of 1750–1900 °C, in the induction furnace by two methods; constant volume and constant weight experiments. The constant volume experiments were performed using a 10 cm thick carbon layer in the crucible, whereas for the constant weight experiments, the total raw material weight was

kept constant according to the stoichiometry. The total quantities of SiC obtained by both the approaches did not show any significant variations between them.

One of the major results emerged from the present study was the formation of elemental Si in the SiC particles at temperatures much lower than the theoretical Si production temperature (~1800 °C). The experiments conducted in the induction furnace produced Si in the SiC particles at temperatures < 1750 °C. To validate results from the induction furnace experiments, i.e., production of SiC and Si using the selected carbon sources, small-scale experiments were performed in the graphite tube furnace in a more controlled environment. These experiments also yielded Si in the SiC particles at 1674 °C, for a higher SiO pressure using (SiO_2 + Si), and their quantities increased with increasing temperatures. Hardly any condensate formation was observed on the surfaces of the SiC particles, based on the EPMA-BSE images. The formation of elemental Si at lower temperatures shows that the condensation reactions are slow and hence, the SiO pressure is not in thermodynamic equilibrium with the condensed phases.

During the SiC production with (SiO_2 + Si), the total SiO(g) pressure is presumed to be close to 1 atm in the lower part of the carbon materials, which is high enough to produce Si at lower temperatures. This pressure range is higher than the equilibrium pressure required for the condensation reaction, which verifies that the condensation reaction is kinetically hindered. This is also observed in the industrial furnaces where the Si yield is typically in the range of 80–90%. This Si loss indicates a much higher SiO pressure existing in the charge, higher than the equilibrium pressure required for the condensation reactions.

Various excavation reports have revealed that when β-SiC formed in the outer zone comes to the inner zone of the furnace, the higher temperatures transform it to α-SiC containing various polymorphs of SiC. To study the structural variations occurring in SiC at these higher temperature zones, heat-treatment experiments were performed in the graphite tube furnace at temperatures 2100–2450 °C. β-SiC with no elemental Si and varying amounts of elemental Si in them were heat-treated. Results from the heat-treatment experiments showed that there are three main factors that influence the extent of transformation to α-SiC; the temperature, amount of elemental Si in the β-SiC particles, and type of the carbon material that produced the β-SiC. The charcoal-converted β-SiC particles easily transformed to α-SiC at 2100 °C, compared with the β-SiC from coal and pet-coke. Moreover, the amount of elemental Si in SiC particles enhanced the transformation to α-SiC at 2100 °C.

A hot-press furnace was also chosen to check whether temperature, time, and pressure have any influence on the transformation of β-SiC to α-SiC. The β-SiC with 9 wt.% Si was heat-treated at 2000 and 2100 °C, at different pressures and holding durations. They did not

transform to α-SiC after these experiments. The in situ hot-press furnace cannot operate at temperatures above 2100 °C. Therefore, further work with higher temperatures, pressures, and holding durations are required to confirm their influence on α-SiC formation.

As the main constituents around the arc are Si and carbon, at around 3000 °C, quite large amounts of $SiC_2(g)$, $Si_2C(g)$, and Si(g) are produced. As these gases flow from the arc region to the regions of relatively lower temperatures in furnace, they condense at around 2000 °C. Most of the gases condense into solid SiC (α-SiC) and elemental Si. As Si(g) and $SiC_2(g)$ has higher equilibrium concentrations than the other carbon and Si bearing gas species, these two gases could react together to form precipitates of α-SiC at temperatures lower than 2000 °C.

The laboratory-produced SiC samples were compared with three samples of SiC obtained from the industry. Based on excavations and temperature distribution in the industrial furnace, SiC would be located at different regions in different forms. In the outer zone, at temperatures < 1700 °C, SiC crystals in the shape of whiskers (β-SiC) had formed, when coal was used as the main carbon source. In the inner zone, where the temperatures range from 1800 °C and above, the partly converted SiC that entered this region completely transformed to SiC. Thick surface crystals of different sizes and shapes had formed in the pores of the coal particle. The SiC structures were dense, which indicated formation of elemental Si in them. Based on the laboratory experiments (at 1750–1900 °C) using charcoal, coal, and pet-coke, the SiC produced by the direct reaction of carbon with SiO(g) was confirmed as β-SiC. The β-SiC formed in the outer zone of the furnace transforms to α-SiC, when it reaches the inner zone of the furnace, close to the cavity where the temperatures are ≥ 2000 °C. The SiC obtained from industry, which had been exposed to a temperature ≥ 2000 °C, had completely transformed to α-SiC.

7 Novelty and industrial significance

Though the physical and structural properties of commercial SiC are well documented, the formation processes as well as properties of SiC formed during the industrial production of Si have not been investigated extensively. This motivated the research presented in this thesis, where I predominantly analyzed formation of different types of SiC from various carbon sources that are generally used in the industrial production of Si. Analyzing the characteristics of SiC produced from different carbon materials and the changes they undergo at higher temperatures are relevant to the Si industry and several other fields, including development of high-temperature power electronic devices. This study investigated transformation of β-SiC to α-SiC at temperatures higher than 2000 °C. The influences of temperature, properties of original carbon materials, and presence of elemental Si in β-SiC, on the extent of its transformation to α-SiC were analyzed.

This study validates the efficacy of charcoal-converted β-SiC particles to easily transform to α-SiC at 2100 °C, even without a significant presence of any known impurities in the original carbon source. Another pivotal finding from this study was the presence of elemental Si in β-SiC particles, which played a crucial role in enhancing the extent of their transformation to α-SiC.

So far, we believed that Si is produced at a temperature of 1811 °C and a pSiO(g) of 0.67 bar. However, in this study, formation of elemental Si in SiC particles was observed even at 1674 °C at higher SiO pressures. This shows that the gas phase will not be in equilibrium with the condensation products. The formation of Si in SiC particles was found to be directly proportional to the increasing temperatures. Thus, the current findings prove that it is possible to produce Si in SiC particles quite higher up in the furnace, even at temperatures lower than 1800 °C, provided the partial pressure of SiO(g) is favorable.

Being one of the main electrical conducting materials in the crater wall, SiC plays an active role in the energy distribution inside the furnace for Si process. Despite having same composition, each SiC polytype has its own unique set of electronic properties. Conductivity of SiC varies with temperature, depending on the number of polytypes present in it. This study identified and analyzed the structures of SiC and the various polytypes formed in them, produced over a wide range of temperature (1647–2450 °C) attainable in laboratory-scale experiments. Results obtained from the analysis would certainly provide the industry with an insight into the key factors influencing Si production and intermediate formation of SiC in the process, and the importance of choosing the right carbon material, for efficiently producing Si.

Another novel aspect of this research was the discovery of SiC crystals in the shape of micro-bullets grown on the charcoal substrate. Despite high density stacking faults in the growth direction, the sizes and morphologies of the micro-bullets were relatively homogeneous, i.e., their growth was quite robust at the synthesis temperature (~1750 °C). These findings present the SiC ceramic industry with an opportunity to explore the possibility of developing novel light-weight high-temperature resistant materials from bio-carbons that possess anisotropic porosities.

8 Future work

As the present work produced the highest concentration of SiC from charcoal, it will be interesting to investigate the production of β-SiC and elemental Si using different charcoal sources. A detailed analysis of the rates of β-SiC to α-SiC transformation at various pressures and time durations could give more insight into the efficient formation of α-SiC, which might have an impact in the Si industry. Computational modeling of the transformation of β-SiC to α-SiC would be an interesting approach for further research.

In each type of material, both porosity and cell wall thickness are different, and the type of material in itself is different. As this study utilized only one of each type of those materials, the influence of their main characteristics, i.e., porosity and cell wall thickness, on β–SiC formation should further be investigated. Myrhaug [20] and Ramos [49] investigated different types of charcoals and found results similar to the present study. Myrhaug [20] also found similar conclusions with two types of coals. Previous results for coal (Buø [99], Raanes and Grey [21], Myrvågnes and Lindstad [106], and Myrvågnes [39]), used coal rank as a major influence rather than the porosity and cell wall thickness, although the latter was not reported.

While the carbon to β-SiC production has been previously investigated at 1650 °C, the present study is one of the few works that has performed the reaction at a wider temperature range. The results showed the significance of the SiC surface crystals. As a next step, quantifying the amount of SiC surface crystals versus pore wall-SiC transformation should be executed, to evaluate if the SiC surface crystals could be of equal importance industrially.

The predominant theory that prevails today is that the elemental Si is produced in the industrial furnaces only at around a high temperature of 2000 °C. However, this study proved that small quantities of Si could be produced even at lower temperatures, both in the SiC structures as well as during the condensation to SiO_2 and Si. It would be interesting to comprehend the governing mechanisms behind this, and total modeling of the Si producing mechanisms in an industrial furnace would provide further information on the role each of these mechanisms plays in the Si formation. Another goal would be to determine the role of rates of SiC reactions in the formation of β- or α-SiC.

This thesis has tried to study the role of total pressure on the β-SiC to α-SiC transformation at high temperatures. However, the effect of total pressure, i.e., pressure at the lower part of the furnace, on the β-SiC to α-SiC transformation should also be further investigated.

One of the theories suggests that the α-SiC forms through a gas phase reaction. This could be of special interest around the arc area in an industrial furnace. Plasma experiments in a graphite crucible with liquid Si could simulate this industrial condition, which could validate if the gas would condensate to form α-SiC at lower temperatures.

Bibliography

[1] G. L. Harris. *Properties of silicon carbide*. INSPEC, the institution of Electrical Engineers, United Kingdom, 1995.

[2] H. Abderrazak and E. S. B. H. Hmida. Silicon carbide: synthesis and properties. *Properties and applications of Silicon Carbide*, pages 361–388, 2011. doi: https://doi.org/10.5772/15736.

[3] P. Greil, T. Lifka, and A. Kaindl. Biomorphic cellular silicon carbide ceramics from wood: I. processing and microstructure. *Journal of the European Ceramic Society*, 18(14):1961–1973, 1998. doi: https://doi.org/10.1016/ S0955-2219(98)00156-3.

[4] P. Greil, T. Lifka, and A. Kaindl. Biomorphic cellular silicon carbide ceramics from wood: II. mechanical properties. *Journal of the European Ceramic Society*, 18(14):1975–1983, 1998. doi: https://doi.org/10.1016/ S0955-2219(98)00155-1.

[5] L. H. Lindstad. *Recrystallization of silicon carbide*. PhD thesis, Dr.Ing.thesis, Department of Metallurgy, NTNU, Trondheim, Norway, 2002.

[6] A. Schei, J. K. Tuset, and H. Tveit. *Production of high silicon alloys*. Tapir Trondheim, Norway, 1998. doi: https://books.google.no/books?id= ZFkfAAAACAAJ.

[7] K. Tang, E. J. Øvrelid, G. Tranell, and M. Tangstad. Thermochemical and kinetic databases for the solar cell silicon materials. In K. Nakajima and N. Usami, editors, *Crystal Growth of Si for Solar Cells. Advances in Materials Research*, volume 14, pages 219–251. Springer, Berlin, Heidelberg, 2009. doi: https://doi.org/10.1007/978-3-642-02044-5_13.

[8] B. Andresen. Operational aspects of the metallurgical silicon process. *Silicon for the Chemical and Solar Industry XIII*, pages 63–74, 2016.

[9] A. M. Valderhaug. *Modelling and control of submerged-arc ferrosilicon furnaces*. PhD thesis, Universitetet i Trondheim Norges Tekniske Høgskole (Norway), 1995.

[10] M. A. Krokstad. Elektrisk resistivitet i industrielle sic-lag. Master's thesis, Institute for material technology, NTNU, Trondheim, Norway, 2014.

[11] I. T. Zherdev, I. I. Polyakov, V. E. Semenov, I. I. Barashki, D. P. Moskovtsev, and E. S. Yaskov. Critical rate of rotation for ferrosilicon furnace baths. *STAL IN ENGLISH-USSR*, (5):406, 1968.

[12] I. T. Zherdev, D. P. Moskovtsev, and I. I. Polyakov. Dimensions of the gas spaces in ferrosilicon furnaces. *STAL IN ENGLISH-USSR*, (8):635–636, 1965.

[13] I. T. Zherdev, I. I. Polyakov, D. P. Moskovtsev, and E. S. Yaskov. Methods and results from investigations of the operation of ferrosilicon furnaces. In *6th Inter- national Congress of Electroheat*, page 113, June 1968.

[14] Y. Otani, M. Saito, K. Usui, and N. Chino. The inner structure in submerged arc furnaces. In *6th International Congress of Electroheat*, page 112, 1968.

[15] M. Tangstad, M. Ksiazek, and J. E. Andersen. Zones and materials in the Si furnace. In *Proceedings: Silicon for the chemical and solar industry XII, Trondheim, Norway, June*, pages 24–27, 2014.

[16] M. Ksiazek, M. Tangstad, and E. Ringdalen. Five furnaces five different stories. In *Silicon for the Chemical and the Solar Industry XIII. Kristiansand, Norway*, pages 33–42, 2016.

[17] G. Tranell, M. Andersson, E. Ringdalen, O. Ostrovski, and J. J. Stenmo. Reaction zones in a fesi75 furnace–results from an industrial excavation. In *The Twelfth International Ferroalloys Congress: Sustainable Future*, pages 709–715, Helsinki, Finland, 2010.

[18] E. Ringdalen. SiC structures and SiC transformations in industrial Si-production. In *Silicon for the Chemical and Solar Industry XIV, Svolvær, Norway*, 2018.

[19] S. Jayakumari and M. Tangstad. Formation of elemental silicon in β-SiC particles. In *Silicon for the Chemical and Solar Industry XIV, Svolvær, Norway*, 2018.

[20] E. H. Myrhaug. *Non-fossil reduction materials in the silicon process - properties and behavior*. PhD thesis, Institute for material technology, NTNU, Trondheim, Norway, 2003.

[21] O. Raanes and R. Gray. Coal in the production of silicon rich alloys. In *INFACON VII*, 201–219. Trondheim, Norway, 1995.

[22] T. Lindstad, S. Gaal, S. Hansen, and S. Prytz. Improved SINTEF SiO-reactivity test. In *Proceedings of the XI International Conference on Innovations in the Ferro Alloy Industry*. New Delhi, India, 2007.

[23] E. A. Nordbø. Interaction of SiO-gas and charcoal and the formation of SiC and Si. Master's thesis, Institute for material technology, NTNU, Trondheim, Norway, 2019. URLhttps://ntnuopen.ntnu.no/ntnu-xmlui/handle/11250/2623366. accessed on March 29, 2020.

[24] D. Pandey and P. Krishna. The origin of polytype structures. *Progress in Crystal growth and Characterization*, 7(1-4):213–258, 1983.

[25] W. F. Knippenberg. Growth phenomena in silicon carbide. *Philips Research Report*, 18:161–274, 1963.

[26] H. Zhou and R. N. Singh. Kinetics model for the growth of silicon carbide by the reaction of liquid silicon with carbon. *Journal of the American Ceramic Society*, 78(9):2456–2462, 1995. doi: https://doi.org/10.1111/j.1151-2916. 1995.tb08685. x.

[27] R. Deike and K. Schwerdtfeger. Reactions between liquid silicon and different refractory materials. *Journal of the Electrochemical Society*, 142(2):609, 1995.

[28] A. Ciftja. *Solar silicon refining; Inclusions, settling, filtration, wetting*. PhD thesis, Institutt for materialteknologi, NTNU, Trondheim, Norway, 2009.

[29] E. A. Nordbø. The formation of SiC in liquid silicon in contact with graphite with temperature cycles.

[30] A. Schei and 0. Sandberg. Back reactions during production of silicon metalin a submerged arc electric furnace. In Grjotheim Førland and Urnes Motzfeldt, editors, *Selected Topics in High Temperature Chemistry*, pages 141–150. Universitetsforlaget, Oslo, Norway, 1966.

[31] M. B. Muller, S. E. Olsen, and J. K. Tuset. Heat and mass transfer in the ferrosilicon process. *Scandinavian Journal of Metallurgy*, (1):145–155, 1972.

[32] J. Vangskåsen. Metal-producing mechanisms in the carbothermic silicon process. Master's thesis, Institutt for materialteknologi, NTNU, Trondheim, Norway, 2012.

[33] M. Ksiazek. Elkem Bjølvefossen excavation 2016. Technical report, SINTEF Industry, Trondheim, 2016.

[34] M. Ksiazek. Wacker-1 si-furnace excavation. Technical report, SINTEF Industry, Trondheim, 2020.

[35] K. F. Jusnes. Finnfjord fesi75 furnace excavation-2. Technical report, SINTEF Industry, Trondheim, 2018.

[36] M. Ksiazek. Elkem Salten excavation 2018. Technical report, SINTEF Industry, Trondheim, 2019.

[37] M. B. Folstad and M. Tangstad. Slag in the tapping area in a Si furnace. In *Silicon for the Chemical and Solar Industry XV, Trondheim, Norway*, 2020.

[38] F. Li. *SiC production using SiO2 and C agglomerates*. PhD thesis, Institutt for material teknologi, NTNU, Trondheim, Norway, 2017.

[39] B. Monsen, M. Tangstad, and H. Midtgaard. Use of charcoal in silicomanganese production. In *Proc. of the 10th Int. Ferroalloys Cong. INFACON X, Cape Town, South Africa*, pages 392–404, 2004.

[40] V. Myrvågnes. *Analyses and characterization of fossil carbonaceous materials for silicon production*. PhD thesis, Institute for material technology, NTNU, Trondheim, Norway, 2008.

[41] I. Suarez-Ruiz, F. Rubiera, and M. A. Diez. New trends in coal conversion, 2019. doi: https://doi.org/10.1016/C2016-0-04039-1. accessed March 26, 2020.

[42] B. H. Bowen and M. W. Irwin. Coal characteristics. *CCTR Basic Facts File*, 8, 2008.

[43] *Coal, Kentucky Geological Survey, University of Kentucky*, . URL https:// www.uky.edu/KGS/coal/. accessed March 26, 2020.

[44] B. G. Miller. *Clean coal engineering technology*. Elsevier, 2010.

[45] Chapter 4 - Carbonisation processes, URL http://www.fao.org/3/X5328E/x5328e05.htm#chapter%204%20%20%20carbon. accessed March 9, 2020.

[46] Charcoal Production, URL https://energypedia.info/wiki/Charcoal_ Production. accessed November 30, 2018.

[47] Chapter 2. Wood carbonisation and the products it yields, UR http://www.fao.org/3/x5555e/x5555e03.htm. accessed October 14, 2019.

[48] G. R. Surup. *Renewable reducing agents for the use in ferroalloy industries*. PhD thesis, Faculty of Engineering and Science, Specialisation in Renewable Energy, 2019.

[49] D. C. Ramos. *QUALITY OF EUCALYPTUS CHARCOAL FOR USE IN SILICON PRODUCTION*. PhD thesis, Universidade Federal de Viosa, 2018.

[50] *Petroleum Coke: Industry and Environmental Issues*, URL https://www.everycrsreport.com/reports/R43263.html. accessed March 9, 2020.

[51] *Petroleum Coke - an overview | ScienceDirect Topics*, URL www.sciencedirect.com/topics/engineering/petroleum-coke. accessed April 1, 2020.

[52] K. Nassau. Synthetic moissanite: A new man-made jewel. *CURRENT SCIENCE-BANGALORE-*, 79(11):1572–1577, 2000.

[53] V. A. Izhevskyi, L. A. Genova, J. C. Bressiani, and A. H. A. Bressiani. Silicon carbide. structure, properties and processing. *Cerâmica*, 46(297):4–13, 2000.

[54] V. Presser and K. G Nickel. Silica on silicon carbide. *Critical Reviews in Solid State and Materials Sciences*, 33(1):1–99, 2008. URL https://www.tandfonline.com/doi/full/10.1080/10408430701718914. accessed February 26, 2020.

[55] A. L. Ortiz, F. Sánchez-Bajo, F. L. Cumbrera, and F. Guiberteau. The prolific polytypism of silicon carbide. *Journal of Applied Crystallography*, 46(1): 242–247, 2013. doi: https://doi.org/10.1107/S0021889812049151.

[56] G. C. Trigunayat. A survey of the phenomenon of polytypism in crystals. *Solid state ionics*, 48(1-2):3–70, 1991.

[57] G. R. Yazdi, T. Iakimov, and R. Yakimova. Epitaxial graphene on sic: a review of growth and characterization. *Crystals*, 6(5):53, 2016. doi: https://doi.org/ 10.3390/cryst6050053.

[58] F. Bechstedt, P. Käckell, A. Zywietz, K. Karch, B. Adolph, K. Tenelsen, and J. Furthmüller. Polytypism and properties of silicon carbide. *physica status solidi (b)*, 202(1):35–62, 1997.

[59] L. K. Frevel, D. R. Petersen, and C. K. Saha. Polytype distribution in silicon carbide. *Journal*

of materials science, 27(7):1913–1925, 1992. doi: https: //doi.org/10.1007/BF01107220.

[60] N. W. Jepps and T. F. Page. Polytypic transformations in silicon carbide. *Progress in crystal growth and characterization*, 7(1-4):259–307, 1983. doi: https://doi.org/10.1016/0146-3535(83)90034-5.

[61] S. Kawanishi and T. Mizoguchi. Effect of van der waals interactions on the stability of SiC polytypes. *Journal of Applied Physics*, 119(17):175101, 2016. doi: https://doi.org/10.1063/1.4948329.

[62] A. R. Granadeiro Costa. *Lattice location of impurities in silicon Carbide*. PhD thesis, Lisbon, IST, 2018. URL https://cds.cern.ch/record/2624048/files/ CERN-THESIS-2018-072.pdf. accessed April 1, 2020.

[63] D. Lundqvist. On the crystal structure of silicon carbide and its content of impurities. *Acta ChemicaScandinavica*,2(1):177,1948.URL http://actachemscand.org/pdf/acta_vol_02_p0177-0191.pdf. accessed March 3, 2020.

[64] P. A. Kistler-De Coppi and W. Richarz. Phase transformation and grain growth in silicon carbide powders. *International Journal of High Technology Ceramics*, 2(2):99–113, 1986.

[65] F. C. Frank. CII. The growth of carborundum: Dislocations and polytypism. *The London, Edinburgh, and Dublin Philosophical Magazine and Journal of Science*, 42(332):1014–1021, 1951. doi: https://doi.org/10.1080/ 14786445108561346.

[66] F. Mercier and S. I. Nishizawa. Bulk and surface effects on the polytype stability in SiC crystals. In *Materials Science Forum*, volume 717, pages 41–44. Trans Tech Publ, 2012. doi: https://doi.org/10.4028/www.scientific.net/MSF. 717-720.41.

[67] S. Limpijumnong and W. R. L. Lambrecht. Total energy differences between SiC polytypes revisited. *Physical Review B*, 57(19):12017, 1998. doi: https: //doi.org/10.1103/PhysRevB.57.12017.

[68] J. A. Powell. *Growth of 2H Silicon Carbide Crystals*. National Aeronautics and Space Administration, 1969.

[69] W. S. Yoo and H. Matsunami. Solid-state phase transformation in cubic silicon carbide. *Japanese journal of applied physics*, 30(3R):545–553, 1991. doi: https://doi.org/10.1143/JJAP.30.545.

[70] H. N. Baumann Jr. The relationship of alpha and beta silicon carbide. *Journal of The Electrochemical Society*, 99(3):109, 1952. doi: https://doi.org/10.1149/ 1.2779671.

[71] H. Nagasawa, K. Yagi, and T. Kawahara. 3C-SiC hetero-epitaxial growth on undulant Si (0 0 1) substrate. *Journal of crystal growth*, 237:1244–1249, 2002. doi: https://doi.org/10.1016/S0022-0248(01)02233-3.

[72] H. Nagasawa and K. Yagi. 3C-SiC single-crystal films grown on 6-inch Si substrates. *physica*

status solidi (b), 202(1):335–358, 1997. doi: https://doi. org/10.1002/1521-3951(199707)202:1<335: AID-PSSB335>3.0.CO;2-Y.

[73] M. Kanaya, J. Takahashi, Y. Fujiwara, and A. Moritani. Controlled sublimation growth of single crystalline 4H-SiC and 6H-SiC and identification of polytypes by x-ray diffraction. *Applied physics letters*, 58(1):56–58, 1991. doi: https: //doi.org/10.1063/1.104443.

[74] R. Yakimova, M. Syväjärvi, T. Iakimov, H. Jacobsson, R. Råback, A. Vehanen, and E. Janzén. Polytype stability in seeded sublimation growth of 4H–SiC boules. *Journal of Crystal Growth*, 217(3):255–262, 2000. doi: https://doi. org/10.1016/S0022-0248(00)00488-7.

[75] V. Heine, C. Cheng, and R. J. Needs. A computational study into the origin of SiC polytypes. *Materials Science and Engineering: B*, 11(1-4):55–60, 1992. doi: https://doi.org/10.1016/0921-5107(92)90190-K.

[76] G. A. Bootsma, W. F. Knippenberg, and G. Verspui. Phase transformations, habit changes and crystal growth in sic. *Journal of Crystal Growth*, 8(4): 341–353, 1971. doi: https://doi.org/10.1016/0022-0248(71)90263-6.

[77] R. I. Scace and G. A. Slack. Solubility of carbon in silicon and germanium. *The journal of chemical physics*, 30(6):1551–1555, 1959. doi: https://doi.org/10. 1063/1.1730236.

[78] R. T. Dolloff. *Research study to determine the phase equilibrium relations of selected metal carbides at high temperatures*. Aeronautical Systems Division, Air Force Systems Command, US Air Force, 1960. URL http://contrails. iit.edu/files/original/WADDTR60-143.pdf. accessed December 19, 2018.

[79] R. W. Olesinski and G. J. Abbaschian. The C-Si (carbon-silicon) system. *Bulletin of alloy phase diagrams*, 5(5):486–489, 1984.

[80] E. A. Gulbransen and S. A. Jansson. The high-temperature oxidation, reduction, and volatilization reactions of silicon and silicon carbide. *Oxidation of metals*, 4(3):181–201, 1972. doi: https://doi.org/10.1007/BF00613092.

[81] E. G. Hoel. *Structures and phase relations in silicomanganese alloys*. PhD thesis, Department of Metallurgy, NTNU, Trondheim, Norway, 1998.

[82] R. N. Hall. Electrical contacts to silicon carbide. *Journal of applied physics*, 29(6):914–917, 1958. URL https://aip.scitation.org/doi/pdf/10.1063/ 1.1723329?class=pdf. accessed December 11, 2018.

[83] L. L. Oden, and R. A. McCune. Phase equilibria in the Al-Si-C system. *Metallurgical transactions A*, 18(12):2005–2014, 1987. doi: https://doi.org/ 10.1007/BF02647073.

[84] T. Nozaki, Y. Yatsurugi, and N. Akiyama. Concentration and behavior of carbon in semiconductor silicon. *Journal of the electrochemical society*, 117(12): 1566, 1970.

[85] F. Durand and J. C. Duby. Carbon solubility in solid and liquid silicon – a review with

reference to eutectic equilibrium. *Journal of phase equilibria*, 20(1):61, 1999. doi: https://doi.org/10.1361/105497199770335956.

[86] H. Dalaker and M. Tangstad. Time and temperature dependence of the solubility of carbon in liquid silicon equilibrated with silicon carbide and its dependence on boron levels. *Materials transactions*, pages 0904060726–0904060726, 2009.

[87] L. Ottem. Løselighet og termodynamiske data for oksygen og karbon i flytende legeringer av silisium og ferrosilisium. Technical report, STF34 F93027, SINTEF Industry, Trondheim, 1993.

[88] K. Yanaba, M. Akasaka, M. Takeuchi, M. Watanabe, T. Narushima, and Y. Iguchi. Solubility of carbon in liquid silicon equilibrated with silicon carbide. *Materials Transactions, JIM*, 38(11):990–994, 1997.

[89] P. Kong, R. M. Young, T. T. Huang, and E. Pfender. Beta-SiC synthesis in an atmospheric pressure convection-stabilized arc. In *7th International Symposium on Plasma Chemistry, Eindhoven, The Netherlands*, page 674, 1985.

[90] D. D. Avrov, A. S. Bakin, S. I. Dorozhkin, V. P. Rastegaev, and Y. M. Tairov. The analysis of mass transfer in system β-SiC–α-SiC under silicon carbide sublimation growth. *Journal of crystal growth*, 198:1011–1014, 1999. doi: https://doi.org/10.1016/S0022-0248(98)01215-9.

[91] O. Levenspiel. *Chemical Reaction Engineering, 3rd Edition*. Wiley, New York, 1999.

[92] J. Szekely. *Gas-solid reactions*. Elsevier, 2012.

[93] J. Szekely and J. W. Evans. A structural model for gas-solid reactions with a moving boundary-II: The effect of grain size, porosity and temperature on the reaction of porous pellets. *Chemical Engineering Science*, 26(11):1901–1913, 1971. doi: https://doi.org/10.1016/0009-2509(71)86033-5.

[94] H. Y. Sohn. Developments in gas-solid reaction analysis. In *Julian Szekely Memorial Symposium on Materials Processing*, pages 35–65, 1997.

[95] A. Schei and S. A. Halvorsen. A stoichiometric model of the silicon process. In *Proc. from the Ketil Motzfeldt Symposium, Trondheim, Norway: University of Trondheim, Norwegian Institute of Technology*, pages 41–56, 1991.

[96] J. K. Tuset and O. Raaness. Reactivity of reduction materials for the production of silicon, silicon-rich ferroalloys and silicon carbide. In *Electric Furnace Conference*, volume 34, pages 101–107, 1976.

[97] J. M. Paull and J. B. See. The interaction of silicon monoxide gas with carbonaceous reducing agents. *Journal of the Southern African Institute of Mining and Metallurgy*, 79(2):35–41, 1978.

[98] F. J. Narciso-Romero, F. Rodrıguez-Reinoso, and M. A. Dıez. Influence of the carbon material on the synthesis of silicon carbide. *Carbon*, 37(11): 1771–1778, 1999. doi: https://doi.org/10.1016/S0008-6223(99)00045-7.

[99] T. V. Buø. Reaction rate of reduction materials for the (ferro) silicon process. In *INFACON VII*, pages 221–231. Trondheim, Norway, 1995.

[100] T. V. Buø, R. J. Gray, and R. M. Patalsky. Reactivity and petrography of cokes for ferrosilicon and silicon production. *International journal of coal geology*, 43(1-4):243–256, 2000.

[101] V. Myrvågnes and T. Lindstad. The importance of coal-and coke properties in the production of high silicon alloys. *Innovations in Ferro Alloy Industry*, pages 18–21, 2007.

[102] V. Andersen. Reaction mechanism and kinetics of the high temperature reactions in the silicon process. Master's thesis, Institute for material technology, NTNU, Trondheim, Norway, 2010.

[103] C. Sindland. Reactivity of Si and SiO_2 mixtures. Specialization Project, NTNU, 2019.

[104] S. Bao, M. Tangstad, K. Tang, and E. Ringdalen. Production of SiO gas in the silicon process. In *The thirteenth International Ferroalloys Congress: Efficient technologies in ferroalloy industry, Infacon XIII, Almaty, Kazakhstan*, 2013.

[105] M. Tangstad, J. Safarian, S. Bao, E. Ringdalen, and A. Valderhaug. Reaction rates of $2SiO_2+SiC=3SiO+CO$ in pellets at elevated temperatures. *Aspects in Mining & Mineral Science*, 2019. doi: https://doi.org/10.31031/AMMS.2019. 03.000558.

[106] W. Hertl and W. W. Pultz. SiO_2 + SiC reaction at elevated temperatures. part 2. effect of added gases. *Transactions of the Faraday Society*, 62:3440–3445, 1966. doi: https://doi.org/10.1039/TF9666202499.

[107] M. Tangstad, M. Ksiazek, V. Andersen, and E. Ringdalen. Small scale laboratory experiments simulating an industrial silicon furnace. In *The twelfth international ferroalloys congress: Sustainable future*, pages 661–670, Helsinki, Finland, 2010.

[108] R. Saadieh, M. Tangstad, and H. Wegge. Simulation of the ferrosilicon process using a small-scale laboratory furnace. In R. T. Jones & P. Den Hoed, editor, *Infacon XV: International Ferro-Alloys Congress*, Cape Town, South Africa, 2018.

[109] K. F. Jusnes. Parameters affecting softening and melting of quartz. Master's thesis, Institutt for materialteknologi, NTNU, Trondheim, Norway, 2016.

[110] P. Juven. Hot pressing and characterization of powder-based silicon substrates for photovoltaic applications. Master's thesis, Institutt for materialteknologi, NTNU, Trondheim, Norway, 2012.

[111] C. O. Gomez, D. W. Strickler, and L. G. Austin. An iodized mounting medium for coal particles. *Journal of Electron Microscopy Technique*, 1(3):285–287, 1984. doi: https://doi.org/10.1002/jemt.1060010307.

[112] S. Jayakumari, P. E. Vullum, A. T. J. van Helvoort, and M. Tangstad. SiC crystalline micro

bullets on bio-carbon based charcoal substrate. *Journal of Crystal Growth*, 545, 2020. doi: https://doi.org/10.1016/j.jcrysgro.2020. 125740.

[113] P. Pirouz and J. W. Yang. Polytypic transformations in sic: the role of tem. *Ultramicroscopy*, 51(1-4):189–214, 1993. doi: https://doi.org/10.1016/ 0304-3991(93)90146-O.

[114] A. L. Ortiz, F. Sanchez-Bajo, F. L. Cumbrera, and F. Guiberteau. X-ray powder diffraction analysis of a silicon carbide-based ceramic. *Materials Letters*, 49 (2):137–145, 2001. doi: https://doi.org/10.1016/S0167-577X(00)00358-X.

[115] R. S. Wagner and W. C. Ellis. Vapor-liquid-solid mechanism of single crystal growth. *Applied physics letters*, 4(5):89–90, 1964. doi: https://doi.org/10. 1063/1.1753975.

[116] G. McMahon, G. J. C. Carpenter, and T. F. Malis. On the growth mechanism of silicon carbide whiskers. *Journal of materials science*, 26(20):5655–5663, 1991. doi: https://doi.org/10.1007/BF00553671.

[117] Y. Li, Q. Wang, H. Fan, S. Sang, Y. Li, and L. Zhao. Synthesis of silicon carbide whiskers using reactive graphite as template. *Ceramics International*, 40(1): 1481–1488, 2014. doi: https://doi.org/10.1016/j.ceramint.2013.07.032.

[118] F. Li and M. Tangstad. Carbothermal reduction of quartz with carbon from natural gas. *Metallurgical and materials transactions B*, 48(2):853–869, 2017. doi: https://doi.org/10.1007/s11663-016-0887-3.

[119] S. Svein and T. Grande. *Chemical thermodynamics of materials: macroscopic and microscopic aspects*. John Wiley & Sons Ltd, Chichester, UK, 2004. doi: https://doi.org/10.1002/0470092688.

[120] R. Tran, Z. Xu, B. Radhakrishnan, D. Winston, W. Sun, K. A. Persson, and S. P. Ong. Surface energies of elemental crystals. *Scientific data*, 3(1):1–13, 2016. doi: https://doi.org/10.1038/sdata.2016.80.

[121] A. Broggi, M. Tangstad, and E. Ringdalen. Characterization of a Si–SiO_2 mixture generated from SiO (g) and co (g). *Metallurgical and Materials Transactions B*, 50(6):2667–2680, 2019. doi: https://doi.org/10.1007/ s11663-019-01678-x.

Appendix A: Calculations

Calculation 1: Stoichiometric calculations to produce SiC using (SiO_2 + Si) as source of SiO(g)

SiO (g) + 2C = SiC + CO (g) (1)

SiO_2 + Si = 2SiO (g) (2)

Multiply reaction (1) by 2

2SiO + 4C = 2SiC + 2CO (g) (3)

(3) – (2) gives:

SiO_2 + Si + 4C = 2SiC + 2CO(g) (4)

Based on (4), a molar ratio of SiO_2:Si:C = 1:1:4 was used to produce SiC.

Calculation 2: Stoichiometric calculations to produce SiC using (SiO_2 + SiC) as source of SiO(g)

$2SiO_2$ + SiC = 3SiO(g) + CO (5)

Multiply reaction (1) by 3

3SiO(g) + 6C = 3SiC + 3CO(g) (6)

(5) - (6) gives:

$2SiO_2$ + SiC + 6C = 3SiC + 2CO(g) (7)

Based on (7), a molar ratio of SiO_2:SiC:C = 2:1:6 was used to produce SiC.

Calculation 3: Chemical analysis calculations

Molar mass of carbon, $M_C = 12.01$ kg/mol

Molar mass of SiC, $M_{SiC} = 40.1$ kg/mol

Molar mass of silicon, $M_{Si} = 28.0855$ kg/mol

The $\%SiC$ in charcoal- and coal-converted SiC was calculated as follows:

$$100\% = \%C_{free} + \%Elemental\ Si + \%SiC$$

$$\%C_{free} = Total\ C - C\ in\ SiC = Total\ C - \%SiC\ \times\ \frac{M_C}{M_{SiC}}$$

$$\%SiC = \left(\%C_{total}\ -\ \%C_{free}\right) \times \frac{Molar\ mass\ of\ SiC}{Molar\ mass\ of\ carbon} = \left(\%C_{total}\ -\ \%C_{free}\right) \times 3.3385$$

$$Si\ in\ SiC = \%SiC \times \frac{Molar\ mass\ of\ Si}{Molar\ mass\ of\ SiC}$$

$$Elemental\ Si = Total\ Si - Si\ in\ SiC$$

The $\%SiC$ in pet-coke-converted SiC, where $\%C_{free}$ was more than 50%, was calculated as follows:

$$100\% = \%C_{total} + \%Si_{total}$$

$$\%SiC = \%Si_{total} \times \frac{M_{SiC}}{M_{Si}}$$

$$100\% = \%C_{total} + \%SiC \times \frac{M_{Si}}{M_{SiC}}$$

$$\%SiC = (100\% - \%C_{total}) \times \frac{Molar\ mass\ of\ SiC}{Molar\ mass\ of\ Si} = (100\% - \%C_{total}) \times 1.428$$

Appendix B: Quantitative XRD fitted diffractograms

Several samples showed a broad peak at around 2θ = 26°. This could arise from either a carbon phase or from a poorly crystalline SiO_2 phase. It was not quantified in the analysis.

Heat-treated β-SiC from charcoal

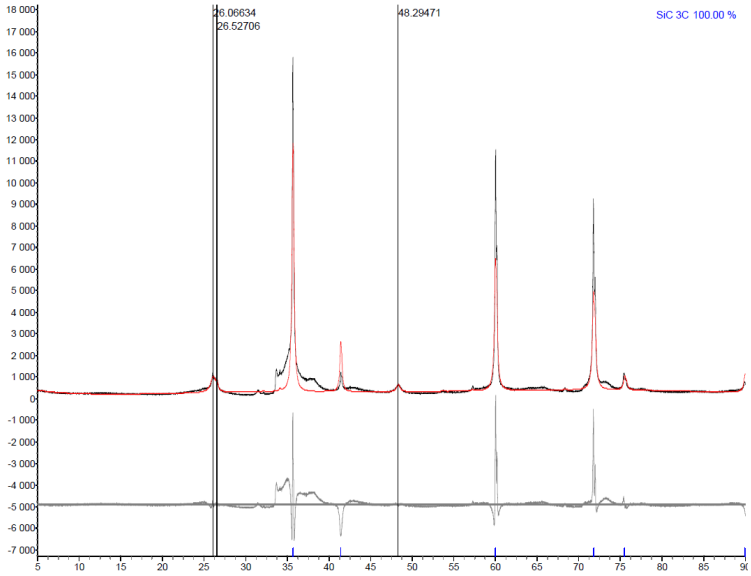

Figure B.1. Fitted diffractogram of charcoal-converted SiC sample with no elemental Si, heat-treated at 2100 °C.

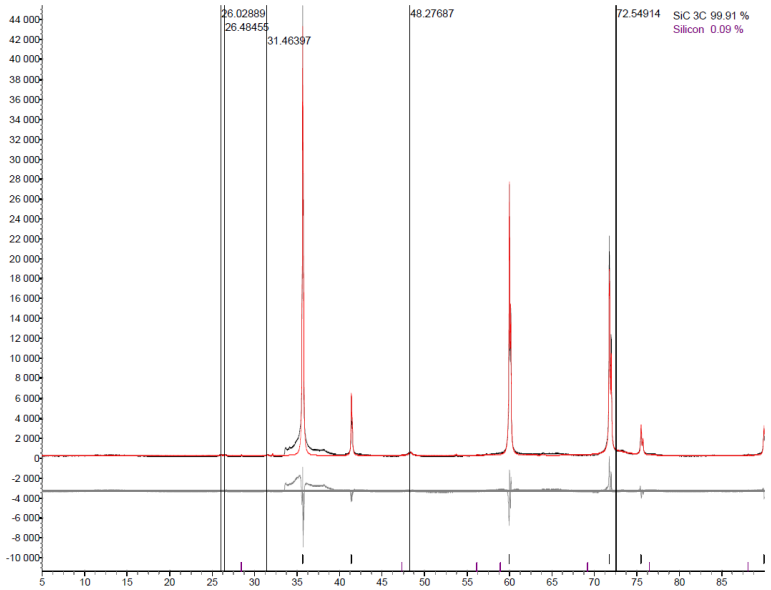

Figure B.2. Fitted diffractogram of charcoal-converted SiC sample with 9 wt.% elemental Si, heat-treated at 2100 °C.

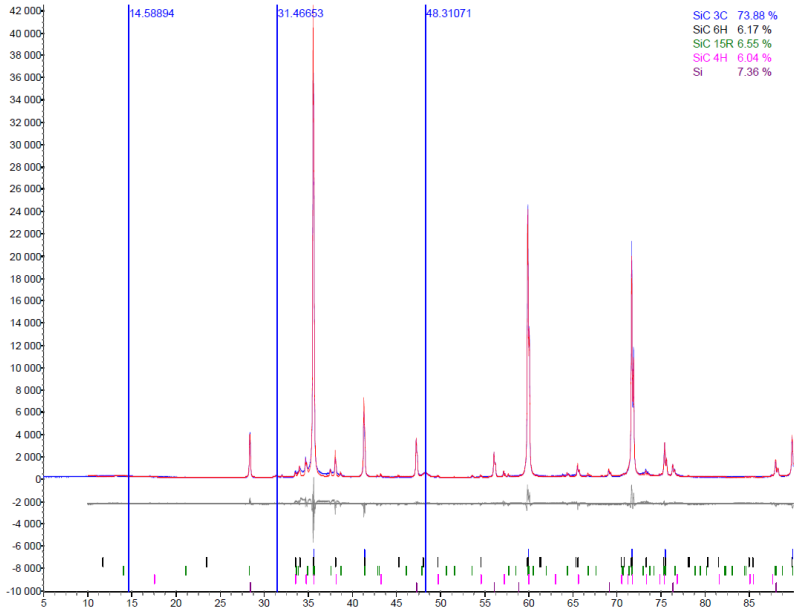

Figure B.3. Fitted diffractogram of charcoal-converted SiC sample with 39 wt.% elemental Si, heat-treated at 2100 °C.

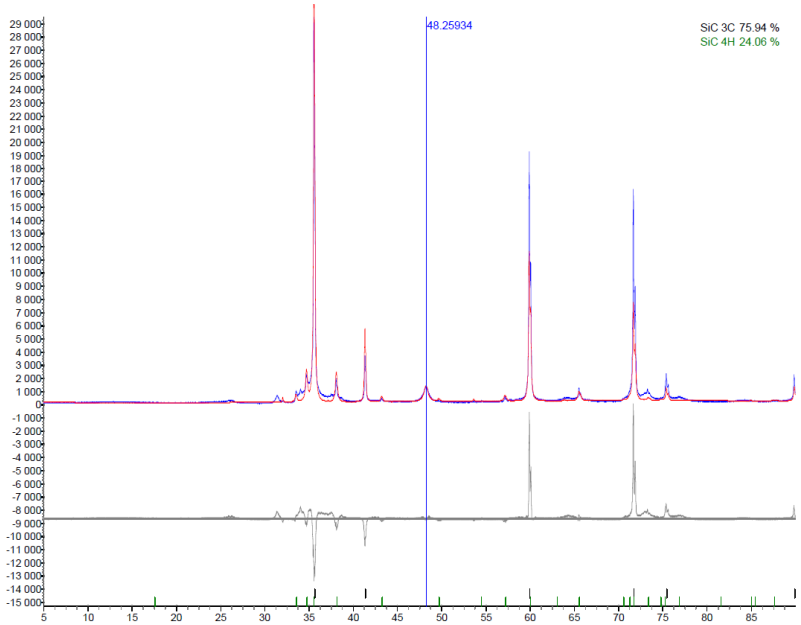

Figure B.4. Fitted diffractogram of charcoal-converted SiC sample with 10 wt.% elemental Si, heat-treated at 2100 °C.

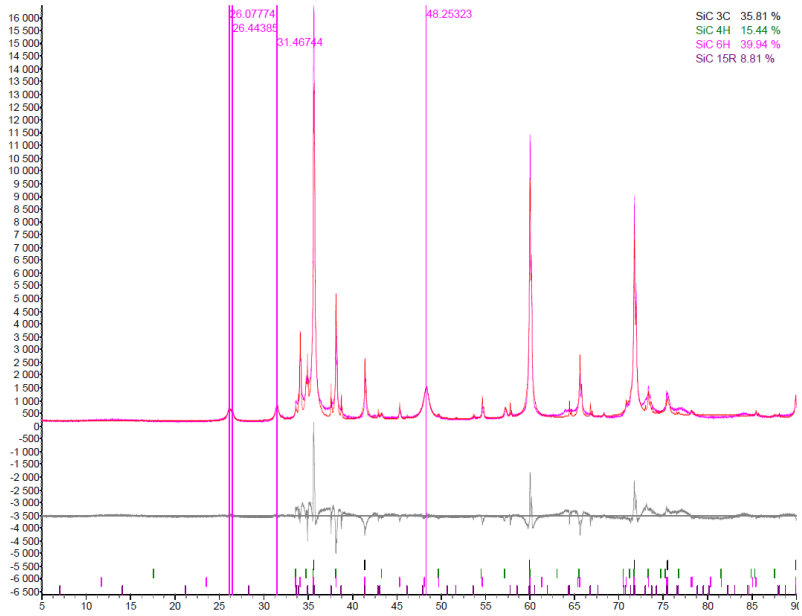

Figure B.5. Fitted diffractogram of charcoal-converted SiC sample with no elemental Si, heat-treated at 2300 °C.

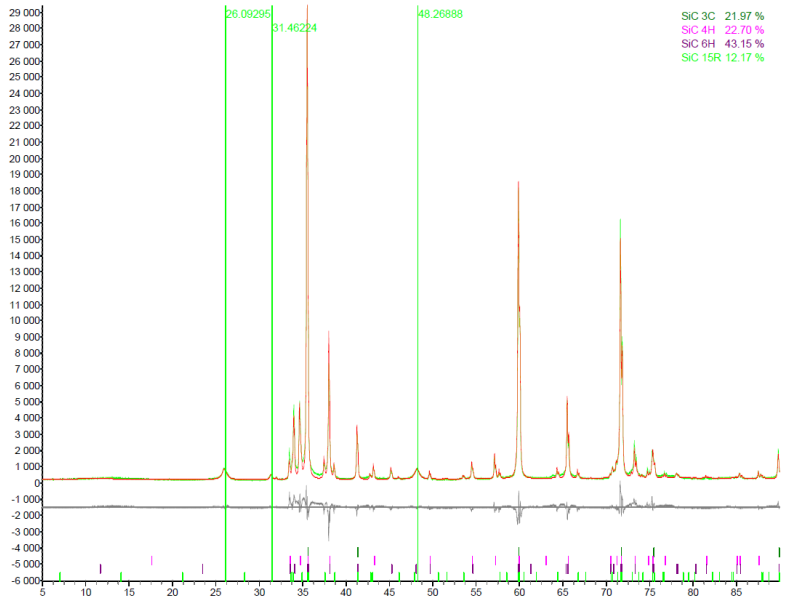

Figure B.6. Fitted diffractogram of charcoal-converted SiC sample with 9 wt.% elemental Si, heat-treated at 2300 °C.

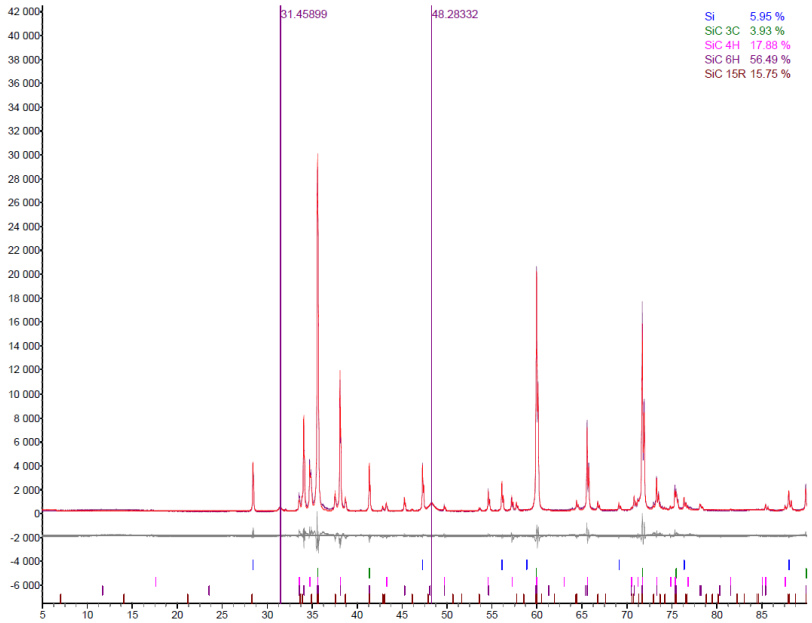

Figure B.7. Fitted diffractogram of charcoal-converted SiC sample with 39 wt.% elemental Si, heat-treated at 2300 °C.

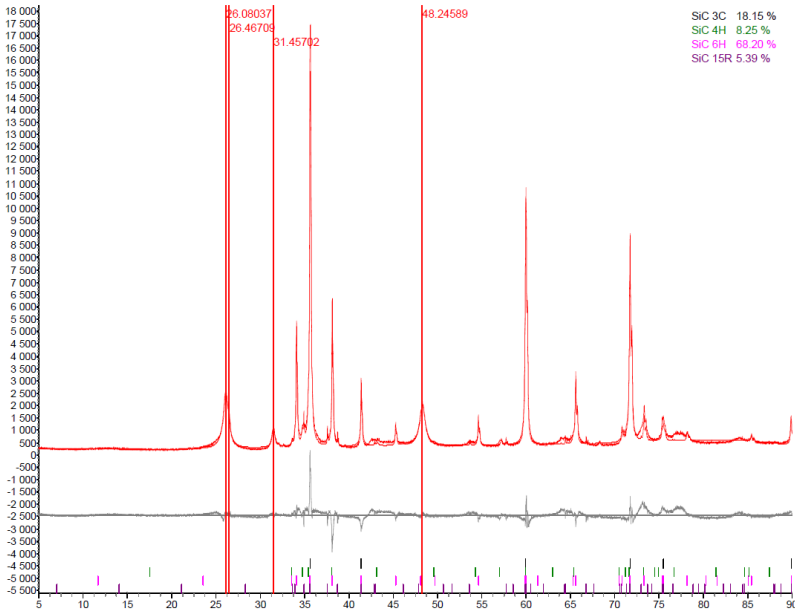

Figure B.8. Fitted diffractogram of charcoal-converted SiC sample with no elemental Si, heat-treated at 2450 °C.

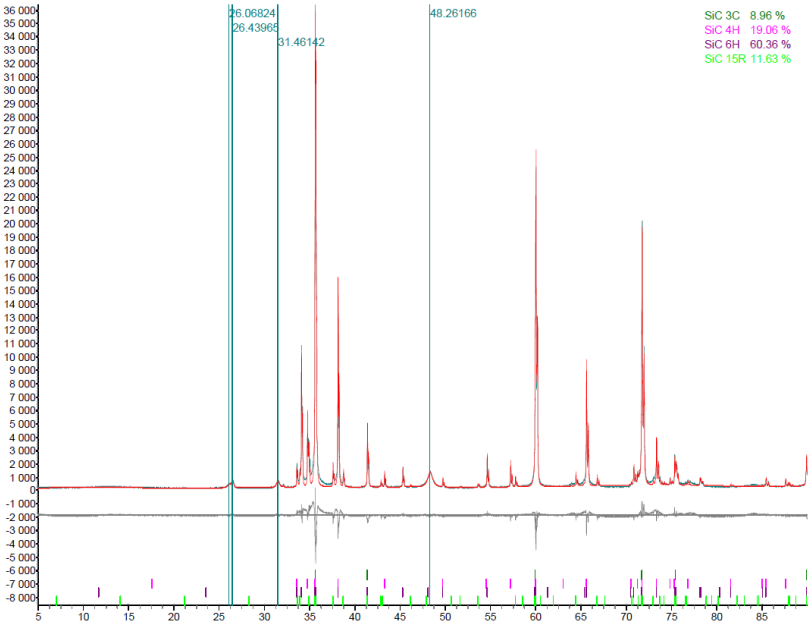

Figure B.9. Fitted diffractogram of charcoal-converted SiC sample with 9 wt.% elemental Si, heat-treated at 2450 °C.

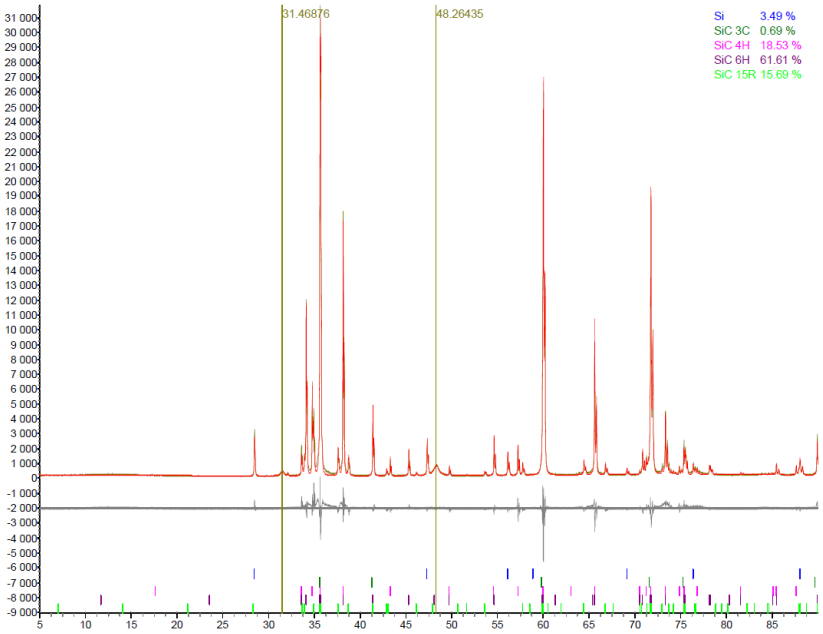

Figure B.10. Fitted diffractogram of charcoal-converted SiC sample with 39 wt.% elemental Si, heat-treated at 2450 °C.

Heat-treated β-SiC from coal

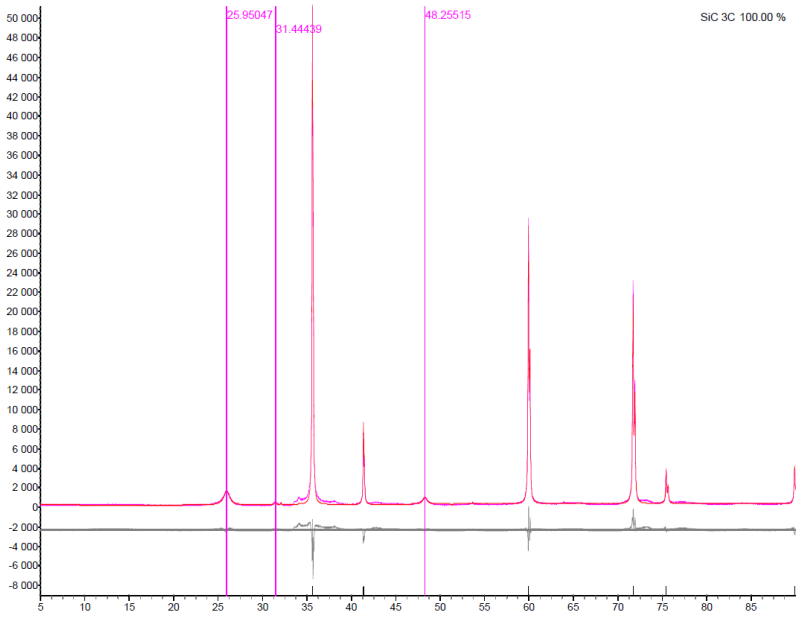

Figure B.11. Fitted diffractogram of coal-converted SiC sample with 9 wt.% elemental Si, heat-treated at 2100 °C.

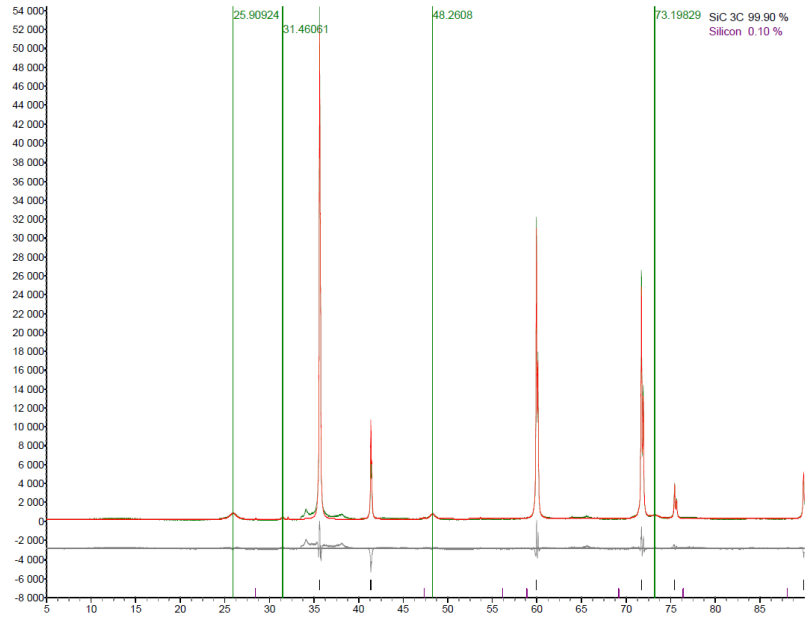

Figure B.12. Fitted diffractogram of coal-converted SiC sample with 24 wt.% elemental Si, heat-treated at 2100 °C.

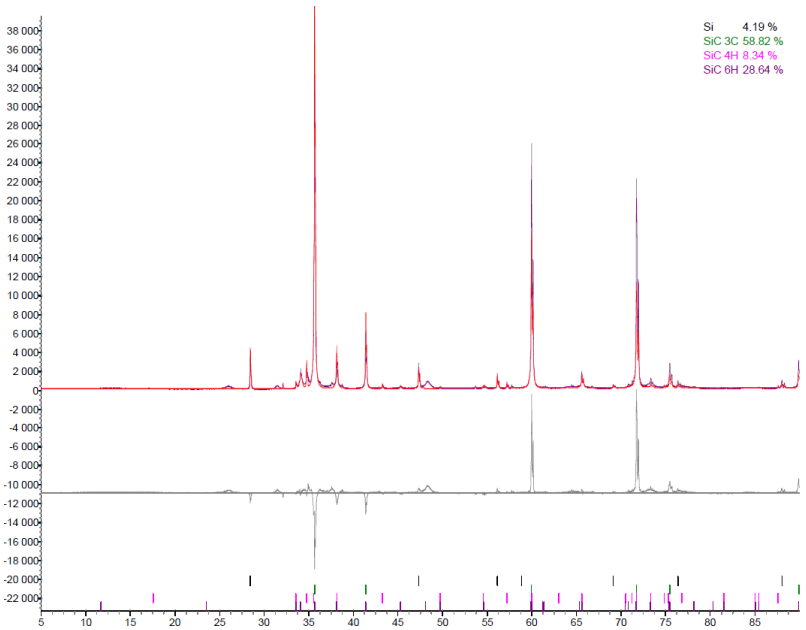

Figure B.13. Fitted diffractogram of coal-converted SiC sample with 24 wt.% elemental Si, heat-treated at 2200 °C.

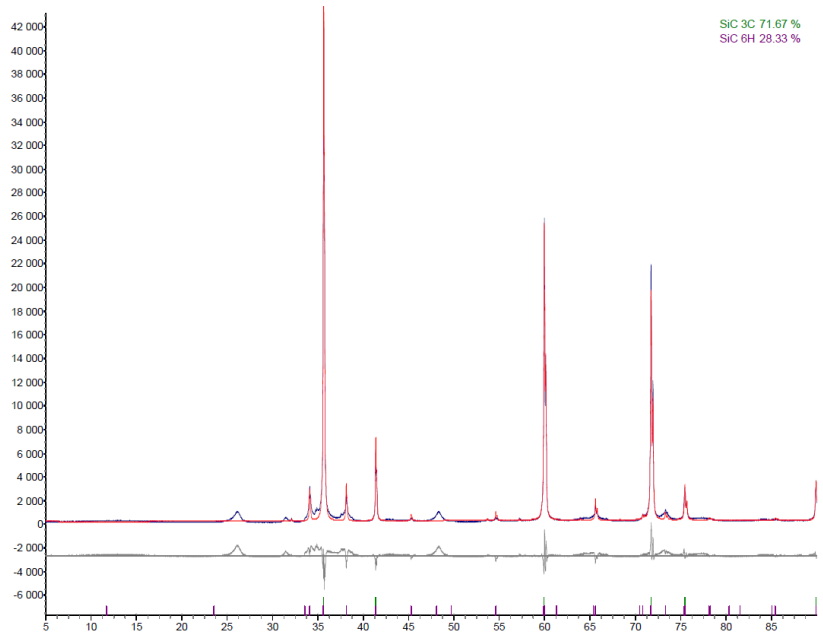

Figure B.14. Fitted diffractogram of coal-converted SiC sample with 9 wt.% elemental Si, heat-treated at 2300 °C.

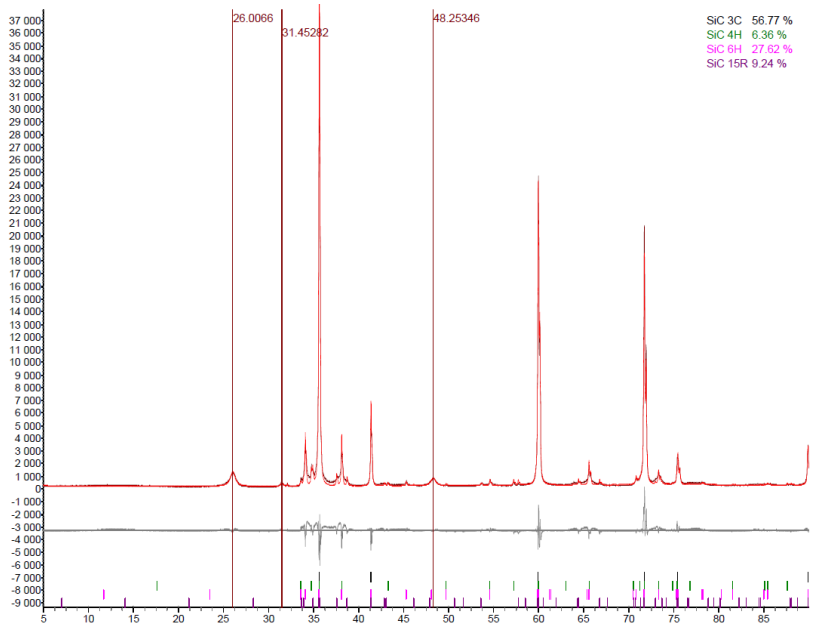

Figure B.15. Fitted diffractogram of coal-converted SiC sample with 24 wt.% elemental Si, heat-treated at 2300 °C.

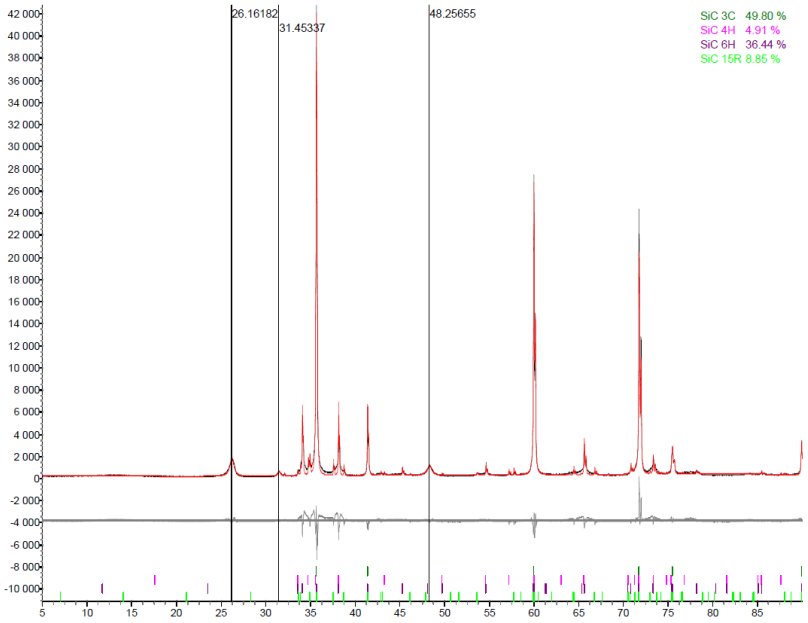

Figure B.16. Fitted diffractogram of coal-converted SiC sample with 9 wt.% elemental Si, heat-treated at 2450 °C.

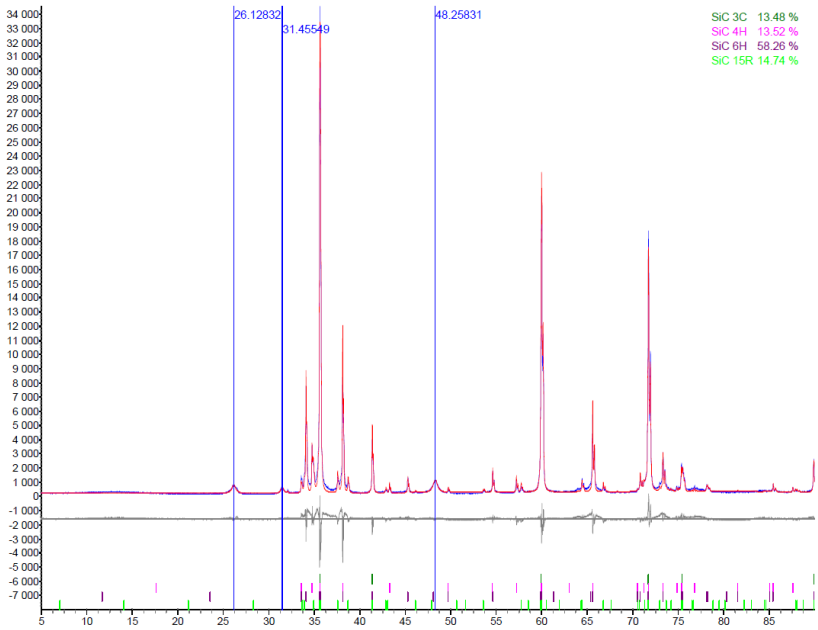

Figure B.17. Fitted diffractogram of coal-converted SiC sample with 24 wt.% elemental Si, heat-treated at 2450 °C.

Heat-treated SiC from pet-coke

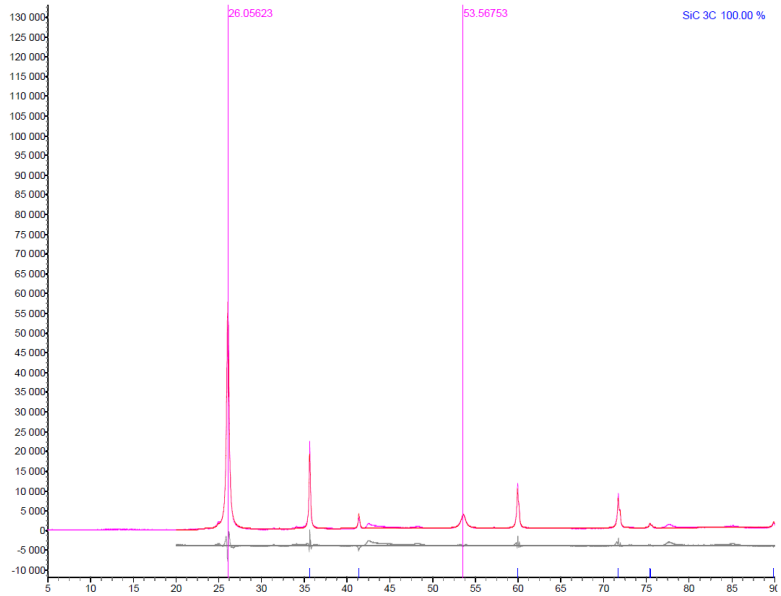

Figure B.18. Fitted diffractogram of pet-coke-converted SiC sample with 8.7 wt.% elemental Si, heat-treated at 2100 °C.

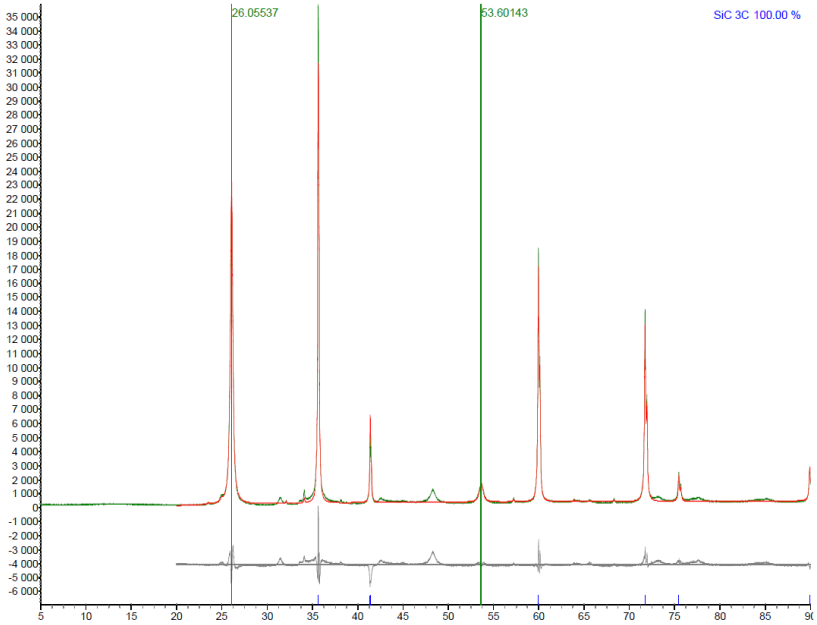

Figure B.19. Fitted diffractogram of pet-coke-converted SiC sample with 18.8 wt.% elemental Si, heat-treated at 2100 °C.

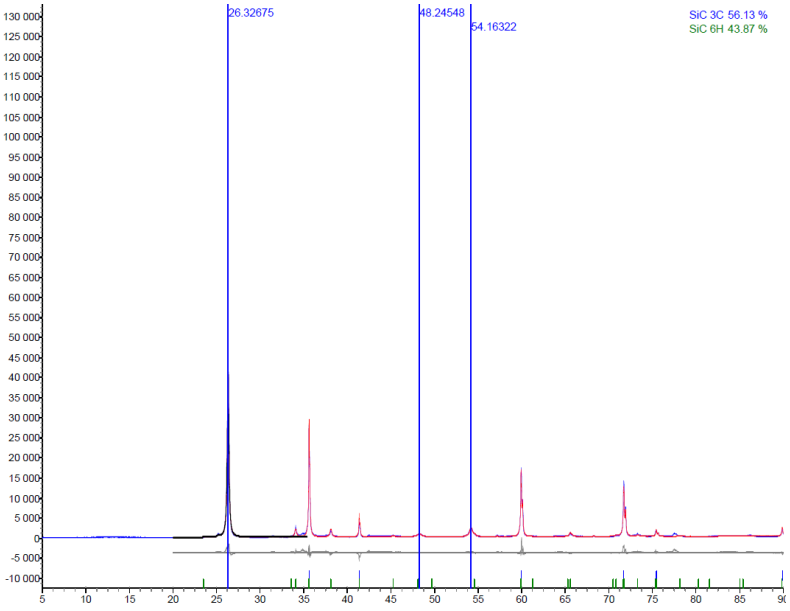

Figure B.20. Fitted diffractogram of pet-coke-converted SiC sample with 8.7 wt.% elemental Si, heat-treated at 2300 °C.

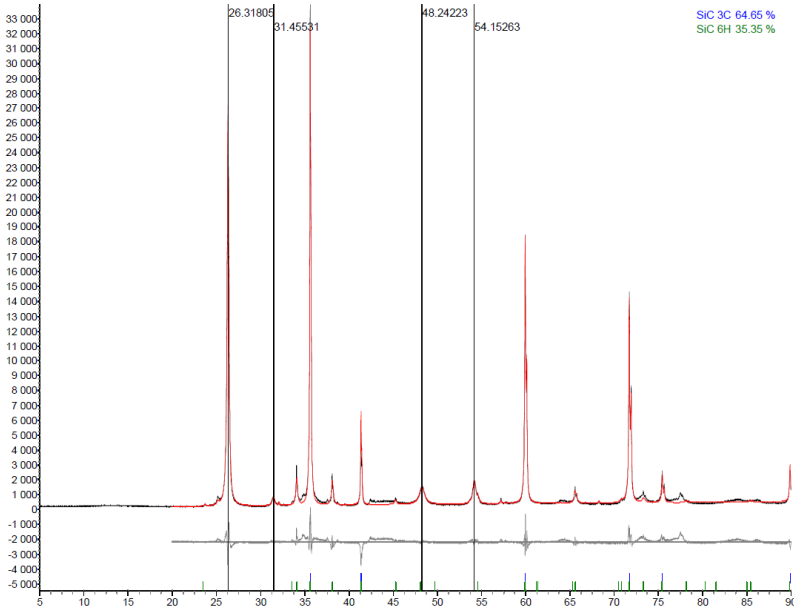

Figure B.21. Fitted diffractogram of pet-coke-converted SiC sample with 18.8 wt.% elemental Si, heat-treated at 2300 °C.

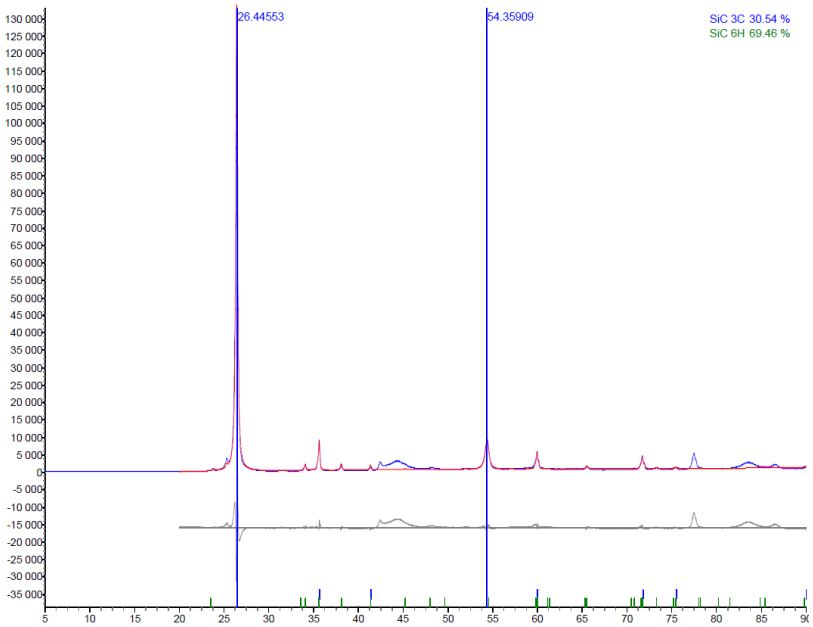

Figure B.22. Fitted diffractogram of pet-coke-converted SiC sample with 8.7 wt.% elemental Si, heat-treated at 2450 °C.

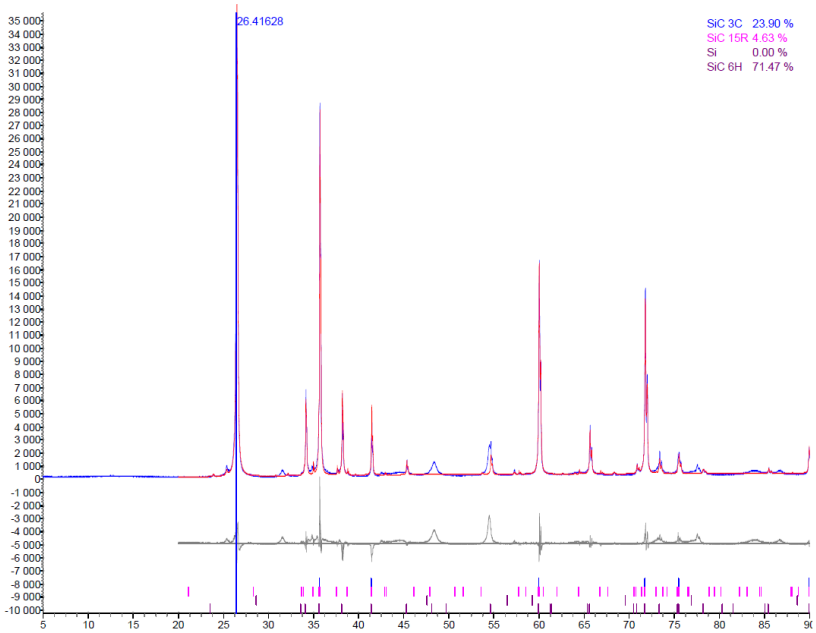

Figure B.23. Fitted diffractogram of pet-coke-converted SiC sample with 18.8 wt.% elemental Si, heat-treated at 2450 °C.